PROGRAMME AND ABSTRACTS

Intermetallics 2019

International Conference

30 September–04 October 2019

Educational Center Kloster Banz, Germany

www.intermetallics-conference.de

Monday, 30 September **School on corrosion and oxidation behaviour of intermetallic phases***	**Tuesday, 01 October**	**Wednesday, 02 October**	**Thursday, 03 October**	**Friday, 04 October**
Seminar room 6	Seminar room 1	Seminar room 1	Seminar room 1	Seminar room 1
09:00–10:30	09:00–10:15	09:00–10:30	09:00–10:30	09:00–10:30
Fundamentals and experimental determination of intermetallics' oxidation p. 8	Silicides I p. 9	Titanium aluminides I p. 12	Phases and phase stability II p. 13	Additive manufacturing of intermetallics p. 16
Coffee break	Coffee break	Coffee break	Coffee break	Coffee break
11:00–12:30	10:45–12:30	11:00–12:30	11:00–12:30	11:00–12:30
High temperature corrosion of intermetallics p. 8	High entropy alloys p. 9	Titanium aluminides II p. 12	Titanium aluminides III p. 13	Silicides II p. 16
Lunch	Lunch	Lunch	Lunch	Lunch
14:00–15:30	14:00–15:30	13:30–22:00	14:00–15:30	
Intermetallic coatings and coatings for intermetallics p. 8	Shape memory / functional intermetallics p. 10		Nickel aluminides and nickel base alloys p. 14	
	Coffee break		Coffee break	
	15:50–17:05		15:50–17:05	
	Phases and phase stability I p. 10	Bus tour Coburg with guided tours and conference dinner	Iron aluminides p. 14	
	Coffee break		Coffee break	
Foyer	17:25–19:10		17:25–18:40	
18:30–20:00	Corrosion		High temperature alloys	
Get together p. 7	p. 11		p. 15	
Seminar room 1	19:30–21:00			
20:00–21:00	Poster session			
Conference opening and opening talk p. 8	p. 17	p. 7		

* The school is especially intended for students and young scientists, the possible number of participants is limited. A registration is necessary.

Dear Colleagues and Friends,

It is meanwhile a pleasant tradition to welcome you at our Intermetallics 2019 conference, as it is already the fourth meeting in this successfully established series of conferences.

Following our traditional scheme the conference focusses on materials based on intermetallic phases (intermetallics) to be envisaged for structural as well as functional applications. With a beneficial combination of high strength, low density and good corrosion resistance, they are specifically suited for applications at high temperatures and in severe environments. As some intermetallic phases show unique physical properties, they are also of interest for various functional applications. In addition, their possible appearance, thermodynamic stability, and role as strengthening phases in High Entropy Alloys (HEAs) or Compositionally Complex Alloys (CCAs) are recent scientific issues, which are also in the focus of this conference.

The choice of local organisers and members of the international advisory board remains virtually unchanged compared to previous conferences, thus providing not only representation of all relevant topics but also a good balance between research and application. Feedback from the previous meetings showed that participants were very much satisfied with the conference, with the exception of parallel sessions in the afternoon, which necessitated some hard decisions which talks they should attend. Therefore, for Intermetallics 2019 the programme has been adjusted to fit into single sessions. As before a high-profile poster session is rounding off the conference. Following the previous successful educational seminars, a 'School on corrosion and oxidation behaviour of intermetallic phases' including possibilities and strategies for protection by appropriate coatings, which is specifically devoted to young researchers up to the PhD level, precedes the conference.

The conference again takes place at the Educational Center Kloster Banz near Bamberg, Germany. The cloister is situated in a remote place above the valley of the river Main. As a well-known educational centre, it is an ideal place for conferences with its good infrastructure and relaxing atmosphere. In addition, being situated in the central part of Germany, it is easily accessible from Nuremberg, Munich and Frankfurt airports.

We are looking forward to welcoming you at Kloster Banz,

Your Intermetallics 2019 Conference Team

Venue
Educational Center Kloster Banz
Hanns-Seidel-Stiftung e. V.
96231 Bad Staffelstein, Germany

Date
30 September–04 October 2019

Scientific organiser
Martin Heilmaier, Karlsruhe Institute of Technology, Karlsruhe, Germany

---

Scientific co-organisers and programme committee
Volker Güther, GfE Metalle und Materialien GmbH, Nuremberg, Germany
Manja Krüger, Forschungszentrum Jülich, Jülich, Germany
Svea Mayer, Montanuniversität Leoben, Leoben, Austria
Martin Palm, MPI für Eisenforschung GmbH, Düsseldorf, Germany
Wilfried Smarsly, MTU Aero Engines GmbH, Munich, Germany
Frank Stein, MPI für Eisenforschung GmbH, Düsseldorf, Germany

---

International advisory board
Bernard Bewlay, GE Global Research Center, Niskayuna, NY/USA
Gabriele Cacciamani, University of Genoa, Genoa, Italy
Helmut Clemens, Montanuniversität Leoben, Leoben, Austria
Nathalie Dupin, Calcul Thermodynamique, Orcet, France
Martin Friák, Institute of Physics of Materials, Brno, Czech Republic
Easo George, Oak Ridge National Laboratory, Oak Ridge, TN/USA
Juri Grin, MPI for Chemical Physics of Solids, Dresden, Germany
Florian Pyczak, Helmholtz-Zentrum Geesthacht, Geesthacht, Germany
Cláudio G. Schön, University of São Paulo, São Paulo, Brazil
Masao Takeyama, Tokyo Institute of Technology, Tokyo, Japan
Michel Vilasi, University of Lorraine, Nancy, France

Conference organisation
Conventus Congressmanagement & Marketing GmbH
Anja Kreutzmann/Julian Unger
Carl-Pulfrich-Straße 1
07745 Jena, Germany
Phone +49 3641 31 16-357/-330
Fax +49 3641 31 16-243
intermetallics@conventus.de
www.conventus.de

Design/Layout
Layout	krea.tif-art UG (limited liability)
Print	Kern GmbH
Circulation	150
Editorial Deadline	01 September 2019

Registration fees

University/institute	600 EUR
Industry	750 EUR
Student	300 EUR
Accompanying person*	150 EUR
Workshop: School on corrosion and oxidation behaviour of intermetallic phases**	included

Social programme***

Get together, 30 September	included
Bus tour to Coburg with conference dinner, 02 October	included

*   Get together and conference dinner is included.
**   Number of participants limited and only for students and young researchers.
*** Registration for the social programme is required.

General terms and conditions
Please find our General Terms and Conditions at www.intermetallics-conference.de.

Opening hours Check-In

Monday	08:00 a.m.–07:00 p.m.
Tuesday	08:30 a.m.–05:00 p.m.
Wednesday	09:00 a.m.–12:30 p.m.
Thursday	09:00 a.m.–05:00 p.m.
Friday	09:00 a.m.–12:00 p.m.

Internet
Wireless-Lan is available for free. You do not need to enter a password/code.

Certificate of attendance
Certificates of attendance will first be made available on the last day of the conference at the check-in desk.

Poster prizes
The three best posters will be awarded with 300 EUR each.

Poster session
Posters will be rated on Tuesday, 01 October, 07:30 p.m. Authors are requested to be present at their posters during the poster session. Drinks and finger food will be served during the poster session.

Pinboards will be numbered. The pinboards are only to be used with the designated pins. You will find your poster number in the programme book on page 24. Please note that all posters should be hanging on Tuesday, 01 October, by 04:00 p.m. and be removed at the latest by Friday, 04 October, 09:00 a.m. Posters that have not been removed by that time will be considered as waste.

Catering
Foods and drinks during the breaks will be provided.
The restaurant "Klosterschänke" is directly located on the premises of Kloster Banz and is open daily from 10:00 a.m.–10:00 p.m. *(subject to change)*.
For your information: the closest city with alternative restaurants is Bad Staffelstein, which is 5.5 km away (approximately 1 hour by foot, 7 minutes by car).

Smoking
Smoking is prohibited inside the entire conference area.

Taxi
Taxi Dütsch • Phone +49 9573 52 06/+49 9571 52 06

Price from Bad Staffelstein to Kloster Banz	about 10 EUR
Price from Lichtenfels to Kloster Banz	about 13 EUR

(Prices are subject to change.)

Submitting your presentation/technical information

Your presentation should be prepared as PDF- or PowerPoint (Office 2016) with 4:3 aspect ratio. For video- and audio-files, please use standard formats (AVI, WMV, MPG) and bring these as separate files to the speakers' ready room. When using videos, please remember to include the required Codec. The use of personal notebooks is possible upon agreement. Please provide an adapter for HDMI if necessary.

In the lecture hall, you will find a lectern with a laptop and presenter with laserpointer. A technical assistant will support you.

Should you wish to use non-digital equipment, please contact us in advance.

....

Time allotment

Please prepare your presentation for the allotted amount of time. Chairs and moderators may interrupt should you overrun your time limit.

Allotted time is assigned as follows (speaking + discussion time):
1. Invited talk   25 + 5 minutes discussion
2. All other single-session talks   12 + 3 minutes discussion

SOCIAL AND CULTURAL PROGRAMME

Get together* • Monday, 30 September

Come together for drinks and snacks. Enjoy the evening and allow yourself interesting conversations with colleagues, old friends and new acquaintances.

06:30 p.m.	Get together
08:00 p.m.	Conference opening
08:15 p.m.	Metals and alloys in commercial aircraft
	Sharvan Kumar (Providence, RI/US)

....

Bus tour to Coburg with guided tours and conference dinner* • Wednesday, 02 October

Enjoy the trip to Coburg with a guided tour through the "Veste" as well as the city of Coburg. Afterwards take the chance to get in touch with colleagues and friends and have an enjoyable evening at the restaurant "Bayrish Pub". The conference dinner includes the awarding of the poster prizes. At around 10:00 p.m. the bus returns from Coburg to Kloster Banz.

Start	01:30 p.m. at Kloster Banz (car park)
Activities	02:30 p.m.–06:00 p.m. guided tours "Veste" and "City tour" Coburg
	06:00 p.m.–10:00 p.m. dinner and award ceremony at restaurant "Bayrish Pub"
	10:00 p.m. departure to Kloster Banz
End	aprox. 10:30 p.m.
Fee	included in the conference fee
	(dinner & 2 drinks at the restaurant)

* A registration is necessary.

09:00 a.m.–03:30 p.m. Seminar room 6	School on corrosion and oxidation behaviour of intermetallic phases

09:00 a.m.	Fundamentals and experimental determination of intermetallics' oxidation Shigenari Hayashi (Sapporo/JP) This lecture will focus on oxidation and the underlying thermodynamic and kinetic fundamentals. Different intermetallic systems such as TiAl are employed to demonstrate the fundamentals and specifics for intermetallics. Additionally common experimental approaches will be discussed such as Thermogravimetric Analysis.

....

10:30 a.m.–11:00 a.m.	*Coffee break*

....

11:00 a.m.	High temperature corrosion of intermetallics Mathias C. Galetz (Frankfurt am Main/DE) Many aggressive environments in which besides oxygen other elements attack the materials such as sulphur or carbon can commonly be found at high temperatures. Such multioxidant atmospheres are discussed in this talk with respect to the resistance of intermetallics under hot corrosion, metal dusting.

....

12:30 p.m.–02:00 p.m.	*Lunch*

....

02:00 p.m.	Intermetallic coatings and coatings for intermetallics Mathias C. Galetz (Frankfurt am Main/DE) Almost all high temperature coating systems rely on intermetallic phases that provide the reservoir of stable oxide formers e.g. all turbine blades in modern aircrafts rely on intermetallics or intermetallic-rich coatings. The application of diffusion coatings is very common and allows the transformation of the surface into an aluminide or silicide phase, which offers a much higher oxidation and corrosion protection than the substrate itself. In this talk the common intermetallic coatings on classical material systems as well as coatings systems or intermetallics will be discussed.

....

06:30 p.m.–08:00 p.m. Foyer	Get together (see page 7)

08:00 p.m. Seminar room 1	Conference opening Martin Heilmaier (Karlsruhe/DE)

08:15 p.m. O–IT–01	Opening talk Metals and alloys in commercial aircraft Sharvan Kumar (Providence, RI/US)

09:00 a.m.–10:15 a.m. Seminar room 1 Chair	Silicides I Sharvan Kumar (Providence, RI/US)
09:00 a.m. O–IT–02	Invited talk: Room-temperature deformation behavior of D8$_\mathrm{I}$-type transition-metal silicides investigated by micropillar compression Kyosuke Kishida (Kyoto/JP)
09:30 a.m. O–SI–01	Laser-based additive manufacturing of Mo-Si-B alloys David Fichtner (Berlin/DE)
09:45 a.m. O–SI–02	Properties of density reduced Mo-XV-Si-B alloys Julia Becker (Magdeburg/DE)
10:00 a.m. O–SI–03	Oxidation barrier coatings with active fillers for Mo-Si-B high-temperature-alloys Caren Gatzen (Jülich/DE)

....

10:15 a.m.–10:45 a.m.   *Coffee break*

....

10:45 a.m.–12:30 p.m. Seminar room 1 Chair	High entropy alloys Manja Krüger (Jülich/DE)
10:45 a.m. O–IT–03	Invited talk: Intermetallic phases, strengthening and correlation to theoretical predictions in rapidly solidified compositionally complex alloys Emma White (Ames, IA/USA)
11:15 a.m. O–HE–01	Precipitation hardening of Cantor alloy containing titanium Uwe Gaitzsch (Dresden/DE)
11:30 a.m. O–HE–02	Development of B2/L2$_1$ precipitation strengthened CCAs in the AlCrFeNiTi system for high temperature structural applications Silas Wolff-Goodrich (Düsseldorf/DE)
11:45 a.m. O–HE–03	Structure-property relationships in B2 ordered lightweight Al-Cr-Nb-Ti-V-Zr refractory high entropy alloys Nikita Y. Yurchenko (Belgorod/RU)
12:00 p.m. O–HE–04	Microstructure and properties of intermetallic strengthened CoCrFeNi$_{2.1}$Nb$_x$ high entropy alloys Upender Sunkari (Hyderabad/IN)
12:15 p.m. O–HE–05	High entropy alloys – materials for the future or elaborate hoax? Claudio G. Schön (São Paulo/BR)

....

12:30 p.m.–02:00 p.m.   *Lunch*

02:00 p.m.–03:30 p.m.	Shape memory/functional intermetallics
Seminar room 1	
Chair	Hiroyuki Y. Yasuda (Osaka/JP)

02:00 p.m. O–SM–01	Size effect on the stress-induced martensitic transformation in Cu-based shape memory alloys
	Jose Fernando Gómez-Cortés (Leioa/ES)

02:15 p.m. O–SM–02	Lath-like martensite in Cu-Zn-Al alloys with low Al concentration
	Tobias Kaaden (Jena/DE)

02:30 p.m. O–SM–03	Martensite stabilisation effect in Ni-rich NiTi shape memory alloy
	Natalia Resnina (Saint Petersburg/RU)

02:45 p.m. O–SM–04	Mechanical properties evaluation for thermoelectric half-Heusler ZrNiSn comparing with Heusler $ZrNi_2Sn$
	Yoshisato Kimura (Yokohama/JP)

03:00 p.m. O–SM–05	New interconnectors for high temperature thermoelectric silicides based devices
	Florian Brix (Nancy/FR)

03:15 p.m. O–SM–06	High temperature stable metallisations for SAW devices
	Marietta Seifert (Dresden/DE)

....

03:30 p.m.–03:50 p.m.	*Coffee break*

....

03:50 p.m.–05:05 p.m.	Phases and phase stability I
Seminar room 1	
Chair	Klaus W. Richter (Vienna/AT)

03:50 p.m. O–PS–01	A systematic investigation on refractory-metal based phase diagrams with and without the Laves phase
	Seiji Miura (Sapporo/JP)

04:05 p.m. O–PS–02	Phase relations between fcc-Co, $L1_2$ $TiCo_3$, and the two coexisting Laves phases C36 and C15 $TiCo_2$
	Frank Stein (Düsseldorf/DE)

04:20 p.m. O–PS–03	Plasticity of topologically close packed phases – from nanomechanics to HR-TEM
	Stefanie Sandlöbes (Aachen/DE)

04:35 p.m. O–PS–04	Non-centrosymmetry – assignment of the absolute structure by X-ray diffraction and EBSD
	Ulrich Burkhardt (Dresden/DE)

04:50 p.m. O–PS–05	Influence of plastic deformation in the disorder-order transition of 18-carat red gold alloys
	Marina Garcia Gonzalez (Villigen/CH)

....

05:05 p.m.–05:25 p.m.	*Coffee break*

05:25 p.m.–07:10 p.m.	Corrosion
Seminar room 1	
Chair	Mathias C. Galetz (Frankfurt am Main/DE)

| 05:25 p.m. | Effect of Nb and V additions on oxidation behavior of α_2-Ti-30at%Al alloys |
| O–CO–01 | Shigenari Hayashi (Sapporo/JP) |

05:40 p.m.	Al-Si based oxidation protection coatings for γ-TiAl produced by magnetron sputtering and
O–CO–02	Arc-PVD
	Peter-Philipp Bauer (Cologne/DE)

| 05:55 p.m. | Oxidation of directionally solidified NiAl–(Cr, Mo) alloys |
| O–CO–03 | Golnar Geramifard (Eggenstein-Leopoldshafen/DE) |

06:10 p.m.	Mechanistic investigation of the high temperature oxidation behaviour of Fe-25Al-1.5Ta
O–CO–04	with various additives in air at 700 °C
	René Daniel Pütz (Aachen/DE)

| 06:25 p.m. | Pre-oxidation of iron aluminides |
| O–CO–05 | Janez Zavasnik (Ljubljana/SI) |

| 06:40 p.m. | Invited talk: High temperature supercritical CO_2 compatibility of intermetallics and cermets |
| O–IT–10 | Bruce A. Pint (Oak Ridge, TN/US) |

| 07:30 p.m. | Poster session |

TOFA 2020
17th DISCUSSION MEETING
on Thermodynamics of Alloys

THERMODYNAMICS OF ALLOYS
AUTUMN 2020
KLOSTER BANZ
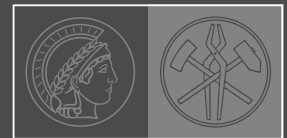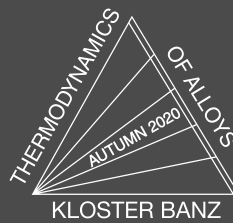
Max-Planck-Institut
für Eisenforschung

2020
28 SEPT–02 OCT

Kloster Banz l Germany
Educational Center

www.tofa2020.de

conventus
CONGRESSMANAGEMENT

09:00 a.m.–10:30 a.m. Seminar room 1 Chair	Titanium aluminides I Svea Mayer (Leoben/AT)	

09:00 a.m.
O–IT–04

Invited talk: Influence of cooling rate and composition on the formation of ribbon shaped borides in cast TiAl alloys
Rui Yang (Shenyang/CN)

09:30 a.m.
O–TA–01

Design approaches and achievements of novel TiAl alloys for jet engine applications under SIP programme in Japan
Masao Takeyama (Tokyo/JP)

09:45 a.m.
O–TA–02

Mechanical properties of SiC fiber reinforced TiAl composite
Keizo Hashimoto (Utsunomiya/JP)

10:00 a.m.
O–TA–03

Influence of C on the relaxation process and the diffusion of Ti in new generation of γ-TiAl intermetallics
Jose M. San Juan (Bilbao/ES)

10:15 a.m.
O–TA–04

Solid phase joining of γ-TiAl parts using diffusion bonding
Marcus Willi Rackel (Geesthacht/DE)

....

10:30 a.m.–11:00 a.m.   *Coffee break*

....

11:00 a.m.–12:30 p.m.
Seminar room 1
Chair

Titanium aluminides II

Masao Takeyama (Tokyo/JP)

11:00 a.m.
O–IT–05

Invited talk: Advanced intermetallic titanium aluminides – from fundamentals to application
Svea Mayer (Leoben/AT)

11:30 a.m.
O–TA–05

TCTI2 – an updated thermodynamic database for multicomponent Ti- and TiAl-based alloys
Yang Yang (Solna/SE)

11:45 a.m.
O–TA–06

Effect of hot forging at lower temperatures on microstructure and mechanical properties of β-solidifying γ-TiAl alloys
Valery Imayev (Ufa/RU)

12:00 p.m.
O–TA–07

Oxidation of Pt-Al coatings on TNM-B1 at 900 °C
Xabier Montero (Franfurt am Main/DE)

12:15 p.m.
O–TA–08

Oxidation protection of gamma-TiAl by the F-effect – ready for industrial application
Hans-Eberhard Zschau (Wurzen/DE)

....

12:30 p.m.–01:30 p.m.   *Lunch*

....

01:30 p.m.   Excursion to Coburg and conference dinner (see page 7)

09:00 a.m.–10:30 a.m. Seminar room 1 Chair	Phases and phase stability II Frank Stein (Düsseldorf/DE)
09:00 a.m. O–IT–06	**Invited talk:** Phase diagram study on the Ti-Al-M-O quaternary systems using soft X-ray emission spectroscopy Hirotoyo Nakashima (Tokyo/JP)
09:30 a.m. O–PS–06	Demixing in $D0_{22}$-like Al–Mo–Ti alloys Andreas Leineweber (Freiberg/DE)
09:45 a.m. O–PS–07	Impact of Mo and disorder on diffusionless transformations in TiAl intermetallic alloys David Holec (Leoben/AT)
10:00 a.m. O–PS–08	Phase equilibria and structural investigations in the ternary system Al-Cu-Zn Klaus W. Richter (Vienna/AT)
10:15 a.m. O–PS–09	Massive transformation in ternary Cu alloys Stephanie Lippmann (Jena/DE)

....

10:30 a.m.–11:00 a.m.	*Coffee break*

....

11:00 a.m.–12:30 p.m. Seminar room 1 Chair	Titanium aluminides III Rui Yang (Shenyang/CN)
11:00 a.m. O–IT–07	**Invited talk:** Additive manufacturing of Ti-48Al-2Cr-2Nb alloys Hiroyuki Yasuda (Osaka/JP)
11:30 a.m. O–TA–09	Production and properties of gas atomized TiAl powders Karin Ratschbacher (Nuremberg/DE)
11:45 a.m. O–TA–10	Processing TiAl via a new production route – additive manufactured (SEBM) and hot isostatic pressed near net shape capsule Julia Bieske (Erlangen/DE)
12:00 p.m. O–TA–11	Characterisation of an electron beam melted TNM titanium aluminide alloy Reinhold Wartbichler (Leoben/AT)
12:15 p.m. O–TA–12	Ingot production, powder atomisation and spark plasma sintering of tungsten containing TiAl alloys Alain Couret (Toulouse/FR)

....

12:30 p.m.–02:00 p.m.	*Lunch*

02:00 p.m.–03:30 p.m.	Nickel aluminides and nickel base alloys
Seminar room 1	
Chair	Martin Heilmaier (Karlsruhe/DE)

| 02:00 p.m. | Atomistics of self-diffusion in a triple-defect A-B binary system – Monte Carlo simulation |
| O–NA–01 | Rafal Kozubski (Krakow/PL) |

| 02:15 p.m. | Ni tracer grain boundary diffusion in a Ni-base alloy containing a graded microstructure |
| O–NA–02 | Sergiy Divinski (Münster/DE) |

| 02:30 p.m. | The synthesis and properties of aligned plate intermetallic nanostructures |
| O–NA–03 | Philip Nash (Chicago, IL/USA) |

| 02:45 p.m. | In-situ investigations of Mo-rich NiAl-(Cr, Mo) composites by synchrotron radiation diffraction during directional solidification |
| O–NA–04 | Camelia Gombola (Karlsruhe/DE) |

| 03:00 p.m. | Effect of thermomechanical treatment on microstructure and mechanical properties of a novel heavily alloyed nickel base superalloy |
| O–NA–05 | Valery Imayev (Ufa/RU) |

| 03:15 p.m. | Investigation of the reactivity in oxidising atmosphere at high temperature of laser beam melted Inconel 625 |
| O–NA–06 | Nicolas Ramenatte (Nancy/FR) |

....

| *03:30 p.m.–03:50 p.m.* | *Coffee break* |

....

03:50 p.m.–05:05 p.m.	Iron aluminides
Seminar room 1	
Chair	Claudio G. Schön (São Paulo/BR)

| 03:50 p.m. | Quantum-mechanical study of Fe-Al-based intermetallic compounds |
| O–IA–01 | Martin Friak (Brno/CZ) |

| 04:05 p.m. | Investigation of the machinability and casting behavior of Fe25Al1.5Ta |
| O–IA–02 | Heiner Michels (Aachen/DE) |

| 04:20 p.m. | Microstructure and mechanical properties of Fe-25Al-1,5Ta without and with different borides and carbides as grain refiners |
| O–IA–03 | Eva Kollmannsberger (Landshut/DE) |

| 04:35 p.m. | First wave combinatorial screening of generic intermetallic strengthened steels |
| O–IA–04 | Nele van Steenberge (Zelzate/BE) |

| 04:50 p.m. | Formation of α_c intermetallic particles in Fe- and Mn-containing Al–Si casting alloys during solidification with different cooling rates |
| O–IA–05 | Hanka Becker (Freiberg/DE) |

....

| *05:05 p.m.–05:25 p.m.* | *Coffee break* |

05:25 p.m.–06:40 p.m.	High temperature alloys
Seminar room 1	
Chair	Martin Palm (Düsseldorf/DE)

05:25 p.m. O–HT–01	Intermetallic A15 precipitation hardening in chromium – alloying strategy Mathias C. Galetz (Frankfurt am Main/DE)
05:40 p.m. O–HT–02	Deformation behavior of Nb_2Co_7 as a promising candidate for a crystal-structure-dependent mille-feuille structured material Toshiaki Horiuchi (Sapporo/JP)
05:55 p.m. O–HT–03	Identification of Laves phases in a Zr or Hf containing γ-γ' Co-base superalloy Florian Pyczak (Geesthacht/DE)
06:10 p.m. O–HT–04	Phase equilibrium among γ-Ni/TCP/GCP oP6 phases in Ni-based alloys at elevated temperatures Ryota Nagashima (Tokyo/JP)
06:25 p.m. O–HT–05	Stabilising the cubic modification of titanium trialuminide in the structure of $Ti-Al_3Ti$ composites Daria Lazurenko (Novosibirsk/RU)

CREEP 2020

2020
14 – 18 JUNE

Kloster Banz
Germany

FAU FRIEDRICH-ALEXANDER UNIVERSITÄT ERLANGEN-NÜRNBERG

SFB/Transregio 103
SUPERALLOY SINGLE CRYSTALS

www.creep2020.de

conventus
CONGRESSMANAGEMENT

15th International Conference on Creep and Fracture of Engineering Materials and Structures

09:00 a.m.–10:30 a.m. Seminar room 1 Chair	Additive manufacturing of intermetallics Alain Couret (Toulouse/FR)
09:00 a.m. O–IT–08	**Invited talk:** Prospects and challenges of electron beam based additive manufacturing of intermetallics Carolin Körner (Erlangen/DE)
09:30 a.m. O–AM–01	Properties and microstructure of nano-structured NiAl-Cr(Mo) in-situ composites processed by additive manufacturing Andreas Förner (Erlangen/DE)
09:45 a.m. O–AM–02	Additive manufacturing of multi-phase V-Si-B alloys Janett Schmelzer (Magdeburg/DE)
10:00 a.m. O–AM–03	Study on the mechanical twinning of α_2 phase in a high Nb-containing TiAl alloy after high temperature deformation Lin Song (Hamburg/DE)
10:15 a.m. O–AM–04	In situ study of beta phase ordering in TiAl alloys by neutron and synchrotron diffraction Victoria Kononikhina (Geesthacht/DE)

....

10:30 a.m.–11:00 a.m.   *Coffee break*

....

11:00 a.m.–12:30 p.m. Seminar room 1 Chair	Silicides II Kyosuke Kishida (Kyoto/JP)
11:00 a.m. O–IT–09	**Invited talk:** Properties of advanced Mo-Si-B alloys Manja Krüger (Jülich/DE)
11:30 a.m. O–SI–05	Plastic deformability in V-rich V-Si-B alloys Georg Hasemann (Jülich/DE)
11:45 a.m. O–SI–06	Microstructure optimisation of directionally solidified $MoSi_2$/Mo_5Si_3 eutectic composites Kosei Takeda (Kyoto/JP)
12:00 p.m. O–SI–07	Characterisation of the oxidation and creep behaviour of novel Mo-Si-Ti alloys Susanne Obert (Karlsruhe/DE)

....

12:15 p.m.–01:30 p.m.   *Lunch bags*

P–01   New mechanism of softening in titanium aluminide – experiment and theory
        Nitish Bibhanshu (Bangalore/IN)

P–02   Analysis of local deformation behavior in TiAl based alloys under tensile loading by digital image correlation
        Yotaro Okada (Tokyo/JP)

P–03   Initial structures effect on O-phase morphology and properties of orthorhombic titanium alloys
        Anatoly Volkov (Verkhnaya Salda/RU)

P–04   Comparative study on the oxidation behavior of two commercial TiAl alloys at 600–900 °C in air
        Lukas Mengis (Frankfurt am Main/DE)

P–05   On the creep deformation and properties of the IRIS TiAl alloy at 850 °C
        Alain Couret (Toulouse/FR)

P–06   Phase equilibria investigations in the ternary Ti–Al–Nb system at elevated temperatures
        Benedikt Distl (Düsseldorf/DE)

P–07   Phase composition and microstructure of TiAlZr alloys
        Fabian Kathöfer (Cottbus/DE)

P–08   Experimental evaluation of the isothermal section of the Ti–Al–Zr ternary system at 1273 K
        Zahra Kahrobaee (Düsseldorf/DE)

P–09   Phase equilibrium and mechanical properties of bcc-V/MAX two-phase alloys
        Hiroto Kudo (Sapporo/JP)

P–10   Structural related intermetallic phases in the Nb-Cu-Sn system
        Jonas Lachmann (Freiberg/DE)

P–11   Alloying impact on phase stability in $ZrAl_3$
        David Holec (Leoben/AT)

P–12   Early stage phenomena of kink formation in the Mg-Zn-Y LPSO phase investigated by micropillar compression
        Kouhei Ohkage (Kyoto/JP)

P–13   Simulation of cyclic functional and mechanical behavior of porous NiTi samples obtained by selective laser melting
        Elizaveta Iaparova (Saint Petersburg/RU)

P–14   Internal friction measurements on a Ni-Ti-Hf high temperature shape memory alloy
        Mikel Pérez-Cerrato (Bilbao/ES)

P–15   Strain variation during isothermal martensitic transformation in $Ti_{49}Ni_{51}$ shape memory alloy
        Aleksei Ivanov (Saint Petersburg/RU)

P–16   Strain variation induced by the martensitic transformation during isothermal holding of $Ti_{40.7}Hf_{9.5}Ni_{44.8}Cu_5$ shape memory alloy
        Elena Demidova (Saint Petersburg/RU)

P–17   Isothermal nature of magnetic-field-induced martensitic transformation in NiCoMnIn metamagnetic shape memory alloy
        Yoshiki Yano (Kyoto/JP)

P–18   Formation of intermetallics during solid-liquid inter-diffusion bonding of Pd/Ni assembly using In interlayer
        Tung-Han Chuang (Taipei/TW)

P–19   Effect of bcc and sigma phase particles on grain growth and strengthening in a CoCrFeNiMn high entropy alloy
        Margarita Klimova (Belgorod/RU)

P–20   Plastic deformation behavior of single crystalline Cr-Co-Ni equiatomic medium entropy alloy
        Kazuki Ehara (Kyoto/JP)

P–21   Thermodynamic stability of a nanocrystalline highly concentrated solid solution alloy
        Matheus A. Tunes (Leoben/AT)

P–22   On grain refinement of Fe-25Al-1.5Ta (at. %) alloy
        Emir Subašić (Aachen/DE)

P–23   Casting of iron aluminides – an investigation in industrial scale
        Bruna N. Ramirez (São Paulo/BR)

P–24   Pro-FeAl – process development for economic, efficient turbine components made out of FeAl
        Michael Ghosh (Aachen/DE)

P–25   Development of Fe-Al-Nb(–B) alloys for high-temperature applications
        Angelika Gedsun (Düsseldorf/DE)

P–26   Precipitation behavior of Nb_2Co_7 from Nb-supersaturated Co-solid solution in Co-rich Co-Nb binary alloys
        Konatsu Yamada (Sapporo/JP)

P–27   Structural and phase transformations occurring during fabrication of Ni-Al-Cr-based alloy reinforced by AlN and Cr_2N
        Maxim S. Gusakov (Korolev/RU)

P–28   Alloying effects in vanadium solid solutions
        Christopher Müller (Magdeburg/DE)

P–29   Plastic deformation behavior of single crystals of Fe-Cr sigma phase at room temperature
        Masaomi Okutani (Kyoto/JP)

P–30   The reaction of refractory carbides (borides) with iridium
        Victor V. Lozanov (Novosibirsk/RU)

P–31   In-situ observation of phase and microstructure evolution during directional solidification of novel intermetallic structural materials
        Camelia Gombola (Karlsruhe/DE)

EXTENDED ABSTRACTS

Intermetallics 2019

30 September–04 October 2019

O–IT–01

Metals and alloys in commercial aircraft

Sharvan Kumar

School of Engineering, Brown University, Providence, RI 02912, USA, Sharvan_Kumar@brown.edu

Abstract

Modern-day, self-propelled, heavier-than-air flight traces its roots back to 1903 when the Wright brothers remained in air for 12 seconds in Kittyhawk, NC. Just 30 years later, Boeing introduced the 247, a 10-passenger, all-metal twin-engine aircraft with a retractable landing gear; soon thereafter, the era of jet engines was ushered in that dramatically changed air-travel. Sixty years later, Boeing rolled out the 777, the biggest twin-engine jet ever to fly at that time and the first aircraft to be produced using computer-aided design and engineering! In the first decade of the 21st century, the full double-decker A380 that could carry more than 550 passengers took to the skies. This dramatic advance in passenger flight is filled with inventions, innovative designs, materials and technology advancements, accidents and lessons learned. Driven by performance and safety, societal needs, economy, government regulations and more, alloy and components design, process development, property assessment and life prediction have all been central to these advances. Here, I will follow this fascinating thread with a focus on alloy development for aircraft fuselage and aircraft engine over time.

O–IT–02

Room-temperature deformation behavior of D8$_l$-type transition-metal silicides investigated by micropillar compression

Kyosuke Kishida[1] and Haruyuki Inui[2]

[1]Department of Materials Science and Engineering, Kyoto University, Kyoto, 606-8501, Japan,
kishida.kyosuke.6w@kyoto-u.ac.jp

[2]Department of Materials Science and Engineering, Kyoto University, Kyoto, 606-8501, Japan,
inui.haruyuki.3z@kyoto-u.ac.jp

Introduction

Alloys containing transition-metal silicides with a general formula of TM_5Si_3 (TM = transition-metal) have been considered as promising materials for ultra-high temperature applications. These include those containing Mo_5SiB_2 and α-Nb_5Si_3 with the D8$_l$-type crystal structures have been investigated extensively in the form of Mo-Mo_5SiB_2, Mo-Mo_3Si-Mo_5SiB_2, Nb/α-Nb_5Si_3 alloys. But, low fracture toughness and ductility at ambient temperatures are still the main drawbacks for these alloys containing TM_5Si_3. The study of plastic deformation behavior of Mo_5SiB_2 and α-Nb_5Si_3 with the D8$_l$ structures is therefore of great interest. For Mo_5SiB_2, the plastic flow has been reported to be extremely difficult to occur unless otherwise the deformation temperature is raised above 1500°C even in single crystals when tested in compression at a strain rate of the order of 10^{-4} s^{-1} [1]. Because of the difficulty of plastic flow, slip systems reported so far for Mo_5SiB_2 are somewhat controversial. The slip system identified for the single crystal after compression along the [021] direction at 1500 °C was {100}[001], although the evidence for this is not sufficiently trustable due to the difficulty in slip plane identification arising from severe oxide formation on the specimen surface and climb motion of dislocations at high temperatures [1]. Recently, we have applied the micropillar compression method to various brittle intermetallic compounds and have confirmed that plastic flow can be observed for some of them even at room temperature if the specimen size is reduced from bulk to micron meter size [2-4]. In the present study, we investigated the plastic deformation behavior of single crystals of Mo_5SiB_2 and α-Nb_5Si_3 with the D8$_l$ structure in compression as a function of crystal orientation at room temperature and specimen size, in order to clarify the operative slip systems and to evaluate their CRSS values.

Materials and Methods

Single crystals of Mo5SiB2 and Nb5Si3 were grown with an optical floating-zone furnace under Ar gas flow. The actual composition of the Mo_5SiB_2 single crystals were determined to be slightly rich in Si and B (Mo - 13.8 at.%Si - 25.7 at.%B). The as-grown single crystal of Nb_5Si_3 was confirmed to be crystallized into its high-temperature modification (β-Nb_5Si_3) with the D8$_m$ structure. The as grown single crystal of β-Nb_5Si_3 was then heat treated at 1500 °C for 96 hours to obtain a polycrystalline ingot of α-Nb_5Si_3. Micropillar single-crystal specimens with a square cross-section having an edge length L ranging from 0.5 to 7.5 μm and an aspect ratio of approximately 1:2~1:3 (1:4~1:5 only for the [001] orientation) were machined from the Mo_5SiB_2 single crystal and α-Nb_5Si_3 polycrystal by focused ion milling (FIB) technique. Four different loading axis orientations, [021], [010], [001] and [$\bar{1}$10], were selected. Compression tests were conducted on a nano-indenter equipped with a flat punch indenter tip at room temperature under the displacement-rate-controlled mode at a nominal strain rate of : 1×10^{-4} s^{-1} . Slip planes were determined by slip trace analysis made on two orthogonal surfaces of the deformed micropillar specimen by scanning electron microscopy (SEM). Dislocation structures in the deformed micropillars were investigated by transmission electron microscopy (TEM) and atomic-resolution scanning transmission electron microscopy (STEM). In addition, generalized stacking fault energy (GSFE) for various slip planes were calculated by the first-principles calculations.

Results and Discussion

For Mo5SiB2, plastic flow was observed at room temperature in a wide range of crystal orientation in the micropillar form, and three different slip systems, (001)<100>, {110}<1$\bar{1}$0> and {0$\bar{1}$1}<111>, were identified to be operative at room temperature [3]. The values of critical resolved shear stress (CRSS) for the three identified slip systems were extremely high all exceeding 2 GPa. The CRSS value for each slip system increases with decreasing specimen size, following the inverse power-law relationship with an exponent of about 0.2, which is much smaller than those reported for FCC and BCC metals. The <100> dislocation on (001) and the <1$\bar{1}$0> dislocation on {110} were confirmed to dissociate into two collinear partials on their slip plane by both experiment and theoretical calculation. For α-Nb_5Si_3, plastic deformation by two different slip systems of (001)<100> and {0$\bar{1}$1}<111> was confirmed, while that by {110}<1$\bar{1}$0> was not. The similarity and differences in plastic deformation behavior between isostructural Mo_5SiB_2 and α-Nb_5Si_3 will be discussed based on the results of the first-principle calculations of GSFE for various slip planes.
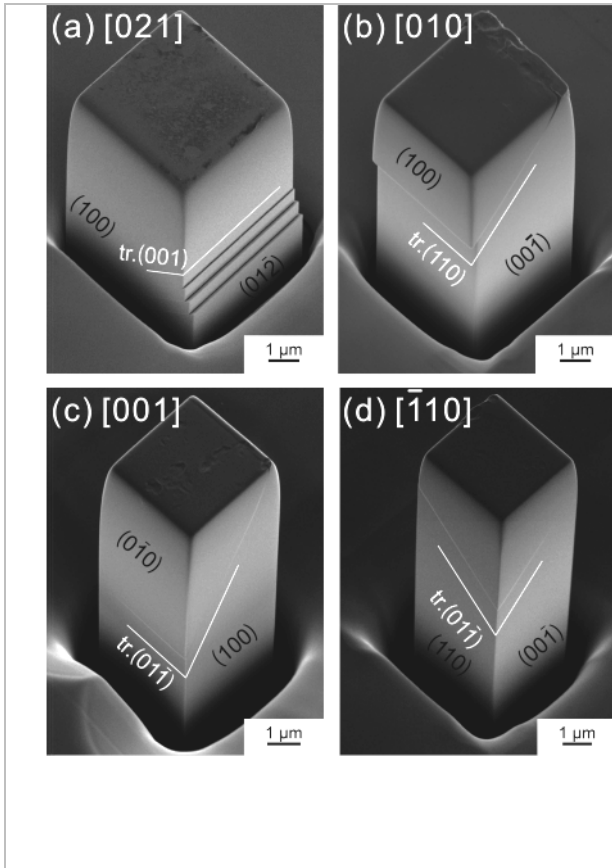
Fig. 1: Deformation markings observed on two orthogonal surfaces of Mo_5SiB_2 single crystalline micropillars with (a) [021], (b) [010], (c) [001] and (d) [$\bar{1}$10] orientations.
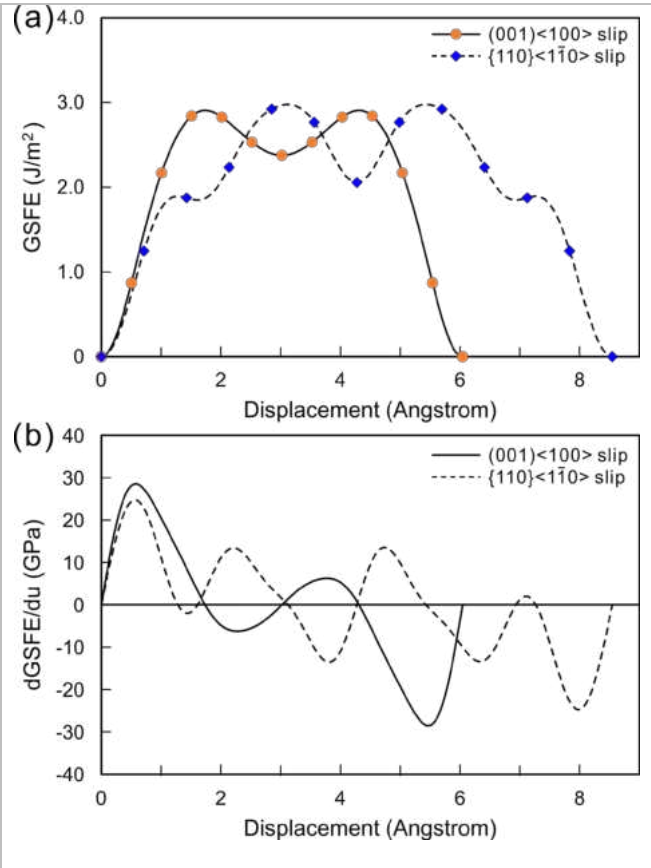
Fig. 2: (a) The calculated GSFE curves and (b) their derivatives for (001)<100> and {110}<1$\bar{1}$0> slip for Mo_5SiB_2.

References

[1]   K. Ito, K. Ihara, K. Tanaka, M. Fujikura, M. Yamaguchi, Intermetallics. **2001**, *9*, 591-602.
[2]   S. Nakatsuka, K. Kishida. H. Inui, MRS Symposium Proceedings. **2015**, *1760*, mrfs14-1760-yy05-09.
[3]   K. Kishida, T. Maruyama, H. Matsunoshita, T. Fukuyama, H. Inui, Acta Materialia. **2018**, *159*, 416-428.
[4]   M. Higashi, S. Momono, K. Kishida, N.L. Okamoto, H. Inui, Acta Materialia. **2018**, *161*, 161-170.

O–SI–01

Laser-based additive manufacturing of Mo-Si-B alloys

David Fichtner[1], Sven Schmigalla[2], Janett Schmelzer[3], Christoph Heinze[1] and Manja Krüger[4]

[1]Siemens AG, Siemensdamm 50, 13629 Berlin, Germany, fichtner.david@siemens.com, christoph.heinze@siemens.com
[2]Institut für Korrosions- und Schadensanalyse, Schwiesaustr. 11, 39124 Magdeburg, Germany, schmigalla@corrlab.de
[3]Otto-von-Guericke Universität Magdeburg, Große Steinernetischstraße 6, 39104 Magdeburg, janett.schmelzer@ovgu.de
[4]Forschungszentrum Jülich GmbH, Institute of Energy and Climate Research (IEK-2), Leo-Brand-Str. 1, 52425 Jülich, Germany, m.krueger@fz-juelich.de

Introduction

The maximum operation temperature of nickel-based superalloys in modern gas turbines limits the reachable efficiency. Therefore, it is important to find a new suitable material class. The search for this material class is quite difficult, due to high technical and economical demands [1]. Compared with other potential alloys, Mo-Si-B-alloys are well examined and show a very high potential [2,3].

The high melting temperature and the strong embrittlement of refractory metals, even by small concentrations of interstitial elements (e.g. oxygen and nitrogen), makes the manufacturing of this material group very difficult. Laser-based additive manufacturing is a very promising manufacturing technology, because it processes the material under inert atmosphere and generate a near net-shape object with a fine microstructure. Hereby, a fine microstructure is very important to improve oxidation resistance [4].

Materials and Methods

Samples of Mo-Si-B-alloys were manufactured on a laser powder bed fusion (L-PBF) machine with a special substrate preheating system. The preheating system can achieve temperatures up to 1200 °C in the substrate. The used powder was generated by gas atomization from a crucible. The chemical composition of Mo-16.5Si-7.5B (at.%) was near-eutectic [5]. Powder from the same supplier was already successfully used for DED in the past [6].

After several optimization steps, crack free L-PBF samples were manufactured and different samples were built to determine the mechanical properties and the oxidation behavior of the material.

Results and Discussion

Fig. 1 shows that low preheating temperatures lead to an excessive network of cracks in the generated samples. The reason for this is the high brittleness of intermetallic materials at low temperatures (e.g. room temperature). The laser-based additive manufacturing of other intermetallic materials was already successfully achieved for some materials (e.g. iron aluminides) in the past [7]. The key for this is using an adequate preheating temperature for the substrate. In general, the preheating temperature should be higher than the DBTT. In this way, it can be insured that the high residual stresses, which results from the high cooling speed of the process can be compensated by deformation on a microscopic scale.

In dependence of the microstructure, Mo-Si-B alloys can have a DBTT of up to around 1100 °C [8].

First tests with a preheating of 1200 °C doesn´t lead to a crack free sample and higher temperatures could not be achieved with this L-PBF machine. Therefore, the process parameters were optimized and modified parameters were used to decrease the number of cracks in the sample.

One important parameter, which strongly influences the DBTT of refractory metals is the concentration of dissolved interstitial elements. Both oxygen and nitrogen have a very strong tendency to embrittle molybdenum even in low concentrations. In welding applications, both elements can lead to brittle failure along the grain boundaries [9].

During the L-PBF the process chamber is constantly flooded with argon gas, but the powder in the powder tank is quite separated from the constant argon flow. Additionally, it is very complicated to remove the air molecules from the gaps between the powder particles. Different methods were tested and finally crack free samples with a height of 10 mm and a side length of 7 mm were successfully manufactured (Fig. 2).

Several different samples were manufactured to determine the mechanical and oxidation properties of the L-PBF sample.

Fig. 1: L-PBF with a preheating temperature of 200 °C	Fig. 2: L-PBF with a preheating temperature of 1200 °C
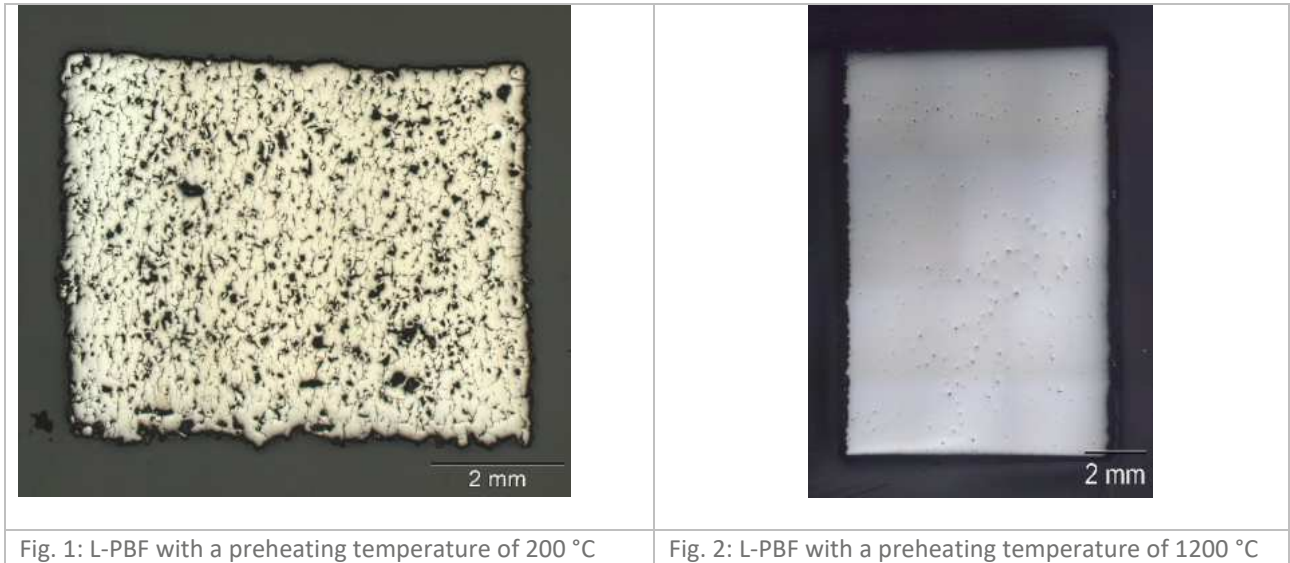
References
[1]   Roger C. Reed, The Superalloys: Fundamentals and Applications. **2008**.
[2]   M. Heilmaier, M. Krüger, H. Saage, J. Rösler, D. Mukherji, U. Glatzel, R. Völkl, R. Hüttner, G. Eggeler, Ch. Somsen, T.Depka, H.-J. Christ, B. Gorr, S. Burk, Metallic Materials for Structural Applications Beyond Nickel-based Superalloys, JOM: The journal of the Minerals, Metals & Materials Society, **2012**, 61 – 67.
[3]   M. Krüger, Innovative metallische Hochtemperaturwerkstoffe. Habilitationsschrift. **2017**.
[4]   Y. Guo, L. Jia, B. Kong, F. Zhang,J. Liu, H. Zhang, Improvement in the oxidation resistance of Nb-Si based alloy by selective laser melting, Corrosion Science, **2017**, *127*, 260-269.
[5]   Georg Hasemann, Microstructure and Properties of Near-eutectic Mo-Si-B Alloys for High Temperature Applications. Dissertation. **2017**.
[6]   J. Schmelzer, S.-K. Rittinghaus, A. Weisheit, M. Stobik, J. Paulus, K. Gruber, E. Wessel, C. Heinze, M. Krüger, Printability of gas atomized Mo-Si-B powders by laser metal deposition, International Journal of Refractory Metals and Hard Materials, **2018**.
[7] G. Rolink, Entwicklung der laserbasierten additiven Fertigung für intermetallische Fe-Al-   Legierungen, Dissertation. **2016**.
[8]   M. Krüger, P. Jain, K.S. Kumar, M. Heilmaier, Correlation between microstructure and properties of fine grained Mo-Mo$_3$Si-Mo$_5$SiB$_2$ alloys, Intermetallics **2014**, *48*, 10-18.
[9]   F. Morito, Effect of impurities on the weldability of powder metallurgy, electron-beam melted and arc-melted molybdenum and its alloys, Journal of Materials Science **1989**, *24*, 3403-3410.

O–SI–02

Properties of density reduced Mo-XV-Si-B alloys

Julia Becker[1], Ulf Betke[1], Rachid St. Touzani[1] and Manja Krüger[2]
[1]Otto von Guericke University, Magdeburg, Germany, julia.becker@ovgu.de
[2]Research Center Jülich GmbH, Jülich, Germany, m.krueger@fz-juelich.de

Introduction

Improving the thermodynamic efficiency of turbines for power plants and aircraft engines is an increasingly important research subject. A slight increase of the gas inlet temperature would already lead to a significant efficiency gain. So, it is necessary to develop new high temperature materials beyond the capability of state-of-the-art Ni-based superalloys since Ni-based alloys are limited in their maximum operating temperatures [1]. Promising candidates for the focused applications are Mo-Si-B alloys, offering a balanced proportion of continuously distributed Mo_{ss} phase and intermetallic phases, which is important to obtain both, good high temperature and acceptable room temperature properties [2]. Hence, the Mo_{ss} phase is an authoritative component of the alloying system. But there is still room for optimization, especially concerning balanced strength and ductility, and most of all the density of this phase, without deteriorating the high temperature properties (creep). A comparison with other suitable lightweight alloying elements, like Ti or Zr, shows that V is a very promising candidate to fulfill these requirements [3]. Hence, V was chosen as an additional alloy component to the most suitable alloy composition Mo-9Si-8B. The present work demonstrates that V effectively reduces the density by about 17 % (for Mo-40V-9Si-8B), while having competitive creep properties without decreasing the fracture toughness as compared to the reference alloy Mo-9Si-8B [4].

Materials and Methods

First investigations were carried out on mechanically alloyed and heat treated Mo-9Si-8B powders having varying amounts of V (10, 20, 30 and 40 at.%). Furthermore, the Mo-40V-9Si-8B alloy was chosen for processing by powder metallurgy via field-assisted-sintering (FAST) and ingot metallurgy using an arc-melter (AM). All microstructures were characterized using a SEM microscope equipped with EDS. For phase identification X-ray diffraction analysis (XRD) was performed. Additional Rietveld refinement helped to derive the preferred V sites in the lattices of the present phases. Three point-bending with notched samples was conducted for fracture toughness determination at room temperature. Compressive creep tests at 1093 °C were performed to prove the creep strength of this new type of alloys. Furthermore, the oxidation behavior was assessed by cyclic oxidation tests between 800 °C and 1100 °C. Additionally an effect of minor additions of Fe on the oxidation and creep resistance was proven.

Results and Discussion

The microstructural characterization of different alloy compositions (Mo-XV-9Si-8B; X=10, 20, 30, 40 at.%) showed that V is soluble in all three phases within the $(Mo,V)_{ss}$-$(Mo,V)_3Si$-$(Mo,V)_5SiB_2$ triangle. The results of Rietveld refinement represented in Fig. 1 indicate that especially in the D8I structure of $(Mo,V)_5SiB_2$ phase, V seems to have a site preference for occupying the higher symmetry 4c Wyckoff position. This effect will be analyzed more detailed in regard to the bonding mechanism using density functional theory (DFT). The fractions of the corresponding phases are not significantly affected by V alloying. Regarding the bulk materials a huge advantage was achieved concerning the density reduction which was around 17 % (for both processing routes, comparing the Mo-40V-9Si-8B alloys to similarly processed Mo-9Si-8B alloys). The FAST Mo-40V-9Si-8B alloy represents a very fine grained microstructure with a continuous Mo_{ss} matrix, whereas the molten equivalent exhibits an intermetallic matrix with a coarser grain size. The fine-grained alloy has a fracture toughness of 13.3 MPa√m, which is a very competitive value compared to other Mo-Si-B alloys. In contrast, the absolute creep strength of the V-substituted FAST alloy is lower compared to reference alloys, but density-related results show that also this alloy offers good potential (Fig. 2). Grain growth heat treatment may help to enhance the creep resistance. The molten Mo-40V-9Si-8B alloy therefore profits from its intermetallic matrix and its homogeneous microstructure. Even compared to Mo-9Si-8B (AM) it shows better specific creep properties due to its lower density and the slightly increased amount of intermetallic phases (53 %) as compared to 47 % in the reference alloy.
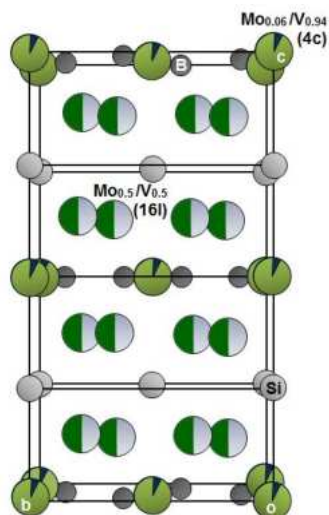
Fig. 1: Projection of the D8$_l$ structure of (MoV)$_5$SiB$_2$ on the (100) plane.
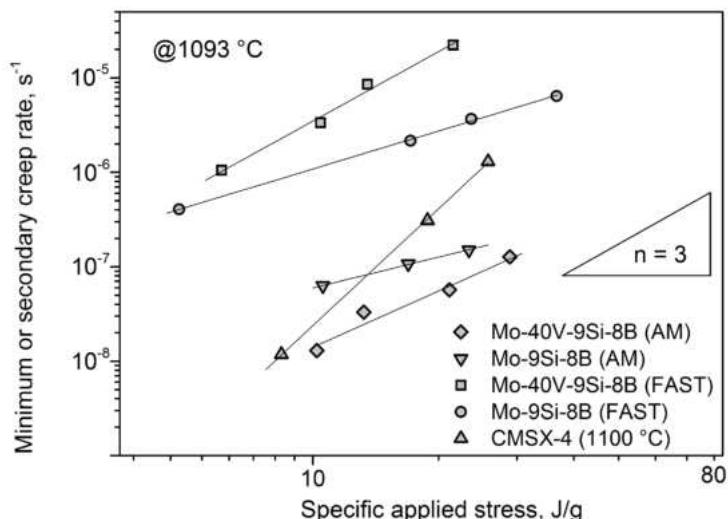
Fig. 2: Double-logarithmic plot of creep rate versus normalized applied stress at 1093 °C.

Last but not least the oxidation resistance is an essential property for high temperature applications, which is investigated by cyclic oxidation tests under atmospheric conditions. The high affinity of V for oxygen and the corresponding oxide formation is responsible for a decrease of oxidation resistance at elevated temperatures (up to 1100 °C). Since Kumar et al. [5] and Sossaman et al. [6] noticed a positive effect of minor Fe additions on the oxidation resistance of Mo-Si-B alloys, 3 % Fe was additionally added to the present Mo-40V-9Si-8B alloys. A non-doped and a Fe-doped Mo-9Si-8B alloy served as reference material to analyze the role and the contributions of the individual elements on the oxidation response of the alloys systematically. However, the investigations show that Fe additions only work effectively at approximately 800 °C for the reference alloy and not in combination with V. With increasing temperatures, a significant decrease of the layer viscosity is observed, which means increased diffusion rates and, therefore, reduced oxidation resistance.

References
[1] R. C. Reed, Cambridge University Press. **2006**.
[2] J. Becker, M. Krüger, Practical Metallography, **2015**, *52*, 295-313.
[3] J. Becker, U. Betke, E. Wessel, M. Krüger, Mater. Today Commun. **2018**, *15*, 314-321.
[4] J. Becker, U. Betke, M. Hoffmeister, M. Krüger, JOM, **2018**, *10*, 2574-2581.
[5] N.K. Kumar, B. Roy, R. Mitra, J. Das, Intermetallics, **2017**, *88*, 28-30.
[6] T. Sossaman, J.H. Perepezko, Corrosion Science, **2015**, *98*, 406-416.

O–SI–03

Oxidation barrier coatings with active fillers for Mo-Si-B high-temperature-alloys

Caren Gatzen[1], Iryna Smokovych[2], Jennifer Lopez Barrilao[1], Michael Scheffler[2] and Manja Krüger[1]

[1]Institute of Energy and Climate Research, Microstructure and Properties of Materials (IEK-2), Forschungszentrum Jülich GmbH, 52425 Jülich, Germany, c.gatzen@fz-juelich.de, m.krueger@fz-juelich.de

[2]Institute of Materials and Joining Technology, Otto-von-Guericke University Magdeburg, Universitätsplatz 2, 39106 Magdeburg, Germany, irina.smokovich@ovgu.de, m.scheffler@ovgu.de

Introduction

Molybdenum-based alloys are promising candidate materials for high temperature applications, but at temperatures above 700 °C in air volatile MoO_3 is formed.[1] The alloying of Mo with Si and B can increase the oxidation resistance, due to the formation of SiO_2/B_2O_3 glass phases on the surface, which react as an oxidation barrier. The oxidation resistance is determined by the Si/B ratio. Furthermore, the coexistence of Mo, Mo_3Si (T1) and Mo_5SiB_2 (T2) phases leads to excellent high temperature strength and creep properties.[1] Nevertheless, at temperatures between 500-900 °C the so-called Mo-pesting still occurs. One approach to prevent the material from oxidation and thus degradation is the application of protective ceramic coatings.[2] In this study, the oxidation behavior of Mo-Si-B-alloys with and without protective coatings was examined. In order to improve the coating performance fillers were added to adjust the high temperature properties of the coating material. It was found that the use of tailored ceramic coatings can drastically increase the oxidation resistance.

Materials and Methods

Coated and uncoated samples of the Mo-Si-B alloys were studied as well as free-standing coatings. The PDC technique (polymer derived ceramic) was used to obtain dense, ceramic coatings. Therefore, the Mo-Si-B alloys were dip coated with a silazane-polymer slurry (PHPS, perhydropolysilazane), afterwards the samples were pyrolyzed for 1h under Ar or N_2 atmosphere (see Figure 1). The coatings were tailored to further increase the oxidation performance by the use of several fillers, for example Si, B, Ti_3SiC_2, Mo_5SiB_2, SiB_6. The oxidation behavior of the coated samples as well as the uncoated alloys was tested at 800 °C and 1100 °C in air. The mass change was examined and the samples were analyzed by means of SEM and XRD.
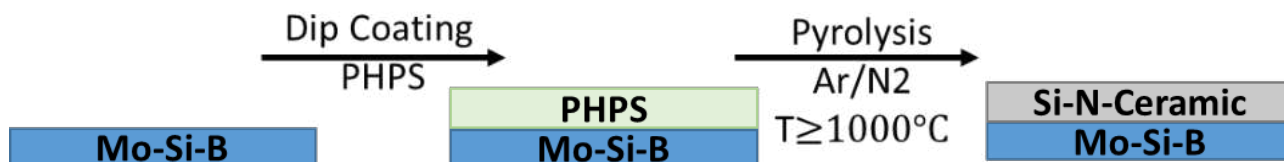
Fig. 1: Schematic illustration of the coating process.

Results and Discussion

The oxidation tests of coated and uncoated Mo-Si-B samples show that even thin PHPS layers (~100 nm) are sufficient to suppress pesting of Mo. In order to further increase the lifetime of the sample, fillers (Si, B, Mo_5SiB_2, SiB_6, Ti_3SiC_2) were added to the coatings. The fillers help to reduce the coating shrinkage during pyrolysis and to adjust the coefficient of thermal expansion in order to reduce thermal stress between coating and substrate. Furthermore, active fillers can act as oxygen scavenger and, in interaction with the coating material, influence the oxidation properties.

It was found that the fillers and/or the ratio of fillers to one another has drastic influence on the coating performance. Especially well-known glass formers, such as boron, drastically influence the coating properties. Different coating microstructures were found after oxidation tests. In case no boron was added, a rough and porous coating surface was observed (Figure 2, left). When boron was added a dense glassy layer was observed on the coating surface, it was found that this layer helps to reduce further oxidation of the sample (Figure 2, right).
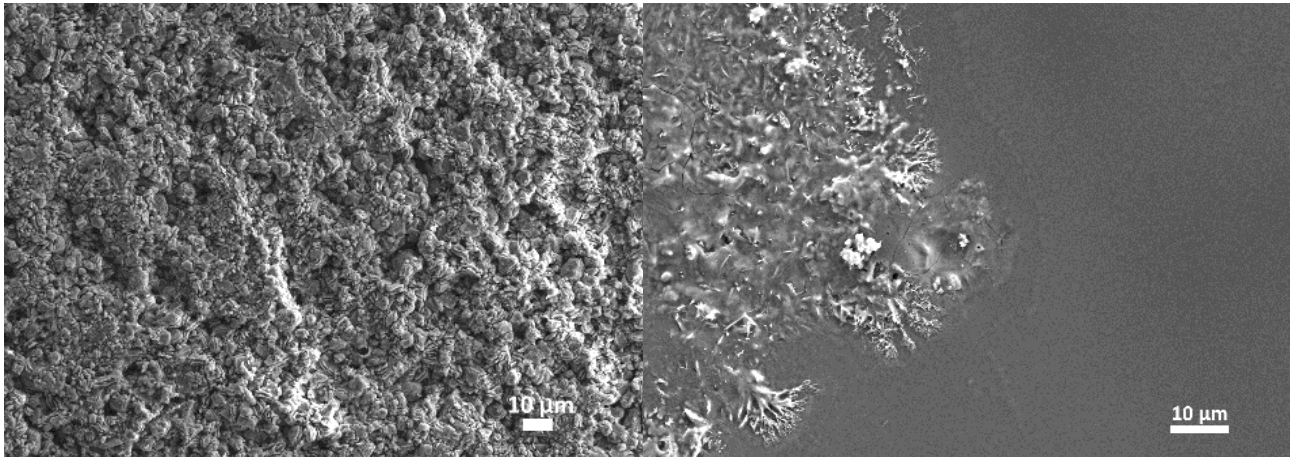
Fig. 2: SEM-Images of coating surfaces after 1000 h oxidation in air at 800 °C (left: PHPS coating with 45% Si filler; right: PHPS coating with 15% B filler).

References
[1]   G. Hasemann, D. Kaplunenko, I. Bogomol, M. Krüger, "Near-Eutectic Ternary Mo-Si-B Alloys: Microstructures and Creep Properties", *JOM Journal of the Minerals Metals and Materials Society* **2016**, *68*, 2847-2853.
[2]   I. Smokovych, G. Hasemann, M. Krüger, M. Scheffler, "Polymer derived oxidation barrier coatings for Mo-Si-B alloys", *Journal of the European Ceramic Society* **2017**, *37*, 4559-4565.

O–IT–03

Intermetallic phases, strengthening and correlation to theoretical predictions in rapidly solidified compositionally complex alloys

Emma White[1], Duane Johnson[2], Nikolai Zarkevich[3], Nicolas Argibay[4], Andrew Kustas[5], Michael Chandross[6] and Iver Anderson[7]

[1]Ames Laboratory of USDOE, 258 K Metals Development, 2415 Pammel Dr, Ames, IA 50011, USA, ewhite@ameslab.gov
[2]Ames Laboratory of USDOE, 130 Spedding, 2416 Pammel Dr, Ames, IA 50011, USA, ddj@ameslab.gov
[3]Ames Laboratory of USDOE, 336 Wilhelm, 2332 Pammel Dr, Ames, IA 50011, USA, zarkev@ameslab.gov
[4]Sandia National Laboratories, New Mexico, 1515 Eubank SE, Albuquerque, NM 87123, USA, nargiba@sandia.gov
[5]Sandia National Laboratories, New Mexico, 1515 Eubank SE, Albuquerque, NM 87123, USA, akustas@sandia.gov
[6]Sandia National Laboratories, New Mexico, 1515 Eubank SE, Albuquerque, NM 87123, USA, mechand@sandia.gov
[7]Ames Laboratory of USDOE, 222 Metals Development, 2415 Pammel Dr, Ames, IA 50011, USA, andersoi@ameslab.gov

Introduction

Compositionally complex alloys (CCAs) are being developed in a paradigm shift from traditional alloy compositions, where a single base element has additional minor alloying additions to achieve desired properties. In CCAs multiple elements (usually >4) are combined in similar or equal ratios, leading to alloys with unique properties as shown in Fig. 1a. These alloys have several defining features including configurational entropy, lattice distortion, sluggish diffusion and a 'cocktail' or mixing effect. [1] While solid solution formation is generally promoted in CCAs, intermetallic (IM) phases are formed under certain compositions and heat treatment conditions. Analogously to steels and superalloys, IM phase precipitation is an effective strengthening mechanism for CCAs through precipitation hardening. As the broad range of CCAs are being newly developed, precipitate morphology, phases and structures have not yet been fully explored and the microstructures need further optimization to achieve the full potential of these materials for advanced applications.

Materials and Methods

Utilizing calculations of energetics for various ordered/disordered states, thermodynamic linear-response, valence electron concentrations and energies of formation, the stable solid solutions and IM phases were predicted for various compositions of CCAs, as seen in Fig. 1c. For experimental validation of the models, samples of each composition were prepared using arc melting, drop casting, injection molding, melt spinning, high pressure gas atomization and additive manufacturing. Starting elemental materials were of at least 99.95wt% purity and were pre-alloyed to minimize reactivity, volatility and reduce melting points. Melt spinning was performed by pressurized ejection of a molten stream onto a rotating copper wheel with continuous ribbon production as shown in Fig. 1e. High pressure gas atomization was performed in a high purity Ar atmosphere with high purity Ar atomization gas in a customized system using ceramics and gas dies to achieve the desired particle size. Additive manufacturing of the atomized powders was performed using an Optomec laser engineered net-shaping (LENS) system through directed energy deposition (DED). Samples were heat treated to examine solid solution stability, IM formation and IM strengthening as seen in Fig. 1b. Characterization of the samples was performed using inductively coupled mass spectrometry (ICP-MS) for composition and LECO combustion analysis for impurities, X-ray diffraction (XRD) and differential scanning calorimetry (DSC) for phase information and scanning electron microscopy (SEM) for microstructural information as included in Fig. 1b and d.

Results and Discussion

The correlation between the modeling efforts and the experimental results show this approach to be effective in predicting CCA IM phases and their stability. The IM phase formation through compositional control and subsequent heat treatments show a path towards optimizing strength and other properties within these alloy families, while leveraging novel processing such as AM, for important advances in manufacturing and energy applications.
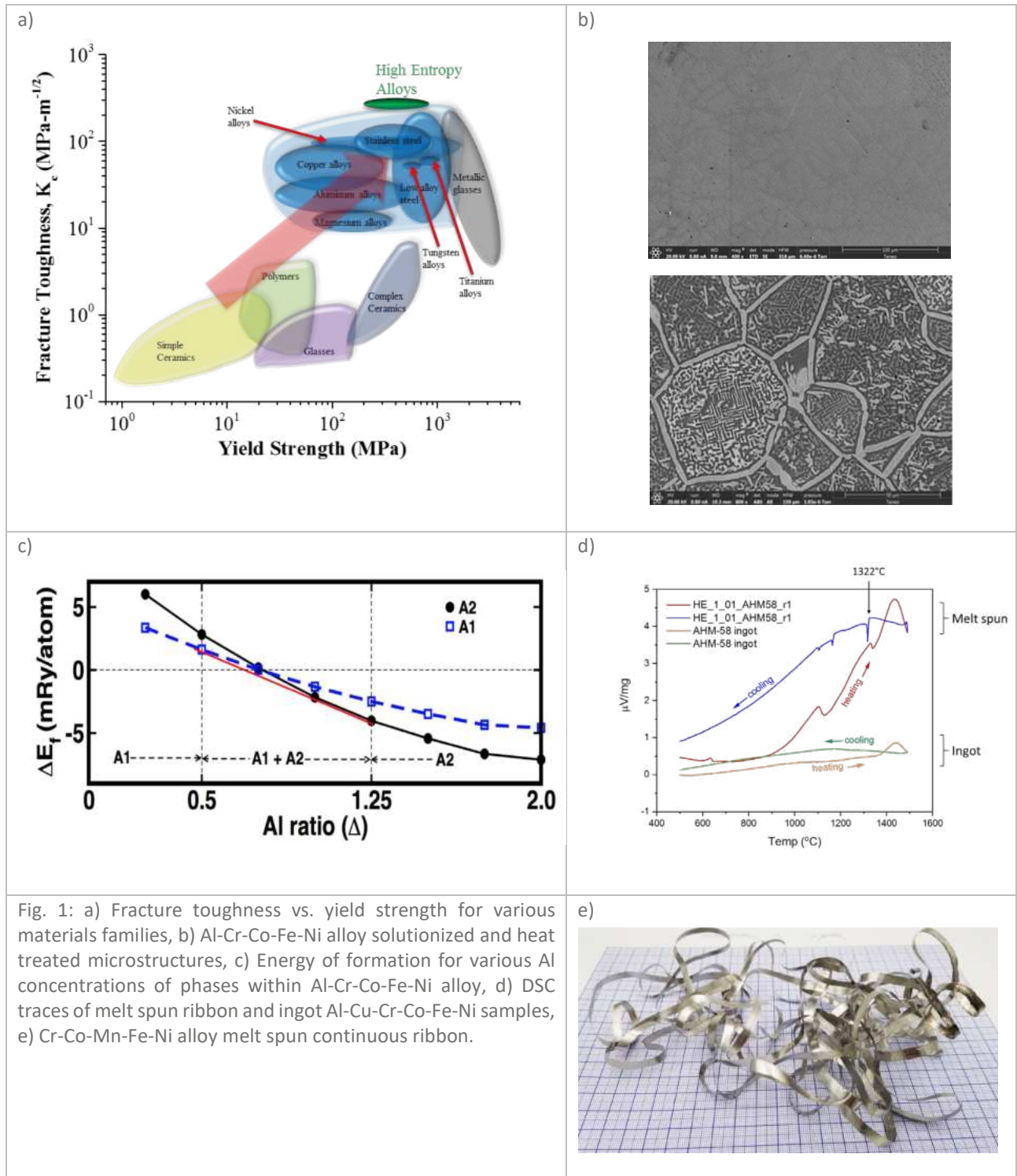
Fig. 1: a) Fracture toughness vs. yield strength for various materials families, b) Al-Cr-Co-Fe-Ni alloy solutionized and heat treated microstructures, c) Energy of formation for various Al concentrations of phases within Al-Cr-Co-Fe-Ni alloy, d) DSC traces of melt spun ribbon and ingot Al-Cu-Cr-Co-Fe-Ni samples, e) Cr-Co-Mn-Fe-Ni alloy melt spun continuous ribbon.

References

[1]   D.B. Miracle, O.N. Senkov, Acta Materialia. **2017**, *122*, 448-511.

O–HE–01

Precipitation hardening of Cantor alloy containing titanium

Uwe Gaitzsch[1], Nadine Eißmann[1,2], Uwe Mühle[2], Thomas Weißgärber[1] and Bernd Kieback [1,2]

[1]Fraunhofer IFAM Dresden, Winterbergstraße 28, 01277 Dresden, uwe.gaitzsch@ifam-dd.fraunhofer.de, nadine.eissmann@ifam-dd.fraunhofer.de, thomas.weissgaerber@ifam-dd.fraunhofer.de, bernd.kieback@ifam-dd.fraunhofer.de

[2]TU Dresden, Helmholtzstraße 7, 01069 Dresden, uwe.muehle@tu-dresden.de

Introduction

High entropy alloys (HEAs) are a material class gaining large research interest, recently. In contrast to conventional alloys, HEAs consist of a (near-) equimolar mixture of at least 4 elements. Remarkably, this complex composition results in a simple microstructure consisting of solid solution phases [1]. Outstanding properties result from this extraordinary microstructure, as for example high strength [2], superior mechanical properties at high [3] as well as low temperatures [4] and excellent wear resistance [5]. One of the most studied HEAs is the Cantor alloy CoCrFeMnNi. It consists of a single phase fcc microstructure and is therefore a highly suitable HEA for basic research, such as deformation behaviour, mechanical properties and phase stability [4,6,7]. Precipitation hardening is the dominating strengthening mechanism in superalloys [8] and shall be adapted to $Co_{19}Cr_{19}Fe_{19}Mn_{19}Ni_{19}Ti_5$ in this research. The required heat treatment to generate precipitations mostly consists of a solution annealing at temperatures above the solvus temperature to dissolve all alloying elements followed by a precipitation heat treatment at medium temperatures to create small precipitations.

Materials and Methods

Commercially available titanium powder (purity higher than 99%) and an atomised equimolar CoCrFeMnNi high entropy alloy powder (see [23] for more production details) were used as starting materials. A $Co_{19}Cr_{19}Fe_{19}Mn_{19}Ni_{19}Ti_5$ (at.%) HEA is prepared by wet mixing. The alloy was melted to allow mixing of the components. Cuboid samples were cut (3 x 5 x 10 mm³) by a precision saw. These cuboids were solution annealed (1250°C, 1h, air) and subsequently quenched in water. The precipitation heat treatment was conducted at 750°C for 2 h, 10 h or 20 h under vacuum. The chemical composition was determined by Zeiss EVO 50 scanning electron microscope (SEM) equipped with EDX. TEM Zeiss Libra 200 MC Cs STEM was used for further analysing of microstructure and chemical composition. The TEM-samples were prepared by using focused ion beam technique ("Helios Nanolab 660" by FEI).

Results and Discussion

The composition in the homogenized state was as intended. During homogenization an oxide layer formed which was not investigated further. However, it did not affect the composition in the inner part of the sample, where the further research was conducted. After precipitation treatment nanoscale second phase particles were detected via TEM, s. fig. 1. It could be proven that the composition of the matrix phase is identical for all samples. Due to the small size of the precipitations also information of the surrounding matrix phases affects the EDX- analysis. Therefore, the exact composition of the precipitations could not be determined and depending on the thickness of the analysed spot the resulting composition of the precipitations vary. The sample spot of the analysed precipitations after a heat treatment of 20 h was very thin, i.e. why the resulting element levels are more accurate than the ones after the 10 h heat treatment. The precipitations probably consist of mainly nickel, titanium and cobalt (see Table 1). The crystal structure of the precipitations could not be analysed, but according to its composition the phase is probably similar to Ni_3Ti precipitations known from superalloys [9,10].
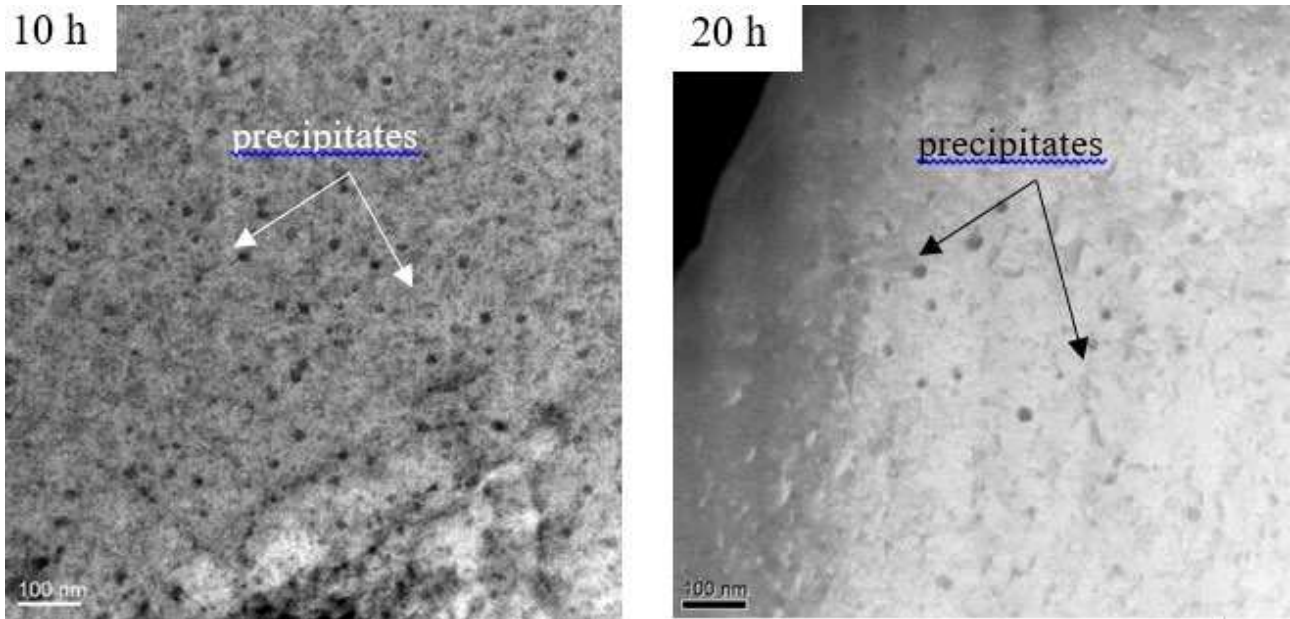
Fig. 1: TEM images of the precipitation hardened alloy after 10 h (left) and 20 h (right) of aging at 750°C.

Table 1: Composition of Ti-HEA for various conditions determined by EDX (at.-%) during TEM-analysis

state	Co	Cr	Fe	Mn	Ni	Ti	phase
Homogenised and quenched sample	20.6	21.1	22.6	16.7	16.9	2.0	matrix
Precipitation heat treatment 10 h	21.2	21.6	21.7	17.5	15.8	2.3	matrix
	20.4	11.0	12.8	9.3	33.6	12.9	precipitation
Precipitation heat treatment 20 h	21.3	20.4	21.4	17.7	16.9	2.2	matrix
	17.8	0.8	2.8	1.4	56.3	20.9	precipitation

The hardness evolution of the samples resembles the typical trend for precipitation hardening. The homogenized (=solution treated) sample starts at 160 HV 5. After 2h at 750°C it increases strongly to 250 HV 5 indicating the formation of precipitations. After 10 h of annealing the hardness increases further to 260 HV 5 indicating the precipitation of more and / or larger precipitates. After 20 h of annealing the hardness decreases to 235 HV 5. This decrease is typically attributed to coarsening of the precipitates causing their distance to each other to grow, an effect known as overaging in precipitation hardened alloys [11].

References
[1]   J.-W. Yeh, Y.-L. Chen, S.-J. Lin, S.-K. Chen, Adv. Struct. Mater. Iii, Trans Tech Pub. **2007**
[2]   Y. Dong, X. Gao, Y. Lu, T. Wang, T. Li, Mater. Lett. **2016**. *169*. 62–64.
[3]   S. Praveen, H.S. Kim, Adv. Eng. Mater. **2018**. *20*. 1700645.
[4]   B. Gludovatz, A. Hohenwarter, D. Catoor, E.H. Chang, E.P. George, R.O. Ritchie, Science. **2014**. *345*. 1153–1158.
[5]   C. Shang, E. Axinte, J. Sun, X. Li, P. Li, J. Du, P. Qiao, et al., Mater. Des. **2017**. *117*. 193–202.
[6]   N.D. Stepanov, D.G. Shaysultanov, N.Y. Yurchenko, S.V. Zherebtsov, A.N. Ladygin, G.A. Salishchev, M.A. Tikhonovsky, Mater. Sci. Eng. **2015**. *636*. 188–195.
[7]   N. Eissmann, U. Gaitzsch, O. Steuer, G. Walther, et al., Proceedings Euro PM. **2018**.
[8]   M.J. Donachie, S.J. Donachie, Superalloys: A Technical Guide, ASM International, **2002**.
[9]   O.A. Ojo, N.L. Richards, M.C. Chaturvedi, J. Mater. Sci. **2004**. *39*. 7401–7404..
[10]   R. Bürgel (Hrsg) Handbuch Hochtemperatur-Werkstofftechnik - Springer. https://www.springer.com/la/book/9783834899071 (accessed March 11, **2019**).
[11]   J.M. Pardal, S.S.M. Tavares, V.F. Terra, M.R. Da Silva, D.R. Dos Santos, MJ. Alloys Compd. **2005**. *393*. 109–113.

O–HE–02

Development of B2/L2$_1$ precipitation strengthened CCAs in the AlCrFeNiTi system for high temperature structural applications

Silas Wolff-Goodrich[1], Marshal Amalraj[2], Konda Pradeep[2,3], Jochen Schneider[2], Gerhard Dehm[1], Christian Liebscher[1]

[1]Max-Planck-Institut für Eisenforschung GmbH, Max-Planck-Straße 1, 40237 Düsseldorf, Germany, s.wolffgoodrich@mpie.de
[2]Materials Chemistry, RWTH Aachen University, Kopernikusstr. 10, 52074 Aachen, Germany
[3]Department of Metallurgical and Materials Engineering, Indian Institute Of Technology, NAC Rd, Chennai, Tamil Nadu 600036, India

Introduction

The need to make energy generation and conversion more sustainable and to reduce the emission of harmful gases requires the development of novel high temperature stable materials. Several of the so-called compositionally complex alloys (CCAs) have been shown to possess unique property combinations and, in some cases, exceptional mechanical properties. There is much promise in the development of cost-effective CCAs with the necessary properties for use in high temperature applications. In particular, alloys with high degrees of both solid solution strengthening and precipitation of creep resistant ordered phases, such as the L2$_1$-Heusler phase, can be realised under this alloy development strategy.

Materials and Methods

In the present study we are exploring the AlCrFeNiTi system, mainly for compositions with 30-35 at.% Fe and varying concentrations of the other four elements, with particular attention paid to the effect of increasing Al content. The aim is to produce alloys with mechanical stability up to 900 C, through achievement of an A2 solid solution matrix with coherent intermetallic precipitates of B2-NiAl and/or L2$_1$-Ni$_2$TiAl structure, and densities of approximately 6 g/cm^3. We have begun screening the composition space in this system using both a compositionally graded thin film produced via magnetron sputtering and bulk arc melted samples. The thin film has been probed along a gradient of increasing Al content at 5 unique compositions and we have produced more than 20 unique alloy compositions via arc melting. The characterization carried out for each composition includes XRD, DSC, SEM, and micro-hardness measurements. Several particularly promising alloy compositions have been further investigated using high resolution TEM and STEM, and initial compression testing results have also been collected.

Results and Discussion

For both the thin film and the arc melted samples we have observed a wide compositional range of stability for the B2/L2$_1$ and A2 phases, with a strong trend towards decreasing lattice parameter mismatch between the ordered and disordered phases with increasing Al content. The agreement between phase formation in the thin film and the bulk specimens is close enough to suggest that the graded thin film approach can be used for further screening of trends in this system, and, in general, can be used synergistically with bulk specimen results for a wider range of alloy systems. In the case of bulk specimens we have identified three primary morphologies in the areas of composition space explored thus far:

   I.   Bulk primary A2 regions with B2/L2$_1$ ordered phase precipitates (Observed in Fig. 1)
   II.   Lamellar regions with alternating A2 and B2/L2$_1$ phase domains (Observed in Fig. 2)
   III.   C14 Laves regions

In addition to quantifying the relative amounts and morphologies of the individual phases which form, we have conducted composition analysis in the individual phases and have observed high degrees of species intermixing in both the disordered A2 solid solution phase and the ordered phases, with off-stoichiometric compositions in the intermetallic phases of particular interest.
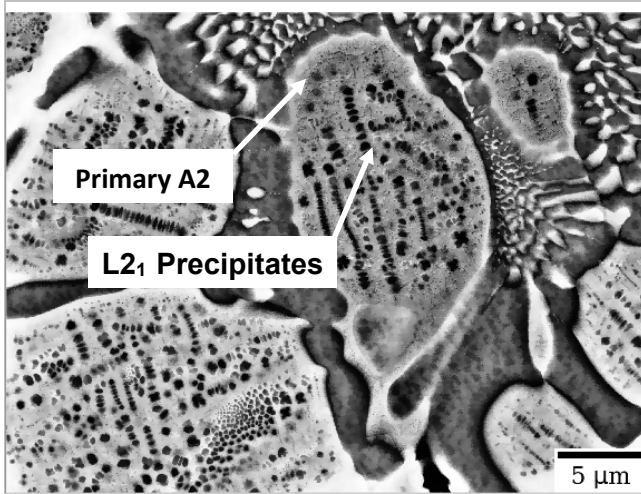
Fig. 1: Alloy exhibiting regions of primary A2 with $L2_1$ precipitates.	Fig. 2: Alloy exhibiting a lamellar, maze-like arrangement of A2 and $B2/L2_1$ precipitates.
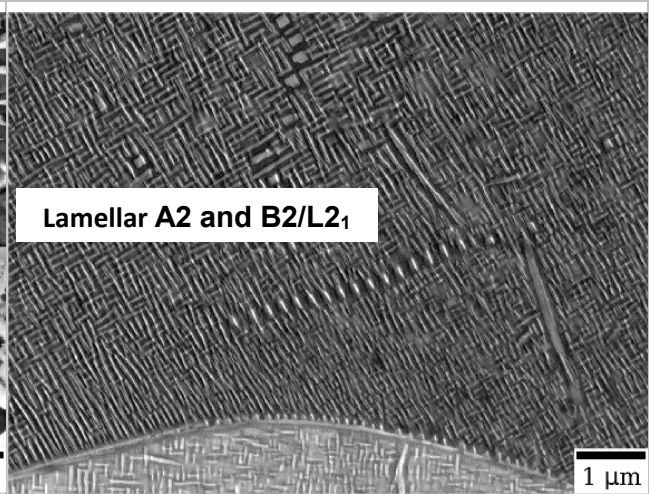
O–HE–03

Structure-property relationships in B2 ordered lightweight Al-Cr-Nb-Ti-V-Zr refractory high-entropy alloys

Nikita Y. Yurchenko[1], Nikita D. Stepanov[2], Gennady A. Salishchev[3] and Sergey V. Zherebtsov[4]

[1]Laboratory of Bulk Nanostructured Materials, Belgorod State University, Belgorod 308015, Russia, yurchenko_nikita@bsu.edu.ru

[2]Laboratory of Bulk Nanostructured Materials, Belgorod State University, Belgorod 308015, Russia, stepanov@bsu.edu.ru

[3]Laboratory of Bulk Nanostructured Materials, Belgorod State University, Belgorod 308015, Russia, salishchev@bsu.edu.ru

[4]Laboratory of Bulk Nanostructured Materials, Belgorod State University, Belgorod 308015, Russia, zherebtsov@bsu.edu.ru

Introduction

Refractory high-entropy alloys (RHEAs) are under consideration for potential high-temperature applications due to their unique properties [1,2]. However, the majority of the developed RHEAs are composed mainly of heavy refractory elements ($\rho > 10$ g/cm^3) that can result in uncompetitive specific strength. In this regard, the alloys based on the Al-Cr-Nb-Ti-V-Zr system with much lower density ($\sim 5.5 - 6.5$ g/cm^3) and good high-temperature properties look more attractive [3–6]. Nevertheless, despite the extensive research in the field of RHEAs and, as a result, the development of a vast number of different compositions, there are no systematic investigations of structure-property relationships that can impede the elaboration of practically operative RHEAs. Therefore, in this work, we tried to establish dependencies between chemical compositions, structures, and mechanical properties of a number of Al-Cr-Nb-Ti-V-Zr RHEAs.

Materials and Methods

The alloys with the nominal compositions of AlNbTiV, AlCr$_x$NbTiV and AlNbTiVZr$_y$ (x, y = 0.25; 0.5; 1; 1.5) were prepared by vacuum arc melting. As-cast ingots were annealed at 1200°C for 24 hours (further – initial state). From the annealed ingots samples for microstructure investigations and isothermal compression tests were cut. Microstructure and phase composition of the alloys in the initial state were studied using X-ray diffraction (XRD), scanning electron microscopy (SEM) and transmission electron microscopy (TEM). The more detailed information on materials and methods is given in [4–6].

Results and Discussion

Experimental investigations of microstructure and phase composition showed that the AlNbTiV alloy in the initial state possessed a single-phase B2 ordered structure (Fig. 1). Addition of Cr to the AlNbTiV alloy at x ≤ 0.5 did not change the phase composition, however, at x = 1 and 1.5, the hexagonal (C14) Laves phase of Cr$_2$Nb-type, enriched with Cr and Nb, precipitated. In turn, an addition of Zr to the AlNbTiV alloy at y ≤ 0.25 led to precipitation of the hexagonal Zr$_5$Al$_3$-type phase, enriched with Zr and Al. At higher (y ≥ 0.5) Zr content, the simultaneous formation of Zr$_5$Al$_3$-type and C14 Laves ZrAlV-type second phases was noted (Fig. 1). The volume fraction of the second phases enlarged with an increase in Cr or Zr content. Also, alloying with Cr or Zr resulted in a decrease in the degree of order of the B2 phase.
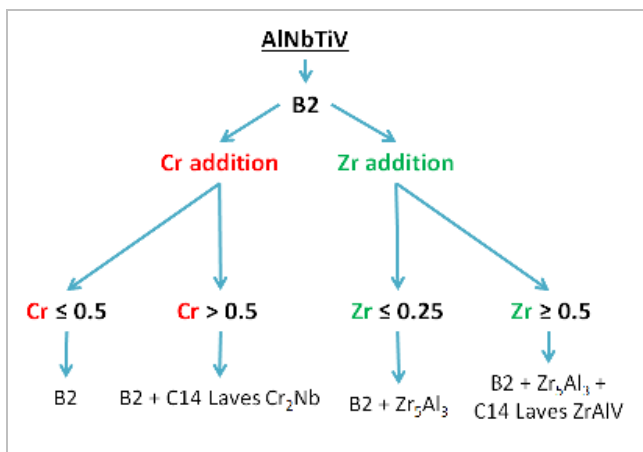
Fig. 1: Schematic representation of the relationships between chemical compositions and structures of the Al-Cr-Nb-Ti-V-Zr alloys	Fig. 2: Schematic representation of the relationships between chemical compositions and mechanical properties of the Al-Cr-Nb-Ti-V-Zr alloys
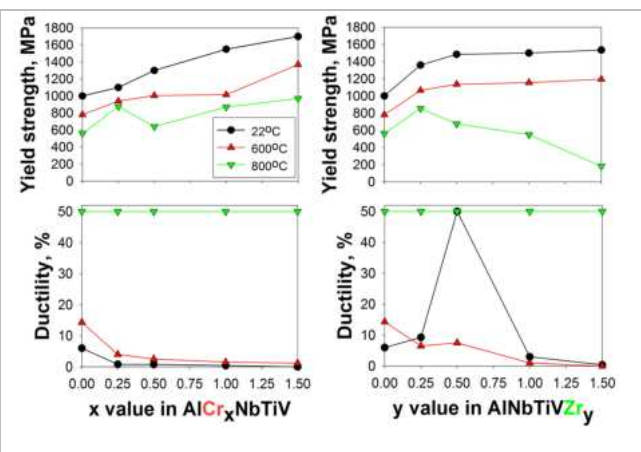
Investigation of mechanical properties revealed that Cr or Zr enhanced strength of the AlNbTiV alloy (Fig. 2). At T = 22-600°C, the strength increased with the increase both Cr or Zr – the alloys with the maximum content of Cr or Zr had the highest yield strength. At T = 800°C, Cr kept almost the same dependence between strength and its content, whereas, in a case of Zr-containing alloys, the $AlNbTiVZr_{0.25}$ alloy had the highest yield strength. The conducted analysis showed that Cr or Zr could increase strength through solid solution strengthening and the formation of second phase particles, and complex dependence of strength on content of alloying element, particularly, at T = 800°C, could be associated with the change in the degree of order of the B2 phase. Also, it was found that Cr decreased ductility at T = 22-600°C. At the same time, Zr at y ≤ 0.5 and T = 22°C increased ductility (Fig. 2). Particularly, the $AlNbTiVZr_{0.5}$ alloy could be plastically deformed up to 50% without fracture that possibly connected with the deformation-induced disordering of the B2 matrix phase. However, at T = 600°C, ductility of the Zr-containing alloys decreased. At T = 800°C, the AlNbTiV, $AlCr_xNbTiV$, and $AlNbTiVZr_y$ (x, y = 0.25; 0.5; 1; 1.5) alloys were found to be ductile. It was established that ductility could be affected by second phase particles and, possibly, the degree of order of the B2 phase.

References
[1]   D.B. Miracle, O.N. Senkov, Acta Mater., **2017**, *122*, 448–511.
[2]   O.N. Senkov, D.B. Miracle, K.J. Chaput, J. Mater. Res. **2018**, *33 (19)*, 3092–3128.
[3]   O.N. Senkov, S.V. Senkova, D.B. Miracle, C. Woodward, Mater. Sci. Eng. A. **2013**, *565*, 51–62.
[4]   N.D. Stepanov, D.G. Shaysultanov, G.A. Salishchev, M.A. Tikhonovsky, Mater. Lett. **2015**, *142*, 153–155.
[5]   N.D. Stepanov, N.Y. Yurchenko, D.V. Skibin, M.A. Tikhonovsky, G.A. Salishchev, J. Alloys Compd. **2015**, *652*, 266–280.
[6]   N.Y. Yurchenko, N.D. Stepanov, S. V Zherebtsov, M.A. Tikhonovsky, G.A. Salishchev, Mater. Sci. Eng. A. **2017**, *704*, 82–90.

O–HE–04

Microstructure and properties of intermetallic strengthened CoCrFeNi$_{2.1}$Nb$_x$ high entropy alloys

Upender Sunkari[1], Seelam R. Reddy[1], Subhradeep Chatterjee[1] and Pinaki P. Bhattacharjee[1]

[1]Department of Materials Science and Metallurgical Engineering, Indian Institute of Technology Hyderabad, Kandi, Sangareddy 502285, Telangana, India, upender@iith.ac.in, ms14m16p000001@iith.ac.in, subhradeep@iith.ac.in, pinakib@iith.ac.in

Introduction

High entropy alloys (HEAs) were originally conceived as multicomponent single phase alloys having simple crystal structures [1]. Recent research in these alloys has been directed at increasing the strength of ductile (FCC) single phase alloys by adding one or more complex intermetallic phases for their potential applications as structural materials. The addition of Nb in the single phase HEAs has been considered very promising for improving high temperature strength properties. However, with the increase in Nb-content, amount of Laves phase in these HEAs [2], potentially resulting in a loss of ductility. In order to restore the ductility in the base alloy and also to maximize the benefits of Nb addition, we have designed and developed novel complex intermetallic containing CoCrFeNi$_{2.1}$Nb$_x$ (x=0.2, 0.4) HEAs by arc melting. In this paper, we present microstructure and mechanical properties of CoCrFeNi$_{2.1}$Nb$_x$ HEAs.

Materials and Methods

Button-shaped ingots of CoCrFeNi$_{2.1}$Nb$_x$ (x=0.2, 0.4, hereafter denoted as Nb$_{0.2}$ and Nb$_{0.4}$ alloys) HEAs were prepared by arc melting under argon atmosphere in a water-cooled copper mold. Annealing treatment on the as-cast HEA samples were performed under argon atmosphere at 800°C for 24 hours followed by water quenching. Microstructural examinations were carried out using a field emission gun (FEG) scanning electron microscope (SEM) (JEOL, JSM-7800F, Japan) equipped with energy dispersive x-ray spectroscopy (EDS) for the compositional analysis. The tensile tests were conducted using table-top universal testing machine (UTM, INSTRON 5967) at room temperature with an initial strain rate of 10^{-3} s^{-1}.

Results and Discussion

The as-cast microstructures of the Nb$_{0.2}$ and Nb$_{0.4}$ HEAs are shown in Fig. 1(a) and 1(d), respectively, reveal that the Laves phase fraction increases with increasing Nb in the alloy. Annealing at 800°C resulted in the precipitation of acicular D0$_{19}$ (ε - phase) precipitates in both HEAs, see Fig. 1(c) and 1(e). However, the fine precipitates were located mainly at the dendritic boundaries in theNb$_{0.2}$ HEA, while they appeared throughout the FCC matrix in the Nb$_{0.4}$ HEA. The tensile test results on the as- cast and annealed HEAs are compared with base alloy CoCrFeNi$_{2.1}$ (without Nb addition, denoted as Nb$_0$), see Fig. 1(c). The Nb$_{0.2}$ HEA showed much better strength-ductility combination as compared to the Nb$_{0.4}$ HEA. The results indicated that intermetallic strengthened CoCrFeNi$_{2.1}$Nb$_x$ HEAs can be developed as advanced high strength HEAs combining high strength and ductility.
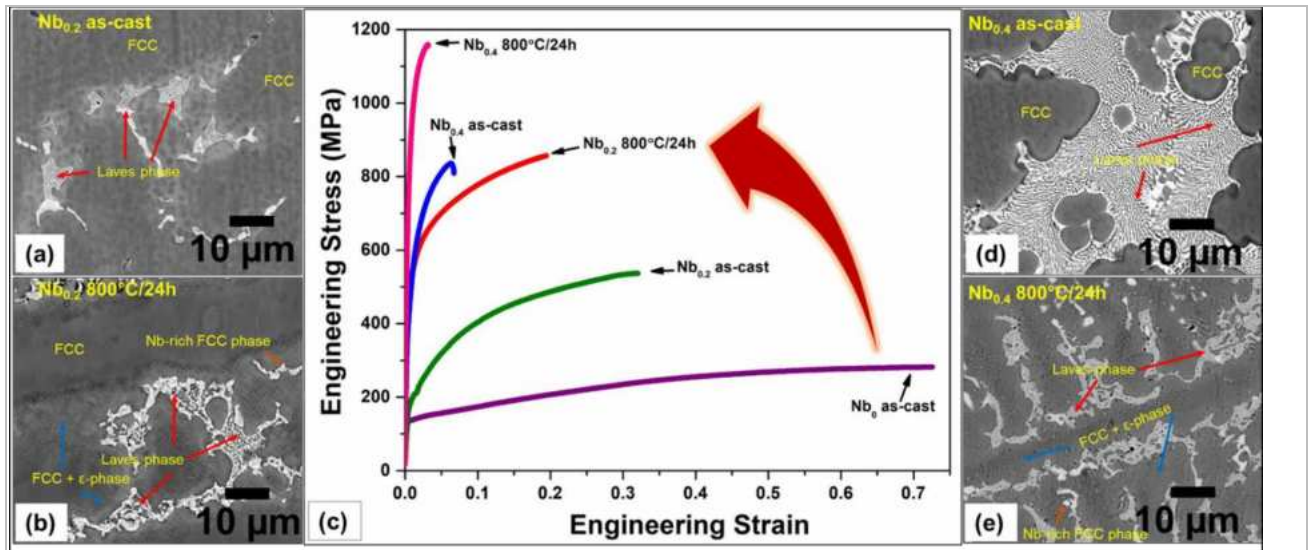
Fig. 1: BSE images showing the representative microstructures of CoCrFeNi$_{2.1}$Nb$_x$ (x=0.2, 0.4) HEAs in as- cast and aged (800°C/24h) conditions (a,b) Nb$_{0.2}$ HEA, (d,e) Nb$_{0.4}$ HEA; (c) Tensile test curves showing engineering stress and engineering strain of CoCrFeNi$_{2.1}$Nb$_x$ HEAs in as-cast and aged (800°C/24h) conditions

References
[1]   J.W. Yeh, S.K. Chen, S.J. Lin, J.Y. Gan, T.S. Chin, T.T. Shun, C.H. Tsau, S.Y. Chang, Advanced Engineering Materials 6(5), **2004**, 299-303.
[2]   F. He, Z. Wang, J. Wang, Q. Wu, D. Chen, B. Han, J. Li, J. Wang, J.J. Kai, Scripta Materialia 146, **2018**, 281-285.

O–HE–05

High entropy alloys: materials for the future or elaborate hoax?

Cláudio G. Schön[1], Thomaz A. Guisard Restivo[2] and Raymundo Arróyave[3]

[1]Department Metallurgical and Materials Engineering, Escola Politécnica da Universidade de São Paulo, São Paulo-SP, Brazil, schoen@usp.br

[2]Universidade de Sorocaba, Sorocaba-SP, Brazil, guisard@dglnet.com.br

[3]Department Materials Science and Engineering, Texas A&M Univeristy, College Station-TX, USA, rarroyave@tamu.edu

Introduction

Materials science has something in common with fashion: from time to time some material class enters in evidence, with the promise to change the world of technology. This happened with structural intermetallics [1], with quasicrystals [2], with bulk metallic glasses [3], with graphene [4], and now, with the high entropy alloys (HEAs). Based on the past examples, it is plausible to believe that the HEAs will find some application niche which will have more or less impact in our technology, depending on their intrinsic technological value. There is, however, a considerable skepticism following the development of HEAs. This is mostly due to the traditional explanation that the remarkable properties observed for these alloys are due to the high value of the maximum configurational entropy which characterize these equimolar multicomponent alloys. The absolute value of the configurational entropy itself is known not to play a great role in determining the thermodynamic equilibrium (only exchanges in entropy are able to do so). The reported unusual properties are, however, validated in some cases by careful experiments and this shows that some intrinsic technological value exist for the HEAs. The logical conclusion is that these unusual properties are not related with the configurational entropy. The present work reviews theoretical calculations by two of the present authors [5,6], while adding new experimental results in cases which bring the HEA idea to extremes. The main message of this work is an answer to the question posed in the title: neither of them (or both of them, depending on how you see it).

Materials and Methods

The theoretical calculations are based on cluster variation method (CVM) simulations in the irregular tetrahedron approximation of BCC systems. The calculations are divided in two parts, in one, a set of prototype calculations in artificial systems characterized by equal and strong interactions between all binary sub-systems (the so called equinteracting systems) is performed, which allows to display the true effect of entropy in thermodynamic equilibrium. These calculations are completed with ab initio calculations in systems $V - Nb - Ta - Mo - W$, $V - Nb - (Ta) - Mo - Al$ and $V - Nb - (Ta) - W - Al$. The stability of the disordered phase is tested by calculating the critical temperature of ordering of the first long-range ordered (LRO) state in each case [5,6].

On the experimental side, one of the authors has elaborated seven BCC alloys called MD (metallic diamond) from a mixture of elemental fine powders (99.9+%). The alloys hold from 6 to 9 distinct metallic elements, which were selected by several criteria based on Hume-Rothery rules and chromium equivalent formulas. The equiatomic alloys hold Cr, Fe, Nb and other refractory metals, as well as Ni and Al in some cases. Compacted pellets were arc melted on a cooled copper hearth. Bulk alloys were prepared for Vickers hardness tests. The as-cast alloys were annealed at 550, 950 and 1300 °C for 1h under argon, and also pack carburized into graphite media at 1150 °C for 2h, followed by normalizing. SEM/ BSE analyses were carried out.

Results and Discussion

The equinteracting system calculations clearly show that the entropy (the value of the entropy of the disordered phase at the critical temperature of LRO, and not the maximum entropy of the alloy) has a minor impact on the stability of the disordered phase, and in some cases, this impact is even contrary to the one prescribed by the HEA paradigm. A stabilization effect of the disordered phase for multicomponent alloys is observed and it is postulated that this effect is a consequence of competing interactions which cannot be resolved by the LRO state on cooling. This effect was dubbed "configurational frustration" by the authors.

The results of the ab initio calculations corroborate this viewpoint. All investigated systems show large deviations of the ideal behavior in the component activities, which vanish only at very large temperatures. These alloys are also characterized by very large short-range order (SRO) parameters close to the critical temperatures for ordering. Finally, the stability of the disordered states is large in all systems but the ones containing Mo and Al. Ironically, these systems are the only ones in which the maximum configurational entropy correlates with the stability of the disordered phase, but this happens at the cost of very large critical temperatures, which are due to a quaternary very stable compound which can resolve configurational frustration.

On the experimental side, SEM/BSE has revealed the alloys have a main matrix phase, in which some second phases are observed precipitated at grain boundaries. The as cast and 950 °C-annealed alloys have shown very high hardness using a micro-Vickers indenter with 2 N load, in the range 900 to 1340 HV. Contrary to that, the 1300 °C annealed alloys are softer, from 430 to 975 HV. Some carburized alloys have been hardened to extreme values, as seen in Table 1.

Table 1: Vickers hardness values for 950 °C-annealed and carburized alloys.

Alloy	Composition	HV annealed	HV carburized
MD-1	CrFeMoNbNiW	600 - 900	560 - 1240
MD-2	CoCrFeMoNbNiTiVZr	1100 – 1340	860 - 1120
MD-3	CoCrFeMnMoNbNiTaV	910 – 1120	720 – 1080
MD-4	$Cr_3FeMoNbTaTiV$	1135 - 1190	1410 – 2170
MD-5	$CrFe_3MoNbTaTiV$	1100 – 1500	800 - 1130
MD-6	AlCrFeMoNbTaTiVW	950 – 990	1005 – 1860
MD-7	AlCrFeNbTiW	940 – 1020	1280 -1755

According to these results, carburized alloy MD-4, 6 and 7 are the hardest metallic alloys ever developed, reaching a dense ceramic level like sapphire. Concurrently, fracture toughness measured at radial cracks from macro-Vickers indentations has resulted in low values within the range 3.5 to 9 MPa.m$^{1/2}$. However, the K_{Ic} values for MD-4 are more promising being in the range 5 – 9 MPa.m$^{1/2}$. Homogenization and thermomechanical treatments should be performed in order to increase these values for further processing.

References
[1]   S. Naka, M. Thomas, T. Khan, Materials Science and Technology, **1992**, *8*, 291 – 298.
[2]   E. Abe, Y. Yan, S. J. Pennycook, Nature Materials, **2004**, *3* , 759 – 767.
[3]   A. Inoue, Engineering, **2015**, *1*, 185 – 191.
[4]   A. K. Geim, Science, **2009**, *324*, 1530 – 1534.
[5]   C. G. Schön, T. Duong, Y. Wang, R. Arróyave, Acta Materialia, **2018**, *148*, 263 – 279.
[6]   C. G. Schön, T. Duong, Y. Wang, R. Arróyave, Journal of Alloys and Compounds, **2019**, *781*, 595 – 605.

O–SM–01

Size effect on the stress-induced martensitic transformation in Cu-based shape memory alloys

Jose F. Gómez-Cortés[1], Valeria Fuster[1,2], María L. Nó[3] and José M. San Juan[1]

[1]Department of Physics of Condensed Matter, Faculty of Science and Technology, University of the Basque Country, UPV/EHU, P.O. Box 644, 48080 Bilbao, Spain, josefernando.gomez@ehu.es, jose.sanjuan@ehu.es

[2]Instituto de Física Rosario, CONICET-Universidad Nacional de Rosario, 2000 Rosario, Argentina, fuster@ifir-conicet.gov.ar

[3]Department of Applied Physics II, Faculty of Science and Technology, University of the Basque Country, UPV/EHU, P.O. Box 644, 48080 Bilbao, Spain, maria.no@ehu.es

Introduction

Stress-induced martensitic transformation in shape memory alloys (SMAs) gives place to the superelastic effect (SE), an exotic behavior that involves a high displacement and a strong actuation, which is promising for application in Micro Electro-Mechanical Systems (MEMS). Previous works have demonstrated a completely reversible and reproducible behavior at the nanoscale in Cu-based SMAs [1,2], even for thousands of cycles and after long-term cycling spanning several years [3,4]. From the fundamental and technological point of view, it is important to know whether there is a size-effect on the critical stress (σ_c) necessary to induce the martensitic transformation in this kind of alloys. Recently we provided the first explicit assessment of a size effect on the critical stress for superelasticity in SMAs at small scales [5], and the present work aims to shed light on this respect studying, by nano-compression tests, pillars with different diameters ranging from micro- to nano-metric scale, on several Cu-based single crystals.

Materials and Methods

Cu-based single crystals of SMAs, from Cu-Al-Ni and Cu-Al-Be systems, were used to mill a large number of pillars on the (001) oriented surface using the focused ion beam technique (FEI Helios 650). The alloys concentrations were selected in order to observe the SE at room temperature. The milling conditions were 30 kV for the gallium I-beam and decreasing currents for the different milling steps, 80, 40 and 24 pA, followed by finishing steps with 15 and 7.7 pA. This procedure was developed to avoid any noticeable influence of potential Ga damage or contamination. Nano-compression tests were performed at room temperature in an instrumented nano indenter Hysitron TI-950, using an sphero-conical 2-μm radius diamond indenter. Pillars from 2 μm down to 250 nm in diameter were produced and tested. In-situ nano-compression experiments inside of the scanning electron microscopy chamber (JEOL 7000F) were also performed using a Hysitron PI-85 in order to observe and verify the superelastic response. All the raw load-displacement curves were treated according to the method described in the reference [5] to obtain the corresponding stress-strain curves necessary to study the related size effect.

Results and Discussion

As an example, a pillar of 310 nm in diameter is shown in Fig. 1 (a) (b), with its respective stress-strain supereleastic response measured during a nano-compression test. All tested pillars exhibited such characteristic superelastic cycle where the critical stress (σ_c) becomes evident, as is indicated in Fig. 1 (b). In Fig. 2 we depict the critical stress (σ_c) as a function of the pillars diameter, including for comparison data measured in different experimental conditions. This graph reveals an strong size effect on the critical stress to induce the martensitic transformation when the pillar diameter is reduced. As can be seen, this characteristic parameter can be increased more than three times respect to the no size-effect regime ($\oslash > 1\mu$m). The observed size-effect is explained in terms of the homogeneous nucleation of the martensite phase, considering that the paucity of defects for heterogeneous nucleation in small volumes leads to a situation in which the martensite must be homogeneously nucleated by a direct shear of the austenite lattice, which requires a much higher applied stress. From this understanding, we propose an atomic-elastic based model (black line in Fig. 2) to describe and quantify the size-effect and the scaling power law for the stress-induced martensitic transformation at small scale, which exhibit similar trend in different Cu-based shape memory alloys, and can be considered as an universal scaling law for this kind of materials.
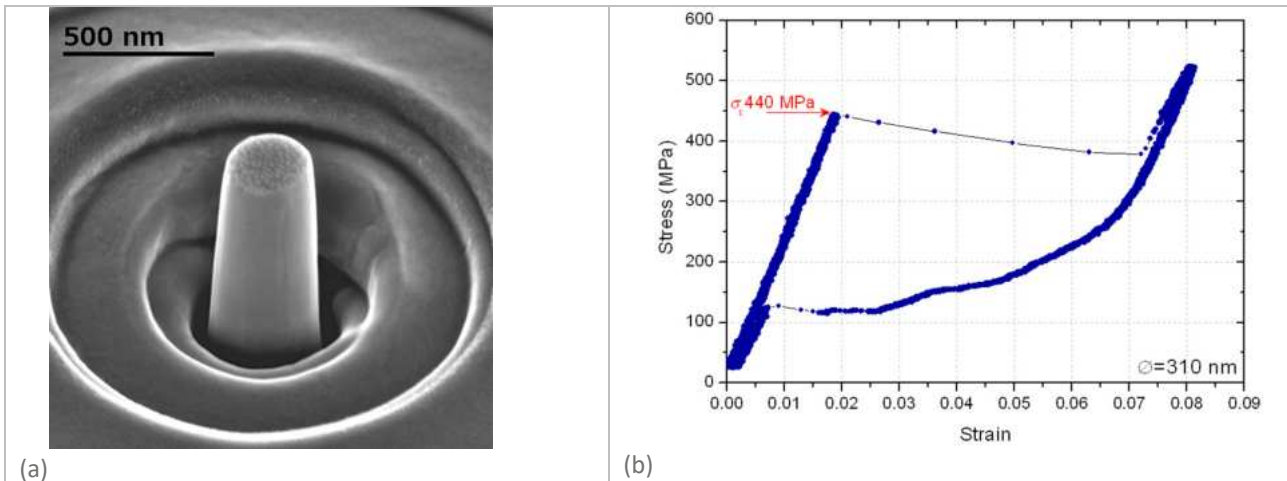
Fig. 1: (a) Cu-Al-Ni pillar with 310 nm in diameter, (b) Stress-strain superelastic response during one stress-induced martensitic transformation cycle obtained by nano-compression.
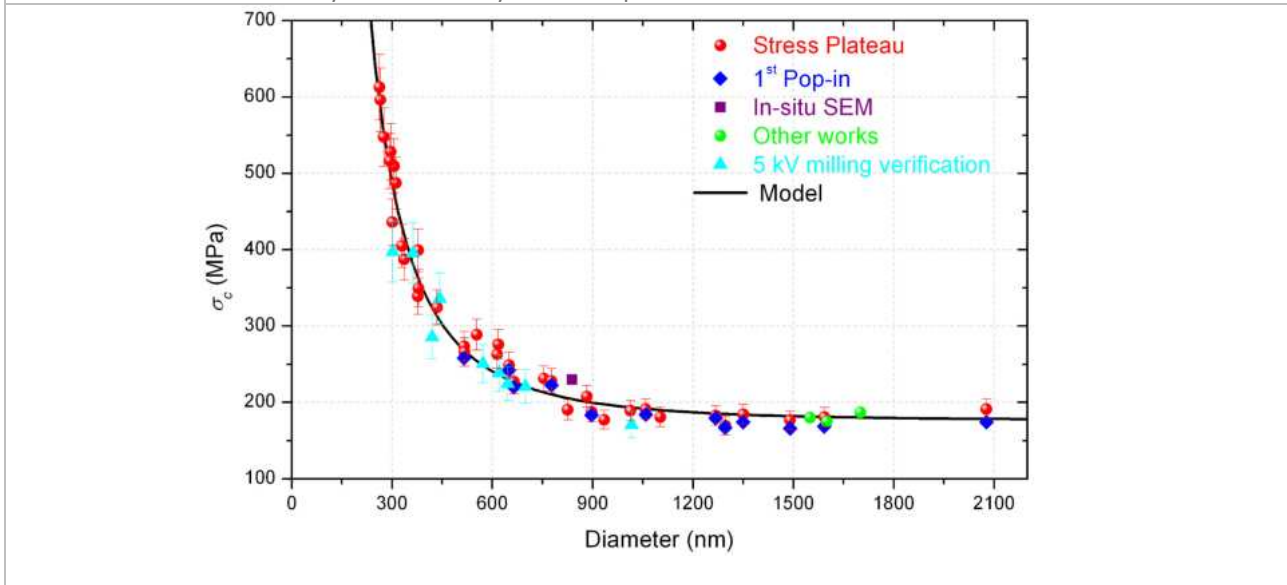
Fig. 2: Size-effect measured in Cu-Al-Ni SMA, on the critical stress (σ_c) for superelasticity versus the pillar diameter, and the prediction of the proposed model [5].

References

[1]   J. San Juan, M.L. Nó C.A. Schuh, Advanced Materials. **2008**, *20*, 272-278.

[2]   J. San Juan, M.L. Nó, C.A. Schuh, Nature Nanotechnology. **2009**, *4*, 415-419.

[3]   J. San Juan, J.F. Gómez-Cortés, G.A.López, C. Jiao, M.L. Nó, Appl. Phys. Letters. **2014**, *104*, 011901.

[4]   J.F. Gómez-Cortés, M.L. Nó, I. Ruíz-Larrea, T. Breczewski, A. López-Echarri, C.A. Schuh, J.M. San Juan, Acta Materialia. **2019**, *166*, 346-356.

[5]   J.F. Gómez-Cortés, M.L. Nó, I. López-Ferreño, J. Hernández-Saz, S.I. Molina, A. Chuvilin, J.M. San Juan, Nature Nanotechnology. **2017**, *12*, 790-797.

O–SM–02

Lath-like martensite in Cu-Zn-Al alloys with low Al concentration

Tobias Kaaden, Markus Rettenmayr and Stephanie Lippmann
Friedrich-Schiller-Universität Jena, Otto Schott Institute of Materials Research, Löbdergraben 32, 07743 Jena, Germany, stephanie.lippmann@uni-jena.de

Introduction

Cu-Zn-Al alloys may show a shape memory effect which is based on the disordered bcc (β) to martensite (M) transformation that can occur in a wide compositional range depending on the ratio of Zn and Al [1]. So far no comprehensive martensite microstructure analysis is available for Al concentrations ≤4wt% [2]. Independent of the initial concentration, the morphology of the martensite phase in Cu-Zn-Al alloys is always described as plate-like [3]. In other alloy systems, the martensite morphology and microstructural length scale are known to strongly depend on i) the alloy composition, e.g. in carbon steels the type of martensite changes from lath (≤0.6wt% C) to plate (>1wt% C) with a transitional structure for concentrations in between, and ii) the cooling rate, e.g. in carbon steels the type of martensite is cooling rate independent, but the microstructure becomes coarser at lower rates [4]. The aim of this work is the investigation of the martensite type and morphology in Cu-Zn-Al alloys depending on the Zn and Al concentration, respectively, as well as on the cooling rate.

Materials and Methods

For increasing the experimental efficiency, diffusion couples that cover a wide range of initial compositions are employed. Alloys with the nominal composition of Cu-Zn30-AlX and Cu-Zn50-AlX (X = 0.5, 0.75, 1.5, all concentrations in wt.%) were melted in a carbon crucible using Pb-free commercial Cu-Zn30 and Cu-Zn50 master alloys and pure aluminum adding borax and sodium carbonate as flux. These alloys were cast into rods with a diameter of 8mm using a permanent mold and cut into cylinders with a height of 5mm. Cylinders with identical Al content, but different Zn content were diffusion bonded in a sealed capsule under argon atmosphere at 800°C for 6h with 2MPa joining pressure. Inside a glove box with controlled atmosphere the oxide layer was removed from the surface using SiC grinding paper (4000grit) and the diffusion capsule was assembled. After diffusion welding, the joined cylinder was cut longitudinally into 10x8mm^2 plates with a thickness of 1mm. The plates were heated to 875°C, held for 10min and subsequently quenched in iced brine (-19°C) or quenching oil (23°C). For microstructural analysis, the quenched samples were mechanically ground (up to 4000grit SiC paper) and polished (3μm and 1μm polycrystalline diamond solution) with a finishing step of vibration polishing (0,05μm polycrystalline diamond solution). Optical microscopy with polarized light was used for the identification of martensite based on its birefringent properties. The concentrations profiles were measured in line scans using a scanning electron microscope and energy-dispersive X-ray spectroscopy.

Results and Discussion

Diffusion welding at 800°C leads to the formation of a one-dimensional Zn concentration gradient from 30wt% to 50wt% over a length of 1200μm and the formation of a fcc (α) / bcc (β) interface parallel to the joining interface. The composition range suitable for martensitic transformations is in the β phase region in the vicinity of the interface. Samples with identical concentration profiles were quenched with two different rates, 2800K/s (in iced brine) and 250K/s (in oil).

After quenching in iced brine, the sample with 0.5wt% Aluminum did not exhibit any martensite. In the samples with 0.75wt% (not shown) and 1.5wt% Al (Fig. 1), martensite forms starting in the β phase region at the α / β interface towards higher Zn concentration (up to 34wt% Zn for 1.5wt% Al). The birefringent contrast allows the identification of individual packets, blocks and laths that are subdivided by twinning, with all these features being known from carbon steels [5]. The martensitic structure is therefore lath-like rather than plate- or needle-like as previously identified in Cu-Zn-Al alloys and does not change in the investigated Zn concentration range. Within one grain, two distinct lath orientations can be present, indicated by different colors under polarized light. After 48h at room temperature, additional martensite needles form and grow further into the β-phase, beyond the Zn concentrations where the martensitic transformation initially stopped. This martensite grows isothermally only in the surface layer and can be removed by grinding and polishing. Isothermal martensite is assumed to form due to surface oxidation that changes the local composition and the martensite start temperature.

The cooling rates during quenching in oil were not high enough to form martensite in the samples with 0.5wt% and 0.75wt%. For 1.5wt% Al, coarse martensitic needles within the β-phase, which is characteristic for plate-like martensite, are observed (Fig. 2). The microstructure is significantly coarser as compared to the one quenched in iced brine.

Fig. 1: Lath-like martensitic microstructure under polarized light at the α/β interface of a diffusion couple with 1.5wt% aluminum after quenching in iced brine	Fig. 2: Plate-like martensitic microstructure under polarized light at the α/β interface of a diffusion couple with 1.5wt% aluminum after oil quenching
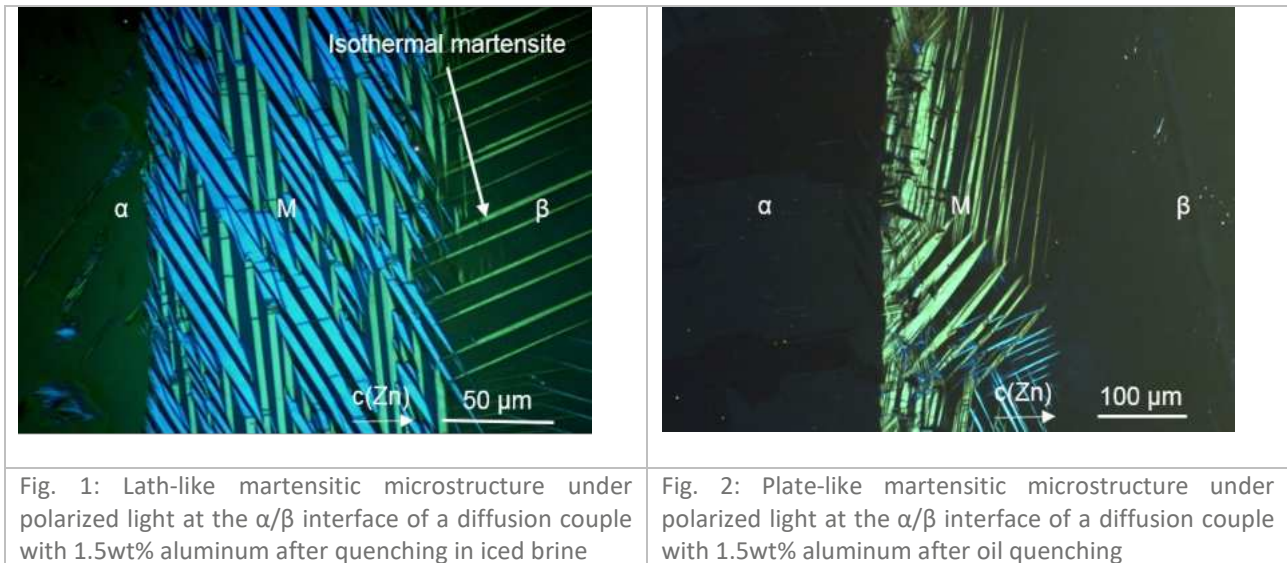
In summary, the formation of martensite was found in Cu-Zn-Al alloys with Zn concentrations between 34.5wt% and 36wt% for 0.75wt% Al and between 32.5wt% and 34wt% for 1.5wt% Al after quenching in iced brine. The observed microstructural type after quenching in iced brine is always lath-like. Lowering the cooling rate from 2800K/s to 250K/s changes the type of martensite from lath-like to plate-like, revealing the dependence of the type of martensite on the cooling rate in Cu-Zn-Al; as expected, the morphology of the martensitic structure becomes coarser with decreasing cooling rate.

References
[1]   M.J. Perricone, in: Metallography and Microstructure, ASM Handbook Vol. 9, ASM International, **2004**, 148-151.
[2]   Z. Stošić D. Manasijevi L. Balanovi T. Holjevac-Grguri U. Stamenkovi M. Premovi D. Mini M. Gorgievski R. Todorovi, Materials Research, **2017**, *20*, 1425-1431.
[3]   N. Kayali S. Özgen O. Adigüel, Materials Research Bulletin, **1997**, *32*, 569-578.
[4]   S. Morito H. Tanaka R. Konishi T. Furuhara T. Maki, Acta Materialia, **2003**, 51, 1789-1799.
[5]   L. Morsdorf C.C. Tasan D. Ponge D. Raabe, Acta Materialia, **2015**, *95,* 366-377

O–SM–03

Martensite stabilization effect in Ni-rich NiTi shape memory alloy

Natalia Resnina[1], Sergey Belyaev[1], Timur Rakhimov[1] and Vladimir Andreev[2,3]

[1]Saint-Petersburg State University, Universityteskaya nab, 7-9, 199034 Saint-Petersburg, Russia, resnat@mail.ru
[2]MATEK-SMA Ltd., Karier 2a – 137, 117449 Moscow, Russia
[3]Baikov Institute of Metallurgy and Materials Science, RAS, Leninskii Pr. 49, 119991 Moscow, Russia

Introduction

Shape memory alloys are widely used as actuators due to their ability for strain recovery on heating of the preliminary deformed samples. At the same time, it is very difficult to predict the temperatures for the strain recovery due to the martensite stabilization effect occurs. This effect is revealed as an increase in the temperatures of strain recovery that depends on the preliminary strain, chemical composition of the alloy and other parameters [1-3]. Thus, to increase an area of the shape memory effect application and to predict the working parameters of the actuators, it is necessary to control this effect. The martensite stabilization effect is well studied in equiatomic NiTi alloys but there are few papers where this effect is observed in the Ni-rich NiTi alloy. At the same time, Ni-rich NiTi alloys may demonstrate different mechanical and functional properties after different heat treatment and it may allow to study how the structure of the alloy influences the martensite stabilization effect. The aim of the present work was to study the martensite stabilization effect in $Ni_{51}Ti_{49}$ alloy subjected to two different heat treatments – quenching or annealing.

Materials and Methods

The $Ni_{51}Ti_{49}$ wire samples with a diameter of 1.5 mm were quenched from 900 °C into water or quenched from 900 °C with subsequent annealling at 450 °C for 2 hour. After quenching the $Ni_{51}Ti_{49}$ alloy underwent the B2 →B19′ transformation whereas, after quenching and annealing the B2 →R→B19′ transformation occurred on cooling. Thus, in the quenched sample the B19′ phase appeared from the B2 phase whereas, in the annealed sample the B19′ phase formed from the R phase. The samples after different heat treatments were deformed in the B19′ or R phases up to different strains from 1 to 7 %, unloaded and subjected to heating – cooling – heating in the temperature range of the martensitic transformation. The maximum given strain was 7 % because the annealed sample failured if the strain exceeded 7%. The simultaneous measurement of the resistivity and the strain during the heating-cooling-heating of the deformed samples was carried out. The value of the martensite stabilization effect was determined as the difference in the start ($\Delta A_s = A_s^1 - A_s^2$) or finish ($\Delta A_f = A_f^1 - A_f^2$) temperatures that were measured on the first and second heating. The recoverable and plastic strains were measured as the value of the shape memory effect and irreversible strain that was found in the sample after heating.

Results and Discussion

The results of this study showed that the martensite stabilization effect took place in the annealed $Ni_{51}Ti_{49}$ alloy after the deformation in the B19′ phase or in the R phase and in the quenched sample after deformation in the B19′ phase. In all studied sample the full strain recovery was observed during the first heating that pointed out the plastic (irreversible) strain was not initiated during the preliminary deformation. It confirmed the conclusion made in [3-4] that the plastic strain was not the main reason for the martensite stabilization effect. The comparison of the values of the martensite stabilization effect showed that shift in the A_s temperature after the deformation in the B19′ phase in the annealed sample was the same as in the quenched sample and both were larger than the shift in the A_s temperature after the deformation in the R phase (Fig. 1a). It means that the deformation in the B19′ phase leads to a decrease in the elastic energy that was stored in the sample during cooling, in the same way despite the heat treatment of the alloy. The deformation in the R phase leads to less decrease in elastic energy because the reorientation of the R phase is accompanied by a less strain variation than in the B19′ phase. The shift in A_f temperature after deformation in the B19′ phase and in the R phase in the annealed sample is the same and this is less than after the deformation in the B19′ phase in quenched sample (Fig. 1b). Thus, one may conclude that the reverse transformation in the deformed quenched sample is realized more "difficult" than in the annealed. As it was assumed in [3], the reason for the martensite stabilization effect may be the loss of the interface coherency during the preliminary deformation in the martensite state. In the annealed sample the Ni_4Ti_3 precipitates that formed during annealing created an internal stress which influenced on the formation of the martensite crystals on cooling. As the martensite stabilization effect (ΔA_f) is less in the annealed sample than in quenched one, then it may be assumed that the martensite structure that appeared on cooing under the stress field created by the Ni_4Ti_3 precipitates, partially suppressed the upset in the interface coherency during the deformation in the martensite state and it decreased the martensite stabilization effect value.
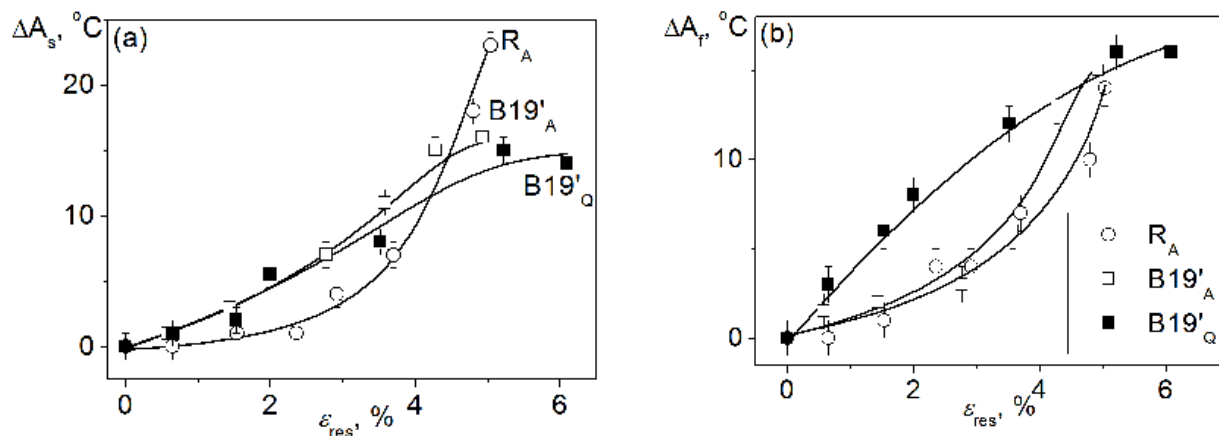
Fig. 1: The dependencies of the martensite stabilization effect ΔA_s (a) and ΔA_f (b) on the residual strain that was measured in the annealed and quenched samples after preliminary deformation in different states. The lower index Q is denoted to quenched sample; A – annealed sample.

References
[1]   M. Piao, K.Otsuka, S. Miyazaki, H. Horikawa, Mater. Trans. JIM, **1993**, *34*, 919-929.
[2]   Y. Liu, D. Favier, Acta Mater., **2000**, *48*, 3489-3499.
[3]   S. Belayev, N. Resnina, E. Iaparova, A. Ivanova, T. Rakhimov, V. Andreev, J. Alloys Compd., **2019**, *787*, 1365-1371.
[4]   X. Yan, J. Van Humbeeck, Mater. Sci. Eng. A, **2012**, *558*, 737–741.

O–SM–04

Mechanical properties evaluation for thermoelectric half-Heusler ZrNiSn comparing with Heusler ZrNi$_2$Sn

Yoshisato Kimura[1], Yusuke Tsubono[1,2], Yaw Wang Chai[3] and Takahito Ohmura[4]

[1]Tokyo Institute of Technology, School of Materials and Chemical Technology, Department of Materials Science and Engineering, Mail-box J3-19, 4259 Nagatsuta-cho, Midori-ku, Yokohama 226-8502, Japan, kimura.y.ac@m.titech.ac.jp
[2]Graduate student *now with* West Japan Railway Company
[3]Tokyo Institute of Technology, School of Materials and Chemical Technology, Mail-box J2-64, 4259 Nagatsuta-cho, Midori-ku, Yokohama 226-8502, Japan, chai.y.aa@m.titech.ac.jp
[4]National Institute for Materials Science (NIMS), Research Center for Structural Materials, 1-2-1 Sengen, Tsukuba, Ibaraki 305-0047, Japan, OHMURA.Takahito@nims.go.jp

Introduction

A half-Heusler type intermetallic compound ZrNiSn is an excellent thermoelectric material which can be used for high temperature applications [1,2]. Improvement of not only thermoelectric performance but also durability and reliability is required aiming for practical applications, and thereby, the evaluation of mechanical properties is one of important subjects for designing and developing high performance thermoelectric materials. Moreover, elastic and plastic deformation behavior is important knowledge for thermoelectric module fabrication. The Half-Heusler (HH) C1$_b$ type ordered structure of ZrNiSn is quite similar to that of Heusler (FH) L2$_1$ type ordered structure of ZrNi$_2$Sn. They have the same ordered structure frame in common, and a half of Ni-site of FH is vacant in HH. The objective of the present work is to understand the mechanical properties of HH ZrNiSn as compared with FH ZrNi$_2$Sn. Mechanical behavior was mainly examined in the atomic-scale using micro-Vickers hardness and nanoindentation measurements at room temperature, and compression test was conducted at high temperatures.

Materials and Methods

Single crystals of ZrNiSn and ZrNi$_2$Sn were fabricated by the unidirectional solidification using the optical floating zone melting method (OFZ) under flowing argon gas atmosphere with the positive pressure. Prior to the OFZ, alloy ingots were prepared using arc-melting. The crystal orientation was analyzed by the back reflection Laue method to select planes, [001], [111], and [121], on which Micro-Vickers hardness measurement and nanoindentation measurement were conducted at room temperature. Micro-Vickers hardness was measured using the condition; load of 980.7 mN and holding time of 10 s. Nanoindentation measurement was conducted using Berkovich indenter (trigonal pyramid tip) under the condition; loading rate of 50 μN/s and maximum load 2000 μN. Additionally, compression tests were carried out at 1173 K and 1273 K under the initial strain rate of 10^{-4} s^{-1} using specimens of 3 x 3 x 6 mm^3 in demension.

Results and Discussion

Averaged value of micro-Vickers hardness 847 HV of HH ZrNiSn is higher than 720 HV of FH ZrNi$_2$Sn. Similarly, values of nanohardness as well as Young's modulus of HH ZrNiSn tend to be larger than those of FH ZrNi$_2$Sn. Here, HH ZrNiSn shows the crystal orientation dependence of nanohardness and Young's modulus that values of [111] are higher than those of other orientation. On the other hand, HH ZrNiSn exhibits extremely low plastic deformability in the micro-scale, having cracks generated from all the four corners of micro-Vickers indentation. However, in the nano-scale, so-called pop-in events [3,4] which are supposed to correspond to the onset of plastic deformation are observed on the load-displacement (*P-h*) curves, where displacement is measured as penetration depth. Typical *P-h* curves measured for HH ZrNiSn and FH ZrNi$_2$Sn are shown in Fig. 1, on which a pop-in event is appered as burst displacement (or abrupt jump in displacement). It is thought that sufficiently high stress to generate dislocations is achieved in the condition of nanoindentation. The relationship between the critical pop-in load P_c and corresponding burst penetration depth Δh is represented in Fig. 2. Linear relationship is observed between P_c and Δh in HH ZrNiSn, showing wide range distribution from 300 to 1800 μN in P_c and from less than 1 to 12 nm in Δh. moreover, P_c tends to have a certain crystal orientation dependency, low values in [111] and high values in [001] and [121]. As compared P_c values of [001] and [121], at the same Δh values, [001] is much higher than that of [121], and plots of [001] are slightly deviated from the linear relationship toward small Δh value. It indicates that number of dislocations generated or/and mobility of dislocations should be somehow restricted in [001], since high P_c value means that released elastic energy is also high in pop-in. On the other hand, P_c observed in ZrNi$_2$Sn is about the same value regardless of crystal orientation. The possible active slip system of ZrNi$_2$Sn is suggested as {110}<110> by the consideration of Schmidt factor while deducing from the slip systems reported for FH phases [5]. Contrary to this, the operative slip system of HH ZrNiSn is not reported according to the best knowledge of the present authors. Deformed microstructure of ZrNiSn was observed and analyzed using transmission electron microscopy (TEM). Specimens were deformed by micro-Vickers indentation with the load of 250 mN. We have determined that there exist two-types of burgers vector, one is <110> type (same as in FH) and the other

is <111> type. Note that a 1/2[110] type dislocation can be dissociated into two 1/4[111] type dislocations, which may indicate that possible slip system of HH ZrNiSn could be the same {110}<110>. Plastically deformed region with high dislocation density extends wider in ductile FH $ZrNi_2Sn$ than in brittle HH ZrNiSn.
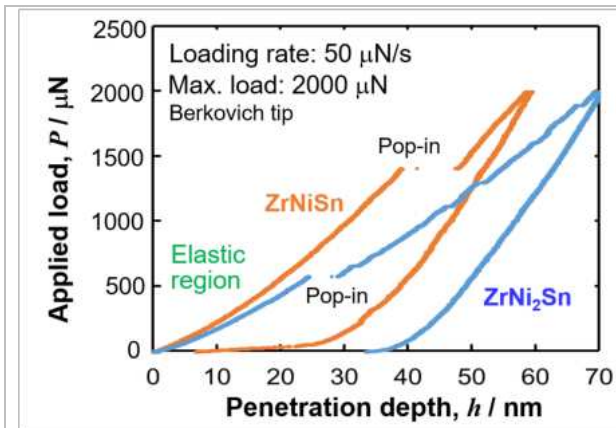
Fig. 1: Typical *P-h* curves with the appearance of pop-in event, measured for HH ZrNiSn and FH $ZrNi_2Sn$ single crystals on OR[111].	Fig. 2: The relationship between critical pop-in load P_c and penetration depth Δh measured for HH ZrNiSn and FH $ZrNi_2Sn$.
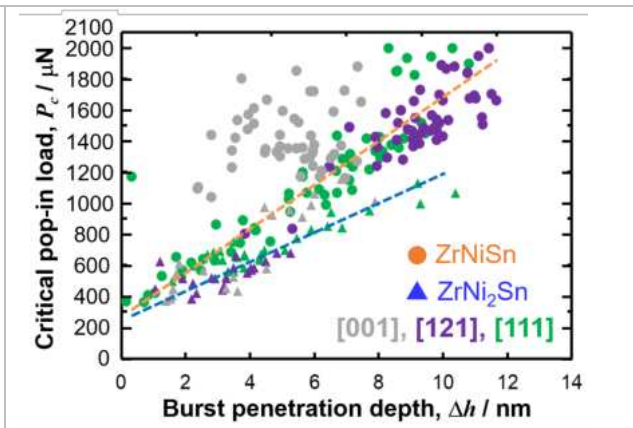
References

[1]   Y. Kimura, T. Tanoguchi, and T. Kita, Acta Materialia. **2010**, *58*, 4354–4361.
[2]   Y. Kimura and Y. W. Chai, JOM (Journal of The Minerals, Metals and Materials Society). **2015**, *67*, 233–245.
[3]   T. Ohmura, L. Zhang, N. Sekido, and K. Tsuzaki, Journal of Materials Research. **2012**, *27*, 1742–1749.
[4]   T. L. Li, Y. F. Gao, H. Bei, and E. P. George, Journal of the Mechanics and Physics of Solids. **2011**, *59*, 1147–1162.
[5]   P. R. Strutt, R. S. Polvani, and J. C. Ingram, Metallurgical Transactions A. **1976**, *7A*, 23–31.

O–SM–05

New interconnectors for high temperature thermoelectric silicides based devices

Florian Brix[1], Pierre Sallot[2], Clara Desgranges[2], Stéphane Mathieu[1] and Michel Vilasi[1]
[1]Université de Lorraine, Institut Jean Lamour, Campus Artem, 2 allée André Guinier, 54011 Nancy, France,
florian.brix@univ-lorraine.fr
[2]Safran-Tech, Materials and Processes Department, Rue des Jeunes Bois, Châteaufort, 78114 Magny-les-Hameaux,
France, pierre.sallot@safrangroup.com

Introduction

Thermoelectric silicides have been extensively studied for converting heat into electricity on semi- conductive junctions with a yield depending on their thermoelectric figure of merit $zT=S^2\sigma T/\kappa$ where S is the Seebeck coefficient, σ the electronic conductivity and κ the thermal conductivity. Among them, disilicides present a relatively low zT but are good applicants for high temperature applications (above 700 K) owing their high stability in air to the formation of a superficial protective layer made of silica [1]. $FeSi_2$ and Higher Manganese Silicides (formula $MnSi_{1.7}$) present both a high stability in air and a thermoelectric zT (respectively 0.2 [2] and 0.7 [3–5]) suitable for low energy applications. In this regard, it is noteworthy that high temperature applications need a good thermal compatibility between constitutive materials which includes a close thermal expansion to avoid stresses during cycling, a low interface resistance and a high chemical stability during ageing. Except for $TiSi_2$ that has been shown in the literature to be an efficient high temperature connector for those materials [6], those aspects remain unexplored to date. This work studies the thermal stability of contacts between $FeSi_2$ and $MnSi_{1.7}$ and a few titanium based silicides $TiSi_2$, $TiMnSi_2$ and $TiFeSi_2$.

Materials and Methods

Diffusion couples were manufactured in two steps: the various studied silicides were melted in high frequency furnace using pure metals and silicon in a water-cooled copper crucible in Ar atmosphere. Then, ingots were ball milled into powders with the use of ZrO_2 ceramic balls at 400 rpm during 10 min to obtain a fine powder. The studied interfaces were obtained subsequently by uniaxial hot pressing on simply stacked powders in a graphite die heated at 1050 °C for 4 h and pressed at 60 MPa in Ar atmosphere.

Results and Discussion

After sintering, interfaces observed by scanning electron microscope in Fig. 1 show that $TiSi_2/MnSi_{1.7}$ couple undergoes phase transformation. $TiMnSi_2$ (space group *Pbam* [8]) and pure silicon are identified at this interface. The same type of diffusion path is observed with the $TiSi_2/FeSi_2$ couple. $TiFeSi_2$ (isostructural of $TiMnSi_2$) and pure silicon form at the interface. The latter nucleates as small studs instead of a continuous border like in the $TiSi_2/MnSi_{1.7}$ diffusion couple. In both systems, the apparition of new phases creates new interfaces which increase the interfacial resistance. As a consequence, the thermoelectric properties of the complete device is globally degraded.
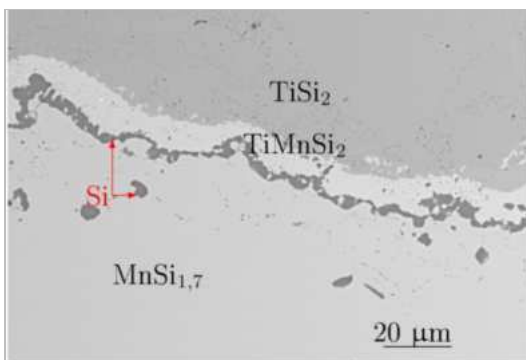
Fig. 1: SEM *post mortem* observation of $TiSi_2/MnSi_{1.7}$ interface
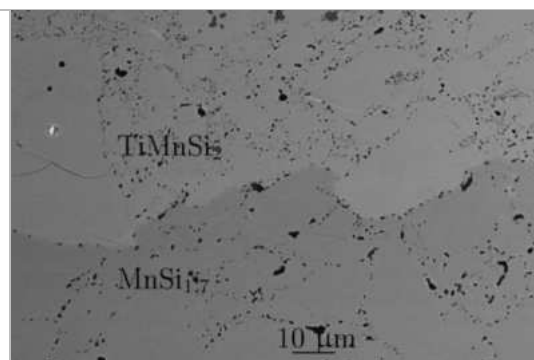
Fig. 2: SEM *post mortem* observation of $TiMnSi_2/MnSi_{1.7}$ interface

In order to avoid this deleterious effect related to the occurrence of multiple interfaces, the intermediate ternary compounds $TiFeSi_2$ and $TiMnSi_2$ were then synthetized and studied as potential optimized interconnectors. SEM observations evidence i) the existence of equilibria between ternary and binary intermetallic compounds, $TiFeSi_2/FeSi_2$ and $TiMnSi_2/MnSi_{1.7}$ respectively (see Fig. 2) and ii) the existence of a continuous solid solution between both ternary compounds (not illustrated here). Moreover, even after a long duration high temperature ageing, the interfaces remain

stable. Finally, their electrical resistivity and thermal expansion coefficient were measured. They showed valuable properties which confirm the applicability of such ternary intermetallic compounds as interconnectors for high temperature silicide thermoelectric devices. Thus, interdiffusion couples enabled to study phase equilibria between phases and should lead to the knowledge of stable systems and is therefore a promising way of choosing materials for creating durable contacts for high temperature applications.

References

[1] K. Kurokawa and A. Yamauchi, Des. Interfacial Struct. Solid State Phenom. 127, **2007**, 227– 232.

[2] M. I. Fedorov, *J Thermoelectr*, **2009**, 2, 51–60.

[3] Y. Kikuchi, Y. Miyazaki, Y. Saito, K. Hayashi, K. Yubuta and T. Kajitani, *Jpn. J. Appl. Phys.*, **2012**, 51, 085801.

[4] T.-H. An, S.-M. Choi, W.-S. Seo, C. Park, I.-H. Kim and S.-U. Kim, *J. Electron. Mater.*, **2013**, 42, 2269–2273.

[5] X. Chen, L. Shi, J. Zhou and J. B. Goodenough, *J. Alloys Compd.*, **2015**, 641, 30–36.

[6] M. Riffel, E. Groß and U. Stöhrer, *J. Mater. Sci. Mater. Electron.*, **1995**, 6, 182–185.

[7] X. Shi, Z. Zamanipour, J. S. Krasinski, A. Tree and D. Vashaee, *J. Electron. Mater.*, **2012**, 41, 2331–2337.

[8] J. Steinmetz, G. Venturini, B. Roques, N. Engel, B. Chabot and E. Parthé, *Acta Crystallogr. B*, **1982**, 38, 2103–2108.

O–SM–06

High temperature stable metallizations for SAW devices

Marietta Seifert[1], Siegfried Menzel[2], Steffen Oswald[3] and Thomas Gemming[4]

[1]Leibniz IFW Dresden, Helmholtzstr. 20, 01069 Dresden, Germany, marietta.seifert@ifw-dresden.de
[2]Leibniz IFW Dresden, Helmholtzstr. 20, 01069 Dresden, Germany, s.menzel@ifw-dresden.de
[3]Leibniz IFW Dresden, Helmholtzstr. 20, 01069 Dresden, Germany, s.oswald@ifw-dresden.de
[4]Leibniz IFW Dresden, Helmholtzstr. 20, 01069 Dresden, Germany, t.gemming@ifw-dresden.de

Introduction

Optimization and process control at high temperatures require sensor systems which operate reliably under these harsh conditions. Therefore, material systems composed of a high temperature stable piezoelectric substrate, optimized barrier and cover layers as well as a high temperature stable working metallization have to be developed. During the last years, various materials or material systems have been investigated regarding their high temperature properties. It appeared that refractory metals like W and Mo [1,2] and high temperature stable Al-based alloys like TiAl [3] and RuAl show promising results after high temperature treatments. As substrate material the high temperature stable $Ca_3TaGa_3Si_2O_{14}$ (CTGS) is often used since it remains piezoelectric even above 1000 °C. However, it is also known that there are strong chemical reactions between this substrate and Al based metallizations on top of it so that the application of suited barrier layers is essential.
This work reports on the improvement of the high temperature stability of RuAl alloys.

Materials and Methods

RuAl thin films with a thickness of 110 nm have been prepared by co-sputtering on CTGS substrates. As a protection against oxidation a 20 nm thick AlN, Al_2O_3 or SiO_2 layer or a combination of AlN and SiO_2 are added on top of the substrate and on top of the whole layer stack. For some experiments, additional thin Al layers are also added on top or below the RuAl film. To determine the influence of the CTGS substrate on the stability of the films, reference samples on thermally oxidized Si substrates were analyzed.
The samples were heat treated in high vacuum and air at up to 900 °C for 10 h and afterwards characterized regarding the phase formation (X-ray diffraction, XRD, in Bragg Brentano geometry and pole figure measurements), chemistry (Auger electron spectroscopy, AES, and energy dispersive X-ray diffraction, EDX) and morphology (cross section imaging and transmission electron microscopy).

Results and Discussion

The annealing experiments reveal a strong dependence of the film performance on the applied barrier and cover layers as well as on the substrate material.
All cover layers realize an oxidation protection of the RuAl film for heat treatments up to 600 °C in air. For these conditions, a strong phase formation and hardly any oxidation are observed. The differences of the performance of the barrier layers become obvious when the samples are annealed at 800 °C in air. Under this condition, the films with AlN barrier and cover layer are oxidized on both substrates. For the other film systems only a minor oxidation of the Al occurs and XRD proves the presence of the RuAl phase. After annealing at 900 °C in air also the other cover layers fail, however, a small RuAl XRD signal is measured for the films with a combined AlN/SiO_2 barrier and cover layer (Fig. 1). A reaction between the CTGS substrate and the film is found for all samples with only an AlN or a SiO_2 barrier.
After a heat treatment at 900 °C under high vacuum the influence of the substrate material becomes obvious. All films on Si substrates show a strong RuAl phase formation. On CTGS, however, only the films with a combined AlN/SiO_2 barrier and cover layer remain stable. For all other samples there is a strong reaction with the CTGS substrate (Fig. 2).

Fig. 1: Results of the XRD measurements for a RuAl film on CTGS with a combined AlN/SiO₂ barrier/cover layer after the different annealing temperatures.	Fig. 2: SEM images of cross sections of the RuAl films on CTGS with an AlN and a combined AlN/SiO₂ barrier/cover layer after annealing at 800 °C in air and 900 °C in high vacuum.
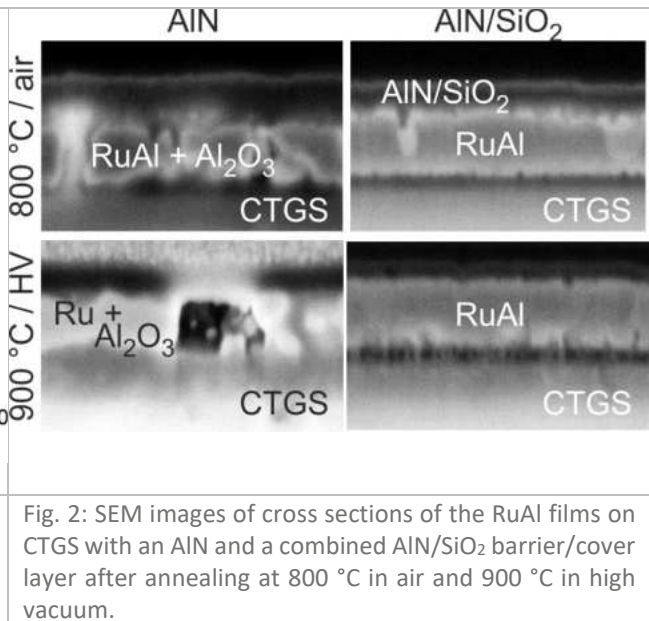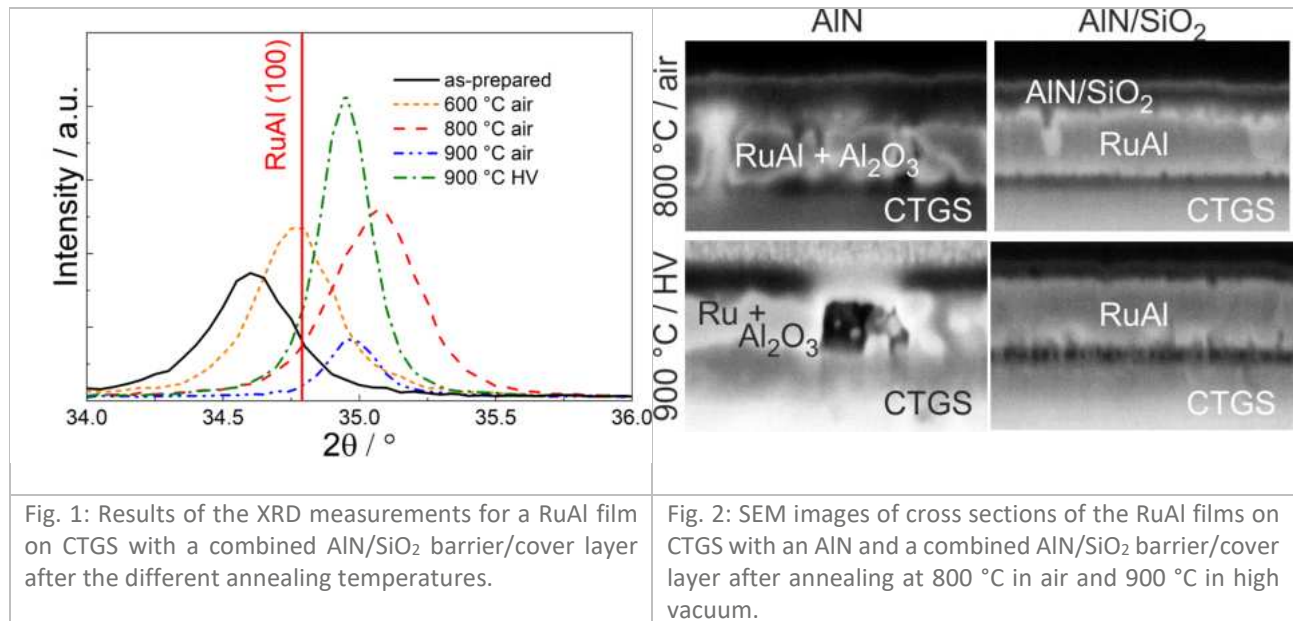
References
[1]   G.K. Rane, M. Seifert, S. Menzel, T. Gemming, J. Eckert, Materials. **2016**, *9*, 101.
[2]   G.K. Rane, W. Ren, M. Seifert, T. Gemming, S. Menzel, Material Science and Engineering B. **2019**, *243*, 69-107.
[3]   E. Lattner, M. Seifert, T. Gemming, S. Heicke, S. Menzel, Journal of Vacuum Science & Technology A: Vacuum, Surfaces, and Films. **2017**, *35(6)*, 061303.
[4]   M. Seifert, G.K. Rane, S. Menzel, T. Gemming, Journal of Alloys and Compounds. **2016**, *688*, 228-240.
[5]   M. Seifert, G.K. Rane, S. Oswald, S. Menzel, T. Gemming, Materials. **2017**, *10*, 277.
[6]   M. Seifert, G.K. Rane, S. Menzel, S. Oswald, T. Gemming, Journal of Alloys and Compounds. **2019**, *776*, 819-825.

O–PS–01

A systematic investigation on refractory-metal based phase diagrams with and without the Laves phase

Seiji Miura[1], Li Peng[2], Satoshi Takizawa[3], Toshiaki Horiuchi[4] and Ken-ichi Ikeda[5]

[1]Division of Materials Science and Engineering, Faculty of Engineering, Hokkaido University, Kita13 Nishi8, Kita-ku, Sapporo 060-8628, Japan, miura@eng.hokudai.ac.jp

[2]Graduate Student, Department of Materials Science and Engineering, Hokkaido University, Kita13 Nishi8, Kita-ku, Sapporo 060-8628, Japan, listen0812@163.com

[3]Division of Materials Science and Engineering, Faculty of Engineering, Hokkaido University, Kita 13 Nishi 8, Kita-ku, Sapporo 060-8628, Japan, takizawa@lms4-ms.eng.hokudai.ac.jp

[4]Laboratory of Advanced Materials for Cold Region, Hokkaido University of Science, Maeda 7-15-4-1, Teine-ku, Sapporo 006-8585, Japan, horiuchi@hus.ac.jp

[5]Division of Materials Science and Engineering, Faculty of Engineering, Hokkaido University, Kita13 Nishi8, Kita-ku, Sapporo 060-8628, Japan, ikeda.ken-ichi@eng.hokudai.ac.jp

In various refractory-metal based alloys such as Nb-Cr alloys, AB_2-type Laves phases appears. It has been pointed out that the atomic size ratio of constituent elements, R_A/R_B, is quite important to understand the stability of Laves phase [1-2]. However, the formation enthalpy of these Laves phases are evaluated to be of the order of several kJ/mol, which is much smaller than that of typical intermetallic compounds such as Ni_3Al and NiAl.

Some refractory-metal based phase diagram show a continuous BCC solid solution with smaller R_A/R_B, and some show BCC-BCC two-phase separations with relatively larger R_A/R_B. Then, with much larger R_A/R_B, the Laves-phase appears. This strongly suggests the atomic size ratio also governs the stability of BCC phase. To investigate the stability of BCC solid solution phase a bonding energy between two refractory elements is required. We performed ab initio calculations based on the density functional theory and obtained formation energies dH for various B2 type structures and also C15-type structures composed of refractory elements, such as NbCr and $NbCr_2$. We have adopted the ultrasoft pseudo potential and the PBE-GGA potential for the calculations. Lattice constants have been optimized and the electronic energies have been obtained for each B2 phase and C15-phase. The package produced by the abinit project [3] was employed for the numerical computations.

It is quite interesting that the formation enthalpy dH of various C15 Laves seemingly increases with decreasing R_A/R_B even in the unstable range with R_A/R_B lower than 1.06. On the other hand, the formation enthalpy dH of various B2 phase is quite small and the interaction between refractory elements are small.

By using a simple pair-interaction model and CALPHAD method with A-B interaction energy evaluated by the formation enthalpy of B2 compounds, the composition dependence of the formation enthalpy of BCC solid solutions with different R_A/R_B was evaluated to understand the effect of R_A/R_B on the phase stability of Laves phases with relatively small formation enthalpy in binary phase diagrams. As the results, it was concluded that with increasing R_A/R_B, the BCC phase shows a miscibility gap, and low-stability Laves phase appears as a stable phase as indicated schematically in Figure.1.

Acknowledgement

References
[1] J.H. Zhu, C.T. Liu, L.M. Pike, P.K. Liaw, Intermetallics. **2002**, *10*, 579–595.
[2] T. Yamanouchi, S. Miura, Materials Transactions. **2018**, *59*, 546-555.
[3] X. Gonze et al., Computer Phys. Comm. **2016**, *205*, 106-131.
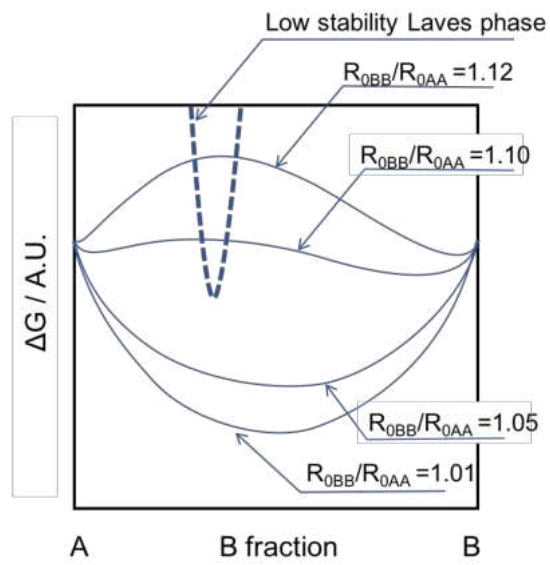
Fig. 1: A semi-schematic drawing of ΔG of BCC phase as a function of B fraction for various atomic size ratio, together with a curve for a low stability Laves phase (dotted line).

O–PS–02

Phase relations between fcc-Co, L1$_2$ TiCo$_3$, and the two coexisting Laves phases C36 and C15 TiCo$_2$

Frank Stein[1], Maisam Merali[1,2] and Philipp Watermeyer[1]

[1]Max-Planck-Institut für Eisenforschung GmbH, Düsseldorf, Germany, stein@mpie.de
[2]Student at St. Catherine's College, University of Cambridge, Cambridge, UK

Introduction

The Co-Ti system is one of the important systems for the development of Co-based superalloys and the only binary Co-X system forming coherent γ/γ' microstructures (fcc-Co with fcc L1$_2$ TiCo$_3$). Even though binary Co-Ti alloys are not suited for applications, this system serves as a basis for development of superalloys, see e.g. [1,2]. Surprisingly, the phase relations and invariant reaction temperatures in the Co-rich part of the system are not very well established.

According to the phase diagram adopted from the assessment of Murray [3] and shown in Fig. 1a), the L1$_2$-ordered TiCo$_3$ phase forms by a peritectic reaction from the fcc-Co solid solution and the liquid phase at a composition of approximately 20 at.% Ti, i.e., far away from the stoichiometric composition of this phase. In addition, the phase diagram shows a eutectic reaction between TiCo$_3$ and the hexagonal C36 Laves phase h-TiCo$_2$ at approximately 24 at.%. However, to the best of our knowledge, the occurrence of a eutectic type of microstructure in this composition range between TiCo$_3$ and h-TiCo$_2$ was never reported in the literature. In contrast to Murray's assessment, a more recent version of the phase diagram presented by Davydov et al. [4] (see Fig. 1b)) does not show a eutectic reaction but instead indicates two independent peritectic reactions. Following this diagram, TiCo$_3$ can form from fcc-Co solid solution at approximately 20 at.% Ti (L + fcc-Co <-> TiCo$_3$) but also from the hexagonal C36 Laves phase at approximately 24 at.% Ti (L + C36-TiCo$_2$ <-> TiCo$_3$).

Another interesting feature of the binary phase diagram is the occurrence of two polytypes of the Laves phase TiCo$_2$, one with the hexagonal C36 and the other one with the cubic C15 structure type. The C36 version is reported to exist at off-stoichiometric compositions on the Co-rich side, while cubic C15 Laves phase should be stable on the Ti-rich side near the stoichiometric composition. Contradicting information exists about the existence and width of a two-phase field between these two Laves phase variants. Until today, there is no real experimental proof of a two-phase field between the two polytypes. The only experimental investigation of this two-phase field was performed by van der Straten et al. [5], who applied diffusion couples. However, they could not clearly detect such a two-phase field and state in their paper "if this gap truly exists then it is apparently too small to be measured."

In order to contribute to the clarification of these problems and to obtain an improved version of the Co-rich part of the phase diagram, we prepared two diffusion couples to produce extended diffusion zones of the Laves phase with a continuous concentration gradient covering the entire stability range of both variants. The composition profiles were determined by electron probe microanalysis (EPMA) along the concentration gradient and phases were identified by electron backscatter diffraction (EBSD) scanning the same areas. Besides these diffusion couples, we prepared a series of alloys that were heat-treated at 800 and 1100 °C to study the two-phase equilibria Co+TiCo$_3$, TiCo$_3$+h-TiCo$_2$, and c-TiCo$_2$+TiCo. The crystal structures were analyzed by X-ray diffraction (XRD). Finally, the liquidus and all invariant reaction temperatures as well as the fcc-Co solvus and Curie temperatures were determined by differential scanning calorimetry (DSC).

Materials and Methods

Diffusion couples Co/TiCo and TiCo$_3$/TiCo were prepared by contacting two blocks of the single-phase materials, wrapping them into Ta foil, and heat-treating them in a pure Ar atmosphere at 1100 °C for 144 h and 168 h, respectively. The resulting diffusion profiles were analyzed by EPMA and EBSD. In addition, eleven binary alloys with compositions between 4 and 50 at.% Ti were synthesized by levitation melting from the pure elements Co and Ti. Heat treatments were performed at 800 °C for 500 h and 1100 °C for 50 h. As-cast and heat-treated samples were analysed by SEM, EPMA, DSC and XRD.

a)

b)
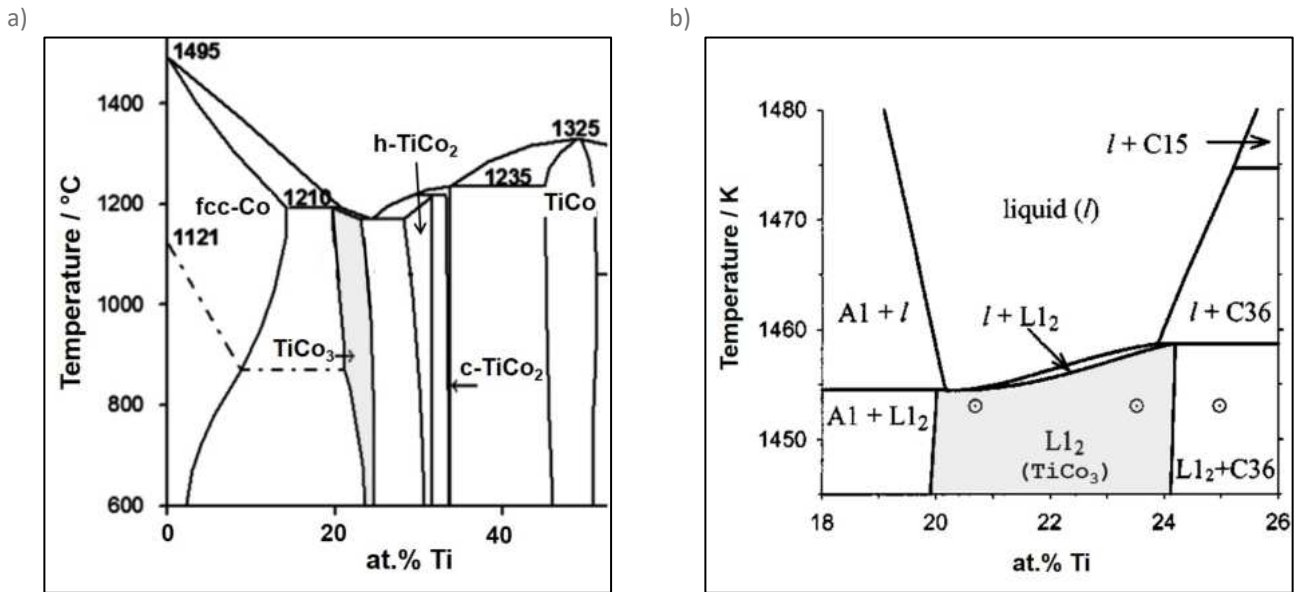
Fig. 1: a) Co-rich part of the Co-Ti phase diagram adopted from Murray [3] indicating peritectic formation of $L1_2$ $TiCo_3$ and a eutectic reaction L <-> $TiCo_3$ + h-$TiCo_2$, and b) alternative version from Davydov et al. [4] indicating formation of $L1_2$ $TiCo_3$ from two independent peritectic reactions.

Results and Discussion

The investigated diffusion couples were found to exhibit an extended diffusion zone around the contact surface with overall thicknesses in the order of 1 mm. The concentration profiles include all phases occurring in this part of the system, i.e., fcc-Co, $TiCo_3$, $TiCo_2$, and TiCo. Both the $L1_2$ $TiCo_3$ phase as well as the Laves phase form extended diffusion zones of 150 to 200 µm in width. Even though EBSD clearly proves a change of the Laves phase structure type from hexagonal C36 to cubic C15 at a well-defined composition within the $TiCo_2$ diffusion zone, EPMA does not indicate any gap in composition within the experimental limits of accuracy (~0.2 at.%). Regarding the formation of the $L1_2$ $TiCo_3$ phase, our results clearly disprove the 'classical' version of Murray (Fig. 1a)), and instead of the 'double-peritectic' version of Davydov et al. (Fig. 2b)), we suggest a peritectic reaction L + h-$TiCo_2$ <-> $TiCo_3$ and a eutectic L <-> fcc-Co + $TiCo_3$. Then, the fact that the composition of this eutectic is above the single-phase $TiCo_3$ field might explain why no eutectic microstructures are observed. More details will be presented and discussed in an article-in-preparation [6] and at the conference.

References

[1]   H.J. Im, S.K. Makineni, B. Gault, F. Stein, D. Raabe, P.-P. Choi, Scr. Mater. **2018**, *154*, 159-162.
[2]   C.H. Zenk, I. Povstugar, R. Li, F. Rinaldi, S. Neumeier, D. Raabe, M. Göken, Acta Mater. **2017**, *135*, 244-251.
[3]   J.L. Murray, Phase Diagrams of Binary Titanium Alloys, ASM Int., Materials Park, OH, USA, **1987**, 59-68.
[4]   A.V. Davydov, U.R. Kattner, D. Josell, J.E. Blendell, R.M. Waterstrat, A.J. Shapiro, W.J. Boettinger, Metall. Mater. Trans. **2001**, *A32*, 2175-2186.
[5]   P.J.M. van der Straten, G.F. Bastin, F.J.J. van Loo, G.D. Rieck, Z. Metallkd. **1976**, *67*, 152-157.
[6]   F. Stein, M. Merali, I. Wossack, P. Watermeyer, in preparation.

O–PS–03

Plasticity of topologically close packed phases – from nanomechanics to HR-TEM

Stefanie Sandlöbes, Sebastian Schröders, James S. K.-L. Gibson and Sandra Korte-Kerzel

Institute for Physical Metallurgy and Metal Physics, Aachen, RWTH Aachen University, Kopernikusstr. 14, 52074 Aachen, Germany, sandloebes@imm.rwth-aachen.de, schroeders.s@duraauto.com, gibson@imm.rwth-aachen.de, korte-kerzel@imm.rwth-aachen.de

Introduction

The μ-phase belongs to the class of topologically close packed (TCP) phases, which form as precipitates in a wide range of materials. TCP phases are highly ordered phases both in terms of chemistry and stacking, covering a wide range of compositions [1, 2]. These phases are usually considered being hard and brittle to their complex crystal structure [3]. The deformation behaviour of such hard and brittle precipitates can have significant effects on the properties of metallic alloys. These may be advantageous, where an alloy is purposefully reinforced, but often the presence of hard precipitates is detrimental and can lead to stress concentrations, crack initiation and local dealloying of the matrix. In the case of topologically close packed phases in nickel-based superalloys all of these effects have been observed, but the underlying properties of these phases are largely unknown, impeding any purposeful discrimination between different precipitates or modelling of the mechanism by which they affect the surrounding material.

We have therefore employed nanomechanical testing and (high resolution) transmission electron microscopy (TEM) imaging to characterize the plastic deformation in the binary Fe_7Mo_6 μ-phase as well as to elucidate the phase's anisotropy. The active slip systems and respective critical resolved shear stresses (CRSS) were determined using micropillar compression and nanoindentation with statistical electron backscatter diffraction (EBSD)-assisted slip trace analysis, and the underlying defect structures confirmed with the TEM.

Materials and Methods

The material synthesis and the deformation and characterization methods applied are described in detail in [4, 5].

Results and Discussion

Using nanoindentation and micropillar compression we observed an average hardness and indentation modulus of 11.7 ± 0.9 GPa and 249 ± 8 GPa for the Fe_7Mo_6 μ-phase. EBSD assisted slip trace analysis around indents showed that slip occurs mainly on the basal and prismatic planes. Specifically, we observed that slip takes place predominately on basal planes in indentation and at a CRSS of 1.92±0.22 GPa or 1.79±0.31 GPa in micropillar compression assuming conventional basal dislocation glide or synchroshear, respectively, Fig. 1 ((a) and (b)).

When the resolved shear stress on the basal planes was low, slip on prismatic planes was activated. The corresponding CRSS for the onset of deformation by dislocation glide on the prismatic planes was measured as 2.11±0.66 GPa by micropillar compression.

Combined analysis of nanoindentation data and TEM characterization of the defect structure underneath corresponding indents showed a strong interaction of growth defects with mobile dislocations. Specifically, softening was observed where dislocations can move along pre-existing defects and hardening where the slip plane intersects them.

Further, we used high resolution TEM (HR-TEM) to investigate the post-deformation defect structure of the Fe_7Mo_6 μ-phase. To this end we have performed HR-TEM analysis on deformed samples revealing stacking faults which are presumably induced by plastic deformation. We have compared these defects to theoretically possible stacking faults within the μ-phase building blocks. The experimentally determined stacking fault configurations were found to match with those formed by snychroshear on the basal planes in the Laves-phase building blocks, Fig. 1 (c). We therefore concluded that plasticity on the basal planes of the Fe_7Mo_6 μ-phase occurs in the Laves-layers of the stacked unit cell by the synchroshear mechanism [6].
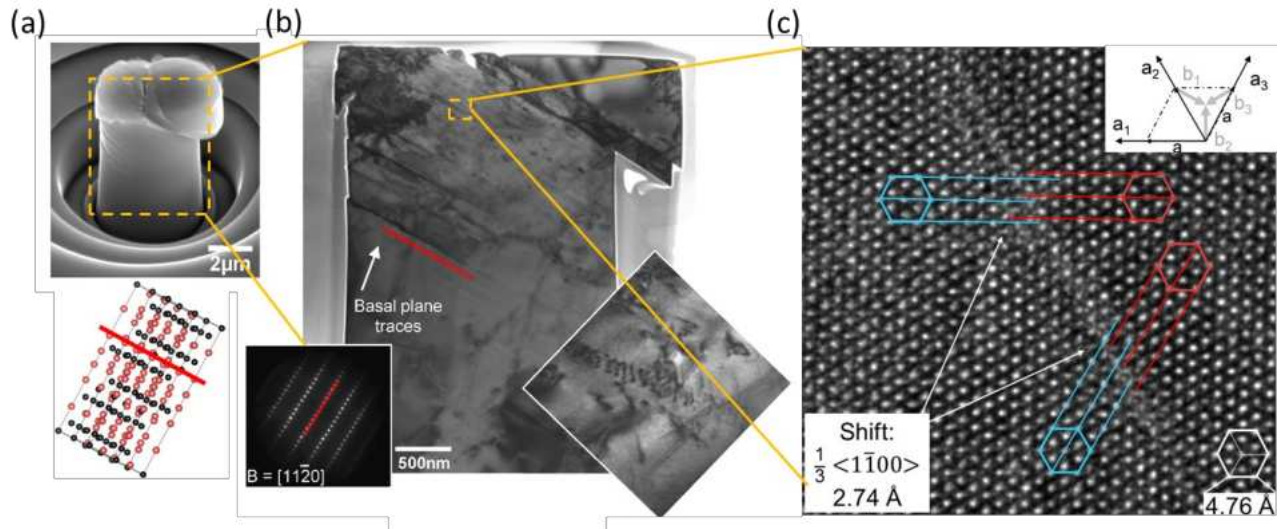
Fig. 1: (a) Secondary electron micrograph of a deformed Fe_7Mo_6 μ-phase micropillar, the crystallographic orientation and activated slip plane are given below the micrograph as a schematic. (b) TEM micrograph revealing dislocation slip bands on the basal plane. (c) HR-TEM micrograph of a stacking fault in deformed Fe_7Mo_6 μ-phase whose structure is identical to that formed by synchroshear in the Laves-phase building blocks. [4, 5]

References

[1] K. Y. Cheng, C.Y. Jo, T. Jin, Z. Q. Hu, Z.Q., Journal of Alloys and Compounds. **2012**, *536*, 7-19.
[2] W. P. Huhn, M. Widom, A. M. Cheung, G. J. Shiflet, S. J. Poon, J. Lewandowski, Physical Review B. **2014**, *89*, 104103.
[3] G. Sauthoff: Intermetallics, first ed. Wiley-VCH, Weinheim, **1995**.
[4] S. Schröders, S. Sandlöbes, C. Birke, M. Loeck, L. Peters, C. Tromas, S. Korte-Kerzel, International Journal of Plasticity. **2017**, *108*, 125-143.
[5] S. Schröders, S. Sandlöbes, B. Berkels, S. Korte-Kerzel, Acta Materialia. **2019**, *167*, 257-266.
[6] J. Guénolé, F.Z. Mouhib, L. Huber, B. Grabowski, S. Korte-Kerzel, Scripta Materialia. **2019**, *166*, 134-138.

O–PS–04

Non-centrosymmetry – assignment of the absolute structure by X-ray diffraction and EBSD

Ulrich Burkhardt[1], Horst Borrmann[1], Marcus Schmidt[1], Aimo Winkelmann[2] and Juri Grin[1]

[1]Max-Planck-Institut für Chemische Physik fester Stoffe, Nöthnitzer Straße 40, 01187 Dresden, Germany, burkhardt@cpfs.mpg.de

[2]Laser Zentrum Hannover, Hollerithallee 8, 30419 Hannover, Germany, a.winkelmann@lzh.de

Introduction

Non-centrosymmetric crystal structures remain both fascinating and challenging because non-centrosymmetry is pre-condition of various physical properties like skyrmions, unconventional superconductivity, ferro-electricity and others. The determination of the absolute structure is often difficult because as twinning often is hard to detect and may lead to reduction or vanishing of related physical effects. Well established diffraction methods for determination or assignment of the absolute structure are X-ray diffraction and convergent beam electron diffraction (CBED) in TEM. Intensity differences of Friedel pairs originate from the anomalous dispersion effect in X-ray diffraction and dynamical scattering of electrons in the TEM. Winkelmann et al. demonstrated that electron backscatter diffraction (EBSD) patterns of α-quartz crystals allow to assign their chirality by comparison of experimental and dynamically simulated EBSD patterns [1]. We have applied both methods - X-ray diffraction and EBSD - on crystals with different absolute structure of the non-centrosymmetric phase CoSi. Flack parameter and cross-correlation values are used to assign the absolute structure on the same crystals as well as EBSD analyses on multi-domain crystals are presented.

Materials and Methods

Based on the results of crystal growth by chemical vapor transport in the system Co/Si [2] crystals of CoSi were grown using iodine as transport agent. In a first step CoSi was synthesized by an isothermal reaction of the elements cobalt and silicon in the presence of iodine at 700 °C in evacuated fused silica tubes during 120 h. In a second step, CoSi crystallized by a chemical transport reaction in a temperature gradient from 700 °C (source) to 800 °C (sink), and transport agent concentration of 0.5 mg/cm^3. Cross-sections of agglomerated crystals are prepared by metallographic methods and, after SiO_2 finishing, allowed to obtain high quality EBSD patterns. Subsequently, X-ray diffraction data sets were collected using single crystal cubes that were extracted on a focused Xe-ion beam system.

CoSi phase crystallizes in the cubic FeSi-type (B20) structure type (space group $P\,2_1 3$) with both elements on fourfold positions $4\,a$ (x, x, x). With respect to a right-handed orthogonal coordinate system, the absolute structure of FeSi with coordinates x_{Fe} = 0.1358 and x_{Si} = 0.844 is assigned to A-form and the enantiomorphic absolute structure with coordinates x'_{Fe} = 1-x_{Fe} and x'_{Si} = 1-x_{Si} is labelled with B-form according to [4].

We used a best-fit pattern matching approach to find the orientation and the enantiomorph corresponding to each experimental Kikuchi pattern. To this end, we optimized the normalized cross-correlation coefficient r between the experimental and the simulated Kikuchi pattern of the reference structure as described in [3]. For each experimental pattern, we obtain two optimized correlation coefficients r_{+E} and r_{-E} for the fit to the reference structure, and the inverted enantiomorph, respectively.

Results and Discussion

Crystal structure determination on cube shaped crystals (l ≈ 40 μm) with A- and B-Form each from X-ray diffraction data result in R$_F$-values close to 1 % and Flack parameters $x \approx 0$ indicating on high quality single crystals and different absolute structure without significant mixing of enantiomorph domains. These crystals were cut out by Xe-FIB technique from larger millimeter size crystals which were characterized before by EBSD analyses. The comparison of these experimental and simulated EBSD pattern clearly revealed always better pattern matching for one of both simulated pattern and thus allow reliable assignment of the absolute structure. X-ray diffraction and EBSD pattern analyses resulted the same assignment. This proves the consistency and reliability for both evaluation processes.

Multi domain CoSi crystals formed by domains with different absolute configuration were found, too. Here, the as-grown surfaces gave excellent Kikuchi pattern. In this case comparably simple experimental set-up is sufficient to assign the absolute structure with high spatial resolution.

References

[1]   A. Winkelmann, G. Nolze, Ultramicroscopy **2015**, *149*, 58-63.doi: 10.1016/j.ultramic.2014.11.013

[2]   O. Bosholm, H. Oppermann, S. Däbritz, Z. Naturforsch. **2000**, *55b*, 1199-1205. doi: 10.1515/znb-2000-1214.

[3]   G. Nolze, R. Hielscher, A. Winkelmann, Crystal Research and Technology **2016**, *52*, 1600252; doi: 10.1002/crat.201600252

[4]   J.C.H. Spence, J.M. Zuo, M.O'Keeffe, K.Marthinsen, R.Hoier, Acta Cryst. A **1994**, *50*, 647-650; doi: 10.1107/S0108767394002850

O–PS–05

Influence of plastic deformation in the disorder-order transition of 18 carat red gold alloys

Marina Garcia Gonzalez[1,2], Steven Van Petegem[1], Nadine Baluc[3], Fanny Lalire[4] and Helena Van Swygenhoven[1,2]

[1]Paul Scherrer Institute SYN/PEM, Villigen, Switzerland, marina.garcia-gonzalez@psi.ch
[2]Ecole Polytechnique Fédérale de Lausanne STI/EDMX/NXMM, Lausanne, Switzerland
[3]CIME, Ecole Polytechnique Fédérale de Lausanne, Switzerland
[4]Varinor S.A., Switzerland

Introduction

Traditional metal processing methods include a series of thermo-mechanical treatments, characterized by fast cooling rates and heterogeneous plastic deformation. As opposed to other colored gold alloys, red gold shows a reduced workability resulting in shape distortion and fracture. These alloys develop a fine microstructure of ordered nano-domains during manufacturing and this is believed to be responsible for the build-up of residual stresses in the material.

Red gold undergoes the same low temperature disorder-order phase transformation as equiatomic AuCu. The addition of Ag lowers the critical temperature for ordering and slow down the ordering kinetics[1]. This solid state phase transformation is known to depend on the thermal treatment parameters [2] but also on the history of the microstructure [3,4]. While many studies focused on the age-hardening behavior and microstructure development after ageing [5–11], very little research has been done to verify the role of plastic deformation on the early stages of ordering. Recrystallization studies on severely deformed AuCu revealed a competition between ordering and recrystallization as a function of temperature [12]. It is very well known that in some materials the strain field of a dislocation facilitates the nucleation of precipitates [13,14]. Possible mechanisms are stress induced local changes in lattice parameters accommodating the precipitate more readily, or locally induced changes in chemical composition reducing the critical ordering temperature [15]. It is however not clear if and how dislocations influence the degree of ordering during ageing as some of the reported results are contradictive.

Ex situ experiments performed on naturally aged samples in the deformed and non-deformed condition show a correlation between plastic deformation and degree of ordering. Here we report on in situ synchrotron X-ray diffraction experiments on pre-deformed and non-deformed samples during cooling and subsequent heating addressing the early stages of ordering. The results are complemented by TEM observations.

Materials and Methods

The alloys were prepared by continuous casting from fine metal precursors (Au, Ag, Cu) melt in a graphite crucible to form 18 carat red gold ($Au_{75}Cu_xAg_{(1-x)}$ for x ≥ 20 in %wt.). They were rolled in the form of strips, well homogenized and recrystallized. For the in situ temperature experiments, four samples are heated to 660°C with a heating rate of 100°C/min and kept there for 2min to ensure a complete dissolution of the L10 precipitates. Then the samples are cooled to room temperature using two colling rates: -100°C/min and -800°C/min. Two of the samples were then cold rolled to a thickness reduction of 25% using a Cooks rolling mill 999 AXWA. Finally, all 4 samples are heated at 10K/min until 450°C.

The *in situ* X-ray diffraction experiments are performed at the High Energy Materials Science Beamline (ID31) at ESRF. The X-ray beam had an energy of 79keV and a size of 0.2×0.2mm2. Diffracted X-rays are recorded with a Pilatus 3M detector. Exposure times were 0.1s. The 2D X-ray diffraction patterns are reduced to conventional 1D patterns by azimuthal integration using available routines at ID31. Single peak fitting with PearsonVII functions are performed using our own developed MATLAB routines since full pattern fitting methods cannot be applied. The difficulty in fitting lies in the fact that the lattice parameters of the disordered A1 and the ordered L10 phase are very similar and the large coherency strains in the early stages of precipitation growth.

Electron microscope investigations are carried out in thin foils prepared by mechanical polishing and electrolytic thinning with the double-jet technique in a Tenupol-5. The electrolyte used for this thinning is a mixture of 50%HCl – 30% ethanol-10% glycerol at 3⁰C. Observations are made in a FEI 220S TALOS microscope operating at 200kV. Both bright-field and dark-field observations are made combined with selected area diffraction patterns.

Results

Our experiments confirm that the degree of ordering in red gold is enhanced when the material was priory subjected to plastic deformation. Moreover, higher ordering is present in the surface region of a wire subject to plastic deformation as a result of cold rolling. It is shown that the presence of dislocations induces heterogeneous nucleation of ordered precipitates and enhances both nucleation and precipitate growth which starts at a lower temperature.

References

[1]   H.K. K. Yasuda, Bull Tokyo Med Dent Univ 22, **1975**, 101–111.
[2]   G.J. Dienes, J. Appl. Phys. 22, **1951**, 1020–1026.
[3]   G.C. Kuczynski, R.F. Hochman, M. Doyama, J. Appl. Phys. 26, **1955**, 871–878.
[4]   A.Y. Volkov, V.A. Kazantsev, Phys. Met. Metallogr. 113, **2012**, 62–71.
[5]   M. Ohta, T. Shiraishi, M. Nakagawa, S. Matsuya, J. Mater. Sci. 29, **1994**, 2083–2086.
[6]   T. Shiraishi, M. Ohta, M. Nakagawa, R. Ouchida, J. Alloys Compd. 257, **1997**, 306–312.
[7]   M. Ohta, T. Shiraishi, M. Yamane, K. Yasuda, Dent. Mater. J. 2, **1983**, 10–17.
[8]   L. Pezzato, G. Magnabosco, K. Brunelli, M. Breda, M. Dabalà, Metallogr. Microstruct. Anal. 5, **2016**, 116–123.
[9]   Y. Kim, M. Niinomi, M. Nakai, T. Akahori, T. Kanno, H. Fukui, J. Alloys Compd. 519, **2012**, 15–24.
[10] H-I. Kim, D-H. Lee, J-A. Sim, Y-H. Kwon, H-J. Seol, Mater. Charact. 60, **2009**, 357–362.
[11] R. Ouchida, T. Shiraishi, M. Nakagawa, M. Ohta, J. Mater. Sci. 30, **1995**, 3863–3866.
[12] B.A. Greenberg, G. Hug, O.V. Antonova, T.S. Boyarshinova, Z.M. Pesina, I.N. Sachanskaya, A.Y. Volkov, Intermetallics 5, **1997**, 297–309.
[13] W.A. Curtin, D.L. Olmsted, L.G. Hector Jr, Nat. Mater. 5, **2006**, 875–880.
[14] M. Legros, G. Dehm, E. Arzt, T.J. Balk, Science 319, **2008**, 1646–1649.
[15] A.M. Hunt, D.W. Pashley, J. Phys. Radium 23, **1962**, 846–853.

O–CO–01

Effect of Nb and V additions on oxidation behavior of α_2-Ti-30at%Al alloys

Shigenari Hayashi[1], Domingo Jullian[2] and Masao Takeyama[3]

[1]Faculty of Engineering, Division of Materials Science and Engineering, Hokkaido University, N13-W8, Kitaku, Sapporo 060-8628, Japan, hayashi@eng.hokudai.ac.jp

[2]Faculty of Engineering, Division of Materials Science and Engineering, Hokkaido University,N13-W8, Kitaku, Sapporo 060-8628, Japan, domingo.jullian@gmail.com

[3]School of Materials and Chemical Technology, Tokyo Institute of Technology, 2-12-1, Meguroku, Tokyo 152-8550, Japan, takeyama@mtl.titech.ac.jp

Introduction

TiAl alloys consist of mainly α_2 and γ lamellar structure. These alloys are now used for low-pressure turbine blades because of their specific high strength-to-mass ratio at high-temperatures. In order to obtain excellent mechanical properties from room to high temperatures and good manufacturability by casting and/or forging, the microstructure of TiAl alloys must be appropriately optimized. The optimized microstructure is achieved by different heat-treatments and different compositions. Nb and V are β-stabilizing elements and used for forging-TiAl alloys. One of the critical issues of TiAl alloys is their poor oxidation resistance at temperatures higher than 800°C. The inclusion of alloying elements in TiAl is known to affect oxidation performance. Nb and V are known to be beneficial and detrimental, respectively for oxidation performance; however, the mechanism that is responsible for the Nb/V-effect on oxidation of TiAl alloys is still unknown. In this study, the oxidation behavior of α_2-Ti-30Al with and without Nb and/or V addition is investigated to elucidate the effect of those elements on oxidation.

Materials and Methods

In order to eliminate the effect of microstructure on oxidation performance, single phase α_2-Ti-30at%Al alloys with/without different Nb and V contents are used in this study. All alloy ingots, 12mmφ x 100mm, were produced by Ar-arc melting with constituent pure-metals (>99.9%), and homogenized at 1150°C for 48h. Samples for oxidation test were cut from the homogenized ingots with a thickness about 1mm. Sample surface was finished by #4000 SiC paper followed by 3μm diamond paste. All samples were washed ultrasonically in acetone prior to the oxidation test. Isothermal oxidation test was performed at 800°C for up to 1000h in laboratory air by a horizontal furnace. Several samples were also oxidized by means of a thermobalance.

In situ high-temperature XRD study was also conducted at the synchrotron facility, SPring-8. Evolution of the oxide scale and changes of the lattice-spacing of oxides were observed during oxidation including a heating period. Cross-sections of oxide scale after oxidation were characterized by EPMA, SEM and STEM.

Results and Discussion

Fig. 1 shows the oxidation kinetics of binary and ternary, Fig. 1(a) and quaternary, Fig. 1(b) alloys. Among ternary alloys, Nb addition to the binary alloy reduced oxidation mass gain. 1V addition did not change the oxidation kinetics, but the 3V alloy oxidized faster than the binary alloy. From the oxidation kinetics of the quaternary alloys with both Nb and V, Nb addition was found to be ineffective for reducing the detrimental effect of V addition for oxidation performance.

Fig. 2 shows the cross-sections of oxide scale formed alloys after 1000h of oxidation in air. The thickness of the oxide scale formed on Ti-30Al-6Nb and Ti-30Al-5Nb-1V is similar. The oxide scale formed on those alloys consisted of TiO_2, Al_2O_3, and TiO_2 in this order from the surface. However, the outer TiO_2 was thinner, but the inner TiO_2 layer was slightly thicker for Ti-30Al-5Nb-1V than those for Ti-30Al-6Nb. The oxide scale formed on -5Nb-3V was very thick and consisted of a multilayered structure. TiN precipitates and a γ-TiAl layer were developed on -6Nb alloy below the oxide scale, but internal precipitates of Al_2O_3 were formed on the alloys with V addition. Because a protective Al_2O_3 scale was not formed on all alloys and the inner TiO_2 layer became thicker with V addition. Oxidation kinetics of TiAl is considered to be controlled by mainly the growth of the inner TiO_2 layer.

It is well-known that Nb decreases the growth rate of TiO_2. This beneficial effect of Nb is explained to be due to "doping-effect". Dissolution of Nb^{5+} in TiO_2 (Ti^{4+}) decreases the concentration of oxygen vacancy, resulting in reducing inward oxygen transport. However, V dissolution would also be possible in TiO_2 as V^{5+}, which should reduce the growth kinetics of TiO_2.

HT XRD analysis revealed that the lattice spacing of TiO_2 formed after 30min of oxidation in air at 800°C increased with increasing Nb contents in the alloy. The lattice-spacing of TiO_2 was also increased by V addition. The ionic radius of Nb^{5+} and V^{5+} is 0.78 and 0.68, respectively. Because the ionic radius of Ti^{4+} is 0.745, dissolution of Nb^{5+} in TiO_2 expands the lattice-spacing, while V^{5+} decreases it. Thus, Nb dissolves into TiO_2 as Nb^{5+}, reducing growth kinetics due to the decrease in oxygen transport. However, V dissolves into TiO_2, not as V^{5+} but V^{3+}, which has a larger ionic radius, 0.78, than Ti^{4+}. Increased oxidation mass gain by V addition in Ti-30Al alloy would be caused by a higher concentration of oxygen vacancy due to dissolving V^{3+} ion.
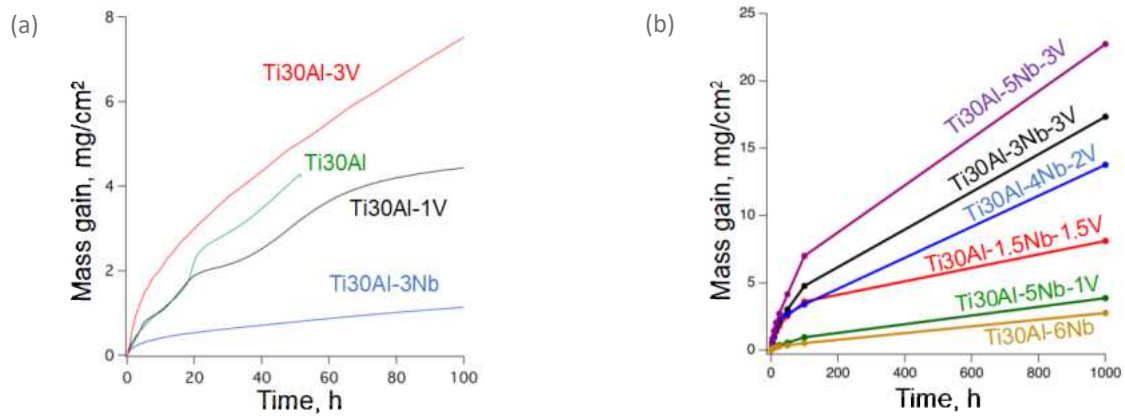
Fig. 1: Oxidation kinetics (a)ternary alloys and (b)quaternary alloys
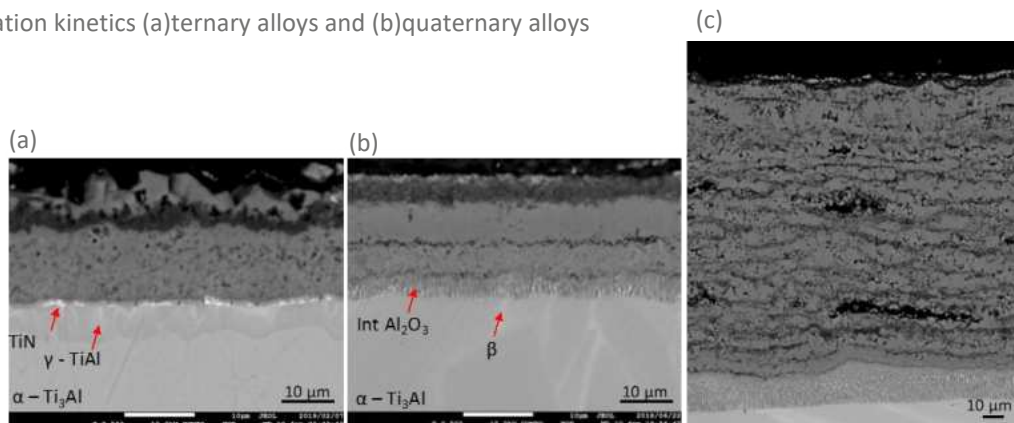
Fig. 2: Cross-sections after oxidation for 1000h in air at 800°C. (a) Ti30Al-6Nb, (b) Ti30Al-5Nb-1V, and (c) Ti30Al-5Nb-3V

Acknowledgements

O–CO–02

Al-Si based oxidation protection coatings for γ-TiAl produced by magnetron sputtering and Arc-PVD

Peter-Philipp Bauer[1] and Nadine Laska[1]

[1]German Aerospace Center (DLR), Institute of Materials Research, Linder Hoehe, 51147 Cologne, Germany, peter-philipp.bauer@dlr.de, nadine.laska@dlr.de

Introduction

Titanium aluminides are already being used in aero engines as substitute for Ni-based alloys. The main benefit is a much lower density than that of Ni-based alloys with a comparable strength. Due to the low oxidation resistance of Titanium aluminides at temperatures above 800 °C [1] their application is limited for instance to low pressure turbines that experience lower temperatures. In order to increase the service temperature, oxidation protection coatings are a potential approach [2]. Al and Si based coatings produced by pack cementation [3, 4] already show promising results. In the present work, Al-Si coatings were produced by PVD processes such as magnetron sputtering and Arc-PVD. Compared to CVD processes the benefit of this technology is the possibility to obtain thinner coatings that are also more resistant against thermal stresses. Additionally, current multi-source PVD systems allow a fine tuning of the composition to achieve the required properties. Moreover, multilayer coatings can be created in which each layer is customized to the requirements, for example as a combination of diffusion barrier and oxidation resistant layer. Regarding high temperature application, a next step could be the deposition of a thermal barrier coating on the oxidation protection coating which then will act as a bond coat as well. For this purpose, cooling holes are required which can be integrated in additive manufactured TiAl parts. In contrast to thermal spraying, PVD technology will allow to deposit a coating without blocking these holes.

Materials and Methods

γ-TiAl was used as a substrate material. Small disks were manufactured with a diameter of 15 mm and a thickness of 1 mm. The specimens were vibratory polished to a roughness of less than R_a=0.1 µm and cleaned ultrasonically with ethanol before the coating process. Vibratory finishing was chosen since it is a commonly used process in industry which allows polishing several parts with complex geometries at the same time. The coatings were produced with a multi-source PVD system. In standard configuration the system is equipped with four magnetron sputter sources. One of these sources can be changed into an Arc-PVD source. Two types of Al-Si coatings were produced with a target composition of roughly 12 at.-% Si deposited by magnetron sputtering. The Al was deposited by Arc-PVD as well as by magnetron sputtering. During sputtering no BIAS voltage was used. Two Arc-PVD processes were carried out, one without BIAS voltage and the second one with a BIAS voltage of -100 V. A subsequent heat-treatment in vacuum was performed for coatings produced without BIAS voltage to obtain the required phases. The coatings were evaluated using XRD, high temperature XRD (HT-XRD), SEM with EDS, serial sectioning in a FIB-SEM and TEM. In order to assess the oxidation behavior, isothermal oxidation tests were carried out in atmosphere at 850 °C for 300 h.

Results and Discussion

With magnetron sputtering, a crystalline coating is obtained even at a process temperature of 200 °C. The coating consists of an Al matrix with Si grains. The HT-XRD analysis shows that after a heat-treatment of 10 h at 550 °C the formation of the $TiAl_3$-phase is complete, initiated by diffusion of Ti from the substrate into the coating. After heat-treatment the coating mainly consists of $TiAl_3$ (Fig. 1a). Additionally, a Si rich area is detected in form of a thin layer at the interface which is attributed most likely to Ti_5Si_3. The function of the Ti-Si layer at the interface is yet to be investigated. Presumably, it can act as a kind of diffusion barrier for Al. This can help to suppress the diffusion of Al from the coating into the bulk material and thus the loss of oxidation protection. After isothermal oxidation the coating-substrate interface is no longer clearly visible and different layers are formed (Fig. 2b). On top, a thin and dense oxide scale consisting of alumina is grown, beneath a Ti_5Si_3 matrix with $TiAl_2$ formed. The Ti_5Si_3 layer at the substrate-coating interface expanded and shows $TiAl_2$ in-between as well. In the former bulk, the Ti content decreased and so an enrichment of Al in the phases occurred as well. Altogether, these layers that are caused by inter-diffusion are thicker than the initial Al-Si coating and the heat-treated formed zone. Thus, the coating can obviously withstand further oxidation. Even if cracks occur inside the oxide scale, an oxidation protection is ensured due to the oxidation resistance of the present phases.

Coatings produced with Arc-PVD without BIAS voltage consist of an Al matrix with Si grains as well. However, due to the higher temperature during the Arc-PVD process the Si grains are bigger than the ones obtained by magnetron sputtering. After heat-treatment and subsequent oxidation, the microstructure and composition of the coating is comparable to the magnetron sputtered coatings. Using a BIAS voltage of -100 V during the Arc-PVD process leads to a diffusion zone in the coating exhibiting a pure Al top layer. The diffusion zone is comparable with the one obtained by magnetron sputtering and heat-treatment. Diffusion occurred since the Arc-PVD produces a high density of ions which leads to a high energy input. In oxidation tests, these coatings performed similar to the magnetron coatings. By using Arc-PVD with BIAS voltage, a subsequent heat treatment is avoided. Therefore, Arc-PVD is a promising approach to create thin Al-Si based oxidation protection coatings. Furthermore, the deposition rate is higher than magnetron sputtering. Thus, shorter process times can be realized.

In summary, this work showed that the PVD route is very promising in order to produce Al-Si based oxidation protection coatings for titanium aluminide components. The Al-12Si (in at.-%) coatings provide excellent oxidation behavior and are promising candidates for an application as a bond coating for thermal barrier coating system.
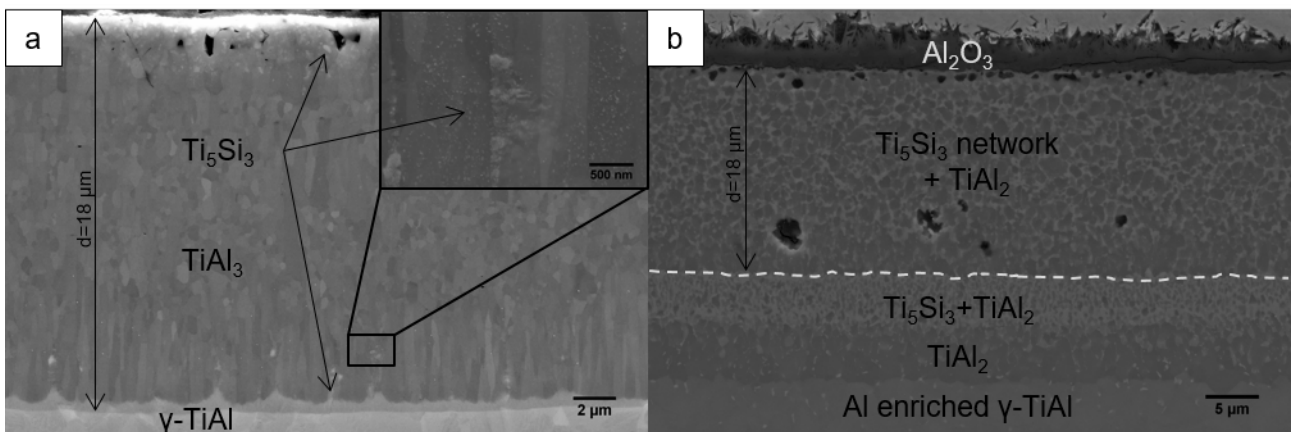
Fig. 3: a) Coating after heat treatment (550 °C, 20 h) with enlarged area; b) Coating after isothermal oxidation in atmosphere (850 °C, 300 h) with former coating-substrate interface (dashed line)

Acknowledgements

References

[1]   Brady, M.P., et al., *The oxidation and protection of gamma titanium aluminides.* Jom, 1996. **48**(11): p. 46-50.
[2]   Laska, N., R. Braun, and S. Knittel, Oxidation behavior of protective Ti-Al-Cr based coatings applied on the γ-TiAl alloys Ti-48-2-2 and TNM-B1. Surface and Coatings Technology, 2018. **349**: p. 347-356.
[3]   Xiang, Z.D., S.R. Rose, and P.K. Datta, Codeposition of Al and Si to form oxidation-resistant coatings on γ-TiAl by the pack cementation process. Materials Chemistry and Physics, 2003. **80**(2): p. 482-489.
[4]   Swadźba, R., et al., Characterization of Si-aluminide coating and oxide scale microstructure formed on γ-TiAl alloy during long-term oxidation at 950 °C. Intermetallics, 2017. **87**: p. 81-89.

O–CO–03

Oxidation of directionally solidified NiAl–(Cr, Mo) alloys

Golnar Geramifard, Peter Franke and Hans J. Seifert

Karlsruhe Institute of Technology, Institute for Applied Materials (IAM-AWP), 76344 Eggenstein-Leopoldshafen, Germany, golnar.geramifard@kit.edu, peter.franke@kit.edu, hans.seifert@kit.edu

Introduction

In the past few decades NiAl-based alloys have been of interest due to the high melting point, good oxidation resistance and low density. However, NiAl has undesirable mechanical properties such as poor ductility and fracture toughness at room temperature. Additionally, the creep resistance and the strength at high temperature are insufficient. To overcome these problems, composite strengthening by Cr and Mo fiber reinforcement is applied.

The NiAl–(Cr, Mo) metal matrix composites exhibit high creep resistance. [1] However, as these alloys are intended for high-temperature applications in turbines, where the materials are in contact with combustion gases, oxidative corrosion processes are presumable. Study of oxidation of NiAl–(Cr, Mo) composites is of interest since unlike the stable α-Al_2O_3 which is produced during oxidation of pure NiAl, Cr_2O_3 and Mo oxides are unstable and volatile at high temperature. So far, the oxidation behavior of these metal matrix composites have been studied only by a few groups. [2, 3]

Materials and Methods

In this work, advanced computational thermodynamics in the materials systems NiAl–Cr–O, NiAl–Mo–O and, NiAl–(Cr, Mo)–O are used together with oxidation experiments. The equimolar ratio of Ni: Al is the main focus.

In order to establish the thermodynamics of the relevant oxides and their equilibria with the metallic composites the literature is evaluated for corresponding data, isothermal sections, isopleths, oxygen activity diagrams etc. Based on these data, a thermodynamic database for the system NiAl–(Cr, Mo)–O is assessed. This new dataset combines data for pure elements and their corresponding binaries and ternaries. The database can be used to predict suitable operational ranges (temperature and oxygen activity) for the metal matrix compounds in turbine applications.

The solution phases are modeled with sublattice model expressed in the compound energy formalism, while both metallic liquid and oxide melts are described with the ionic two-sublattice model. Spinels within this system like Cr_3O_4, $NiCr_2O_4$ and $NiAl_2O_4$ are described using a four-sublattice model. Moreover, metastable oxides like γ-Al_2O_3 (with spinel structure), δ-Al_2O_3 and θ-Al_2O_3, are included.

Experiments are performed to determine missing data for the relevant oxides. In order to investigate the oxidation behavior of NiAl–Cr and NiAl–Mo interfaces, samples of arc-melted NiAl with embedded Cr and Mo are produced. Under defined oxygen partial pressure the specimens are oxidized in a thermobalance at different temperatures. Subsequently, the composition and the microstructure of the oxides formed at the surface are studied. Besides, by using electron backscatter diffraction (EBSD) the interface of NiAl and the Cr phase is investigated. In addition, the oxidation products are investigated also by X-ray diffraction (XRD) and scanning electron microscopy (SEM) equipped with energy dispersive X-ray (EDX).

The provided database from this work is used in Thermo-Calc software to anticipate the phase diagrams, isopleths, isothermal sections, heterogeneous phase reactions and thermodynamic functions.

Results and Discussion

When a NiAl-Cr junction is exposed to high oxygen activities at high temperatures then an oxide scale forms on top of the metals. The oxide consists of a continuous solid solution of Al_2O_3 and Cr_2O_3 with corundum structure. The transport properties of the mixed oxide change strongly with composition.

At high Cr-contents the diffusion of the metals as well as the diffusion of oxygen is quite fast while at high Al-contents the diffusion of all species are much slower. This behaviour causes a relatively thick oxide layer to form over chromium, which consists of almost pure Cr_2O_3. This is shown with the yellow colour in figure 1. Over the NiAl matrix at a sufficient distance from the junction, only a thin oxide scale is formed consisting of almost pure Al_2O_3 which is shown with the blue colour.

At the vicinity of the interface of NiAl and Cr, due to the faster diffusion in the high Cr-content region, Cr diffuses over the Al_2O_3 and causes formation of an oxide layer in which the composition changes from almost pure Al_2O_3 (blue) in contact with the metal, to almost pure Cr_2O_3 (yellow) in contact with the gas. The Cr content in the oxide scale also decreases as we go further away from the junction towards the NiAl.
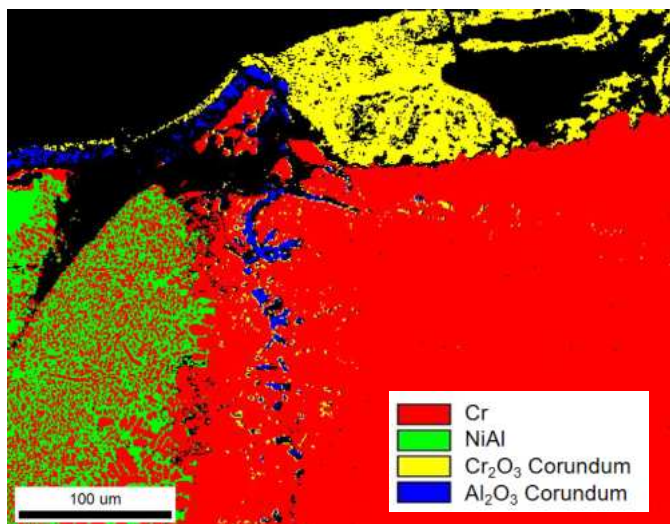
Fig. 1: EBSD image of NiAl-Cr interface with oxide layers at the surface after oxidation at 1300°C in 0.13 bar O_2 in Ar for 50 hours.
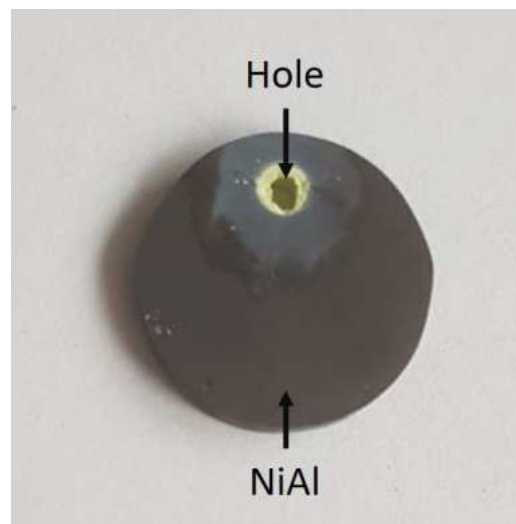
Fig. 2: NiAl-Mo oxidized at 800°C in 0.13 bar O_2 in Ar for 50 hours

Oxidation of NiAl–Mo composite is also investigated in this work. NiAl–Mo samples show a huge weight loss during oxidation at 800°C, which is due to formation of volatile Mo oxides species. At this temperature, the Mo fibers are severely attacked and evaporated under oxidizing conditions with high oxygen activities. The evaporation of the Mo oxides led to formation of a hole in the specimen as shown in figure 2.

References

[1] C. Seemüller, M. Heilmaier, T. Haenschke, H. Bei, A. Dlouhy, E.P. George, *Intermetallics* 35, **2013**, 110–115.

[2] M.P. Brady, H. Bei, R.A. Meisner, M.J. Lance, P.F. Tortorelli, *Scr. Materialia*. 80, **2014**, 33–36.

[3] Z.-s. Wang, Y. Xie, J.-t. Guo, L.-z. Zhou, Z.-q. Hu, G.-y. Zhang, Z.-g. Chen, *Transactions of Nonferrous Metals Society of China* 22, **2012**, 1582–1587.

O–CO–04

Mechanistic investigation of the high temperature oxidation ehaviour of Fe-25Al-1.5Ta with various additives in air at 700 °C

René Daniel Pütz and Daniela Zander

Chair of Corrosion and Corrosion Protection, RWTH Aachen University, Intzestraße 5, 52072 Aachen, Germany

r.puetz@gi.rwth-aachen.de, d.zander@gi.rwth-aachen.de

Introduction

Iron aluminides are considered as a potential material to substitute e.g. stainless steels in high temperature and aqueous environments due to their low material costs, low density, good wear resistance and favourable corrosion behaviour [1-4]. The adverse ductility at room temperature of iron aluminides is still a major drawback, which has prevented the commercial use [4]. Grain refinement during casting route may be a possible procedure to remove the mentioned detriment. In the present work the influence of several potential additives on the high temperature oxidation behaviour was investigated. The major focus is to understand and describe the oxidation mechanisms influenced by additives and microstructural changes.

The oxidation experiments were performed by discontinuous thermogravimetric analysis (TGA) in air at 700 °C for 504 h. All examined iron aluminides show a beneficial oxidation resistance compared to a common martensitic steel. Furthermore, the addition of TiB_2 as well as ZrB_2 lead to an increased mass gain in respect to the base alloy Fe-25Al-1.5Ta (at. %), which may be caused by a more pronounced selective oxidation of phases.

Materials and Methods

The casted iron aluminides examined in this investigation were provided by ACCESS e.V., Aachen, Germany as cylindrical rods with a diameter of approximately 15 mm. Different additives (e.g. TiB_2 or ZrB_2) were added to the chosen base material Fe-25Al-1.5Ta to investigate their influence on the high temperature oxidation behaviour. Additionally, the martensitic stainless steel X10CrWMoVNb9-2 (1.4901) was selected as a reference material.

To characterise the iron aluminide material and oxidised samples, various methods were performed including light optical microscopy (LOM), X-ray diffraction (XRD), scanning electron microscopy (SEM) and energy dispersive X-ray spectrometry (EDS).

Specimens with dimension (9 mm x 9 mm x 3 mm) were cut from rods, ground to 1200 grit and ultrasonically cleaned in ethanol. Subsequently, the surface area was determined by stereomicroscopy. Discontinuous high temperature oxidation experiments were performed in air in a chamber furnace at 700 °C for approximately 504 h. The TGA samples, which were placed inside an alumina crucible to collect potential spallation, were extracted at various times and cooled for 30 min in air to room temperature. Weighing was performed by a semi-micro balance with a precision of 10^{-5} g.

Results and Discussion

The high temperature oxidation behaviour was investigated by TGA to compare the mass change of different alloys. Those data revealed an increased mass gain by the addition of TiB_2 and even more severe by the addition of ZrB_2 compared to the base alloy Fe-25Al-1.5Ta. However, the mass gain of all examined iron aluminides were less pronounced compared to X10CrWMoVNb9-2.

X-ray diffractograms and EDS analysis of SEM top view and cross section images indicate the formation of Fe_2O_3, Al_2O_3 and Ta_2O_5 after the performed oxidation experiments, which were also observed during oxidation of Fe-25Al-2Ta [5]. Iron rich oxides grew mainly at grain boundaries where Fe_2Ta Laves-Phases were present while the formation of an Al-rich scale was found on the FeAl $D0_3$ substrate (Fig. 1 a)). Its equiaxed morphology [6] and the detected XRD spectra suggest the development of a hexagonal α-Al_2O_3 structure. Its formation is assumed to relate to a proposed template effect based on the presence of Fe_2O_3 during the initial oxidation stage [6]. To clarify, if metastable alumina were formed besides a proposed stable corundum structure [7], further TEM investigations are underway.

TiB_2 additions led to a more pronounced agglomeration of Fe_2Ta Laves-Phases inside grains. SEM top view and cross section images confirmed the growth of iron rich oxides on top of those Laves-Phases (Fig.1 b)). Furthermore, a mixed oxide was formed underneath Fe-rich oxides, which possibly promoted cracking of oxides and resulted in a facilitated ingress of oxygen. When zirconium diborides were added, zirconium rich oxides were additionally formed (Fig.1 c)). The development of deeper oxide protrusions could be promoted due to the high oxygen affinity of zirconium. Aluminium rich oxides were formed in between oxidised phases and FeAl matrix, which could be related to the preferred transport of oxygen along interfaces [8] and selective oxidation of Al. These phenomena may explain the increased mass gain compared to Fe-25Al-1.5Ta.
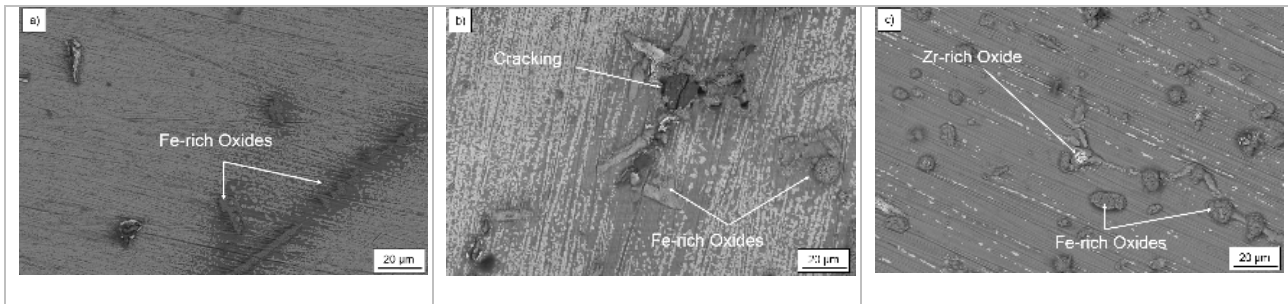
Fig. 1: SEM-BSE top view images after discontinuous oxidation in air at 700 °C for 504 h of a) Fe-25Al-1.5Ta b) Fe-25Al-1.5Ta+TiB$_2$ and c) Fe-25Al-1.5Ta+ZrB$_2$

References
[1]   N.S. Stoloff, Materials Science and Engineering A. **1998**, *258*, 1-14.
[2]   N.S. Stoloff, C.T. Liu, S.C. Deevi, Intermetallics. **2000**, *8,* 1313-1320.
[3]   T.N. Kutz, D. Zander, Corrosion, **2017**, *73*, 648-654.
[4]   D.G. Morris, M.A. Muños-Morris, Advanced Engineering Materials. **2011**, *13*, 43-47.
[5]   A. Hotař, M. Palm, Intermetallics. **2010**, *18*, 1390-1395.
[6]   P. Brito, H. Pinto, A. Kostka, Corrosion Science. **2016**, *105*, 100-108.
[7]   B. Pöter, F. Stein, R. Wirth, M. Spiegel, Zeitschrift für Physikalische Chemie. **2015**, *219*, 1489-1503
[8]   F.H. Stott, G.C. Wood, Materials Science and Technology, **1988**, *4*, 1072-1078.

O–CO–05

Pre-oxidation of iron aluminides

Janez Zavašnik[1,2], Jian Peng[1] and Martin Palm[1]
[1]Max-Planck-Institut für Eisenforschung GmbH, 40237 Düsseldorf, Germany, m.palm@mpie.de
[2]Jožef Stefan Institute, 1000 Ljubljana, Slovenia

Introduction

Iron aluminides, i.e. alloys based on the intermetallic phases Fe_3Al and $FeAl$, have currently again become of interest for a variety of applications [1]. Based on novel alloy concepts for iron aluminides, alloys with improved strength and acceptable ductility have been developed. Besides better oxidation and wear resistance and lower density, it is their lower price which makes them an attractive alternative to 9-12 wt.% Cr steels or to Ni- and Co-based superalloys. Though their corrosion behavior is in general considered as good, it may vary considerably within different aggressive environments. E.g. for aqueous corrosion, specifically under acidic conditions, the corrosion resistance is only mediocre, comparable to that of cast iron. To improve the wet corrosion resistance, formation of a thin oxide scale by pre-oxidation has been investigated. However, results were conflicting, as some reports found an improved corrosion resistance [2] while others saw no beneficial effect [3, 4]. Within a systematic investigation of the wet corrosion behavior of Fe–Al alloys also the effect of pre-oxidation has been investigated [5]. As it was found to substantially increase the aqueous corrosion resistance, a detailed investigation of the protective oxide scale has been performed.

Materials and Methods

Fe-25Al (in at.%) has been produced by induction melting. By X-ray diffraction (XRD) it was confirmed that the alloy is $D0_3$-ordered, i.e. Fe_3Al. Slices of the alloy were cut by electrical discharge machining, ground to P4000 and degreased before oxidizing in air at 1000 °C for 188 h. Aqueous corrosion was performed in sulphuric acid (H_2SO_4; 0.0126 M). To test the stability against the electrolyte, the sample was immersed for 308 h before the open circuit potential (OCP) and potentiodynamic polarization curves were determined [5].

The oxide scale before and after aqueous corrosion testing was initially characterized by grazing incident XRD and scanning electron microscopy (SEM) [5]. To investigate possible alterations of the scale after aqueous corrosion testing in detail, a cross section of the scale was observed by transmission electron microscopy (TEM). The bulk sample was pre-coated with Pt to protect the sample surface, and an electron-transparent lamella was prepared by site-specific focused ion beam (FIB) lift-out by dual-beam SEM. C_s corrected TEM and scanning TEM (STEM) investigations were carried out at 300 keV using a high-resolution CMOS camera for conventional TEM imaging, and a high angle annular dark field detector (HAADF) for STEM imaging. STEM elemental maps were recorded by energy dispersive spectroscopy (EDS).

Results and Discussion

After pre-oxidation, a dense and well adherent oxide scale formed. While the main constituent of the scale was α-Al_2O_3 (alumina), traces of spinel-type $FeAl_2O_4$ (hercynite) were also detected by GI-XRD [5]. Comparison of the potentiodynamic polarization curves of Fe-25Al without prior oxidation treatment showed that pre-oxidation substantially improved the aqueous corrosion behavior. The oxide scale is still protective after prior immersion and indication was found that re-passivation occurred in case of failure at small defects [5].

By selected area diffraction (SAD) in the TEM, the phases that form the matrix (Fe_3Al) and the oxide scale (α-Al_2O_3, $FeAl_2O_4$) were confirmed. The overall thickness of the scale is about 2 µm. It consists of two distinct layers of about equal thickness. The upper layer is formed by euhedral, randomly oriented alumina and hercynite grains. The alumina grains have a size of about 200 nm while the hercynite grains are somewhat smaller. The lower layer is formed by elongated alumina grains. These grains have preferentially grown along the *c* direction, forming pillars vertical to the Fe–Al matrix. EDS revealed that the alumina grains at the top of each layer contain a traceable amount of Fe, as has been shown for Fe-28Al oxidized at 1000 °C [6]. A few pits have formed during corrosion testing. However, they are only observed at hercynite grains.

An outer layer containing a mixture of iron oxides or spinel and Al_2O_3 and an inner layer of pure Al_2O_3 are frequently observed as scales on oxidized iron aluminides [7, 8]. In the initial stages of oxidation of Fe–Al, an iron oxide and Al_2O_3 are growing concurrently. Later on hercynite forms and together with Al_2O_3 it forms a layer which blocks the outward

Fig. 1: a) bright-field TEM micrograph of alumina scale cross-section, with superimposed EDS Fe Kα map; dotted line marks the pillar-grain transition zone. Small red square in central right part is enlarged in b), unravelling pure matrix-alumina contact without exsolutions or intermediate phases.
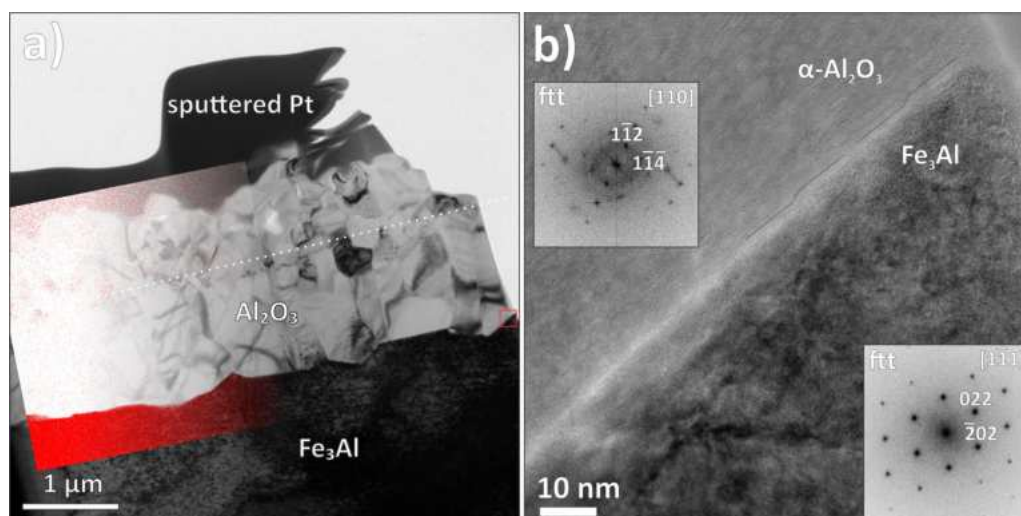
diffusion of Fe^{2+} [9]. Finally, underneath this layer a continuous Al_2O_3 layer forms, which is dense and protective. The actual kinetics of the scale formation depends on the Al content of the alloy, temperature, partial O_2 pressure etc., and on metastable modifications of Al_2O_3 (γ, θ…), which form in the initial stages of oxidation [10]. In the present case only α-Al_2O_3 is observed, i.e. temperature and time were sufficient that the metastable modifications transformed completely to stable alumina.

While in the initial stages of scale formation there may be a thin (5 nm) intermediate layer of metastable Al_2O_3 between the Fe–Al matrix and alumina [8], such a layer is not observed in the present case. The columnar alumina apparently grows into the Fe_3Al matrix, thereby developing low-indexed Wulff facets, which additionally improve adhesion between oxide and matrix. When the sample is cooled down after oxidation, compressive stresses develop within the scale [11]. These stresses, which compress the grain boundaries of the alumina pillars, may be essential for the excellent wet corrosion behavior. As the corrosion is expected to progress mainly along the grain boundaries, the change of microstructure and chemical segregation between a randomly-oriented top layer and the underlying columnar layer can additionally protect the matrix by a combination of reduced permeability via grain boundaries, and improved corrosion resistance of high-purity underlying alumina pillars.

References

[1] M. Palm, F. Stein, G. Dehm, Annu. Rev. Mater. Res. **2019**, *473*, in press.
[2] M.L. Escudero, Scr. Mat. **2003**, *48*, 1549-1554.
[3] R.A. Buchanan, R.L. Perrin, in: R.R. Judkins (Ed.): Proc. 11th Annu. Conf. on Fossil Energy Materials. Oak Ridge National Laboratory, **1997**, 159.168.
[4] M.F. Lopez, M.L. Escudero, Electrochim. Acta. **1998**, *43*, 671-678.
[5] J. Peng, et al., Corr. Sci. **2019**, *149*, 123-132.
[6] D.B. Lee, G.Y. Kim, J.G. Kim, Mat. Sci. Eng. **2003**, *A339*, 109-114.
[7] V. Shankar Rao, M. Norell, V.S. Raja, Corr. Sci. **2003**, *45*, 2717-2728.
[8] B. Pöter, et al., Z. Phys. Chem. **2005**, *219*, 1489-1503.
[9] P. Tomaszewicz, G. Wallwork, Oxid. Met. **1983**, *19*, 165-185.
[10] R. Prescott, M.J. Graham, Oxid. Met. **1992**, *38*, 73-87.
[11] P.Y. Hou, A.P. Paulikas, B.W. Veal, Mat. Sci. Forum. **2006**, *522-523*, 433-440.

O–IT–10

High temperature supercritical CO_2 compatibility of intermetallics and cermets

Bruce A. Pint

Oak Ridge National Laboratory, Oak Ridge, TN, USA

In both open and closed supercritical CO_2 (sCO_2) cycles, there is interest in exploring the maximum temperatures possible for materials, particularly above 750°C. As an initial assessment of potential candidate materials, several Fe- and Ni-based aluminides were exposed at 750°C/300 bar in high purity CO_2. Specimens of Fe_3Al and Ni_3Al performed poorly after 500 h, while better results were obtained for FeAl and NiAl specimens. To explore the highest temperature concepts, screening experiments are being conducted at 1200°C in 1 and 20 bar CO_2 (subcritical). Cermets have been suggested as possible candidates. However, it is not surprising that Mo and W specimens performed poorly under these conditions, exhibiting high mass losses after only 20-40 h. Even FeCrAl compositions were heavily attacked after <100 h and no metallic specimens have been exposed for longer than 100 h. The only candidates being evaluated at 1200°C beyond 100 h are SiC and $MoSi_2$. Similar testing will be conducted at 1000°C for comparison. Research sponsored by the US Department of Energy, Office of Fossil Energy.

O–IT–04

Influence of cooling rate and composition on the formation of ribbon shaped borides in cast TiAl alloys

Renci Liu [1], Xi Wang[1], Ruxin Cao[1,2], Yuyou Cui[1] and Rui Yang[1]

[1]Institute of Metal Research, Chinese Academy of Sciences, Shenyang 110016, China, ryang@imr.ac.cn
[2]College of Mechanical and Power Engineering, China Three Gorges University, Yichang 443002, China

Precision casting is arguably the most cost effective processing route for gamma TiAl as far as components of complex shapes are concerned. To ensure service performance the castings normally should have nearly fully lamellar microstructure with uniform, fine colonies. Boron addition into TiAl alloys was found to be very effective in achieving this goal by forming spherical or short bar boride particles that limit grain growth, but the strategy fails when the boride is present in the shape of long, curved ribbons. Our detailed experimental investigations showed that the formation of ribbon shaped boride is strongly dependent on the cooling rate during solidification. Composition of the alloy, including contents of B, Al, and Nb, also plays a role. Examples will be given of borides formed in cast 4522XD and TNM alloys and some differences in the formation mechanism of the borides can be attributed to the different levels of Nb content in the two alloys. We then established a model that accounts for the mechanisms of the formation of ribbon boride and the influences of the various factors mentioned above. In this talk, the main results of the work will be presented.

O–TA–01

Design approaches and achievements of novel TiAl alloys for jet engine applications under *SIP* programme in Japan

Masao Takeyama

Department of Materials Science and Engineering, School of Materials and Chemical Technology, Tokyo Institute of Technology, S8-8, 2-12-1, Ookayama, Meguro-ku, Tokyo 152-8552, Japan, takeyama@mel.titech.ac.jp

Introduction

Innovation of structural materials is urgently being required for contribution to worldwide issues on energy and environment, and high performance jet engine development with higher thrust-to-weight ratio is one of them, since more than 42,000 new airplanes are to be produced by 2037 [1]. Titanium aluminides based on γ-TiAl are one of the materials to be further developed. Currently a cast TiAl alloy of Ti-48Al-2Nb-2Cr (at.%) and a wrought TiAl alloy Ti-43.5Al-4Nb-1Mo-0.1B (TNM) are being applied commercially to low pressure turbine (LPT) blades for jet engines, although the possibility of the wrought alloy development using β-Ti phase was originally proposed by our group [2]. From this kind of circumstance, in Japan a five-year National project of "*Structural Materials for Innovation* (SM⁴I)" in *Cross-ministerial Strategic Innovation Promotion Program* (SIP) was started in 2014 [3], and challenging R&D activities on innovative structural TiAl alloys aiming at LPT and high-pressure compressor (HPC) blades for jet engines have been placed in this project, where Tokyo Tech is committed to as a technical leader and takes responsibility for the alloy design in collaboration with Hokkaido Univ. and industries (Kobe Steel, Ltd. and IHI Co.). Hokkaido University studied the oxidation behavior of the alloys proposed. Kobe Steel is in charge of casting and recycling process technologies, and IHI is in charge of the blade fabrication and forming process technologies for the proposed alloys. In this presentation, since we have successfully developed novel wrought alloys, our design principle/approach as well as the importance of β phase for improvement of mechanical properties are introduced.

Design Principle

Figure 1 shows a microstructure design principle for wrought TiAl alloys with superior mechanical properties. Addition of β-Ti stabilizing transition elements M to Ti-Al binary system has already been known to form a three-phase coexisting region of β-Ti/α-Ti (α_2-Ti$_3$Al)/γ-TiAl phases, and the region shifts toward the binary edge with decreasing temperature in any ternary systems. Note that the change in α to α_2 phase is not a "second-order" transformation but a "first-order" transformation through either a ternary transition

peritectoid reaction ($\beta+\alpha\rightarrow\alpha2+\gamma$) or ternary eutectoid reaction ($\alpha\rightarrow\beta+\alpha2+\gamma$), depending on M. Such a movement of the three-phase coexisting region creates a unique transformation pathway of $\beta+\alpha\rightarrow\alpha\rightarrow\alpha2+\gamma\rightarrow\beta+\gamma$, which makes it possible to develop wrought alloys. In order to design superior wrought alloys with high toughness, we extend the ternary knowledge to Ti-Al-M$_1$-M$_2$ quaternary (multi-component) systems, to identify the composition range of the transformation pathway. Thus, what we need first are reliable Ti-Al-M ternary phase diagrams and reliable thermodynamic database (DB), which can reproduce the experimental phase diagrams. In general, an equivalency concept is commonly used for multi-component alloy design, and in case of the quaternary system, M$_1$ equivalency of M$_2$, $k_{M1/M2}=X^c_{M1}/X^c_{M2}$, can be estimated from each ternary system where X^c_M is the critical concentration of M element beyond which β phase

Fig. 1 Flow of the design principle for novel wrought TiAl alloys based on calculated phase diagrams in Ti-Al-M$_1$-M$_2$ quaternary systems using our thermodynamic database.

appears at given temperatures. Then, you can convert the multi-component systems to a ternary system of Ti-Al-M$_1$ᵉq. However, the equivalency does not work for TiAl alloy systems even though the two elements are in the same group of the periodic table. The combined additions considerably stabilize the β phase, especially in case that the concentration ratio of the two M elements (M$_1$/M$_2$) is nearly equal to unity, indicating that the negative interaction between the two elements has to be taken into account in calculation. Note that the similar behavior is observe in any combinations of eligible M elements. Therefore, in order to design the wrought alloys in multi-component systems with the unique transformation pathway, following the three factors in order are important in calculation of the phase diagrams: (1)

aluminum concentration dependence, (2) temperature dependence, (3) M_1 and M_2 concentration ratio dependence, since all these factors strongly influence the high and low temperature β phase regions. Figure 2 shows an example for a vertical section in the quaternary system. The experimental diagram is in good agreement with the one calculated using our thermodynamic DB (Figs. 2 (a) and (b)) in the position of the unique phase transformation pathway (the dotted line), but obviously not with the one calculated using the existing DB [4] (Fig. 2 (c)). The high temperature β phase existing above the α single phase region is effective for hot forging process, and the volume of 20 % at forging temperatures makes it possible to hot forged the sample by one stroke with a true compressive strain of more than 1.2 at strain rate of 10/s, fast enough to prevent heat transfer from a small piece of sample such as HPC blade during forging process. The residual β phase after the forging can be eliminated completely by the $\beta \rightarrow \alpha$ phase transformation along the pathway. In addition, thermodynamically stable β phase existing below the α single phase region can be used to control the

Fig. 2 Vertical sections in Ti-Al-M_1-M_2 quaternary system at a fixed Al concentration: (a) experimentally determined, (b) calculated based on our DB, (c) calculated based on existing DB [4]

microstructure. In general, the existence of the β phase is blindly believed to be detrimental for mechanical properties. However, this is not always true. The ductility and fatigue crack growth resistance at room temperature as well as creep life to 1% strain at 1073 K can be improved by using the β phase and even better than those of the existing alloys [5,6]. The detailed properties and the mechanism for the improvement will be discussed. This study was carried under the research project of SIP in JST (Japan Science and Technology Agency).

References

[1]   Boeing Commercial Market Outlook 2018-2037 (2018). Available at
      http://www.boeing.com/commercial/market/commercial-market-outlook/ (2018)
[2]   M. Takeyama and S. Kobayashi, *Intermetallics*, 13, 993 (2005).
[3]   Structural Materials for Innovation (SM⁴I), Heat Resistant Alloys and Intermetallic Compounds (2014). Available at
      http://www.jst.go.jp/sip/k03/sm4i/en/project/project-b.html
[4]   N. Saunders in *Gamma Titanium Aluminides*, edited by Y.-W. Kim, D.-M. Dimiduk, and M.-H. Loretto (TMS, Warrendale, PA 1999), pp. 183-188.
[5]   H. Wakabayashi, L. J. Signori, A. Shaaban, R. Yamagata, H. Nakashima, M. Takeyama: MRS Advances, 2019 MRS, DOI: 10.1557/adv. 2019.113
[6]   L. J. Signori, T. Nakamura, Y. Okada, R. Yamagata, H. Nakashima, M. Takeyama, Intermetallics. **2018**, *100*, 77–87.

O–TA–02

Mechanical properties of SiC fiber reinforced TiAl composite

Keizo Hashimoto[1,2], Hiroaki Okazaki[1] and Yuta Morito[1]

[1]Department of Aerospace Engineering, Teikyo University

[2]Advanced Instrumental Analysis Center, Teikyo University 1-1 Toyosatidai, Utsunomiya, Japan,

hasimoto@ase.teikyo-u.ac.jp

Introduction

Although metal matrix composites for the high temperature structural material have been investigated extensively[1,2], applications of MMC have been limited. Among many combinations between the ceramic fibers and matrix materials, combination of SiC fiber and TiAl based intermetallic compounds has been expected to be one of the best combination since both SiC fiber and TiAl show the heat resistance and low density. Lack of the affordability of TiAl sheet has been inhibited the development of the TiAl base composites. Among several approaches[3,4], SiC fiber reinforced TiAl has been successfully fabricated in 1997[5] by present authors group. However, investigation has not been hardly found to follow the results of our SiC/TiAl composites. In this study, the fabrication conditions of SiC fiber and TiAl sheet using the hot press in a vacuum have been investigated[6]. The purpose of this research is to understand the relationships between process conditions and mechanical properties of SiC/TiAl composites. Furthermore the reaction layers between fiber and TiAl matrix have been analysed in detail. Results would lead to establish the most appropriate fabrication condition of composite.

Materials and Methods

TiAl ingots were remelted by the plasma arc melting (PAM) facility. Then they received HIP process at 1323K for homogenizing treatment in order to eliminate casting defects. Ingots were compressed up to 80% deformation at 1473K, in a vacuum atmosphere to get fine microstructure which shows a superplastic deformation capability above 1473K. The sheets of γ-TiAl specimens whose thickness were 0.2mm were cut by the diamond multi wire saw machine. Using a specially designed jig, five TiAl sheets (20x20x0.2mm^3) and properly chopped SiC fibers were laminated in layer by layer as shown in Fig.1. Unidirectional compression on the preform were carried out by means of the hot press facility at various temperatures in a vacuum. After the preform was set in the chamber, temperature was raised with heating rate 15K/min, and kept for 40min. Preform was hot pressed under the condition of 7.0-8.0MPa for 10min. SiC/TiAl specimens were cut from composites perpendicular to the fiber direction by the diamond wheel saw, and then polished by diamond powder. Cross section of the specimens were observed by SEM-EDS operated at 15keV. Micro- indentation apparatus has been utilized to evaluate the pull out strength of matrixTiAl and a SiC fiber. Mechanical properties of unidirectional composite specimens (7.5x20.4x0.9mm^3) have been examined by three point bending tests at room temperature.

Results and Discussion

Determination of an adequate hot press condition for SiC/TiAl composite is the most important purpose of this study. The volume fraction of fiber in matrix is examined from the cross-section of SEM photographs. Based on the SEM observations, composites of 1473, 1498 and 1523K are well deformed and show relatively good interfaces. Matrix TiAl has deformed significantly around the fibers and the initial TiAl sheets have bonded together perfectly as like a bulk TiAl specimen. The thickness of reaction layers between SiC fiber and TiAl matrix has been strongly affected on the hot press temperatures. Optimum conditions of consolidation have been determined as following: pressure is 8.0 MPa, temperature is 1498K.

Mechanical properties of SiC/TiAl have been evaluated by means of the three points bending test using strain gauge attached on the bottom side of the specimen. Specimen (8.0 MPa, 1498K) whose fiber volume fraction was 8.0% shows bending strength of 290MPa and strain of 0.15%, respectively. Based on the three points bending data, elastic modulus for fiber direction would be calculated. Elastic constant of fiber direction is 193GPa. Youngs modulus of fiber is 400-415GPa and its matrix TiAl is 164GPa respectively, therefore, ideal elastic constants would be 182-184GPa according to apply the law of mixture. It is demonstrated that this SiC/TiAl composite material shows excellent elastic properties.

In order to examine the pull out strength of SiC fiber quantitatively, micro-indentation on a single fiber were carried out. Figure 2 shows an observation of SiC fiber pull out after micro-indentation, arrow in Fig.2 is indicating the scar of the diamond. Load cell placed under the specimen has monitored the received force during indentation. At the top, the force reached to 8.8N. The area of interface was 1.4×10^{-12} m^2 (specimen thickness 0.10mm, SiC fiber diameter 0.133mm). Estimated pull out strength was 202MPa, that is reasonable values since tensile strength of TiAl matrix was 505MPa and the maximum shear stress would be the half of tensile strength. Reaction layers and the interface between SiC fiber and TiAl have been analyzed by SEM-EDS and XRD. At least two or more reaction layers have been formed. These reaction layers can be explained based on the Si-Ti-C ternary equilibrium phase diagram at 1373K[7].

Summary

SiC fiber reinforced TiAl composites have been successfully fabricated using hot press method. Optimum temperature and pressure have been determined. SiC/TiAl composite having relatively low fiber volume fraction shows nearly an ideal elastic property applying the law of mixture. Effects of interface layers on the mechanical properties of composites have been discussed.
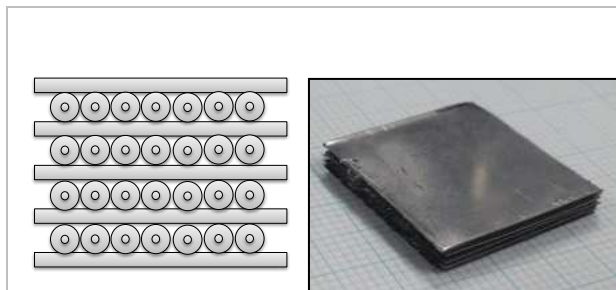
Fig. 1 Schematic drawing of SiC/TiAl arrangement and preform	Fig. 2 Observation of SiC fiber pull out after indentation by diamond pyramid
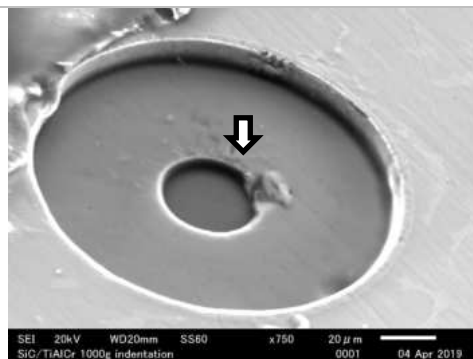
References

[1] W.W.Macy, M.A.Shea, R.Perez, R.E.Newcomer and D.L.Morris , Aerospace Eng. **1990**,17-21
[2] T.M.F.Ronald ,Advanced Materials & Processes,**1989**, 29-37
[3] C.G. Rhode,Intermetallic Matrix Composites II, MRS Symposium Proc. Eds. D.B.Miracle, D.L.Anton and J.A.Graves, **1992** , 273, pp.17-29
[4] S.Djanarthany, J.C.Viala and J. Bouix, Materials Science and Engineering, **2001**,300(A), 211-217
[5] H.Nakatan, M.Imuta, Y.Shimada, Y.Mizuhara and K.Hashimoto, Materia, **1998**, 37,4 , 277-279.
[6] K.Hashimoto, T.Ando, H.Kato and R.Kono, PRICM9 Eds.by T.Furuhara, M.Nishida and S.Miura, The Japan Institute of Metals and Materials, **2016**, 239-242
[7] J. J. Wakelkamp, F. J. J. van Loo, and R. Metselaar ,''Phase Relations in the Ti–Si–C System,'' J. Euro. Ceram. Soc., **1991**, 8 ,3,135–139

O–TA–03

Influence of C on the relaxation process and the diffusion of Ti in new generation of γ-TiAl intermetallics

José M. San Juan[1], L. Usategui[1], Thomas Klein[2,3], Svea Mayer[3], Helmut Clemens[3] and María L. Nó[4]

[1]Department Fisica Materia Condensada, Facultad de Ciencia y Tecnología, Universidad del País Vasco UPV/EHU, Apdo 644, 48080 Bilbao, Spain, jose.sanjuan@ehu.es

[2]Austrian Institute of Technology, Lamprechtshausenerstraße 61, Postfach 26, 5282 Braunau am Inn, Ranshofen, Austria, thomas.klein@ait.ac.at

[3]Department of Material Science, Montanuniversität Leoben, Roseggerstr. 12, 8700 Leoben, Austria, svea.mayer@unileoben.ac.at, helmut.clemens@unileoben.ac.at

[4]Department Fisica Aplicada II, Facultad de Ciencia y Tecnología, Universidad del País vasco UPV/EHU, Apdo 644, 48080 Bilbao, Spain, maria.no@ehu.es

Introduction

In the last decades there has been a growing interest in developing new intermetallic families, which would be able to improve the specific performances of superalloys at high temperature, and the Ti-Al-Nb-Mo family, called TNM, was developed to fulfill the required performances. In particular, the creep resistance should be improved and consequently the study of the diffusion mechanisms and the associated relaxation processes becomes very useful to get a deep understanding of the physics involved during creep. Previous works on several γ-TiAl alloys show a relaxation process associated to the diffusion of Ti in the α_2 phase [1,2], as well as an internal friction at high temperature, which is associated to the creep behavior [3]. At present, new generation of γ-TiAl, called TNM+, is being developed to improve the creep resistance by microalloying with C and Si through the formation of different precipitates [3]. However, C atoms in solid solution could have a secondary effect on creep resistance by slowing down the diffusion of Ti in the constitutive phases. The aim of the present work is to study the relaxation process associated to the Ti diffusion in α_2 phase in several alloys with different amounts of C in solid solution, in order to evaluate its potential influence on such relaxation process.

Materials and Methods

Several γ-TiAl alloys were investigated, the TNM alloy, and two alloys based on the TNM concept. The second alloy is an experimental C-rich alloy whose chemical composition is Ti-43Al-4Nb-1.5Mo-0.1B-0.5C. And the third alloy was named TNM+ and is refined with nominal additions of 0.3 at% C and 0.3 at% Si, with chemical composition Ti-43.3Al-4.02Nb-0.96Mo-0.12B-0.34C-0.31Si. These alloys were processed by plasma arc melting, subsequent casting and a further hot isostatic pressing at 1200ºC and 200 MPa for 4 h. Internal friction measurements were performed in a mechanical spectrometer working in torsion and in sub-resonant mode, between 300ºC and 950ºC, at different frequencies from 2 Hz to 0.01 Hz.

Results and Discussion

In Figure 1, the internal friction spectra measured at different frequencies as a function of temperature are plotted for the C-rich alloy. A relaxation peak appears in between 900 K and 1150 K, depending on frequency, superimposed to a high temperature background of the internal friction. From previous results [1,2] we know that this peak is associated to the diffusion of Ti in the α_2 phase and we will denote as P(α_2). From these results, the Arrhenius diagram corresponding to this relaxation peak can be obtained, and is plotted in Figure 2, allowing to measure the activation energy of E_{act} = 3.4 eV, which is much higher than the one measured for the same relaxation peak in the TNM alloy in which C is not present. Similar studies and analysis have been performed in all alloys and in different microstructural conditions. The details of the experimental results are given in reference [4] and will be published soon [5]. From these results it becomes evident that the presence of C in solid solution in the phase α_2, increases the activation energy of the relaxation peak P(α_2) and consequently the C atoms increase the activation energy for the diffusion of Ti in this phase, slowing down the diffusion processes. The analysis of this phenomenon, in alloys with different amount of C, allows us to quantify the influence of C on the diffusion of Ti in α_2 phase. An atomistic model is proposed to give account of the interaction between C in solid solution and Ti atoms during the short distance diffusion process involved in the internal friction experiments.

Conclusion

The influence of C in solid solution on the short distance diffusion of Ti in the α_2 phase has been evidenced in several γ-TiAl intermetallics. The analysis of the internal friction spectra has allowed quantifying such influence, in which the C atoms slow down the short distance diffusion of Ti in α_2. An atomistic model is proposed to explain the potential involved mechanism responsible for this phenomenon.
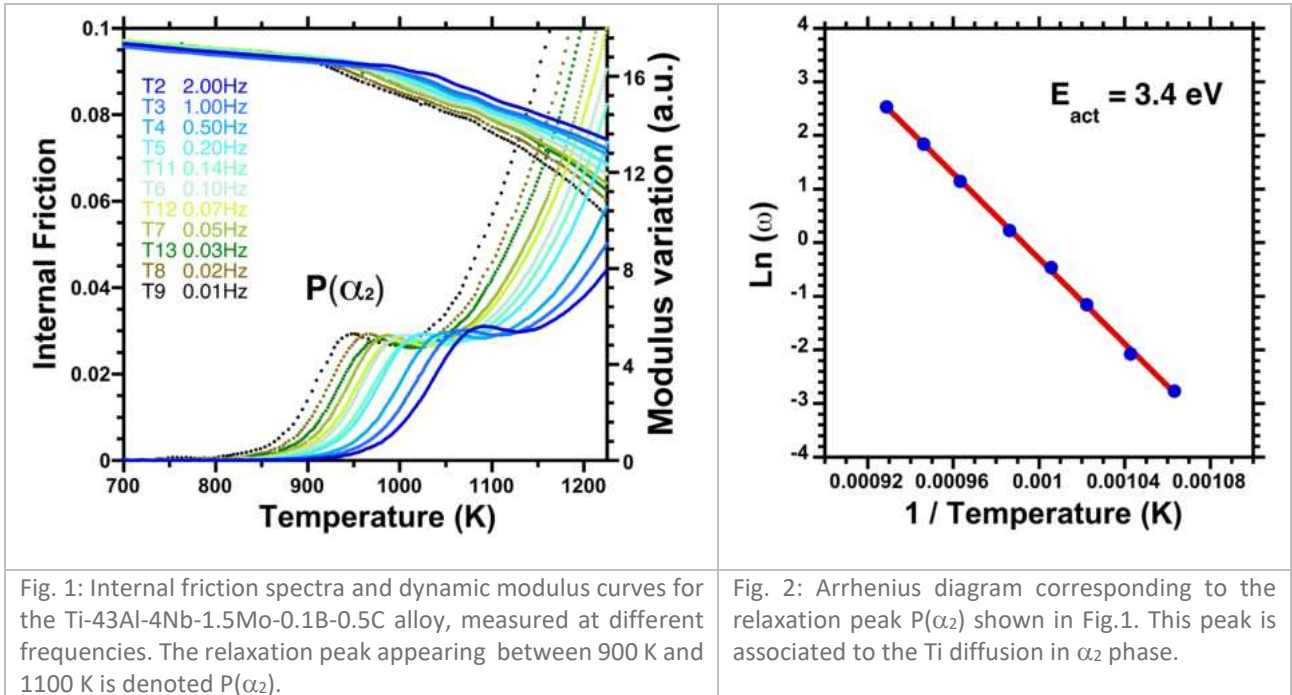
Fig. 1: Internal friction spectra and dynamic modulus curves for the Ti-43Al-4Nb-1.5Mo-0.1B-0.5C alloy, measured at different frequencies. The relaxation peak appearing between 900 K and 1100 K is denoted $P(\alpha_2)$.

Fig. 2: Arrhenius diagram corresponding to the relaxation peak $P(\alpha_2)$ shown in Fig.1. This peak is associated to the Ti diffusion in α_2 phase.

References

[1]   J. San Juan, P. Simas, T. Schmoelzer, H. Clemens, S. Mayer, M.L. Nó, Acta Materialia. **2014**, *65*, 338-350.

[2]   M. Castillo-Rodriguez, M.L. Nó, J.A. Jimenez, O. Ruano, J. San Juan, Acta Materialia. **2016**, *103*, 46-56.

[3]   T. Klein, L. Usategui, B. Rashkova, M.L. Nó, J. San Juan, H. Clemens, S. Mayer, Acta Materialia. **2017**, *128*, 440-450.

[4]   L. Usategui, PhD Thesis, University of the Basque Country, Bilbao, Spain, **2018**.

[5]   L. Usategui, T. Klein, M.L. Nó, S. Mayer, H. Clemens, J. San Juan. To be published, **2019**.

O–TA–04

Solid phase joining of γ-TiAl parts using diffusion bonding

Marcus W. Rackel[1], Florian Riedlberger[1], Dirk Matthiessen[1], Jonathan D. H. Paul[1], Andreas Stark[1], Jan Oke Peters[2], Thomas M. Gartner[2] and Florian Pyczak[1]

[1]Helmholtz-Zentrum Geesthacht, Centre for Materials and Coastal Research, Max-Planck-Straße 1, 21502 Geesthacht, Germany

[2]Lufthansa Technik AG, Weg beim Jäger 193, 22335 Hamburg, Germany

Introduction

Lightweight γ-based TiAl alloys were recently successfully introduced into civil aero engines as a structural blade material to partially replace the twice as heavy nickel-based superalloys [1]. For nickel-based blades, repair processes including welding and brazing are well established in order to reuse the blades and extend their life cycle, as well as to reduce material use and costs. Those processes are particularly suitable for repairing damaged or worn blade parts, but have not been commercially applied for γ-based TiAl blades. In the current work two commercially used γ-TiAl alloys [2] Ti-48Al-2Nb-2Cr and Ti-43.5Al-4Nb-1Mo-0.2B (all compositions in at.%) were investigated with regard to repair processes. In particular, diffusion bonding has been investigated as a possible repair process for damaged or worn γ-based TiAl parts. The microstructure developed during the bonding process and the corresponding mechanical properties have been determined. By optimising the parameters of diffusion, it was possible to reach tensile strength and ductility in diffusion bonded samples that were comparable to the base material.

Materials and Methods

The Ti-48Al-2Nb-2Cr alloy (4822) was produced by casting followed by hot isostatic pressing, while the Ti-43.5Al-4Nb-1Mo-0.2B alloy (TNM) was produced by casting followed by hot isostatic pressing and forging. All diffusion bonding experiments were performed in a modified MTS 810 servohydraulic testing machine. Diffusion bonding was performed under vacuum at four different temperatures below the γ-solvus temperature using three different compressive stress levels that were below the yield stress. Additionally, in-situ high-energy diffraction experiments were performed at the Helmholtz-Zentrum Geesthacht run High-Energy Materials Science beam line P07 at the Deutsches Elektronen-Synchrotron Hamburg [3]. A modified quenching and deformation dilatometer, DIL 805A/D from TA instruments, combined with a PerkinElmer 1621 flat panel detector were used to simulate the diffusion bonding process in-situ. A photon energy of 100 keV (λ = 0.1240 Å) with a beam size of 0.1 x 0.5 mm² was used to scan over the bonding zone in a stepwise manner. Diffraction patterns were analyzed using Fit2D software [4] and MAUD [5]. Scanning electron microscope investigations (SEM) were performed using a Zeiss Gemini using back-scattered electron contrast (BSE).

Results and Discussion

Diffusion bonding was not successful at temperatures below 1000 °C for either alloy. At higher temperatures above 1000 °C, in both alloys sound joints could be produced. The TNM alloy showed changes in the substrate microstructure (e.g. lamellar coarsening) after bonding at higher temperatures. In contrast, there seem to be no significant microstructural changes in the substrate of the cast 4822 alloy, except for some grain growth at and across the joint. The number and size of these grains increased with increasing bonding temperature. To investigate the influence of the process parameters on the mechanical properties, two sets of bonding parameters were chosen and tensile test specimens were produced from bonded cylinders. The tensile tests were carried out at room temperature, 650 °C and 750 °C. The Young's modulus of the bonded specimens was equal to the reference material at each testing temperature. For the TNM alloy, the samples bonded at lower stresses showed higher yield stresses. Nevertheless all bonded specimens reached similar fracture stresses as the specimens from the reference material. The bonded 4822 samples showed a wider distribution of properties. The samples bonded at higher temperatures exhibiting higher plastic strains. Furthermore, it was found that TNM samples tended to break in the diffusion joint zone during room and high temperature tensile tests. While 4822 specimens tested at room temperature, tend to brake within the substrate material and samples tested at high temperatures failed in the joint zone.

We were able to show that diffusion bonding is possible for both the TNM and 4822 alloys without significantly changing the microstructure. Additionally the bonded specimens showed mechanical properties that were comparable to the non-bonded reference specimens.
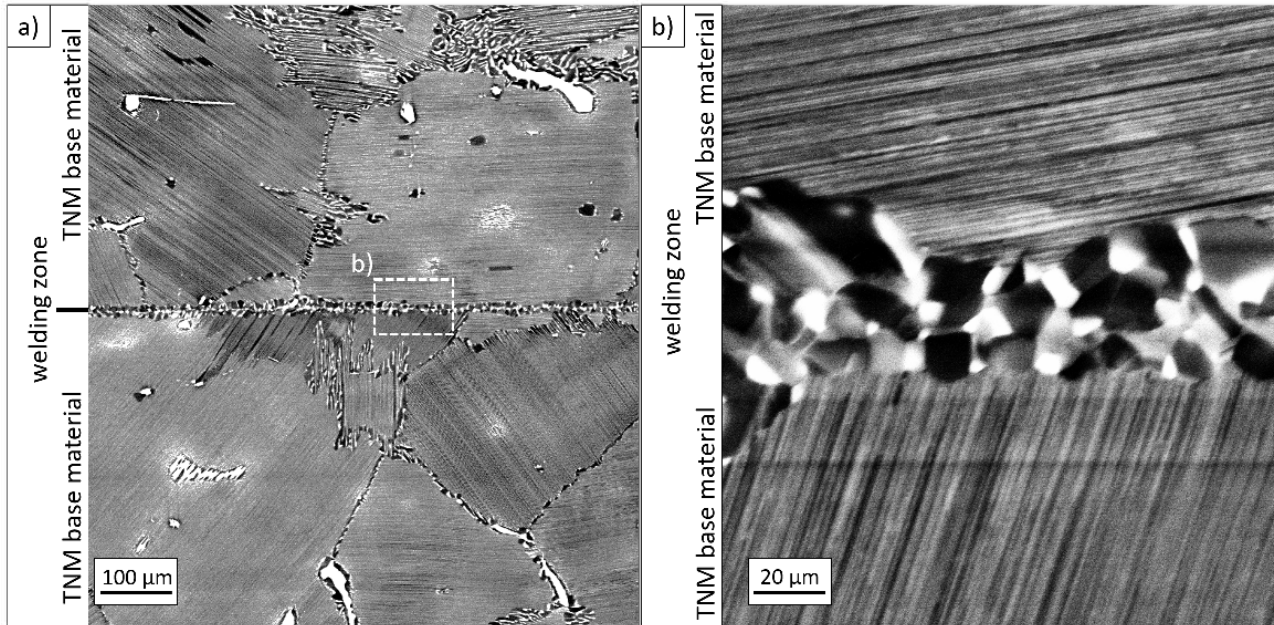
Fig. 1: SEM images in BSE mode a) diffusion bonding zone of two successfully bonded TNM alloy parts. b) High magnification of area within the dashed line box in (a), the bonding zone is located in the middle of the image and does not significantly differ from other grain boundaries within the alloy.

References

[1]   F. Appel, Gamma Titanium Aluminide Alloys. Wiley-VCH, **2011**.
[2]   B. P. Bewlay, TiAl alloys in commercial aircraft engines. Materials at High Temperatures. **2016**, 33(4-5), 549-559.
[3]   N. Schell, The High Energy Materials Science Beamline (HEMS) at PETRA III. Materials Science Forum. **2014**, 772, 57-61.
[4]   A. P. Hammersley, FIT2D: An Introduction and Overview. ESRF Internal Report. **1997**
[5]   L. Lutterotti, Total pattern fitting for the combined size-strain-stress-texture determination in thin film diffraction. Nuclear Instruments and Methods in Physics Research, Section B: Beam Interactions with Materials and Atoms. **2010**, 268(3-4), 334-340.

O–IT–05

Advanced intermetallic titanium aluminides – from fundamentals to application

Svea Mayer

Department of Materials Science, Montanuniversität Leoben, Franz Josef-Str. 18, 8700 Leoben, Austria,
svea.mayer@unileoben.ac.at

Introduction

In recent years, the demand for **innovative high-temperature lightweight structural materials** has become increasingly important, especially in relation to current issues of energy and environmental politics, since the rapidly expanding global economic network and the increasing mobility are an emerging problem with regard to energy consumption and environmental degradation. The air traffic alone holds a share of about 3.5% of the human-induced climate change and is expected to grow steadily over the next years. In this context, new programs are launched worldwide on a political and scientific / technical level to reduce aviation as well as automobile emissions. In particular, the regulations of the European Union prescribe strict stipulations regarding the permitted emissions from aero- and combustion engines. Apart from reducing harmful greenhouse gases (CO_2, NO_x), the focus lies also on a noticeable decline of noise. Thus, future generations of aircraft and automotive engines must be designed in such a way that they meet the abovementioned requirements, together with reduced fuel consumption and maintenance costs. Aside from new and improved design concepts, the use of innovative high-temperature lightweight structural materials, such as **intermetallic γ-TiAl based alloys**, plays a key role [1].

Due to their attractive properties, such as a low density (3.9 - 4.2 g·cm^{-3}, depending on composition and constitution), high specific yield strength and stiffness (Fig. 1), creep resistance up to about 800°C in addition to good oxidation and burn resistance, intermetallic titanium aluminides based on the γ-TiAl phase meet the demands as structural high-temperature lightweight materials in the aircraft and automotive industry, as turbine blades of aero-engines, turbocharger turbine wheels of automotive diesel engines and high-performance valves for the application in racing cars, where they have been envisaged to replace heavier Ni- and Ti-based alloys particularly in the temperature range of 600°C to 800°C [2,3].
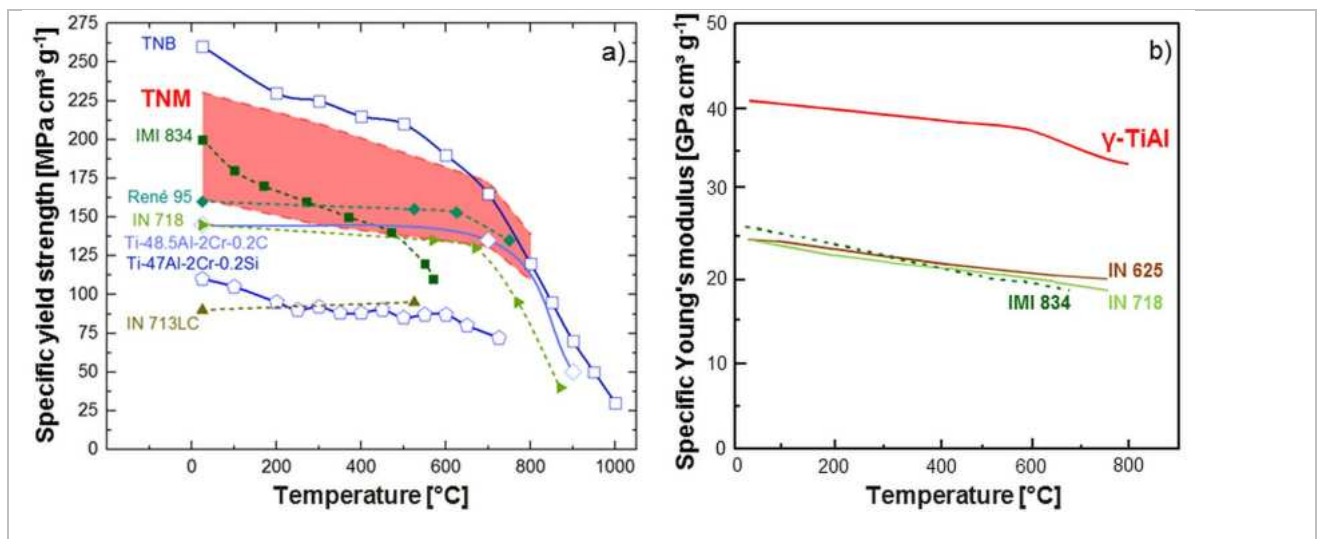
Fig. 1: a) 0.2% specific yield strength and b) specific Young's modulus as a function of temperature of selected structural materials in comparison with intermetallic γ-TiAl based alloys. The area in red represents data obtained for TNM alloys with different microstructures [2,3].

Since binary titanium aluminides do not meet the required properties for application, γ-TiAl based alloys are modified with transition metal alloying elements, such as Nb, Mo, Cr, or W. The resultant benefits are the improvement of the mechanical properties, the oxidation resistance and the possible adjustment of phase fractions and phase transformation mechanisms that enable, for instance, the application of particular processing routes, such as casting, hot forging and additive manufacturing (AM), or the adjustment of tailored microstructures by means of smart heat treatments [4,5].

Alloy Design Strategy for Advanced Titanium Aluminides

A representative of such an advanced intermetallic γ-TiAl based alloy is the so-called **TNM alloy** with a nominal chemical composition of Ti-43.5Al-4Nb-1Mo-0.1B (at.%), which was developed by the working group on "Phase Transformations and High-Temperature Materials" at the Department of Materials Science, Montanuniversität Leoben, using state-of-the-art experimental methods and theoretical approaches in cooperation with European as well as international universities, research facilities and industries. The name TNM corresponds to an acronym according to the alloying elements (T stands for TiAl, N for Nb and M for Mo) [3,6]. In particular, the alloy design has a beneficial effect on the solidification pathway (L → L + β → β → …) and hot deformation behavior and, subsequently, on microstructure and material properties due to an enhanced microstructural homogeneity, a weak casting texture, minor segregations, and a refined microstructure [7]. Finally, post-forging multi-step heat treatments ensure an improved chemical and microstructural homogeneity, along with increased room temperature (RT) ductility and creep strength at elevated temperatures [2].

The aim of this presentation is to summarize the particular development achievements of the novel intermetallic β-solidifying γ-TiAl based TNM alloy **from fundamental research to application**. For the alloy design a profound knowledge of the thermodynamics and kinetics of occurring phase transformations depending on chemical composition is an essential prerequisite. Thus, thermodynamic calculations, such as those obtained by the CALPHAD (CALculation of PHAse Diagrams) method, have been applied to predict phase diagrams of the multi-component alloying system together with first-principles calculations to study the preferential site occupation of the selected alloying elements. As the commercial TiAl database developed by Saunders [8] was unreliable in predicting phase fractions as a function of temperature because of the high proportion of β-stabilizing elements, the existing database was modified with the aid of concomitant experimental studies, such as in situ diffraction techniques employing synchrotron radiation and neutrons. The relationship between microstructure and engineering properties for high-temperature application is also the topic of discussion, where the microstructural features were analyzed by means of high-resolution characterization techniques, such as transmission electron microscopy (TEM) and atom probe tomography (APT), leading to the determination of a two-step heat treatment for the adjustment of the final microstructure with balanced mechanical properties. A short summary and outlook follows at the end of the presentation, wherein the alloy design is shown for a creep-improved so-called TNM[+] alloy, which exhibits small additions of C and Si to further enhance the high-temperature capability [9].

References

[1]   IPCC Special Report, in: J.E. Penner, D.H. Lister, D.J. Griggs, D.J. Dokken, M. McFarland (Eds.): Aviation and the Global Atmosphere. Cambridge Univ. Press, Cambridge, UK, **1999**.

[2]   S. Mayer, P. Erdely, F.D. Fischer, D. Holec, M. Kastenhuber, T. Klein, H. Clemens, Advanced Engineering Materials. **2017**, *19*, doi:10.1002/adem.201600735.

[3]   H. Clemens, S. Mayer, Advanced Engineering Materials. **2013**, *15*, 191-215.

[4]   E. Schwaighofer, H. Clemens, S. Mayer, J. Lindemann, J. Klose, W. Smarsly, V. Güther, Intermetallics. **2014**, *44*, 128-140.

[5]   M. Kastenhuber, T. Klein, H. Clemens, S. Mayer, Intermetallics. **2018**, *97*, 27-33.

[6]   H. Clemens, W. Wallgram, S. Kremmer, V. Güther, A. Otto, A. Bartels, Advanced Engineering Materials. **2008**, *10*, 707-713.

[7]   D. Zhang, G. Dehm, H. Clemens, Scripta Materialia. **2000**, *42*, 1065-1070.

[8]   N. Saunders, in: Y-W. Kim, D.M. Dimiduk, M.H. Loretto (Eds.): Gamma Titanium Aluminides 1999. TMS, Warrendale, PA, USA, **1999**.

[9]   T. Klein, L. Usategui, B. Rashkova, M.L. Nó, J. San Juan, H. Clemens, S. Mayer, Acta Materialia. **2017**, *128*, 440-450.

O–TA–05

TCTI2 – an updated thermodynamic database for multicomponent Ti- and TiAl-based alloys

Yang Yang, Hai-Lin Chen, Qing Chen and Anders Engström

Thermo-Calc Software AB, Råsundavägen 18, 16967 Solna, Sweden, yang@thermocalc.com

Introduction

CALPHAD (CALculation of PHAse Diagrams) has played an important role in alloy design and process optimization for decades. The quality of CALPHAD simulations by large depends on the accuracy of the database being used. This work updates a thermodynamic database (TCTI2) within a 27-element framework (Ag-Al-B-C-Co-Cr-Fe-H-Hf-Mn-Mo-N-Nb-Ni-O-Pd-Pt-Re-Ru-Si-Sn-Ta-Ti-V-W-Y-Zr). It consists of 269 assessed binary systems and 95 assessed Ti-containing ternary systems. Calculations with TCTI2 help to understand phase equilibria, phase transformation and microstructure evolution in titanium alloys and thus to accelerate the material design. TCTI2, together with its compatible mobility database MOBTI3, can be also used for simulating diffusion-controlled phase transformation and precipitation kinetics. This database is expected to efficiently support further development of Ti- and TiAl-based alloys with a reduction of costly trial and error experiments.

Database overview

The TCTI2 database has been developed in a systematic way in order to cope with the complexity in the phase relations and phase transformations in titanium alloys. Based on an extensive crystallographic investigation of all solid phases, the phases having the same crystal structure are generally modelled as one phase, unless they are tactically treated as two groups according to the major constituents in certain cases. Appropriate thermodynamic models are selected and used for different types of phases. The common solution phases (liquid, Bcc_A2 (βTi) and Hcp_A3 (αTi and α')) are modelled as substitutional solutions [1]. Most intermetallic compounds and their solutions, such as α_2 phase ($AlTi_3\_D0_{19}$), γ phase ($AlTi\_L1_0$) and ω_o-Ti_4Al_3Nb phase (B8$_2$_omega) are described with sublattice models [1]. The ordered B2 phase is modeled with the so-called partition model [2,3] in conjunction with its disordered counterpart, Bcc_A2.

All necessary volume data (including molar volume and thermal expansion) have been assessed with the implemented model [4,5] for most solution phases and intermetallic phases in TCTI2. This enables one to calculate volume fraction of phases, density and thermal expansivity, as well as lattice parameters for cubic structures using Thermo-Calc.

Applications

Typical calculated examples for various properties in titanium alloys are presented in this work with the emphasis on validation against experimental observations in multi-component commercial alloys.

A central point for thermomechanical treatment of conventional Ti-alloys is the β-transus temperature which is of critical importance to alloy design. A comparison between observed and calculated β-transus temperatures is made for a wide variety of typical commercial Ti-alloys and is shown in Fig. 1. The dash lines indicate an uncertainty of ±20 °C.

Thermophysical properties, such as density, enthalpy (H_T-H_{298}), thermal expansion, *etc.*, are normally required as input for process (casting, welding) simulations. A major achievement of TCTI2 is that such data can be readily calculated for different alloys from room temperature into the liquid state, which is of vital importance for process simulation but difficult to measure or otherwise estimate. Fig. 2 shows the calculated density of liquid TiAlNb compared with experimental data [6,7].
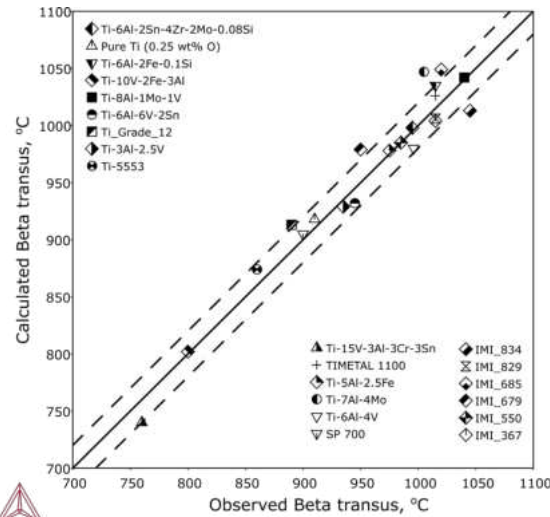
Fig. 1 Comparison between experimentally observed and predicted β-transus temperatures for Ti-Alloys.
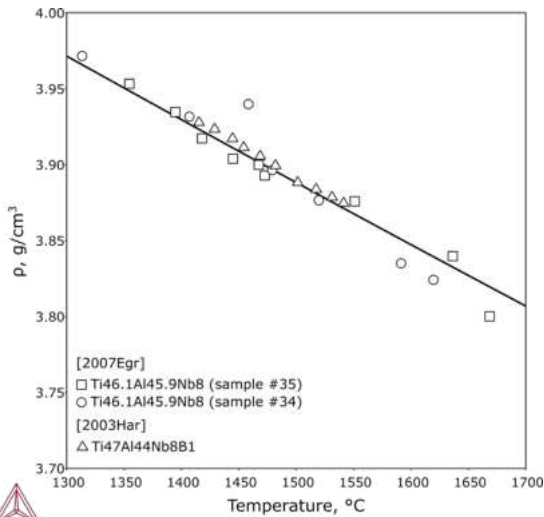
Fig. 2 Density of liquid TiAlNb.

References

[1]   H.L. Lukas, S.G. Fries, B. Sundman, Computational thermodynamics: The Calphad Method, Cambridge University Press. **2007**.

[2]   I. Ansara, N. Dupin, H. L. Lukas, B. Sundman, J. Alloys Compd. **1997**, *247*, 20–30.

[3]   N. Dupin, I. Ansara, B. Sundman, Calphad. **2001**, *25*, 279–298.

[4]   X.-G. Lu, M. Selleby, B. Sundman, Acta Mater. **2005**, *53*, 2259–2272.

[5]   X.-G. Lu, M. Selleby, B. Sundman, Calphad. **2005**, *29*, 68-89.

[6]   I. Egry, R. Brooks, D. Holland-Moritz, R. Novakovic, T. Matsushita, E. Ricci, S. Seetharaman, R. Wunderlich, D. Jarvis, Int. J. Thermophys. **2007**, *28*, 1026-1036.

[7]   R. Harding, R. Brooks, G. Pottlacher, J. Brillo, Thermo-physical properties of a Ti-44Al-8Nb-1B alloy in the solid and molten conditions, in: Gamma Titanium and Other Metallic Aluminides, TMS, Warrendale, PA, **2003**, 75-82.

O–TA–06

Effect of hot forging at lower temperatures on microstructure and mechanical properties of β-solidifying γ-TiAl alloys

Valery Imayev, Artem Ganeev and Renat Imayev

Institute for Metals Superplasticity Problems of Russian Academy of Sciences, Ul Khalturina, 39, Ufa, Russian Federation, vimayev@mail.ru, artem@imsp.ru, renat_imayev@mail.ru

Introduction

Intermetallic γ-TiAl based alloys represent engineering materials for light-weight and high-temperature applications up to 750°C due to their low density, good oxidation and creep resistance combined with high specific mechanical properties. The different γ-TiAl alloys can be classified as falling into the following categories: i) "conventional" alloys (the alloys solidifying through the peritectic reaction(s)); ii) high niobium-containing alloys; iii) β-solidifying alloys; iv) high-alloyed "beta-gamma" alloys solidifying through the β phase and containing a considerable amount of the β phase; v) massively transformed alloys. From the most general point of view, γ-TiAl alloys can be subdivided into two groups: the alloys solidifying solely through the β phase and the alloys solidifying through peritectic reaction(s). It has been well documented that γ-TiAl alloys solidifying completely through the β phase have some advantages as compared to peritectically solidifying ones [1-3]. These include: i) better chemical homogeneity (owing to a lower level of dendritic segregation), ii) reduced casting texture, and iii) a refined casting microstructure resulted from solid-state phase transformations (in the case of appropriate alloying). Although a number of excellent research works devoted to β-solidifying γ-TiAl alloys have been performed [2-5], further improvements in mechanical properties via alloy/microstructure designing and improvements in hot working and post-working heat treatment are desirable. The present work was aimed to study the microstructure and mechanical properties of some β-solidifying γ-TiAl alloys subjected to hot forging at lower temperatures and post-forging heat treatment with emphasis on attaining refined microstructures with a mean grain/colony size less than 30 μm. Taking into account a limited hot workability of β-solidifying γ-TiAl alloys, hot forging was performed first at higher temperatures and then at lower temperatures using enhancement of the hot workability attained due to microstructure refinement after hot forging at higher temperatures. Another approach applied in the present work was associated with using small deformation values at lower hot working temperatures.

Materials and Methods

Three γ-TiAl alloys (A1-A3) are considered in the present work: 1) Ti-45Al-5Nb-1Mo-0.2B (for the sake of simplicity hereafter Ti-45), 2) Ti-43.7Al-4.2Nb-0.5Mo-0.2B-0.2C (Ti-43.7), 3) Ti-44Al-5Nb-0.2B (Ti-44) (in at. %). The alloys were produced by vacuum arc remelting and subjected to hot forging and post-forging heat treatment. Cylindrical workpieces of the Ti-45 and Ti-43.7 alloys were forged in the α+β(B2)+γ phase field and then at lower temperatures, in the α$_2$+β(B2)+γ phase field, followed by post-forging heat treatment. The summed strains imparted during forging of the cast Ti-45 and Ti-43.7 alloys were $e≈1.2$ and 4, respectively. The forging procedures are described in more details in refs. [6,7]. Cylindrical workpiece of the Ti-44Al alloy was subjected to forging in the α$_2$+γ phase field to a small strain value ($e≈0.2$), followed by near the same heat treatment as in the case of the Ti-45 and Ti-43.7 alloys. The post-forging heat treatment included annealing in the α+β(B2)+γ (for the Ti-45 and Ti-43.7 alloys) or α+γ (for the Ti-44 alloy) phase field and ageing at 900°C (2 h). Mechanical tests were performed for the produced conditions of the alloys. All samples were prepared by electrospark cutting followed by fine grinding of work surfaces. The microstructure examination was carried out for the cross sections of the forged workpieces using scanning electron microscopy (SEM) in backscattering electron (BSE) mode.

Results and Discussion

Different microstructures ranging from near fully lamellar to duplex were obtained in the alloys under study. Table 1 represents microstructure characteristics and mechanical properties obtained for the alloys. The produced microstructures differed in the grain/colony size, the volume fraction of lamellar constituent, the fraction of the β(B2) phase and the interlamellar spacing. The Ti-45 and Ti-43.7 alloys in the cast and heat treated conditions had a similar near fully lamellar structure. Comparing the room temperature tensile properties of these alloys in the cast and heat treated conditions, one can conclude that the carbon addition reduced the room temperature ductility. Hot forging at lower temperatures, in the α$_2$+β(B2)+γ (for the Ti-45 and Ti-43.7Al alloys) or α$_2$+γ (for the Ti-44 alloy) phase field led to microstructure refinement due to dynamic recrystallization/globularization processes during hot forging. The hot forged conditions of the Ti-45 and Ti-43.7Al alloys showed excellent superplastic properties at 900-1000°C [6,7] and superplastic elongations were significantly higher in the case of the Ti-43.7Al alloy that is associated with a higher strain value imparted during hot forging ($e≈4$ vs. $e≈1.2$). Subsequent heat treatment in the α+β(B2)+γ (for the Ti-45 and Ti-43.7Al alloys) or α+γ (for the Ti-44 alloy) phase field led to formation of duplex structures with a mean grain/colony size

of d=6-15 µm. The duplex structures provided higher strength and ductility both at room and elevated temperatures. As was shown for the Ti-45 alloy, the refined duplex structure reduced significantly the long-term strength (creep resistance) at 700°C as compared with the near fully lamellar condition. At the same time, the Ti-44Al alloy with the duplex structure containing predominantly the lamellar constituent demonstrated the creep resistance similar to that of the Ti-45 alloy with near fully lamellar microstructure.

The experiments performed for the Ti-44 alloy showed that hot forging can be used with respect to as-cast β-solidifying alloys at lower temperatures (in the α_2+β(B2)+γ or α_2+γ phase field) if small strain values and isothermal conditions are applied. It was revealed that the strain value e≈0.2 led to occurrence of recrystallization/globularization processes during forging and post-forging heat treatment that gave quite reasonable mechanical properties if comparing with those of the cast β-solidifying γ-TiAl alloys.

Table 1: Microstructure characteristics and mechanical properties obtained for some β-solidifying γ-TiAl alloys after hot forging and heat treatment

Alloy	Processing / Microstructure	Tensile properties				Long-term strength at 700°C (100 h.)
		20°C		700°C		
		UTS, MPa	δ, %	UTS, MPa	δ, %	
Ti-45 [6]	Cast + HT / NFL, d≈50 µm, $V_{\beta(B2)}$=1.7%	670	0.9	672	3.1	>450
	HF (e≈1.2) + HT / DP, d≈8 µm, V_{LC}≈20%, $V_{\beta(B2)}$=1.3%	860	3.1	790	6.5	>350
Ti-43.7	Cast + HT / NFL, d≈62 µm, $V_{\beta(B2)}$<0.5%	600	0.3	-	-	-
	HF (e≈4) + HT / DP, d≈6 µm, V_{LC}≈20%, $V_{\beta(B2)}$<0.5%	930	1.4	774	3.9	>350
Ti-44	HF (e≈0.2) + HT / DP, d≈15 µm, V_{LC}≈65%, $V_{\beta(B2)}$ – n.a.	730	1.25	706	4.9	>350

HT - heat treatment, HF – hot forging, NFL or DP – near fully lamellar or duplex structure, V_{LC} – the volume fraction of lamellar constituent, $V_{\beta(B2)}$ - the volume fraction of the β(B2) phase.

References
[1]   R. Imayev, V. Imayev, M. Oehring, F. Appel, Intermetallics, **2007**, 15, 451-460.
[2]   H. Clemens, W. Wallgram, S. Kremmer, V. Güther, A. Otto, and A. Bartels, Adv. Eng. Mater. **2008**, 10, 707-713.
[3]   H. Clemens and S. Mayer, Adv. Eng. Mater. **2013**, 15, 191-215.
[4]   E. Schwaighofer, H. Clemens, S. Mayer, J. Lindemann, J. Klose, W. Smarsly, V. Güther, Intermetallics, **2014**, 44, 128-140.
[5]   S. Bolz, M. Oehring, J. Lindemann, F. Pyczak, J. Paul et al., Intermetallics, **2015**, 58, 71-83.
[6]   T.I. Nazarova, V.M. Imayev, R.M. Imayev, R.R. Mulyukov, The Phys. of Met. Metallogr., **2016**, 117(10), 1038-1046.
[7]   V.M. Imayev, A.A. Ganeev, R.M. Imayev, Intermetallics, **2018**, 101, 81-86.

O–TA–07

Oxidation of Pt-Al coatings on TNM-B1 at 900 °C

Xabier Montero[1], Lu Gan[2], Hideyuki Murakami[3] and Mathias C. Galetz[4]

[1]DECHEMA-Forschungsinstitut,Theodor-Heuss-Allee 25, 60486 Frankfurt am Main, Germany, montero@dechema.de
[2]NIMS, 1-2-1, Sengen, Tsukuba-Shi, Ibaraki-ken 305-0047, Japan, GAN.Lu@nims.go.jp
[3]NIMS, 1-2-1, Sengen, Tsukuba-Shi, Ibaraki-ken 305-0047, Japan, MURAKAMI.Hideyuki@nims.go.jp
[4]DECHEMA-Forschungsinstitut, Theodor-Heuss-Allee 25, 60486 Frankfurt am Main, Germany, galetz@dechema.de

Introduction

Lightweight materials as titanium alloys can be used to replace heavier nickel base superalloys in aero engines. This replacement is already introduced in the low-pressure turbine of different aircraft engines. Titanium aluminides maintain good mechanical and oxidation protection properties up to around 750°C [1-3]. However, to increase their temperature application range further improvements are necessary. These alloys show limited oxidation resistance due to their fast-growing mixed oxide scale formation and susceptibility to oxygen-induced surface embrittlement at higher temperatures [4-6]. For nickel-based alloys the highest improvements in the oxidation resistance are usually obtained by MCrAlY or by Pt-modified aluminide coatings [7]. These coatings form alumina and reduce internal oxidation of alloys. Motivated by the positive results of Pt-modified aluminide coatings onto nickel-based alloys similar coatings are developed for a TNM-B1 alloy via electroplating and subsequent power pack cementation. Such coatings and their efficacy to protect TiAl alloys at a testing temperature of 900°C in air is presented. Based on such results an optimal coating composition is proposed.

Materials and Methods

Pt-based aluminide coatings were deposited on a TiAl alloy by combining electrochemical deposition of Pt and subsequent Al pack cementation. Third generation TiAl alloy TNM-B1 (Ti-43.5Al-4Nb-1Mo-0.1B [at.%]) consists of γ-TiAl, α_2-Ti$_3$Al and β/β_0-Ti(Al). Pt thickness in the electroplated layer varied between 5 and 1 µm. Pt coated samples were diffusion heat-treated in a high vacuum furnace for 2 h at 1000°C. After Pt diffusion some of the samples were aluminized by pack cementation. Such samples were introduced in NH$_4$Cl, Al, Cr and Al$_2$O$_3$ (2wt.%-24.5wt.%-24.5wt.%-rest) powder mixture and diffusion treated at 900°C for 2h in Ar. This corresponds to a high activity powder pack composition resulting in the TiAl$_3$ phase and an Al-rich titanium modified platinum aluminide. The oxidation resistance of the coatings was tested at 900°C for 140 h. The weight of the samples was measured before and after introducing the samples in the box furnace to determine the efficiency of the coating procedure.

The surface of the samples was investigated using Glow Discharge Optical Emission Spectroscopy (GD-OES) and X-ray diffraction measurements. A cross section of the sample was analyzed by scanning electron microscope. Oxidized samples were galvanically copper-plated before metallographic preparation and polished down to 1 µm diamond suspension.

Results and Discussion

Oxidation of bare TNM-B1 and Pt diffused coatings of different thickness (without aluminisation) show the formation of mixed TiO$_2$/Al$_2$O$_3$ scales in conjunction with the high weight gain shown in figure 1. In the case of bare TNM-B1 spallation of the scale occurred after cooling of the sample as shown in figure 1. Aluminizing of the TNM-B1 substrate as well as aluminizing of the previously Pt diffusion treated TNM-B1 strongly improved the oxidation resistance of the samples. In such cases, pure Al$_2$O$_3$ scales are formed instead of a mixed oxide scale. Both coatings indicate slow growing Al$_2$O$_3$. The differences in the scale growth and changes in the microstructure are currently under investigation and will be discussed.
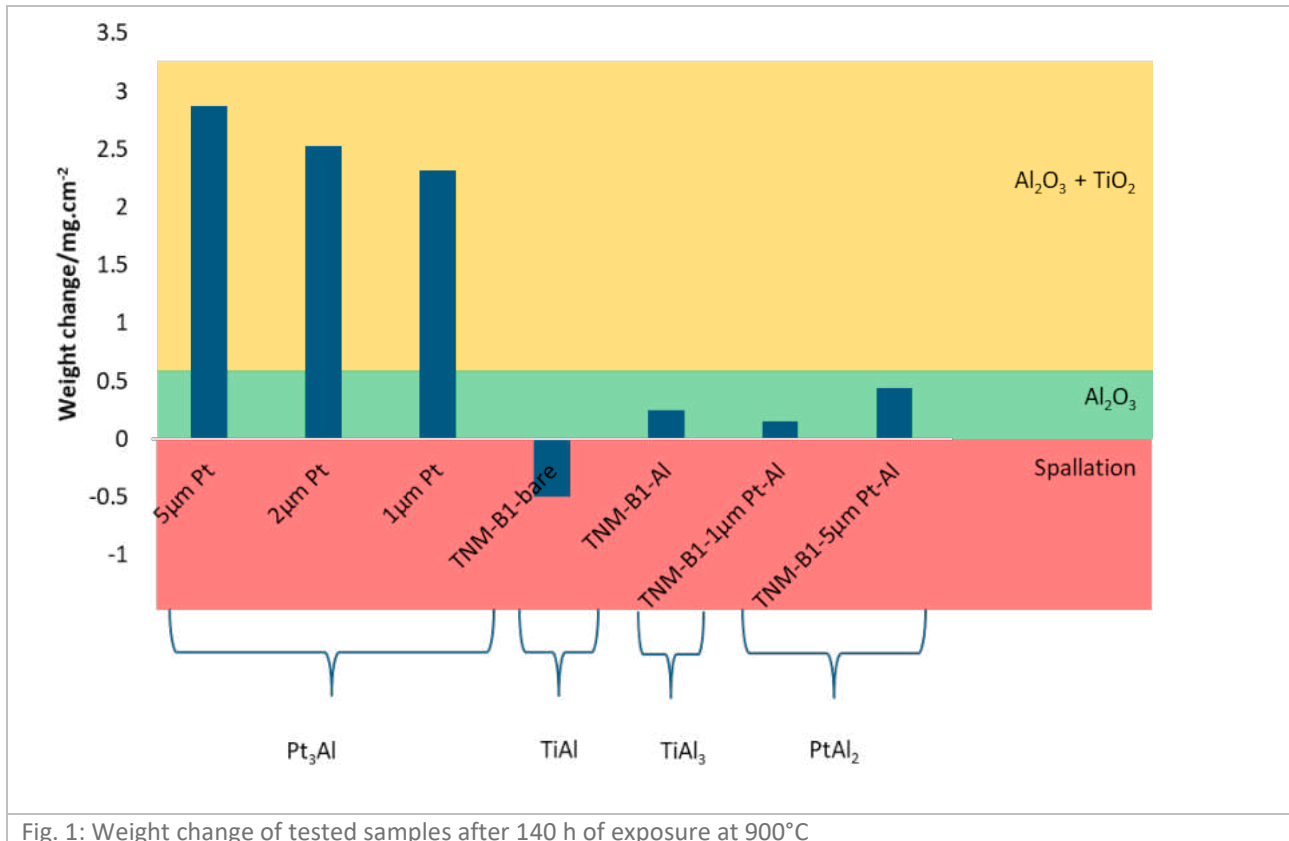
Fig. 1: Weight change of tested samples after 140 h of exposure at 900°C

References

[1] H. Clemens, F. Appel, A. Bartels, H. Baur, R. Gerling, V. Güther, K. Kestler, in: G. Lütjering, J. Albrecht (Eds.) Ti-2003, Science and Technology, Volume IV, Wiley-VCH Verlag, Weinheim **2004**, 2123-2136.

[2] H. Kestler, H. Clemens, in: M. Peters, C. Leyens (Eds.), Titanium and Titanium alloys, Wiley-VCH Verlag. Weinheim **2002**, pp. 369-400.

[3] H. Clemens, S. Mayer, Advanced Engineering Materials 15 (4) **2013** 191.

[4] F. Appel, J.D.H. Paul, M. Oehring, Gamma titanium aluminide alloys: science and technology. Weinheim: John Wiley & Sons; **2011**.

[5] A. Straubel, S. Friedle, M. Schütze, N. Laska, R. Braun, C. Leyens, in: Y.W. Kim, W. Smarsly, J. Lin, D. Dimiduk, F. Appel (Eds.) Gamma titanium aluminide alloys 2014: A collection of research on innovation and commercialization of gamma alloy technology. **2014**, 105-109

[6] X. Wu, A. Huang, D. Hu, M.H. Loretto, Intermetallics 17 (7) **2009** 540-552

[7] J.R. Nicholls, K.A. Long, N.J. Simms, in: J.A.R. Tony (Eds.) Shreir's Corrosion. Diffusion coatings. Elsevier, Oxford **2010**, 2532-2555

O–TA–08

Oxidation protection of gamma-TiAl by the F-effect – ready for industrial application

Hans-Eberhard Zschau[1], Bernd Möller[2], Dietmar Emig[2], Daniel Hipper[2], Alexander Donchev[3] and Mathias C. Galetz[3]

[1]Werkstoffprüfung und –forschung, Roitzscher Weg 32 c, 04808 Wurzen, Germany, dr.zschau@hotmail.com
[2]Fluor Technik System GmbH, Altebergstrasse 27-29, 36341 Lauterbach, Germany,
b.moeller@fts-de.com, d.emig@fts-de.com, d.hipper@fts-de.com
[3]DECHEMA-Forschungsinstitut, Theodor-Heuss-Allee 25, 60486 Frankfurt, Germany,
donchev@dechema.de, galetz@dechema.de

Introduction

γ-TiAl alloys form a non-protective mixed oxide scale of TiO_2 / Al_2O_3 on the surface at temperatures above 800°C. A surface modification with fluorine can change the oxidation mechanism into the growth of a dense protective alumina scale. A thermodynamic model was developed explaining this Fluorine effect [1]. Beam line ion implantation was used to verify the conditions predicted by the thermodynamic model [2] and to study the long-term behavior of the oxidation protection. However, a cost-effective method of surface doping with fluorine in an industrial scale was still missing. In the present work industrial gas phase fluorination was applied to achieve the conditions of the F-effect for γ-TiAl alloys. The results obtained with ion implantation serve as a benchmark to identify the optimized parameters for gas phase fluorination. In the second part of the work, the long-term performance of gas fluorinated alloy was studied under isothermal and cycling conditions.

Materials and Methods

Commercial alloy GE 4822 with elemental composition Ti-48Al-2Nb-2Cr (at.%) was chosen. The alloy was casted by Feinguss Blank GmbH, Riedlingen, in coupons with size of 10 x 10 x 2 mm^3. Half of the samples were polished on both sides down to 4000 grit SiC followed by ultrasonic cleaning. The other half of the samples obtained a surface treatment by blasting with Korund particles. These samples are referred to have an "as received" surface. All samples were exposed in the industrial fluorination equipment of Fluor Technik System GmbH (FTS) using a gas atmosphere of (N_2-10%F_2). The parameter set defining the fluorination process are temperature, time of exposure and 2 gas pressures. The gas fluorination was performed using at least 30 parameter sets to meet the suitable F-concentration and F-dose. The non-destructive PIGE (Proton Induced Gamma-ray Emission) was used to determine the F-depth profiles. The PIGE-measurements were carried out at the 2.5 MV Van de Graaff-accelerator of the Goethe-University Frankfurt. The depth profiling was performed by using the nuclear reaction 19F(p, $\alpha\gamma$)16O at resonance energies of 340 keV and 484 keV, resp. A NaI(Tl) scintillation counter detected the high energetic γ-rays (5-7 MeV). The screening process worked as follows: Only those samples showing F-profiles suitable for the F-effect were oxidized isothermally (100..500 h/900°C/lab air). Finally metallographic cross-sections were prepared after oxidation to study the oxide structure by using SEM/EDX. As result of the screening process an optimized parameter set was obtained. After gas fluorination by using this parameter set further samples were oxidized isothermally and cyclically for 1000 h/900°C. Thermogravimetric analysis (TGA) was carried out (600h/900°C/ synthetic air) to reveal the kinetics of oxide scale growth.

Results and Discussion

The F-treatment by beam line ion implantation showed the best results so far for the F-effect between the implantation parameters of 1 x 10^{17} and   2 x 10^{17} F cm^{-2} / 20 keV. The maximum F-content was found between 20 – 40 at.% [2].
The results show a strong dependence of the obtained F-depth profiles with respect to the parameter set of gas fluorination. These values meet the optimal part of the corridor recommended by F-implantation studies as mentioned above. Optimal fluorine enrichment on the surface is characterized by a maximum F-concentration of 30-45 at.% and an integral F-dose of (2..4) x 10^{17} F cm^{-2}. After isothermal oxidation (1000 h/900°C) the surface is covered with a 2-3 μm thin protective alumina scale (fig. 1). Cyclic oxidation was performed at 900°C with a number of 480 cycles (1 cycle: 60 min hot, 50 min cold). A thin (2-3 μm) protective adherent alumina scale was found on the surface.
The mass gain measured with TGA (600 h/900°C/ synthetic air) reveals a distinct alumina kinetics for the oxide growth. As result the gas fluorination process offers a cost-effective method for industrial fluorination of γ-TiAl-alloys.
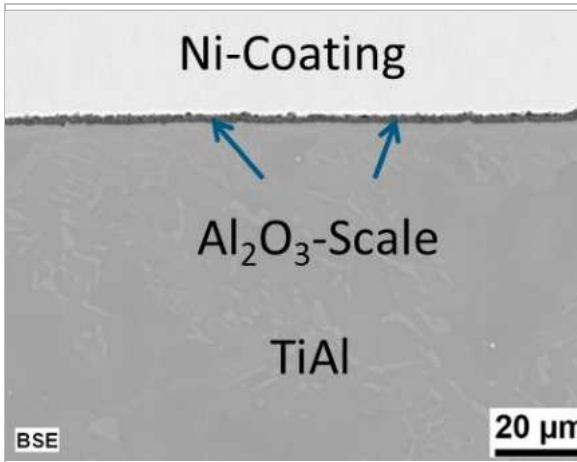
| Fig.1: Protective alumina scale on the sur-face of γ-TiAl-alloy GE 4822 after iso-thermal oxidation (1000 h/900°C/air). | Fig. 2: TGA-curve of a gas fluorinated sample of alloy 2 (GE 4822) during oxidation (600 h/900°C/synth. air). |
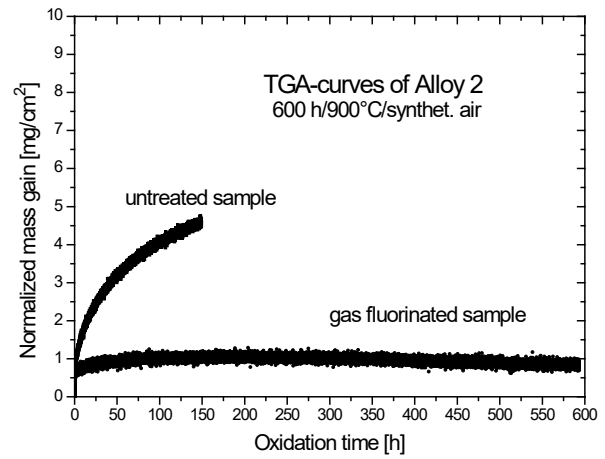
References

[1]   A. Donchev, B. Gleeson, M. Schütze, Intermetallics. 11, **2003,** 387-398.

[2]   H.-E. Zschau and M. Schütze, in: Mark S. Goorsky (Ed.): Ion Implantation. InTech, Rijeka, **2012**, 409-436. Ebook: http://www.intechopen.com/books/ion-implantation

O–IT–06

Phase diagram study on the Ti-Al-M-O quaternary systems using soft X-ray emission spectroscopy

Hirotoyo Nakashima, Yuta Kimoto and Masao Takeyama

Department of Materials Science and Engineering, School of Materials and Chemical Technology, Tokyo Institute of Technology, 2-12-1, Ookayama, Meguro-ku, Tokyo, Japan, nakashima.h.aa@m.titech.ac.jp

Introduction

Dispersion of β-Ti phase is effective in toughening and strengthening of γ-TiAl based alloys [1, 2]. For further optimization of the mechanical properties, control of the volume fraction and morphology of the β phase based on the phase diagrams is necessary. Thus, we have constructed the multi-component phase diagrams of TiAl alloys having transition metal elements, M (M: V, Nb, Cr, Mo) which solves substitutionally. In any Ti-Al-M ternary systems, the β phase is stabilized against the α-Ti phase and directly in equilibrium with γ phase, resulting in the existence of the $\beta+\alpha+\gamma$ three-phase coexistence region [3]. On the other hand, interstitial elements such as carbon, nitrogen and oxygen are qualitatively known to stabilize the α (or α_2-Ti$_3$Al) phase against the γ phase. From some atom probe experiments, these interstitials are reported to partition into α phase [4]. However quantitative manner has not been clarified because of its technical difficulty and a lack of systematic study, even though those elements are inevitably contained as impurities. Recently we applied the soft X-ray emission spectroscopy (SXES) to quantify the oxygen content in each phase and establish the optimum conditions [5]. SXES is originally developed for the evaluation of bonding electron states [6]. However, it is also useful for quantitative analysis of light elements, by using its high energy-resolution in ultra-soft X-ray regime (<1000 eV). In the present study, we prepared a series of TiAl alloys with various oxygen (O) content, and have examined phase equilibria among the β, α, α_2, γ phases as well as the partitioning behavior of solute oxygen among the phases in Ti-Al-M-O quaternary systems using SXES.

Materials and Methods

The Ti-(43-47)Al-(0-15)M (in at.%) ternary alloys containing oxygen up to 1.5 at.% were prepared by vacuum arc melting to about 120 g button ingot. The oxygen contents in the alloys were analyzed by inert gas fusion method. All as-cast alloys were homogenized at β- or α single-phase region using vertical furnace with MoSi$_2$ heating elements. Prior to the heat treatment, the chamber was evacuated down to 5×10^{-3} Pa, and then filled with high purity Ar (O$_2$ < 0.1 vol.ppm). After holding, samples were directly dropped down into the water. The subsequent equilibration heat treatments were conducted at temperature from 1653 K to 1273 K for up to 2 months. Homogenized samples wrapped with Ta foil were encapsulated into silica tube, evacuated and backfilled with Ar. After the equilibration, samples were water quenched by breaking the capsule. Microstructure observation and composition analysis were done by FE-EPMA equipped with WDS and SXES. The major constituent elements (Ti, Al, Nb, Cr) were analyzed by WDS with an acceleration voltage of 20 kV. The oxygen content of the phases present was analyzed by a calibration method obtained using the homogenized samples by SXES with the third reflection of the oxygen Kα peak at 175 eV. The acceleration voltage, probe current and dwell time used for SXES were optimized in Ti-43Al binary alloys in order to maximize the accuracy and minimize the dispersion. The sample surfaces were sputtered by Ar-ion in exchange chamber just before the analysis to remove the oxygen-rich layer forms during sample preparation.

Results and Discussion

At all temperatures studied, formation of oxides is not observed. At 1473 K, Ti-44Al-4Cr without oxygen (0.13 at.%O as an impurity) shows the $\beta+\alpha+\gamma$ three-phase microstructure and the volume fraction of the β phase (V_β) is about 40 % (Fig 1 (a)). By adding oxygen in solution, V_β decreases and 1.0O shows $\alpha+\gamma$ two-phase microstructure (Fig 1 (b)). The compositions of the constituent elements of each phase present in the alloys equilibrated at 1473 K are analyzed by WDS and plotted in (Fig. 2). By the addition of 1.0 at.% oxygen, the $\beta+\alpha+\gamma$ three-phase tie triangle shifts toward the higher Al and Cr content side by 1.5 and 1.0 at.%, respectively, suggesting the strong α stabilizing effect of oxygen. The oxygen content in each phase present in Ti-44Al-4Cr ternary alloys are plotted as a function of the oxygen content in the alloy, together with that in Ti-43Al binary alloys (Fig. 3). Oxygen is preferentially partitions into the α phase, whereas hardly dissolves in the γ phase, in both systems. O content in the γ is almost constant regardless of the O content in the alloys, and shows smaller value in the Ti-Al-Cr ternary system. The temperature dependence of the oxygen effect on the phase equilibria in Ti-Al-Nb and Ti-Al-Cr systems will be discussed.
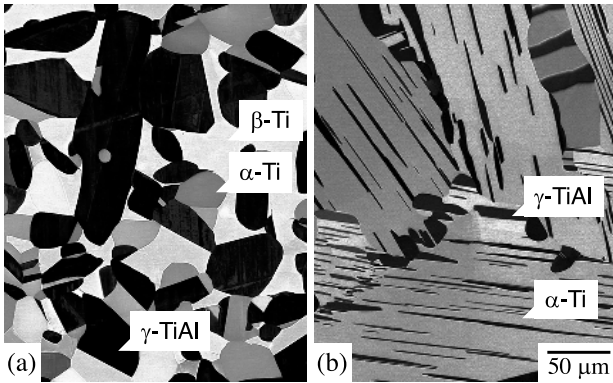
Fig. 1: BEIs of Ti-44Al-4Cr alloys containing (a) 0.1 and (b) 1.0 at.% oxygen equilibrated at 1473 K.
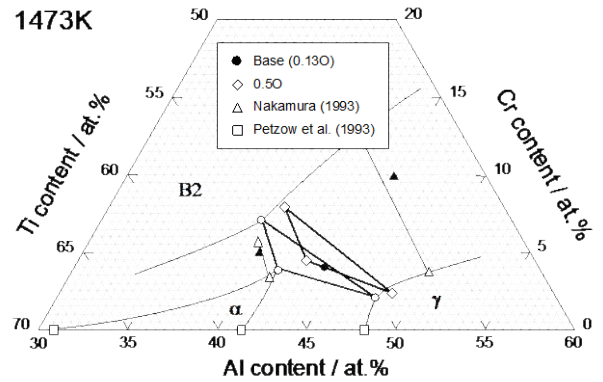
Fig. 2: Isothermal section of Ti-Al-Cr system showing the change in Al and Cr content in the phases present in Ti-44Al-4Cr without and with oxygen equilibrated at 1473 K.
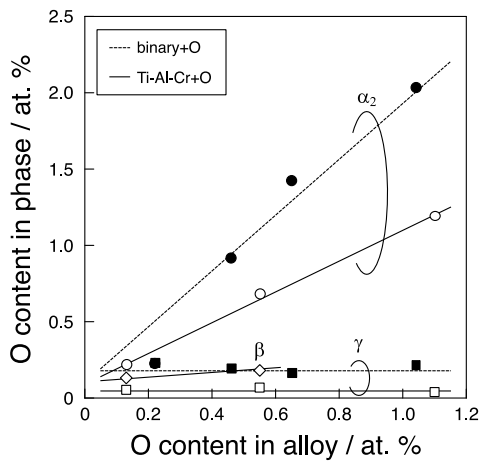
Fig. 3: Change in O content in the phases present in Ti-43Al and Ti-44Al-4Cr alloys with O content in the alloys at 1473 K.

References

[1]   L. J. Signori, T. Nakamura, Y. Okada, R. Yamagata, H. Nakashima, M. Takeyama, Intermetallics. **2018**, *100*, 77–87.

[2]   R. Yamagata, Y. Okada, H. Wakabayashi, H. Nakashima, M. Takeyama, MRS Advances. under review.

[3]   M. Takeyama, S. Kobayashi, Intermetallics, **2005**, *13*, 993-999.

[4]   A. Menand, H. Zapolsky-Tatarenko, A. Nérac-Partaix, Mater. Sci. Eng. **1998**, A250. 55-64.

[5]   A. Kinouchi, H. Nakashima, M. Takeyama, Intermetallics 2017, **2017**, O-TA 04, 61-62.

[6]   S. Ishii, M. Terauchi, Y. Sato, N. Tamura, M. Aono, H. Abe, Microscopy, **2018**, *67*, 244–249.

O–PS–06

Demixing in D0$_{22}$-like Al–Mo–Ti alloys

Andreas Leineweber, Benedikt Distl, Mario J. Kriegel and Stefan Martin

Institute of Materials Science, TU Bergakademie Freiberg, Gustav-Zeuner-Straße 5, 09599 Freiberg, Germany,
andreas.leineweber@iww.tu-freiberg.de, b.distl@mpie.de, mario.kriegel@iww.tu-freiberg.de,
stefan.martin@iww.tu-freiberg.de

Introduction

Phase equilibria in Al–Ti base systems receive considerable attention, in particular, due to their importance for Ti–Al based alloys for high-temperature applications. Even phase-equilibrium data from technologically less relevant compositions are relevant information for putting together thermodynamic databases within the framework of the CALPHAD method. Such databases are, in turn, important input information for planning of heat treatment and, in particular, for modelling of diffusion and phase transformations occurring during processing.

Against this background there have been various activities in the recent years to study phase equilibria in the Al–Mo–Ti system [1-4], revealing in particular information about the AlMo and Al$_{63}$Mo$_{37}$/τ high-temperature phases which are stabilized to lower temperatures by incorporation of Ti [1,2].

The present contribution deals with the encounter of a most likely metastable phase. For high Al contents of about 75 at.% Al an orthorhombic variant of D0$_{22}$-TiAl$_3$ has been detected in an as-solidified 73Al-22Mo-5Ti (at.%) alloy. D0$_{22}$-TiAl$_3$ belongs to a series of fcc-based aluminides ScAl$_3$ (L1$_2$), ZrAl$_3$ (D0$_{23}$) and TiAl$_3$/NbAl$_3$ (D0$_{22}$; see Fig. 1), which are formally interconvertible by antiphase boundaries perpendicular to one of the $\langle 100 \rangle_{fcc}$ directions and which roughly occur with increasing electron concentration. Monoclinic Al$_8$Mo$_3$ and Al$_3$Mo also constitute fcc-based superstructures, which, however, are more complex than those of the afore-mentioned group-iii-v transition metal trialuminides.

Materials and Methods

Alloys were produced by arc melting and were, partly, subjected to subsequent heat treatment under inert-gas atmosphere. Solid alloys were investigated by optical microscopy, scanning electron microscopy in combination with electron-backscatter diffraction (EBSD), transmission Kikuchi diffraction and energy-dispersive X-ray (EDX) analysis, transmission electron microscopy (TEM; including specimen preparation by focused-ion-beam milling, FIB) as well as by powder X-ray diffraction (P-XRD).

Results and Discussion

P-XRD data of as-solidified 73Al-22Mo-5Ti (at.%) implied presence of two-predominant phases: tetragonal D0$_{22}$-ε-(Ti,Mo)Al$_3$ and a closely related phase exhibiting the same type of superstructure, however, with an orthorhombic distortion ($a \neq b$) whereas the c axis was of very similar length as for the D0$_{22}$ phase. This orthorhombic variant of the D0$_{22}$ structure will be referred to as D0$_{22}'$. Similar diffraction evidence was also obtained from as-solidified alloys of other compositions, however, always together with tetragonal D0$_{22}$-ε-(Ti,Mo)Al$_3$. SEM from polished cross sections of the alloys exhibited a needle-like microstructure being too fine for conventional EBSD analysis, since a strong overlap of different Kikuchi patterns occurred. Nevertheless, a dominant pole in the overlapping Kikuchi patterns was attributable to the c axis of the D0$_{22}$/D0$_{22}'$ structures.

By means of FIB milling a lamella perpendicular to this c axis was cut out and further thinned to achieve transparence for electrons (Fig. 2). A scanning-TEM image reveals a two-phase microstructure with rectangle-shaped domains. EDX analysis reveals higher Mo contents in the regions with darker contrast in Fig. 2. By means of selected area electron diffraction and transmission Kikuchi diffraction the anticipated $[001]_{D0\_22/D0\_22'}$ foil normal was confirmed. The bright areas were further identified as tetragonal D0$_{22}$ and the dark areas as orthorhombic D0$_{22}'$ in two different orientations differing by 90° rotation around $[001]_{D0\_22'}$. The phase boundaries are located approximately on $\{110\}_{D0\_22/D\_022}$ planes. Hence, the microstructure consists of long channels of the two phases.

All attempts to equilibrate the D0$_{22}'$ phase by annealing in the solid state failed. This phase instead decomposes into the D0$_{22}$-ε-(Ti,Mo)Al$_3$ and the monoclinic Al$_8$Mo$_3$ phase (also a fcc superstructure; see above).

Theoretical analysis of the reported crystal structure data of the monoclinic Al_8Mo_3 equilibrium phase and of the orthorhombic crystal structure of the Mo-rich $D0_{22}'$ encountered in the as-solidified alloys reveals some common features, if one considers the eigenvectors and –values of the Aizu strain tensor [6] describing internal distortion of the fcc structure due to superstructure formation. In fact, it turns out that the monoclinic Al_8Mo_3 superstructure shows a similar "orthorhombic" metrical distortion as found for the Mo-rich $D0_{22}'$ phase. On that basis it is suggested that the currently reported $D0_{22} + D0_{22}'$ microstructure is the product of some demixing of initially formed (upon solidification) $D0_{22}$-like solid into Mo-rich and Mo-poor regions, with the Mo-rich regions showing already some structural properties of the stable Al–Mo phases (in particular Al_8Mo_3). The specifically observed microstructure shows some similarities of checker-board microstructures reported for demixed microstructures consisting of (cubic) $L1_2$ and tetragonal $L1_0$ (the latter in two orientations) as occurring in the Co–Pt system (Co_3Pt + CoPt; [7]) which form due to optimization of misfit strains between the two phases.
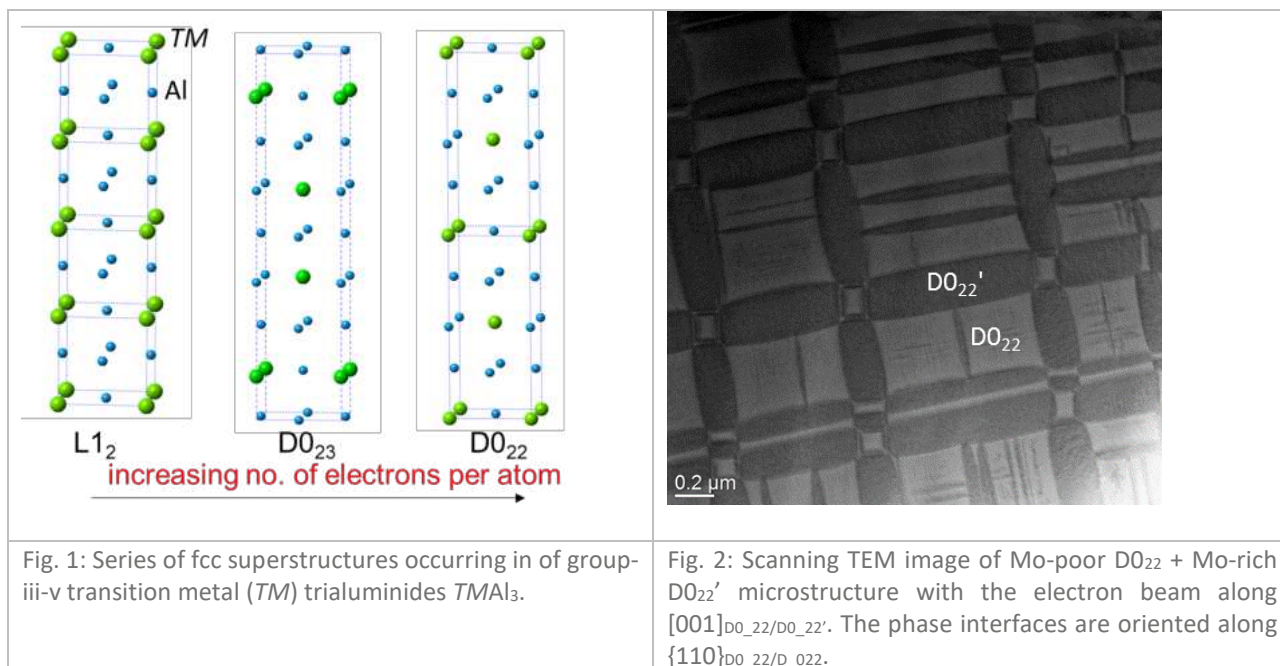
Fig. 1: Series of fcc superstructures occurring in of group-iii-v transition metal (*TM*) trialuminides *TM*Al_3.	Fig. 2: Scanning TEM image of Mo-poor $D0_{22}$ + Mo-rich $D0_{22}'$ microstructure with the electron beam along $[001]_{D0\_22/D0\_22'}$. The phase interfaces are oriented along $\{110\}_{D0\_22/D\_022}$.

References
[1] M.J. Kriegel, A. Walnsch, O. Fabrichnaya, D. Pavlyuchkov, V. Klemm, J. Freudenberger, D. Rafaja, and A. Leineweber, Intermetallics **2017**, *83*, 29-37.
[2] M.J. Kriegel, O. Fabrichnaya, M. Conrad, V. Klemm, J. Freudenberger, and A. Leineweber, Journal of Alloys and Compounds **2017**, *706*, 616-628.
[3] X.M. Huang, L. L. Zhu, G.M. Cai, H.S. Liu, Z.P. Jin, Journal of Materials Science, **2017**, *52*, 2270-2284.
[4] V.T. Witusiewicz, A.A. Bondar, U. Hecht, O.M. Stryzhyboroda, N.I. Tsyganenko, V.M. Voblikov, V.M. Petyukh and T. Ya. Velikanova, Journal of Alloys and Compounds **2018**, *749*, 1071-1091.
[5] M.E. Eberhardt, K.S. Kumar, J.M. MacLaren, Philosophical Magazine B **1990**, *61*, 943-956.
[6] K. Aizu, Journal of the Physical Society of Japan **1970**, *28*, 706-716.
[7] C. Leroux, A. Loiseau, D. Broddin and G. van Tendeloo, Philosophical Magazine B **1991**, *64*, 57-82.

O–PS–07

Impact of Mo and disorder on diffusionless transformations in TiAl intermetallic alloys

David Holec[1], Neda Abdoshahi[1], Mohammad Dehghani[2], Andrei V. Ruban[2,3], Martin Friák[4,5,6], Mojmír Šob[5,6,7] and Jürgen Spitaler[2]

[1]Department of Materials Science, Montanuniversität Leoben, Franz-Josef-Strasse 18, 8700 Leoben, Austria, david.holec@unileoben.ac.at
[2]Materials Center Leoben Forschung GmbH, Roseggerstrasse 12, 8700 Leoben, Austria
[3]Royal Institute of Technology, Department of Materials Science, 10044 Stockholm, Sweden
[4]Department of Condensed Matter Physics, Faculty of Science, Masaryk University, Kotlářská 2, Brno 611 37, Czech Republic
[5]Institute of Physics of Materials, Academy of Sciences of the Czech Republic, Žižkova 22, Brno 616 62, Czech Republic
[6]Central European Institute of Technology, CEITEC MU, Masaryk University, Kamenice 5, Brno 625 00, Czech Republic
[7]Department of Chemistry, Faculty of Science, Masaryk University, Kotlářská 2, Brno 611 37, Czech Republic

Introduction

Titanium aluminides have become widely popular for aerospace and automotive applications due to their light weight, favorable mechanical properties and excellent oxidation resistance. To tune the alloy properties to fulfill industrial requirements, many alloying elements are used. In this sense, Mo and Nb are prominent elements as they stabilize the bcc-based phase which allows for hot temperature workability. Recently, a model Ti-Al-Mo alloy has been reported to exhibit martensitic transformation upon rapid cooling [1,2].

Materials and Methods

We employ Density Functional Theory (DFT) as implemented in Vienna Ab initio Simulation Package to perform our first principles calculations. Electron-electron interactions are described on the level of the generalized gradient approximation. The impact of Mo and chemical disorder was studied using a supercell approach and complemented with Green's functions based DFT calculations, using the coherent potential approximation implemented in the Exact Muffin-Tin Orbitals (EMTO) code. The transformation path connecting the bcc-like and hcp-like states shown in Fig. 1 was adapted from that in Ref. [3].

The base structure of interest is bcc-based disordered β-TiAl and its ordered variant β_o-TiAl (B2 structure). Based on the experimentally reported martensitic hexagonal structure, we have considered also the hcp based α-TiAl structure and an ordered hexagonal variant B19-TiAl. Finally, we have included the γ-TiAl (layered, tetragonally distorted fcc structure).

Results and Discussion

The β_o-TiAl structure was shown to be mechanically as well as dynamically unstable [4]. The tetragonal transformation path (so called Bain's path) connects the β_o-TiAl with the most stable γ-TiAl structure with no barrier (Fig. 2). This suggests a thermodynamic driving force of about 0.140 eV/at. for a spontaneous transformation between β_o and γ-TiAl. Similarly, the transformation from β_o to B19 can also proceed without any barrier (Fig. 1), however, experiencing a smaller driving force of approx. 0.095eV/at. [5].

The disordered β-TiAl is still unstable, however, the phonon density of states corresponding to imaginary frequencies is significantly reduced as compared with the ordered variant. This may be interpreted as a stabilizing effect of structural disorder. Also the related energy difference between β and α is significantly reduced signifying stabilizing by disorder. Another transformation path connecting all cubic structures, namely trigonal distortion of a bcc structure along its body diagonal leading to simple cubic and later to fcc structures, was also tested for the β_o to γ. Not only this path exhibits large maxima of over 6 eV/at., but even more importantly, the final structure has different symmetry than the γ-TiAl, caused by the ordering of the binary phase, and therefore can be ruled out from further analysis [6].

Finally, we have also studied the impact of Mo alloying. Fig. 2 shows how replacing Al with Mo (hence leading to Ti-rich compositions) leads to relative stabilization of the β_o with respect to the γ structure (Fig. 2).

In this contribution, we will present details of these transformation paths, interplay between Mo alloying and structural disorder and a detailed comparison with available experimental data.

Fig. 1: Energy landscape for transformation of the ordered B2-TiAl structure to the hexagonal B19-TiAl.

Fig. 2: Impact of alloying Mo on the transformation energetics between the ordered B2-TiAl(Mo) and the L1$_0$ γ-TiAl(Mo) structures.
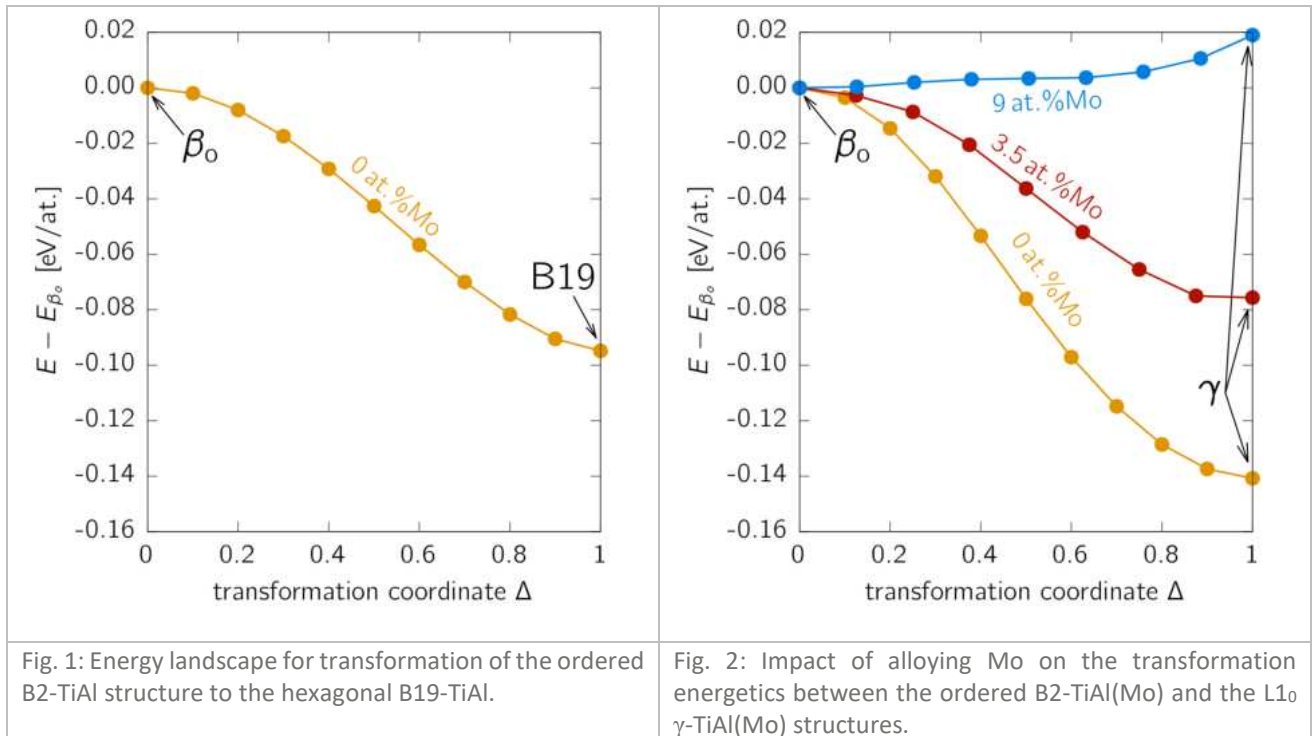
References

[1] M. Musi, P. Erdely, B. Rashkova, H. Clemens, A. Stark, P. Staron, N. Schell, and S. Mayer, Mater. Charact. **2019**, *147*, 398-405.

[2] M. Friák, and M. Šob: Ab initio study of the bcc-hcp transformation in iron, Phys. Rev. B **2008,** *77*, 174117.

[3] S. Mayer, M. Petersmann, F.D. Fischer, H. Clemens, T. Waitz, and T. Antretter, Acta Mater. **2016**, *115*, 242-249.

[4] D. Holec, D. Legut, L. Isaeva, P. Souvatzis, H. Clemens, and S. Mayer, Intermetallics **2015**, *61*, 85-90.

[5] N. Abdoshahi, M. Dehghani, A.V. Ruban. J. Spitaler, D. Holec, in preparation.

[6] N. Abdoshahi, M. Friák, M. Šob, D. Holec, in preparation.

O–PS–08

Phase equilibria and structural investigations in the ternary system Al-Cu-Zn

Klaus W. Richter[1], Ondrej Zobac[2] and Ales Kroupa[3]

[1]Department of Inorganic Chemistry- Functional Materials, Währingerstraße 42, 1090 Wien, Austria, klaus.richter@univie.ac.at

[2]Department of Inorganic Chemistry- Functional Materials, Währingerstraße 42, 1090 Wien, Austria, ondrej.zobac@univie.ac.at

[3]Institute of Physics of Materials AS CR, Zizkova 22, 616 62 Brno, Czech Republic, kroupa@ipm.cz

Introduction

The Al–Cu–Zn ternary system has been investigated intensively in the past because of its technical importance for developing of light-weight alloys. However, several areas of the phase diagram are not well understood and discussed controversially. Our work is focused on several doubtful regions of the phase diagram which have not yet been satisfactorily resolved in the scientific literature and on the divergent results from the experimental and theoretical publications [e.g. 1, 2]. Major topics were the extensions of the γ_1- and γ_2- solid solution phases (with primitive and base-centered brass structures) , the crystal structure and homogeneity ranges of the reported τ and τ' phase fields and the phase boundary of the liquid phase at different temperatures.

Materials and Methods

Samples were prepared from the pure metals by melting them in closed and evacuated silica ampoules with alumina crucibles inside to avoid direct contact with the silica. The annealing times were varied between one day and eight weeks depending on composition and equilibration temperature. The characterization was done by combining dynamic and isothermal standard methods for experimental phase diagram investigation. Phase identification was done by powder X-ray diffraction and crystallographic parameters (including site occupation factors) of specific phases of interest were determined by Rietveld refinements. Single crystal X-ray diffraction was used for structure determination of the τ' phase. Microstructures and phase compositions of long-term annealed samples were determined by scanning electron microscopy in combination with energy dispersive X-ray spectroscopy (SEM-EDX). The temperatures of phase transitions in selected samples were measured by differential thermal analysis (DTA) in evacuated and carbonized quartz glass ampoules. All results are combined with existing literature data to improve the existing thermodynamic model for the Al-Cu-Zn system using a CALPHAD-type thermodynamic assessment.

Results and Discussion

The isothermal sections at 400, 550, 700 and 820°C of the ternary system were studied in detail including the investigation of various samples annealed in the semi-liquid state. The exact mutual solubility between the two γ-brass phases in Al-Cu and Cu-Zn was studied as a function of temperature. As both phases have almost the same diffraction pattern (apart from some very small extra lines in the primitive structure), the determination of the two-phase fields was challenging. However, the corresponding small two-phase field was found at 400°C as well as at 550°C, in principal agreement with the prediction by Liang [2], but much smaller than modelled there (compare Figure 1).

The temperature and composition range of the τ and τ' ternary phases was studied in detail. It turned out that the corresponding composition range is crystallographically complex showing composition areas with cubic CsCl-type structure (τ) and a related rhombohedral structure type (τ') and an intermediate composition range with apparently incommensurate modulation. For the two commensurate composition range a constituent defect mechanism was developed based on Rietveld refinement results. The thermodynamic model for the τ/τ' phase range is selected according to those refinement results.

Combining the results from SEM-EDX and XRD, the complete description of four isothermal sections of the Al-Cu-Zn phase diagram was proposed.

The ternary phase diagram Al-Cu-Zn is reassessed by the CALPHAD approach. The assessment is based on published experimental data [2] and on our new experimental results. The liquid phase is remodeled for better agreement with the experimental results. We use a four-sublattice model for γ_AlCu and γ_CuZn phases and nonstoichiometric models for τ and τ' ternary phases which corresponds better to their structure.
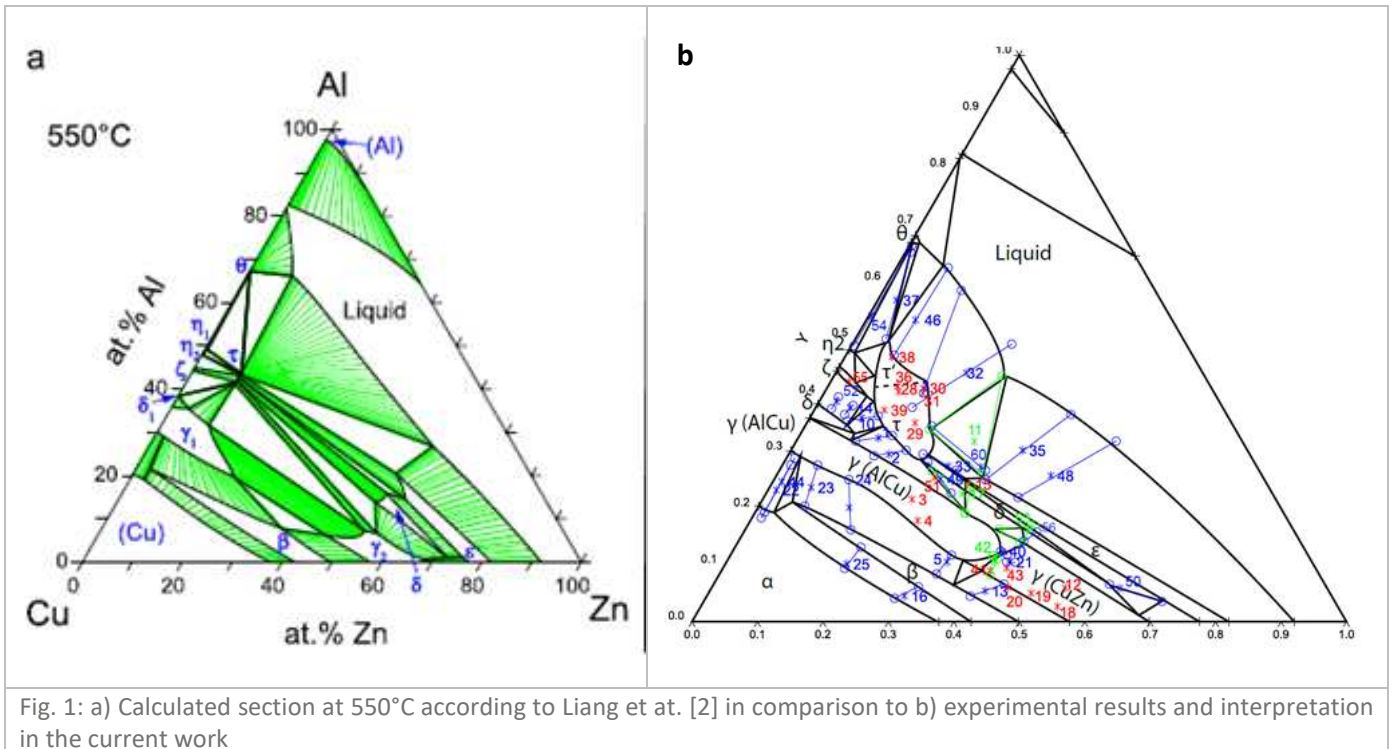
Fig. 1: a) Calculated section at 550°C according to Liang et at. [2] in comparison to b) experimental results and interpretation in the current work

References

[1] G. Ghosh, J.van Humbeeck, P. Perrot, Al–Cu–Zn ternary phase diagram evaluation, Ternary Evaluations, MSI, Materials Science, International Services GmbH, Stuttgart, **2004**.

[2] S.M. Liang, R. Schmid–Fetzer, Thermodynamic assessment of the Al–Cu–Zn system, Part III: Al–Cu–Zn ternary system, CALPHAD. **2016**, *52*, 21–37.

O–PS–09

Massive transformation in ternary Cu alloys

Stephanie Lippmann, Tobias Kaaden and Markus Rettenmayr

Friedrich-Schiller-Universität Jena, Otto Schott Institute of Materials Research, Löbdergraben 32, 07743 Jena, Germany, stephanie.lippmann@uni-jena.de

Introduction

For solid state phase transformations there are two limiting cases, particularly diffusion controlled and interface controlled transformations (for which the martensitic transformations are the most prominent case). For diffusion controlled phase transformations, only a slight deviation from the local equilibrium at the interface is necessary to drive the interface, but local equilibrium can safely be assumed. The consequence is solute partitioning at the interface and transformation rates that are determined by the volume diffusion in the adjacent phases. The diffusionless martensitic transformations proceed with ultrasonic speed. Somewhere in between the two limiting cases is the massive transformation: similarly as the martensitic transformation it is concentration invariant, but diffusion nearby the migrating interface is frequently postulated [1,2]. There are numerous alloy systems in which massive transformation occurs, and for each system the transformation rate is different [3]. Massive transformation is limited to a small range of initial compositions and undercoolings. The aim of this work is the investigation of the effect of alloying Al to binary Cu-Zn alloys on the occurrence and the kinetics of massive transformation.

Materials and Methods

For massive transformation both cooling rate and composition need to be in a relatively narrow range. Theoretically, calculated phase equilibria can be used to identify a concentration range that is common to the two phases involved in the transformation; practically, the precision of the thermodynamic description is generally insufficient if tenths of a percent are relevant. In this work, samples with suitable concentration profiles, particularly diffusion couples and diffusion multiples, are employed in order to identify favorable conditions in the quenching experiments. For more details on e.g. the experimental set-up (in-house made diffusion capsule) or the microstructure of the sample prior to quenching see Ref. [4]. From the diffusion couples and multiples, plate shaped samples were cut, heated to the single phase region and subsequently quenched in ice brine. An alternative experimental method is rapid heating using a new in-house developed pulse heating device. The cooling or heating curves were recorded using thermocouples or an infrared camera. The microstructures are analyzed using light and electron microscopy, the solute concentration profiles are measured using EDX analysis.

Results and Discussion

Microstructures after quenching in iced brine are shown in Fig.1, they consist of two phases (α and β). The Zn concentration in the samples increases from left to right. The sample in Fig.1a is free of Al, the sample in Fig.1b has a uniform Al concentration of 0.5wt.%. In both samples, the α-Phase has two different morphologies. At lower Zn concentrations, there are large α–grains that coarsened during diffusion welding. Between the coarse-grained α und the β phase, α phase with blocky morphology has formed during quenching, typical for massive transformation. Comparing the extension of the massively transformed "α_m" in Fig.1a and b, it is clearly visible that the α_m volume decreases with the addition of Al. In the frame of the work documented in detail in Ref. [4], it is shown that a further increase of the Al concentration leads to a further decrease of the massively transformed zone. Combining recorded quenching rates and calculated phase equilibria, it was shown that the rate of massive transformation decreases with increasing Al concentration as well.
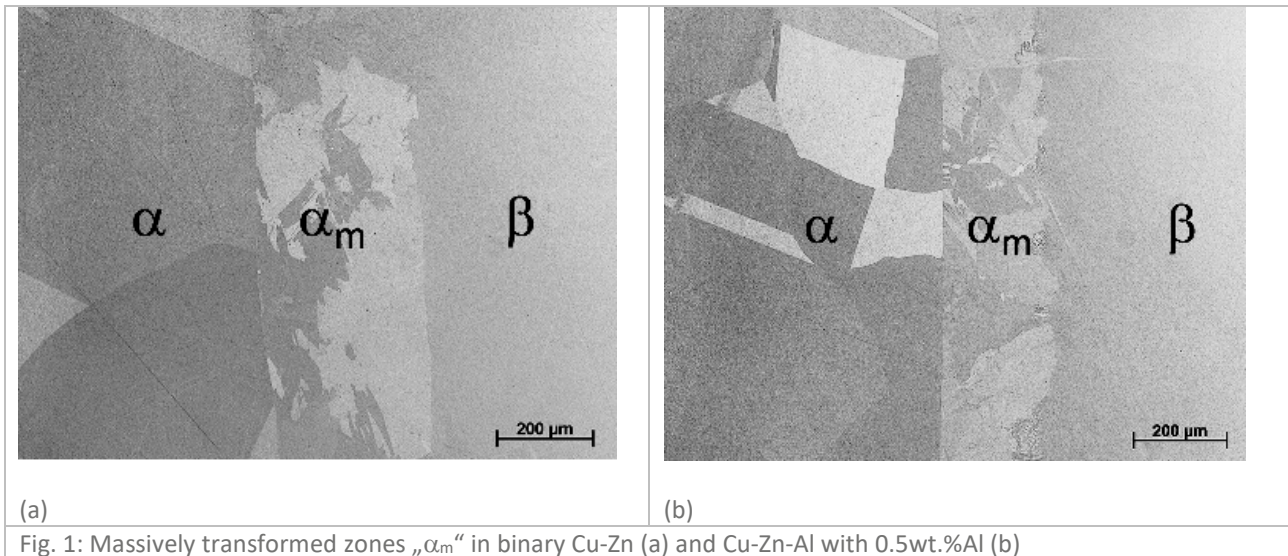
Fig. 1: Massively transformed zones „α_m" in binary Cu-Zn (a) and Cu-Zn-Al with 0.5wt.%Al (b)

For discussing the influence of Al on the kinetics of massive transformation, the complexity in multicomponent systems (see e.g. ref. [5]) and interface thermodynamics [6] need to be considered. In binary systems there is a well-defined tie-line for a given temperature, whereas in multicomponent systems the relevant tie-line that is selected by the migrating interface is the one that leads to consistency of interface velocity and solute fluxes in both phases in the vicinity of the interface. The adjustment of the tie-line will lead to different concentration gradients of the solute elements in front of the interface and thus influence the interface velocity. This may be responsible for the different widths of the massively transformed zones in Fig. 1. Another possible reason is that the addition of Al reduces the part of the total driving force that drives the interface migration. If the total driving force is available to drive the interface (parallel tangent construction to the Gibbs free energy curves), the migrating interface reaches its highest possible velocity. In the present case, this may not be the case, even though the Al concentrations are so low that the phase equilibria do not differ significantly. However, during massive transformation there is energy dissipation inside the interface due to "trans-interface diffusion", i.e. the adjustment of chemical potentials of the species that consumes a part of the total driving force. The addition of Al increases the energy dissipation due to trans-interface diffusion, and only a part is available for driving the interface migration which causes the interface to slow down.

In summary, an efficient method to determine suitable concentrations for massive transformation in multicomponent system is presented. The influence of the addition of Al on the transformation rate in Cu-Zn alloys is quantified. A decrease in the transformation rate upon alloying with Al is discussed considering the increased complexity of multicomponent systems and interface thermodynamics.

References
[1] T.B. Massalski, J.H. Perepezko: Scripta Metallurgica. **1975**, *6*, 743-752.
[2] M. Hillert: Metallurgical Transactions **1984,** *15,* 411-419.
[3] J.H. Perepezko: Metallurgical Transactions. **1984**, *A15*, 437-447.
[4] S. Lippmann, T. Kaaden, P. Wutzler, M. Rettenmayr: submitted.
[5] A. Borgenstam, A. Engstrom, L. Höglund, J. Ågren: Journal of Phase Equilibria and Diffusion **2000**, *21*, 269-280.
[6] M. Hillert, M. Rettenmayr, Acta Materialia. **2003**, *51*, 2803-2809.

O–IT–07

Additive manufacturing of Ti-48Al-2Cr-2Nb alloys

Hiroyuki Y. Yasuda[1], Ken Cho[2], Mitsuharu Todai[3], Minoru Ueda[4],

Masao Takeyama[5] and Takayoshi Nakano[6]

[1]Division of Materials and Manufacturing Science, Graduate School of Engineering, Osaka University, 2-1, Yamada-oka, Suita Osaka 565-0871, Japan, hyyasuda@mat.eng.osaka-u.ac.jp

[2]Division of Materials and Manufacturing Science, Graduate School of Engineering, Osaka University, 2-1, Yamada-oka, Suita Osaka 565-0871, Japan, k_cho@mat.eng.osaka-u.ac.jp

[3]Department of Environmental Materials Engineering, Institute of Niihama National College of Technology, 7-1 Yagumo-cho Niihama, Ehime 792-8580, Japan, todai@mat.niihama-nct.ac.jp

[4]Metal Technology Co. Ltd., Harmony Tower 27F, 1-32-2 Honcho, Nakano-Ku, Tokyo 164-8721, Japan, mueda@kinzoku.co.jp

[5]Department of Materials and Engineering, School of Materials and Chemical Technology, Tokyo Institute of Technology, 2-12-1 Ookayama, Meguro-ku, Tokyo 152-8550, Japan, takeyama@mtl.titech.ac.jp

[6]Division of Materials and Manufacturing Science, Graduate School of Engineering, Osaka University, 2-1, Yamada-oka, Suita Osaka 565-0871, Japan, nakano@mat.eng.osaka-u.ac.jp

Introduction

Titanium Aluminides (TiAl) with excellent strength-to-weight ratio are expected to be a potential candidate for low pressure turbine of aircraft jet engine. Recently, TiAl low pressure turbine blades fabricated by casting and hot forging were installed in GEnx and PW1100G-JIM engines, respectively [1]. However, TiAl is so active that contamination from crucible and oxidation can be of significant concern. More recently, additive manufacturing has attracted much attention since the process can easily build 3D objects with arbitrary shape [2]. In particular, electron beam melting (EBM) is favorable for the fabrication of TiAl turbine blade since it's mold-free and done in vacuum. It is interesting to note that the EBM process can control not only the macroscopic shape but also the microstructure of TiAl alloys, which is closely related to the temperature distribution during the process. Moreover, the microstructure formed under an optimum condition is suitable for room temperature ductility of TiAl alloys [3-5]. In this paper, we report our recent understanding of the microstructure and mechanical properties of TiAl alloys fabricated by EBM process.

Materials and Methods

Ti-48Al-2Cr-2Nb (at.%, 48-2-2) raw powder of which average diameter is approximately 100 μm was prepared by Ar gas atomization process. Cylindrical rods (10 mmϕ x 90 mm) of 48-2-2 alloys were fabricated by EBM machine (Arcam A2X) operated at 60 kV. The angle (θ) between the building and cylinder directions was set to 0°, 45° and 90°. The detail of the fabrication process is well described in our previous papers [3-5]. Microstructure of the alloys was observed using an optical microscope (OM) and a scanning electron microscope (SEM). Tensile tests were performed at ambient and high temperatures at a strain rate of 1.7×10^{-4} s^{-1}. Fatigue tests were conducted at room temperature and 750°C with a frequency of 10 Hz. A minimum creep rate of as-built samples was measured at 760°C and at 105 MPa.

Results and Discussion

Microstructure of 48-2-2 alloys built by EBM depends strongly on the process parameters such as beam current, scanning speed, scanning pitch, and so on. At high energy input, fine lamellar structure composed of Ti_3Al (α_2) and TiAl (γ) phases is formed. On the other hand, near-γ structure is observed at low energy input. This is because temperature distribution around melt pool reflects the energy density of the EBM process. It is also interesting to note that at an optimum fabrication condition, a layered structure consisting of the duplex-like structure and the equiaxed γ grains, which is perpendicular to the building direction, can be seen in as-built samples (Fig. 1). The chain of the γ grains is terms as "γ band". It is well known that the microstructure of Ti-rich TiAl alloys changes with decreasing annealing temperature in the following order: full lamellar, near-lamellar, duplex and near-γ structure [1]. Temperature distribution around melt pool and cyclic feed/fusion of the powder layers during the EBM process cause the formation of the layered structure [3].

Mechanical properties of TiAl fabricated by the EBM process are dependent on the layered structure. At θ = 45°, shear deformation occurs parallel to the γ band, which leads to the improvement of room temperature ductility [3]. For instance, a tensile elongation at room temperature exceeds 2.5% at an appropriate condition, even without hot isostatic pressing (HIP). Moreover, the width of the γ bands and the size of the γ grains also influence the ductility at room temperature. At room temperature, fatigue strength at θ = 0° is lower than that of the cast alloys with HIP process. In contrast, the specimens built at θ = 45° exhibit superior fatigue properties at room temperature even in as-built state. Anisotropy in the tensile elongation and the fatigue properties of as-built samples becomes insignificant with increasing temperature. HIP process can eliminate pores formed during the EBM process and is effective in the improvement of

fatigue properties, especially at high temperatures. With respect to creep properties, a minimum creep rate at 760°C is comparable to that of cast alloys and is independent of θ.

The microstructure of 48-2-2 alloys, developed in large samples (e.g. turbine blade), is sometimes inhomogeneous depending on the temperature distribution during the EBM process. Thus, in order to get the homogenous microstructure by the EBM process, the process parameters should be changed for each location. It is also noted that 48-2-2 turbine blades built at θ = 45° demonstrate large tensile elongation (>2%) at room temperature.
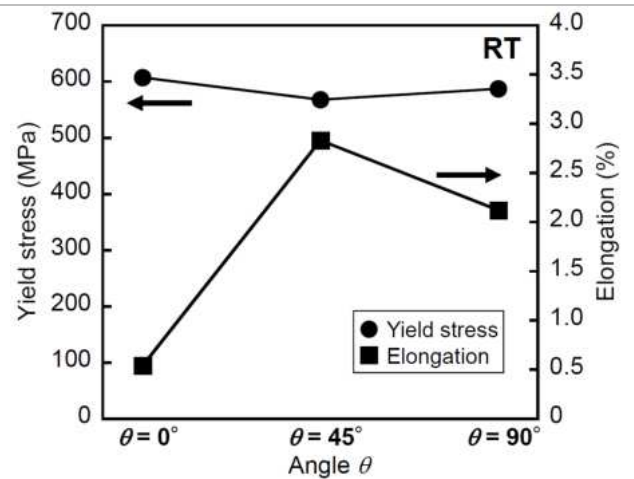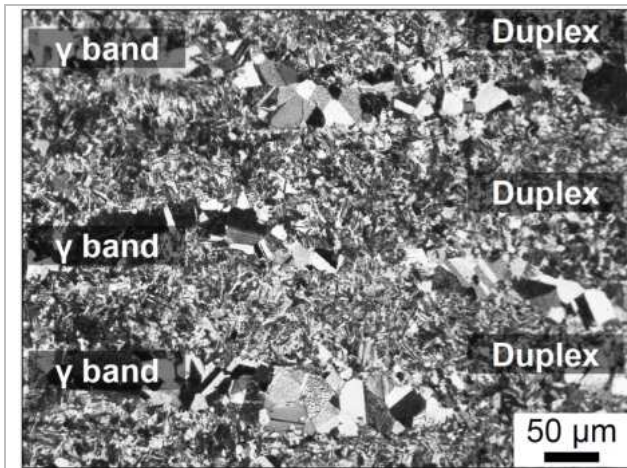
Fig. 1: Layered structure formed during the EBM.	Fig. 2: Dependence of mechanical properties on θ.

References

[1] Y.-W. Kim, JOM, **1994**, *46*, 30–39.

[2] D. Herzog, V. Seyda, E. Wycisk, C. Emmelmann, Acta Materialia, **2016**, *117*, 371–392.

[3] M. Todai, T. Nakano, T. Liu, H.Y. Yasuda, K. Hagihara, K. Cho, M. Ueda, M. Takeyama, Additive Manufacturing, **2017**, *13*, 61–70.

[4] K. Cho, R. Kobayashi, J. Y. Oh, H. Y. Yasuda, M. Todai, T. Nakano, A. Ikeda, M. Ueda, M. Takeyama, Intermetallics, **2018**, *95*, 1–10.

[5] K. Cho, R. Kobayashi, T. Fukuoka, J. Y. Oh, H. Y. Yasuda, M. Todai, T. Nakano, A. Ikeda, M. Ueda, M. Takeyama, Materials Science Forum, **2018**, *941*, 1597–1602.

O–TA–09

Production and properties of gas atomized TiAl powders

Karin Ratschbacher[1], Janny Lindemann[2], Melissa Allen[1] and Volker Güther[1]
[1]GfE Metalle und Materialien GmbH, Nuremberg, Germany
[2]GfE Fremat GmbH, Brand-Erbisdorf, Germany

Introduction

Advances in Additive Manufacturing (AM) of TiAl components by powder bed fusion technologies or blown powder technologies based on EBM (Electron Beam Melting), SLM (Selective Laser Melting) and LMD (Laser Metal Deposition) has led to an increase in demand of spherical TiAl powders. Among the applicable atomization technologies, the EIGA processing (Electrode Induction Gas Atomization) provides a reasonable set of melting and atomizing parameters for adjusting the resulting particle size distributions to the different AM technology needs.

Materials and Methods

TiAl based ingots are being produced via single step VAR processing (Vaccum Arc Remelting) from Ti sponge, Al and masteralloys. The ingots are remelted and effectively homogenized in a VAR Skull Melter followed by centrifugal casting in permanent moulds [1] to cylindrical EIGA electrodes (see Figure 1). The diameter of such electrodes is typically in the range between 50 mm and 80 mm, mainly depending on TiAl alloy composition and resulting processing capabilities for both electrode manufacturing and gas atomization. The EIGA processing principle is shown in Figure 2. The crucible free melting procedure saves energy and prevents very effectively the pick-up of metallic or ceramic impurities.

Fig. 1: Centrifugally cast EIGA electrodes for gas atomization
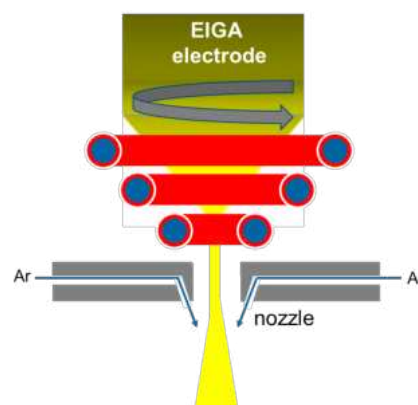
Fig. 2: Sketch of EIGA process

Melting, gas atomization, screening via vibrating tumbling sieving and packing into sealed plastic cans is done under controlled Argon atmosphere in order to minimize the pick-up of gaseous impurities, particularly of oxygen and nitrogen.

Results and Discussion

Chemical analysis is based on XRF (alloying elements), ICP (metallic impurities) and LECO combustion (gases). The conversion process of the as-cast EIGA electrodes to powder does not have any influence on the chemical composition. An effective and approved recycling technology based on ISM (Induction Skull Melting) allows to convert electrode remains and oversized powder fractions into new EIGA consumable electrodes. This will lead to remarkable cost savings in case of large-scale industrial powder production.

Physical powder properties such as sphericity, Ar porosity, particle size distribution, apparent density and flowability depend on gas atomization parameters namely the nozzle diameter, the Ar flow rate, the TiAl melt rate and the corresponding shape of the induction coil. Within a given frame it is possible to adjust the atomizing parameters to different requirements on the particle size distribution in order to optimize specific powder yields to subsequent processing via MIM, SLM, LMD or EBM. Figure 3 shows the typical shapes of EBM and SLM TiAl powder received by EIGA processing.
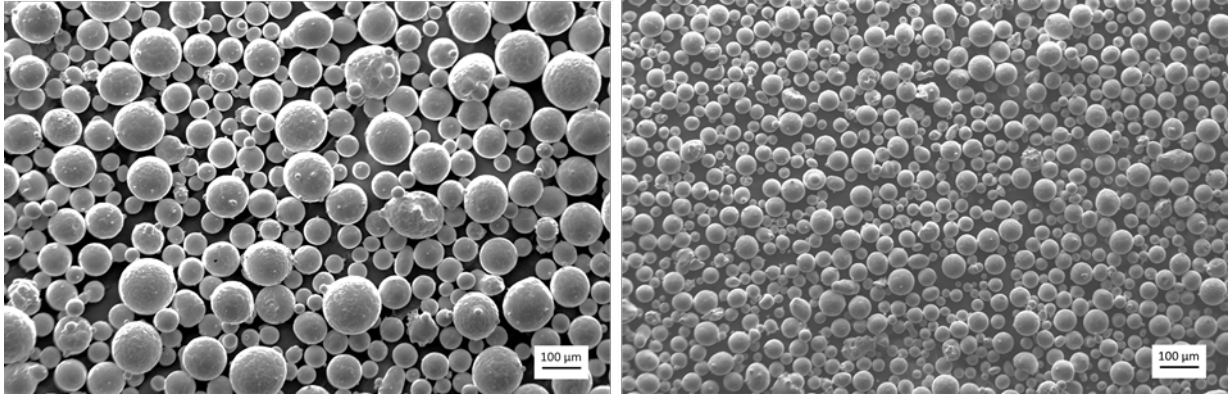
Fig. 3: SEM micrographs of EIGA TiAl powders exhibiting typical particle size distributions for EBM (right) and SLM (left)

Next steps

The fast-growing demand for spherical TiAl powders requires further efforts for technology improvements. One of the key steps to increase the productivity is to enlarge the electrode diameters without decreasing specific powder yields. Target is to balance the pouring capability of EIGA electrode production with the melting capability in the EIGA furnace.

References

[1] V. Güther, M. Allen, J. Klose, H. Clemens, Metallurgical Processing of Titanium Aluminides on Industrial Scale, Intermetallics 103, **2018**, 12-22.

[2] V. Güther, K. Ratschbacher, J. Lindemann, Manufacturing of TiAl Powders Based on Electrode Induction Gas Atomization, presentation at the Titanium Europe **2019**, 13-15th May 2019, Vienna, Austria.

O–TA–10

Processing TiAl via a new production route – additive manufactured (SEBM) and hot isostatic pressed near net shape capsule

Julia Bieske[1], Martin Franke[2], Carolin Körner[3] and Martin Schloffer[4]

[1]Neue Materialien Fürth GmbH, 90762 Fürth, Germany, julia.bieske@fau.de
[2]Neue Materialien Fürth GmbH, 90762 Fürth, Germany, martin.franke@nmfgmbh.de
[3]Neue Materialien Fürth GmbH, 90762 Fürth, Germany, carolin.koerner@fau.de
[4]MTU Aero Engines AG, 80995 Munich, Germany, martin.schloffer@mtu.de

Introduction

γ-TiAl-based alloys are considered for high-temperature applications due to low density (3.9 - 4.2 g/cm^3), high specific yield strength, good oxidation resistance, and good creep properties up to high temperatures [1–4]. The major application of γ-TiAl is in jet engines, where weight savings and their resistance to titanium fire are key advantages [2]. Several manufacturing techniques for turbine blades from TiAl are available: casting, forging, PM (powder metallurgy), and SEBM (selective electron beam melting) [2]. One drawback of additive manufacturing is selective evaporation especially of Aluminum. Compared to raw material (powder), additively manufactured components show locally (layer wise) reduced Aluminum content which results in inhomogeneous microstructures and properties [5]. A new production route (combination of SEBM and HIP) is investigated to overcome this disadvantage. A near net-shaped, closed capsule is manufactured via SEBM. The capsule contains sintered powder which is fully consolidated via hot isostatic pressing. No selective evaporation takes place for the inner capsule, ensuring a homogeneous microstructure after removing the capsule. Experiences of producing parts from gas atomized (VIGA)TNM by SEBM and hot isostatic pressing (HIP) will be discussed. Further microstructure and mechanical properties of TNM samples, produced via near net shape route, are presented and compared to conventional manufacturing techniques.

Materials and Methods

In this study gas atomized TNM alloy with a nominal composition of Ti-43.5Al-4.0Nb-1.0Mo-0.1B (at. %) and a particle fraction of 45 µm – 125 µm was used. Near net shaped capsules were produced on an A2X SEBM machine from Arcam EBM, a GE Additive Company. The additive manufactured capsule (wall thickness < 2 mm; density > 99.9 %) is necessary for the HIP cycle and can be removed mechanically at the end of the HIP process. Densification of raw material (sintered powder with pack density 50 %) is provided by HIP cycle (100 MPa; 1225 °C; 3 h). Pressure is applied at temperatures above 800 °C (> brittle–ductile transition temperature). Microstructure (light microscope) and mechanical properties (tensile test) of TNM samples are analyzed and an evaluation of the feasibility (current limitations) of the new near net shape capsule production route is carried out.

Results and Discussion

It is possible to produce parts with different levels of complexity via near net shape route. However, the investigations reveal a circular network structure for the inner capsule after HIP. On the surface of powder particles, a shell of nearly lamellar (NL) microstructure (containing large lamellar colonies and only small amounts of globular γ- and β_o-phases) is visible. The inner particle areas show a triplex microstructure (lamellar colonies, globular γ-grains and β-phase with a B2-structure (β_o)). Tensile tests display a reduced ductility for the near net shape route (SEBM+HIP) compared to conventional techniques. With microstructural inhomogeneity (circular lamellar network structure) the ductility is decreased. The reason for this phenomenon is the interaction of powder particles with atmospheric oxygen. If the powder is not handled consistently under inert conditions, oxygen is increasingly applied to the powder surface (poor oxidation resistance) and the formation of large lamellar colonies is provoked. Smarsly et al. [6] assumes beside the lamellar colonies micropores along the shell structure which can reduce the ductility.
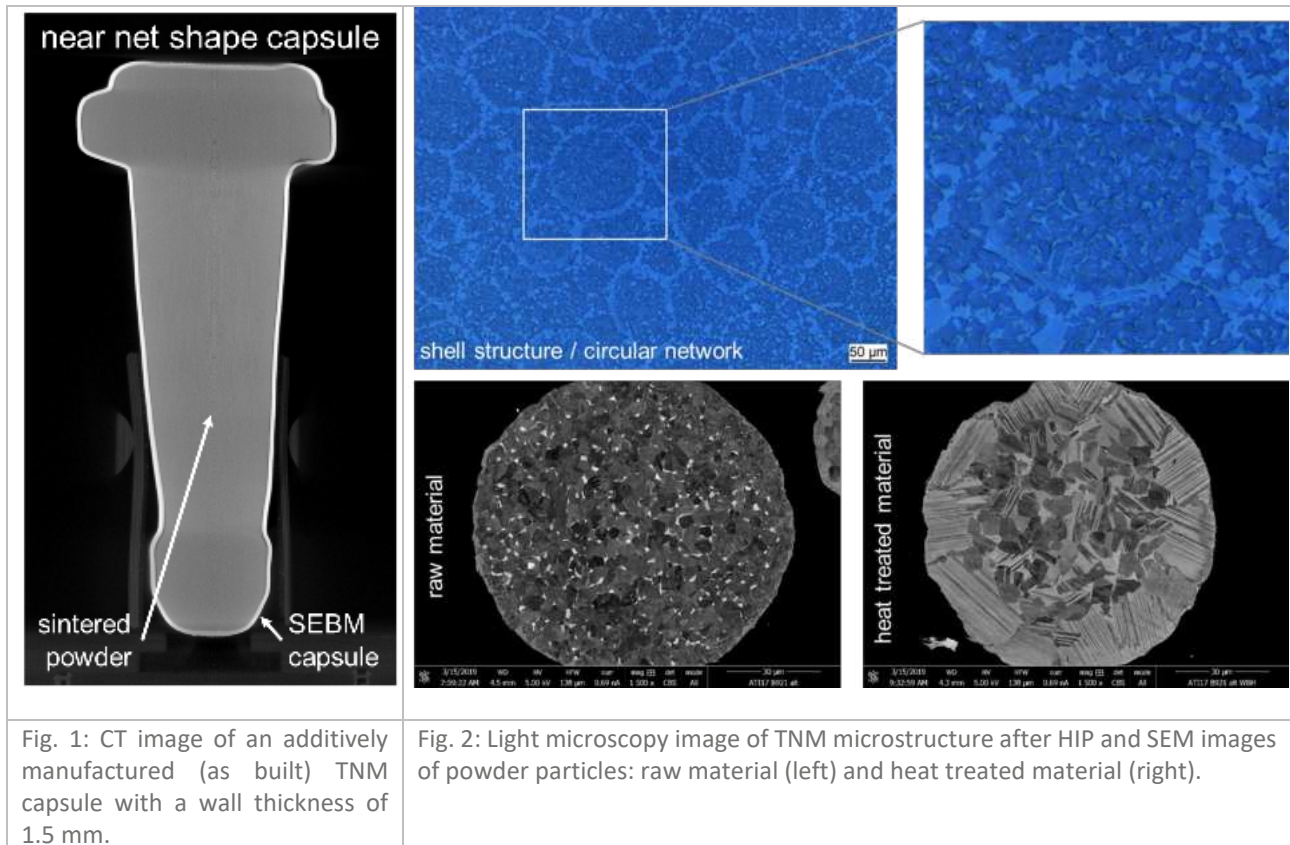
Fig. 1: CT image of an additively manufactured (as built) TNM capsule with a wall thickness of 1.5 mm.	Fig. 2: Light microscopy image of TNM microstructure after HIP and SEM images of powder particles: raw material (left) and heat treated material (right).

References

[1] M. Kastenhuber, T. Klein, B. Rashkova, I. Weißensteiner, H. Clemens, S. Mayer, Phase transformations in a β-solidifying γ-TiAl based alloy during rapid solidification. **2017** Intermetallics, 91, 100–109.

[2] B. P. Bewlay, S. Nag, A. Suzuki, M. J. Weimer, TiAl alloys in commercial aircraft engines. Materials at High Temperatures 33. **2016**, S. 549–559.

[3] H. Clemens, S. Mayer, Design, Processing, Microstructure, Properties, and Applications of Advanced Intermetallic TiAl Alloys. Advanced Engineering Materials. **2013**, 15/4, 191–215.

[4] S. Mayer, P. Erdely, F. D. Fischer, D. Holec, M. Kastenhuber, T. Klein, H. Clemens, Intermetallic β-Solidifying γ-TiAl Based Alloys – From Fundamental Research to Application. Advanced Engineering Materials. **2017**, 19/4, 1-27.

[5] J. Schwerdtfeger, C. Körner, Selective electron beam melting of Ti–48Al–2Nb–2Cr : Microstructure and aluminium loss. Intermetallics, **2014**, 49, 29–35

[6] W. Smarsly, Y. T. Lee, G. Welsch, Microporosity in Hot Isostatically Pressed Ti-6Al-4V Powder Compacts. Metallurgical Transactions A. **1985**, Volume 16A, 1831-1834.

O–TA–11

Characterization of an electron beam melted TNM titanium aluminide alloy

Reinhold Wartbichler, Helmut Clemens, Svea Mayer

Department of Materials Science, Montanuniversität Leoben, Franz-Josef-Str. 18, 8700 Leoben, Austria,

reinhold.wartbichler@unileoben.ac.at

Introduction

Intermetallic γ-TiAl based alloys offer outstanding creep properties, high specific yield strengths and sufficient oxidation resistance at an application temperature range from 600-800 °C and are, owing to these properties, a weight-saving candidate for the substitution of heavy Ni-based superalloys in the aeronautic and automotive sector [1]. The 4th generation process-adapted TNM alloy with a nominal composition of Ti-43.5Al-4Nb-1Mo-0.1B [at.%] is an example for outcomes of long-term research and development that matured into application as a structural material for low pressure turbine blades leading to increased engine efficiencies as well as lower CO_2, NO_x and noise emissions [2]. Electron Beam Melting (EBM), an innovative additive manufacturing technology, allows the production of components with complex geometry, integrated functions as well as decreased lead times and additional weight saving potentials due to topology optimizations [3]. Due to its high processing temperatures EBM is a promising candidate to manufacture titanium aluminide alloys, but suffers from the evaporation of high vapor-pressure elements like Al and the formation of banded microstructures, which may affect the mechanical properties negatively [4,5]. The properties and characteristics of TNM alloys manufactured by EBM are still mostly unknown and were, therefore, addressed in the scope of this work to correlate respective microstructures and material characteristics to the nature of the EBM process.

Materials and Methods

Against this background a 4th generation titanium aluminide alloy with the composition of Ti-42.1Al-4.1Nb-1.0Mo-0.1B (in at. %) was manufactured by EBM using an Arcam A2X machine. Microstructures were examined by visible light as well as scanning electron microscopy. Electron probe micro analysis was employed to gain insights on the present processing-related chemical distributions along the building direction. To study the phase distributions as well as existing orientation relationships electron backscattering diffraction was utilized. Furthermore, X-ray diffraction was applied to establish the phase fractions.

Results and Discussion

The electron beam melted TNM alloy revealed a three-phase microstructure of γ-TiAl, α_2-Ti$_3$Al and β_o-TiAl, which corresponds to the phase equilibrium at the preheating temperature of the EBM process of around 1050 °C (Fig. 1, building direction is upwards). Manufacturing via EBM leads to a processing related loss of Al of around 1.5 at. % due to evaporation. Utilizing electron probe micro analysis made it apparent that Al and the present phases are not homogeneously but rather layer-wise distributed leading to a higher share of γ-phase in Al-rich sections and α_2-Ti$_3$Al taking up a higher phase fraction in Al-depleted zones. The application of electron backscattering diffraction showed that the solidification during EBM of the TNM alloy took place via the β-phase preferably along the [100] direction. The columnar primary β-grain structure is still visible in the orientation maps across several built layers. In addition, a grain selection process is forming a characteristic $(001)_\beta$ fibre texture in building direction. The electron beam melted TNM alloy suffers from processing related Al-evaporation leading to inhomogeneous distributions of its respective equilibrium phases and volume fractions, which can be correlated to the thermodynamic equilibrium at the preheating temperature of the EBM process. The texture and the solidification and phase transformation pathway exhibiting Burgers and Blackburn orientation relationships between the γ-, α_2- and β_o-phase is still present and recallable for the electron beam melted TNM alloy. Therefore, TNM alloys manufactured by EBM combine the characteristics of additively manufactured titanium alloys in terms of pronounced fibre textures with the features of additively manufactured titanium aluminides and their processing related loss of Al and its inhomogeneous distribution.
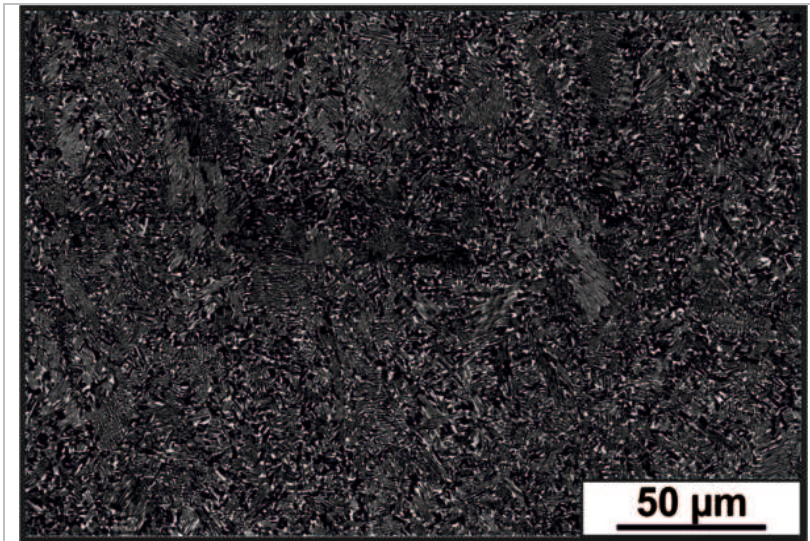
Fig. 1: Back-scattered electrons image of the microstructure of the TNM alloy manufactured via EBM revealing a three-phased microstructure of γ, α_2 and β_o phase.

References

[1] D.M. Dimiduk, Materials Science and Engineering A. **1999**, 263, 281-288.

[2] S. Mayer, P. Erdely, F. D. Fischer, D. Holec, M. Kastenhuber, T. Klein, H. Clemens, Advanced Engineering Materials. **2017**, 19, 1600735.

[3] C. Körner, International Materials Reviews. **2016**, 61, 361-377.

[4] J. Schwerdtfeger, C. Körner, Intermetallics. **2014**, 49, 29-35.

[5] M. Todai, T. Nakano, T. Liu, H. Y. Yasuda, K. Hagihara, K. Cho, M. Ueda, M. Takeyama, Additive Manufacturing. **2017**, 13, 61-70.

O–TA–12

Ingot production, powder atomization and spark plasma sintering of tungsten containing TiAl alloys

Alain Couret[1], Melissa Allen[2], Jean-Philippe Monchoux[1], Florian Pyczak[3], Marcus Willi Rackel[3], Pierre Sallot[4] and Marc Thomas[5]

[1]CEMES, Université de Toulouse, CNRS, 29 rue Jeanne Marvig, 31055 Toulouse, France, alain.couret@cemes.fr
[2]GfE, Metalle und Materialien GmbH, Höfener Straβe 45, Nürnberg, Germany, Melissa.Allen@gfe.com
[3]Helmholtz-Zentrum Geesthacht, Institute for Materials Research, 21502 Gesthacht, Germany, Marcus.Rackel@hzg.de
[4]Safran Tech, Materials & Processes, Rue des Jeunes Bois, Châteaufort, 78114 Magny-Les-Hameaux, France, pierre.sallot@safrangroup.com
[5]ONERA/DMAS, 29 Avenue de la Division Leclerc, BP 72, 92322 Châtillon Cedex, France, marc.thomas@onera.fr

Introduction

During the last decade, the Powder Metallurgy (PM) route has become more widely used to manufacture γ-TiAl components for structural applications at high temperatures owing to the emergence of new processes as Spark Plasma Sintering (SPS) and Additive Manufacturing (AM). In parallel, refractory elements, such as W, Nb, Mo and Ta, have been proved to increase high temperature strength and oxidation resistance of these intermetallic alloys [1]. However, the low diffusivity and high melting point of these elements make the pre-alloyed powder processing more difficult. In this context, the present institutes and companies have joined their efforts to provide some detailed information about the successive steps of this powder production route in the case of the W-containing IRIS-TiAl alloy [2]. The final goal of this project is to provide and secure a PM route in order to produce γ-TiAl alloys containing refractory elements suitable for industrial processing.

Materials and Methods

The material was produced in three steps as described thereafter. First, from WAl_4 master alloys, AlB master alloys, titanium sponges and aluminum, medium size ingots were elaborated by induction skull melting at GfE company [3]. Second, these ingots were atomized using the EIGA process (Electrode Induction Melting Gas Atomisation) at Helmholtz-Zentrum Geesthacht [4]. Finally, the collected and sieved powders were densified using SPS by CEMES at the PNF2 of Toulouse (Plateforme Nationale de Frittage Flash/CNRS of Toulouse, France) [5].
Two chemical compositions given in Table 1 were investigated (called GfE 1 and GfE 2 in the following). Materials were studied after each successive step: ingots, powders and SPS billets.

	Ti	Al	W	B	Nb	Si	C		O
GfE 1	48.80	49.07	1.79	0.08	0	0.14	0.03		730
GfE 2	48.46	48.50	1.79	0.07	0.73	0.27	0.11		1200

Tab. 1: Chemical composition of the GfE 1 and GfE 2 ingots given in at. % for the elements and in ppm for oxygen.

Chemical compositions have been measured by Inductively Coupled Plasma Spectroscopy (ICP), while the microstructures were investigated by using Light and Scanning Electron Microscopies (SEM) and Energy-dispersive X-ray spectroscopy (EDS) in the SEM. Mechanical properties were assessed by tensile tests which were performed at room temperature and at 800°C.

Results and Discussion

The macrostructure of ingots, microstructure of EIGA powders and billets are summarized in Fig. 1. The ingot exhibits a columnar solidification macrostructure with the formation of a central equiaxed area, which laterally extends from the middle to the top of the bar. ICP measurements have shown an excellent chemical homogeneity along the longitudinal axis of the bar. SEM micrographs in back scattered electron mode of the powder particles and SPS billets reveal bright zones and it is tempting to associate those to chemical heterogeneities in terms of tungsten distribution. However, local measurements have demonstrated that the W content in these bright-contrast areas is approximately 1 at.% higher than the average composition. More generally, local chemical analyses have been performed by EDS-SEM to follow the various phase transformations of the material during the whole processing route, as well as to identify the potential species segregations. Tensile tests have shown a limited influence of such heterogeneities on the mechanical properties of the alloy at room and high temperatures.
To elucidate the impact of atomization process on this phenomenon, one particular batch of powder obtained by PIGA atomisation (Plasma Inert-Gas Atomisation) and the resulting SPS material, for which the pre-alloyed material was fully re-melted using a plasma torch before atomisation, will be also presented and analysed in comparison to the EIGA products.
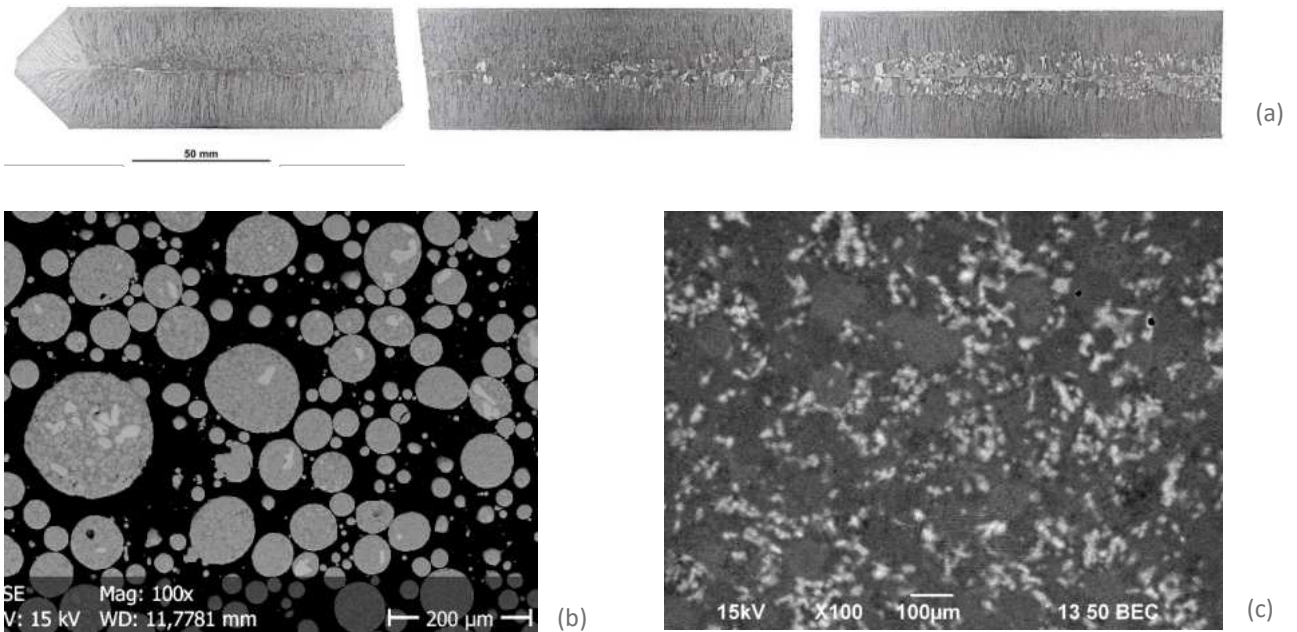
Fig. 1 : Macrostructure of the ingot GfE2 (a) and microstructure of powder particles GfE1 (b) and SPS billets GfE1 (c).

In the discussion section, a description of the various steps of the PM processing route from atomization to densification and an interpretation of the origin of these chemical heterogeneities will be presented and discussed.

References

[1]   F. Appel, J. Paul, M. Oehring: Gamma Titanium Aluminides : Science and Technology, © Wiley-VCH Verla GmbH &Co. KGaA **2011**.
[2]   T. Voisin, J. P. Monchoux, C. Deshayes, M. Thomas, A. Couret, Metallurgical and Materials Transactions 47A, **2016**, 12, 6097-6108.
[3]   V. Güther, M. Allen, J. Klose, H. Clemens, Intermetallics. **2018**, 102, 12-22.
[4]   R. Gerling, H. Clemens, F.P. Schimansky, Advanced Engineering Materials **2004**, 6, 23-38.
[5]   A. Couret, T. Voisin, M. Thomas, J. P. Monchoux, JOM **2017**, 69, 2576-2582.

O–NA–01

Atomistics of self-diffusion in a triple-defect A-B binary system – Monte Carlo simulation

Rafal Kozubski[1], Jan Betlej[1], Piotr Sowa[1], Graeme E. Murch[2] and Irina V. Belova[2]

[1]M. Smoluchowski Institute of Physics, Jagiellonian University, Lojasiewicza 11, 30-348 Krakow, Poland,
rafal.kozubski@uj.edu.pl

[2]Centre for Mass and Thermal Transport in Engineering Materials, School of Engineering, The University of Newcastle,
Callaghan 2308, Australia

Introduction

The present work aims at the determination and detailed analysis of the impact of the tendency for 'triple-defect disordering' (TDD) on self-diffusion of the components in B2-ordering A-B binaries. The simulation study addresses vacancy-mediated atomic migration processes in a B2 superstructure of a TDD system loosely resembling Ni-Al and provides a deep understanding of the diffusion phenomenon which is crucial for any effective development of material technologies. Particular reference to Ni-Al – e.g. by adapting in the model specific relationships between the atomic-jump migration energies yielded by *ab-initio* calculations concerning this system, follows from the fact that the related experimental results, to which the simulation findings might be compared, concern almost exclusively Ni-Al.

Methods

Determination of the equilibrium configurations of the A-B binaries was based on the Schapink model [1] where a lattice gas A-B-V treated as a regular *ternary* system decomposes into two phases: one with the vacancy concentration $C_V \ll 1$ and another (unrealistic) one with $C_V \approx 1$. The lattice-gas phase with $C_V \ll 1$ being in equilibrium with the one with $C_V \approx 1$ is identified with the binary A-B crystal with an equilibrium atomic configuration and equilibrium vacancy concentration. The phase equilibria in the lattice gas were examined using a standard algorithm of Semi Grand Canonical Monte Carlo (SGCMC) simulations.

Vacancy-mediated self-diffusion of A- and B-atoms was simulated by means of the standard Residence-Time KMC algorithm in samples whose atomic and vacancy configurations were formerly equilibrated by SGCMC runs. The self-diffusion coefficients D_X for X-atoms (X = A, B) were evaluated from the standard Einstein-Smoluchowski relationship using the monitored mean-square-distance (MSD) travelled by X-atoms (X = A, B) within the MC-time t.

The evaluated diffusivities were analysed in terms of the dynamics of atomic jumps to vacancies parameterized by independently evaluated average atomic-jump frequencies $w_{\mu \to \nu}^{(X)}$ defined as average numbers of jumps performed by *one X-atom* from μ-sublattice sites to vacancies residing on ν-sublattice sites within a unit KMC-time and by also independently evaluated tracer correlation factors [2]. The average atomic-jump frequencies were expressed in terms of the atom-vacancy pair correlations $C_{XV}^{(\mu\nu)}$ (parameters of the equilibrium configuration) and the associated migration energies (parameters of atomic-jump kinetics).

The system was modelled with Ising-type nn and nnn pair interactions between atoms *and vacancies* and with migration-barrier parameters controlling the heights of the migration barriers encountered by the jumping atoms. The migration barriers were effectively dependent of local atomic configurations.

Results and Discussion

Perfect correspondence between the isothermal composition dependences of the evaluated tracer diffusivities D_X, average atomic-jump frequencies $w_{\mu \to \nu}^{(X)}$ and atom-vacancy pair correlations $C_{XV}^{(\mu\nu)}$ (Fig.1) enabled complete elucidation of the observed macroscopic features of the A- and B-atom diffusivities in terms of the dynamics of elementary atomic jumps.
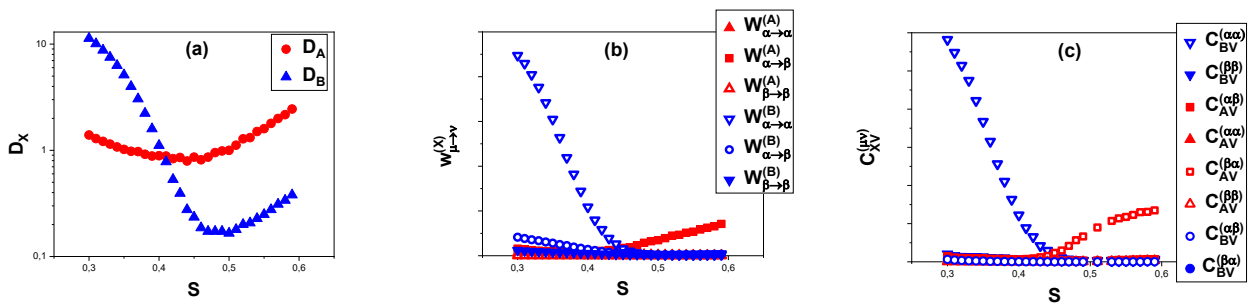
Fig.1. Isothermal concentration dependences of (a) tracer diffusivities D_X; (b) average atomic-jump frequencies $w_{\mu \to \nu}^{(X)}$ and (c) atom-vacancy pair correlations $C_{XV}^{(\mu\nu)}$ evaluated for $A_S B_{1-S}$ binaries.

MC simulation of vacancy-mediated tracer diffusion of the components of a B2-ordering binary systems $A_S B_{1-S}$ showing a tendency for TDD and loosely resembling the Ni-Al revealed that [3]:

- High B(Al)-atom diffusivity in B(Al)-rich binaries is due to enhanced B(Al)-antisite migration via jumps to nnn α-vacancies. The diffusivity strongly increases with increasing B(Al)-atom concentration because of the strong increase of both α-vacancy and B(Al)-antisite concentrations caused by a gradual decay of the system tendency for TDD.
- The isothermal concentration dependence of the B(Al) atom tracer diffusivity definitely shows a 'V'-shape with a minimum at the stoichiometric composition ($S = 0.5$). The atomistic origins of the shape, as well as of the position of the minimum are explained.
- Although the 'V'-shape is observed also in the case of the isothermal concentration dependence of the A(Ni) atom tracer diffusion, its atomistic origin is different. The minimum is located at $S < 0.5$ – away from the stoichiometric composition. This finding might suggest the reason for the discrepancies between the related experimental results.

References
[1] F.W. Schapink, Scr. Metall., **1969,** 3, 113-116.
[2] H. Bakker, in: G. E. Murch and A. S. Nowick (Eds.): Diffusion in Crystalline Solids. Academic Press, Orlando, **1984**, 189-256.
[3] J. Betlej, P. Sowa, R. Kozubski, G.E. Murch, I.V. Belova: submitted to Intermetallics. **2019.**

O–NA–02

Ni tracer grain boundary diffusion in a Ni-base alloy containing a graded microstructure

Sai Rajeshwari[1,2], S. Sankaran[2], Harald Rösner[1], Sergiy Divinski[1] and Gerhard Wilde[1]

[1]Institute of Materials Physics, University of Münster, 48149 Münster, Germany
[2]Department of Metallurgical & Materials Engineering, IIT Madras, Chennai 600036, India

Introduction

The Nickel-base 602CA alloy with an improved corrosion resistance is commercially used in high temperature applications. The presence of copious amounts of chromium carbides in this alloy at the grain boundaries and in the matrix leads to a complex diffusion behavior [1] at high temperatures which demands a detailed understanding of the diffusion mechanisms. At service conditions, the material is often subjected to thermal fatigue, which requires a surface microstructure modification in favor of compressive residual stresses in order to enhance the life time.

In the present work, the diffusion along GB in the 602CA alloy containing a graded microstructure using Ni as a tracer is investigated and carefully compared with a coarse grained microstructure. The graded microstructure is achieved for the alloy 602CA through two routes namely, ultrasonic nanocrystal surface modification (UNSM) [2] and the novel high reduction (per pass) cold rolling (HRCR) [3]. Tracer diffusivity to a depth of 50 µm has been reported to be significantly enhanced due to the presence of non-equilibrium GBs in surface mechanical attrition treated (SMAT) copper in comparison to diffusivities along HAGBs [4]. Similar modifications of grain boundaries probably are expected in the Ni-base alloy, too. However, we will document the importance of phase transitions at the grain boundaries which impact the GB diffusion transport, too.

Materials and Methods

The graded microstructure in the commercial 602CA alloy (Nicrofer® 6025 HT [5]) was generated via the UNSM technique and the HRCR process, respectively. A static load of 20N and 50% dynamic load was used in the UNSM process [2] and a total reduction of 40% by cross-directional HRCR [3] was performed on the alloy sheets. 10 mm diameter discs cut from the treated or coarse grained sheets were used for the radiotracer experiments. Details of the tracer experiments can be found in Ref. [4]. The ^{63}Ni radioisotope was used as a tracer in the present investigation. The penetration profiles measured after annealing at temperatures in the range of 403-873 K for suitable annealing times (t) are plotted in the coordinates of the relative specific activity (which is proportional to the layer concentration, $\bar{c}$) against the penetration depth (y). The diffusion coefficients, D_{gb}, and the triple products, P, were obtained according to Eqs. 1 & 2 under the conditions of the Harisson's C- and B-type kinetic regimes [6], respectively. Below, D_v is the volume diffusion coefficient.

$$D_{gb} = -\frac{1}{4t}\left(\frac{\partial ln\bar{c}}{\partial y^2}\right)^{-1}. \tag{1}$$

$$P = 1.308\sqrt{\frac{D_v}{t}}\left(-\frac{\partial ln\bar{c}}{\partial y^{\frac{6}{5}}}\right)^{-\frac{5}{3}}. \tag{2}$$

Results and Discussion

The penetration profiles measured for the coarse-grained alloy in the B-type regime revealed the existence of two distinct diffusion branches which are characterized as slow, S, and fast, F, diffusion paths. The profiles are analyzed according to Eq. (2) to determine the triple products P_S and P_F, the results are shown in Fig. 1. The triple products of both, the slow and fast diffusion paths exhibit Arrhenius-type temperature dependencies.

The microstrctural investigation revealed the presence of at least two distinct families of GBs, decorated curved GBs and straight GBs. An extended analysis of the penetration profiles and the microstructure allowed to suggest that these two families of the internal interfaces are likely to be the reason for the appearance of the two distinct short-circuit diffusion paths.

The diffusion coefficients D_{gb} measured in the C-type regime exhibit a rather anomalous trend with marginal temperature dependence and strong time dependence of the diffusion coefficients. This behavior in the coarse grained alloy is attributed to the GB phase transitions [7] and incomplete elastic strain relaxation by carbide precipitation at the GBs. The diffusion coefficients determined under these conditions are not material contants and are effective values which depend on the annealing conditions, i.e. temperature and time.

The deformation of pure metals leads to the formation of metastable, deformation-modified GBs [4]. Contrary, the diffusion coefficients D_{gb} measured for deformed UNSM 20N50% alloy (Fig. 1) and the triple products in the case of HRCR are not enhanced with respect to the values determined for the coarse-grained alloy, Fig. 1. Moreover, in the B-type kinetics, the diffusion coefficients in materials with a graded microstructure are even smaller than those for the coarse-grained reference alloy. This behavior indicates a sophisticated interplay of the GB phase transitions (segregation, precipitation) and the deformation-induced modifications of GB structures and phase composition. Detailed microscopic studies are required.
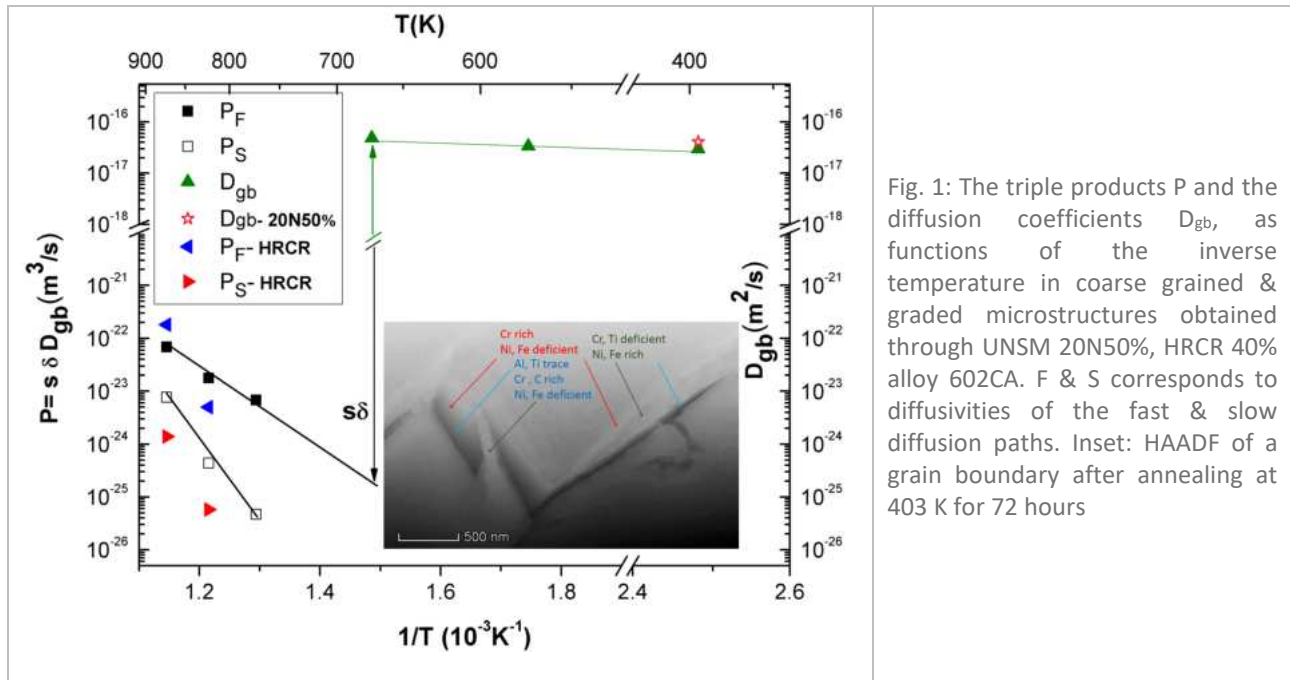
Fig. 1: The triple products P and the diffusion coefficients D_{gb}, as functions of the inverse temperature in coarse grained & graded microstructures obtained through UNSM 20N50%, HRCR 40% alloy 602CA. F & S corresponds to diffusivities of the fast & slow diffusion paths. Inset: HAADF of a grain boundary after annealing at 403 K for 72 hours

References

[1] R. Pillai, H. Ackermann, H. Hattendorf, S. Richter, Corros. Sci. **2013**, 75, 28–37.

[2] A. Cherif, Y. Pyoun, B. Scholtes, J. Mater. Eng. Perform. **2010,** 19, 282–286.

[3] K. Sai Rajeshwari, P. Aditya, J. Rohit, S. Sankaran, I. Samajdar, Vijay K.Vasudevan, Gerhard Wilde: submitted to Materials Characterization, **2019**.

[4] Z.B. Wang, K. Lu, G. Wilde, S. V. Divinski, Acta Mater. **2010**, 58, 2376–2386.

[5] VDM ® Alloy 602 CA Nicrofer 6025 HT, **2017**.

[6] L.G. Harrison, Trans. Faraday Soc., **1961**, 57, 1191.

[7] S.J. Dillon, M. Tang, W.C. Carter, M.P. Harmer, Acta Mater. **2007**, 55, 6208–6218.

O–NA–03

The synthesis and properties of aligned plate intermetallic nanostructures

Philip Nash[1], Kathy Ho[2] and Yang Zhou[3]

[1]Thermal Processing Technology Center IIT, Chicago, IL 60616, USA, nash@iit.edu
[2]Thermal Processing Technology Center IIT, Chicago, IL 60616, USA, kho2@hawk.iit.edu
[3]Shanghai Key Laboratory of Advanced High-temperature Materials and Precision Forming, Shanghai Jiao Tong University, No. 800, Dongchuan Road, Shanghai 200240, China

Introduction

Intermetallic compounds find use in both structural and functional applications. Often such applications require that an intermetallic compound is distributed on a nanostructured scale. Utilizing a discontinuous precipitation transformation a synthesis technique has been developed which produces an aligned plate nanostructure of an intermetallic compound throughout the whole volume. This microstructure may be useful for structural applications. It may also be useful for functional applications particularly through dealloying to produce a large surface area of the intermetallic phase. A great advantage of this processing route is that the functionalized material is still attached to the substrate which can then be used for structural support. This synthesis technique is applicable to any alloy system in which an intermetallic compound can precipitate by a discontinuous precipitation transformation. We will illustrate the technique and present some mechanical property results for the Ni-Co-Al system.

Materials and Methods

The details of the synthesis of the DP structure and the dealloying process have been described previously [1].

Results and Discussion

The results demonstrate that a discontinuous precipitation (DP) transformation, Fig. 1, can go to completion in certain Ni-Co-Al alloys in a range of temperatures typically lower than those used to produce continuous precipitation (CP). At intermediate temperatures the DP transformation is only partial since the driving force is reduced by continuous precipitation ahead of the advancing grain boundary. The product of the precipitation transformations is a nickel solid solution (γ) and an intermetallic phase based on Ni_3Al (γ'). A complete DP structure exhibits higher hardness, yield and tensile strength, but lower ductility than a comparable CP structure, Fig. 2 [2]. The lamellar spacing and volume fraction of intermetallic phase can be controlled through composition and aging temperature. Since the DP transformation is nucleated at grain boundaries the kinetics of the transformation can be greatly accelerated by refining the grain size through cold work and recrystallization.

The lamellar structure produced by DP is typically on the order of 50 to 100 nm spacing. Dealloying the structure, removing the γ phase by electrolytic etching, can produce a nanostructure consisting of γ' plates with voids between them of similar size. This structure has a high specific surface area suitable for functional applications such as catalysis or heat transfer. At the same time the structure is attached to the substrate since the plates are extensive and the structure quite tortuous. Thus the functional surface has a structurally supportive substrate that is produced by a simple processing technique. Although we have demonstrated this synthesis technique using Ni-Co-Al alloys, the technique is applicable to any alloy system susceptible to complete DP transformation. This would allow for the selection of the type of intermetallic phase present at the functionalized surface.

The main difficulty in applying this technique to other systems lies in the fact that the discontinuous precipitation transformation does not have a sound theoretical basis from which one can make predictions. Addressing the problems related to DP almost fifty years ago Hornbogen [3] wrote "*The most important of these problems is the question: in which alloy systems and under which conditions does d.p. occur. In spite of some attempts to find rules, our knowledge is predominantly empirical*". Unfortunately this question still remains to be answered resulting in limiting the application of the proposed technique to systems in which DP has been empirically observed. The comprehensive research performed in this work will provide extensive empirical data that can be used in developing a robust model of the DP transformation.
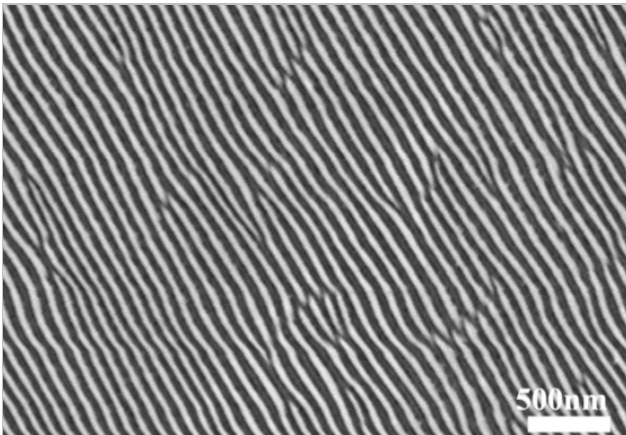
Fig. 1: DP transformation after 40 min aging at 650°C. The light phase is γ'.	Fig. 2: Stress-strain curves for DP, CP and solid solution microstructures of a Ni-49Co-12Al alloy
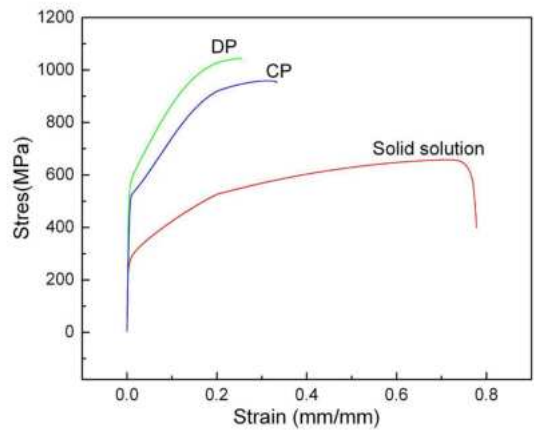
References

[1]   Yang Zhou, Philip Nash, Tian Liu, Naiqin Zhao, Shengli Zhu, Scientific Reports. **2016**, DOI: 10.1038/srep29972.
[2]   Yang Zhou, Fei Zhou, Joao Marcos RibeiroMartins, Philip Nash, Jun Wang, Materials Characterization. **2019**, 151, 612-619.
[3]   E. Hornbogen, Metallurgical and Materials Transactions B. **1972**, *3*(11), 2717–2727.

O–NA–04

In-situ investigations of Mo-rich NiAl-(Cr, Mo) composites by synchrotron radiation diffraction during directional solidification

Camelia Gombola[1], Alexander Kauffmann[1], Ioannis Sprenger[1], Malte Blankenburg[2], Norbert Schell[2] and Martin Heilmaier[1]

[1]Karlsruhe Institute of Technology (KIT), Institute for Applied Materials (IAM-WK), Germany, Camelia.Gombola@kit.edu, Alexander.Kauffmann@kit.edu, Ioannis.Sprenger@kit.edu, Martin.Heilmaier@kit.edu
[2]Helmholtz-Zentrum Geesthacht, Institute of Materials Research, Germany, Malte.Blankenburg@hzg.de, Norbert.Schell@hzg.de

Introduction

During the past decades, investigations have been carried out on materials based on the intermetallic phase NiAl due to its higher melting temperature and thermal conductivity, lower density and excellent high-temperature oxidation resistance as compared to Ni-based superalloys [1]. However, the monolithic intermetallic B2-phase suffers from low creep resistance and insufficient strength at elevated temperatures as well as from poor fracture toughness at room temperature [2]. These disadvantages can be compensated by alloying NiAl with refractory metals such as Mo, Cr, V and Re and applying directional solidification (DS), resulting in the formation of an *in-situ composite* with NiAl matrix and an embedded reinforcing phase [3,4]. Besides the quasi-binary NiAl-34Cr and NiAl-10Mo alloys, NiAl-(34-y)Cr-yMo alloys are well investigated where y is the range between 0 and 6 at.% [5-7]. As the eutectic trough connecting the two (almost) pseudo-binary eutectics [8] has not been fully investigated regarding microstructural evolution so far, we report on the directional solidification of NiAl-xCr-10Mo alloys (0<x<10 at.%) in this contribution. We furthermore focus on in-situ investigations of the microstructural evolution during DS, which were carried out at the High Energy Materials Science beamline (HEMS), operated by Helmholtz-Zentrum Geesthacht, at the PETRA III storage ring at the Deutsches Elektronen-Synchrotron (DESY, Hamburg, Germany).

Materials and Methods

The alloys were produced using an arc-melting device under protective argon atmosphere. Ingots were synthesized from high purity Ni, Al, Cr and Mo (all exhibit a purity of >99.99 %) and re-melted five times to achieve sufficient homogeneity within the samples. The mass loss during arc-melting is less than 0.3 wt.%. Thus, changes in alloy composition by evaporation are negligible. For DS, the alloys were drop-cast into a copper mold of cylindrical shape with 12.5 mm in diameter and 170 mm in length. The casts were directionally solidified using horizontal float zone technique utilizing a single-winding induction coil. The experimental setup was placed at the experimental hutch 3 (EH3) of HEMS where X-ray diffraction in transmission mode at a photon energy of 100 keV was used to investigate the melting zone in-situ during nucleation and growth at the solidification front. Since these mechanisms may be the precursors for crystallographic and morphological texture, the influence of various growth rates, between 18 and 300 mm/h on the microstructural evolution was investigated. Diffraction patterns of each alloy composition and set of parameters were evaluated in terms of orientation relationship and texture appearance. Post mortem microstructural investigations by scanning electron microscopy (SEM) were carried out in order to evaluate the correlation between diffraction based results and microstructural morphology and phase alignment.

Results and Discussion

For as-cast NiAl-xCr-10Mo alloys, it was observed that the fibrous morphology does not change by adding 1.8 at.% Cr to NiAl-10Mo. The volume fraction of the reinforcing phase ((Cr,Mo) solid solution) increases from 12 up to 20 vol.%, which might improve strength, toughness and creep resistance. In contrast, the fibrous morphology of NiAl-34Cr transforms into a lamellar structure by adding 0.6 at.% Mo [8]. A microstructure containing both fibers and lamellae prevail in the alloying range from 1.8 up to 10 at.% Cr whereas even higher amounts of Cr yield in a fully lamellar microstructure. Focusing on fibrous morphology, the first alloy to be tested in-situ was the ternary NiAl-10Mo which serves as reference alloy. An increase in Cr content up to 1.1 at.% Cr, leads to diffraction patterns that exhibit crystallographic texture for all tested withdrawal velocities. Fig. 1 presents a micrograph of the as-cast state of NiAl-0.6Cr-10Mo (Fig. 1a), a sequence of diffraction patterns (Fig. 1b) and a micrograph after DS (Fig. 1c). Both phases solidify simultaneously as evidenced in the diffraction pattern of the solidification front and the occurrence of a preferred crystallographic orientation of the phases is already present in this transition period of solidification. The orientation relationship was found to be the same as in NiAl-10Mo, namely <100>$_{NiAl}$ || <100>$_{(Cr,Mo)}$ and {100}$_{NiAl}$ || {100}$_{(Cr,Mo)}$ which are both aligned parallel to the GD [9,10]. Detailed analysis indicates shifts in Bragg position perpendicular and parallel to GD. Both are suggestive of orientation-depending lattice strain which is caused by the solidification texture as well as the mismatch in CET between the two phases. For the investigated samples, the ratio of lattice parameters $a_{||}/a_{\perp}$ (|| or $\perp$ with respect

to GD) is > 1 for NiAl and < 1 for (Cr,Mo)$_{ss}$, respectively. Accordingly, NiAl is dilated and (Cr,Mo)$_{ss}$ is compressed parallel to GD and vice versa perpendicular to GD.
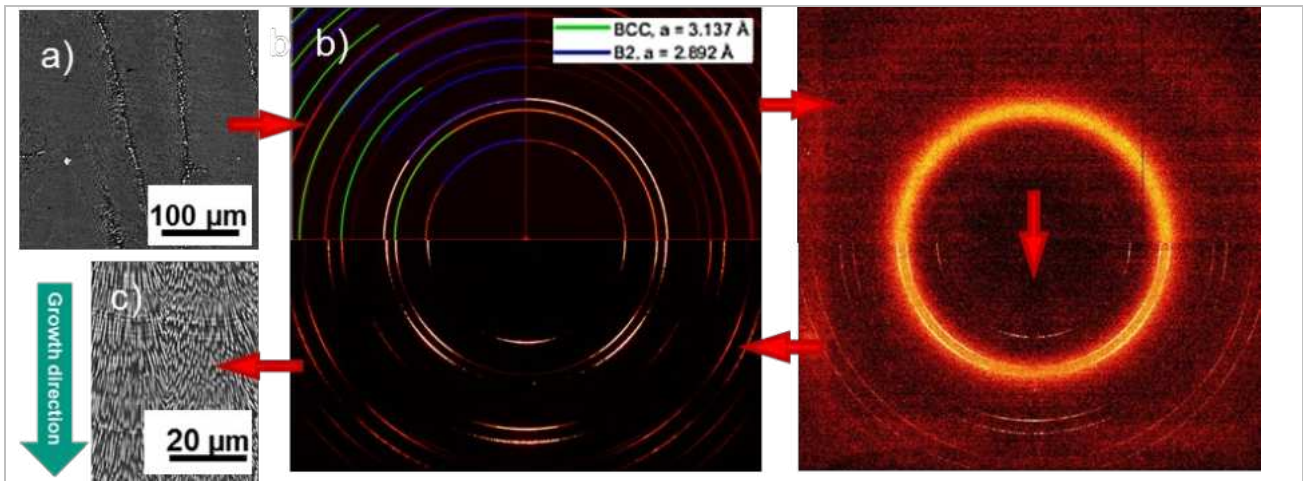
Fig. 1: a) Micrograph (SEM-BSE) of as-cast NiAl-0.6Cr-10Mo. Diffraction patterns of: b) as-cast state (upper left; phases are indicated), entire liquid phase (upper right), b) solidification front (lower right), b) as-DS at RT (lower left), c) Micrograph (SEM-BSE) as-DS.

References
[1]   D.B. Miracle, Acta Metall. Mater. **1993**, 41, 649-684.
[2]   F. Ebrahimi, S. Shrivastava, Acta Mater. **1998**, 461, 493-1502.
[3]   G. Frommeyer, R. Rablbauer, H.J. Schaefer, Intermetallics, **2010**, 18, 299–305.
[4]   J.F. Zhang, J. Shen, Z. Shang, Z.R. Feng, L.S. Wang, H.Z. Fu, Intermetallics, **2012**, 21, 18-25.
[5]   H. Bei, E.P. George, Acta Mater. **2005**, 53, 69-77.
[6]   M. Dudová, K. Kuchařová, T. Barták, H. Bei, E.P. George, C. Somsen, A. Dlouhý, Scripta Mater. **2011**, 65, 699-702.
[7]   D.R. Johnson, X.F. Chen, B.F. Oliver, Intermetallics, **1995**, 3, 99-113.
[8]   J. Peng, P. Franke, H.J. Seifert, Journal of Phase Equilibria and Diffusion, **2016**, 37, 592-600.
[9]   H.E. Cline, J.L. Walter, E. Lifshin, R.R. Russell, Metall. Trans. **1971**, 2, 189-194.
[10] A. Misra, R. Gibala, Intermetallics, **2000**, 8, 1025-1034.

O–NA–05

Effect of thermomechanical treatment on microstructure and mechanical properties of a novel heavily alloyed nickel base superalloy

Valery Imayev[1], Shamil Mukhtarov[1], Alexander Logunov[2], Artem Ganeev[1], Ruslan Shakhov[1] and Renat Imayev[1]

[1]Institute for Metals Superplasticity Problems of Russian Academy of Sciences, Ul Khalturina, 39, Ufa, Russian Federation, vimayev@mail.ru, shamil@anrb.ru, artem@imsp.ru, r.sabbaot@yandex.ru, renat_imayev@mail.ru
[2]PJSC "UEC-Saturn", Pr. Lenina, 163, Rybinsk, Russian Federation, logunov06@rambler.ru

Introduction

Nickel base superalloys are widely used for critical structural components in gas turbine engines (GTE) such as high pressure discs. To improve the fuel efficiency of GTE, it is of great importance to design new Ni-based superalloys to withstand higher operating temperatures and loadings [1,2]. Regarding polycrystalline nickel base superalloys, which are the most competitive from the viewpoint of the production cost, novel nickel base superalloys are designed towards heavier alloying. Particularly, the alloy designing approaches include an increase in the volume fraction of the intermetallic γ' phase precipitates (up to 70%) by increased concentrations of precipitate forming elements [1,2], heavy alloying with elements providing effective substitutional solid solution strengthening and a higher γ' solvus temperature [1-3] etc. In the present study, thermomechanical treatment (TMT) including preliminary heat treatment and canned forging under subsolvus temperatures was developed for the newly designed polycrystalline superalloy SDZhS-15, followed by microstructure characterization and evaluation of mechanical properties. This superalloy has recently been developed by PJSC "UEC-Saturn" (Russia) for turbine disc applications, which is intended for operating temperatures up to 850°C. The mechanical properties in the forged condition are to be compared with those in the cast and heat treated condition. The present paper demonstrates that the superalloy, which might be referred to castable nickel base superalloys, can be successfully forged providing enhanced mechanical properties.

Materials and Methods

The experimental nickel base superalloy SDZhS-15 has the nominal chemical composition Ni-28(Cr,Co)-12.5(Al,Ti,Nb,Ta)-9(Mo,W,Re)-0.17(C,La,Y,Ce,B) (in wt. %). The superalloy ingots with a size of Ø100×180 mm were manufactured by vacuum induction melting. The as-cast ingot was subjected to long-term homogenization in the temperature range of $(T_s\text{-}120) \div T_s$, where T_s is the solvus temperature, followed by solid solution treatment and ageing. This condition (condition 1) was used to evaluate the mechanical properties of the cast superalloy. Before hot forging the as-cast superalloy was subjected to long-term homogenization and heterogenization annealing in the temperature range of $(T_s\text{-}120) \div (T_s\text{+}20)$. The canned forging was fulfilled in a specially designed thick-walled can at subsolvus temperatures under quasi-isothermal conditions to a total strain of $e \approx 1.4$. The forged billet was aged and this condition (condition 2) was used for preparing of samples for mechanical testing. The tensile and long-term strength tests were carried out using flat samples with a gage section of 15×3×1.5 mm^3. The long-term strength was evaluated at T=650°C during 100 h. All samples were prepared by electrospark cutting followed by fine grinding of work surfaces. The microstructure examination was carried out for the cross sections of the forged workpieces using scanning electron microscopy (SEM) in backscattering electron (BSE) mode.

Results and Discussion

Figs. 1 and 2 represent the BSE images of the superalloy in conditions 1 and 2. The cast condition (condition 1) was characterized by a coarse γ grain size (Fig. 1a). The volume fraction of the γ' phase (Ni$_3$(Al,Ti,Nb,Ta)) was defined as about 68%; the γ' phase had a size in the range of 0.1-0.25 μm (Fig. 1b). In the microstructure there were white carbide particles. The canned forging led to development of continuous dynamic recrystallization and microstructure refinement (Fig. 1c) (condition 2). The size of recrystallized γ grains was varied in the range of d=2…60 μm [4]. The microstructure of the forged material contained mostly dispersed γ' precipitates with a size of 0.1-0.3 μm and about 10 vol.% of relatively coarse γ' precipitates with a size of 1-3 μm (Fig. 1c,d). Table 1 represents the mechanical properties of the superalloy in conditions 1 and 2. One can see that TMT led to significant improvement of the mechanical properties. The long-term strength tests carried out for condition 2 at T=650°C and a loading of 1200 MPa revealed that the samples were not fractured during 100 h. The excellent mechanical properties in condition 2 can be explained by a combined effect of the higher amount of the γ' phase, the effective substitutional solid solution strengthening due to heavy alloying with refractory metals, and the refinement of the coarse as-cast structure owing to canned hot forging. The present work demonstrated that heavy alloying of nickel base superalloys with refractory elements including rhenium is not contraindicative for wrought processing. The refined microstructure condition obtained after canned forging and ageing provided superior mechanical properties as compared with those of known disc nickel base superalloys [4].

(a)

(b)

(c)

(d)
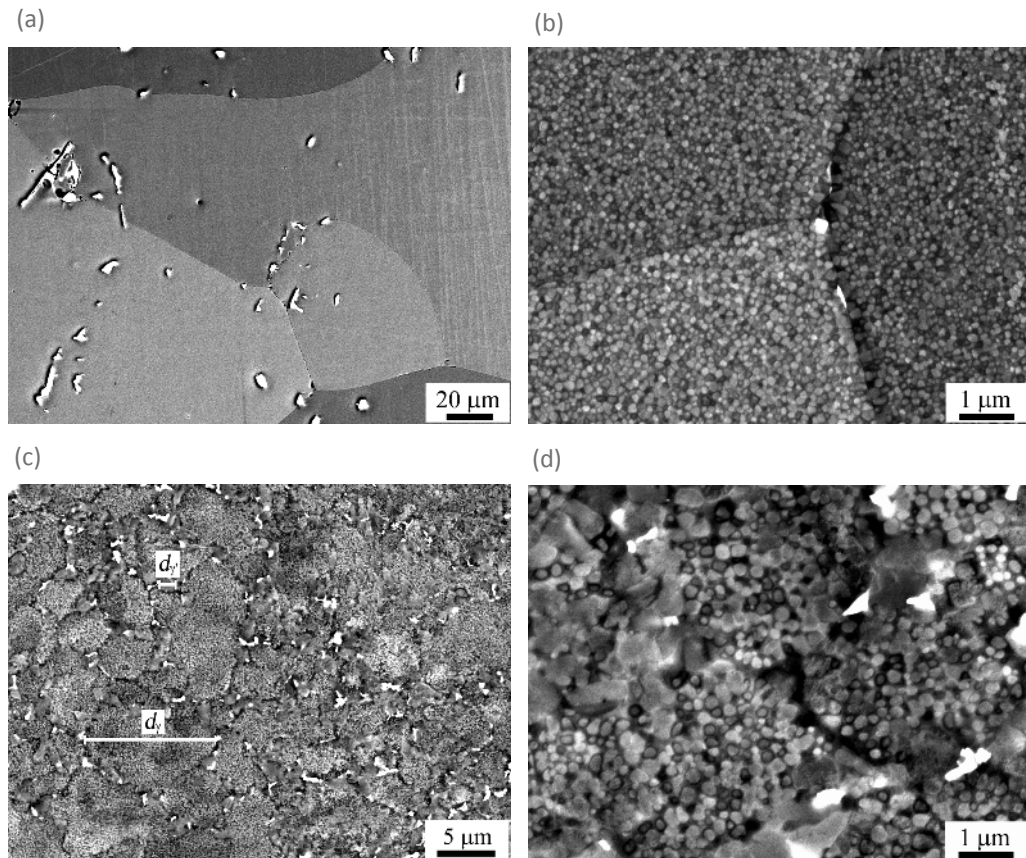
Fig. 1: BSE images of the SDZhS-15 superalloy in conditions 1 (a, b) and 2 (c, d): (b, d) γ' precipitates are coarser in condition 2, (c) a typical recrystallized γ grain and a coarse γ' precipitate are marked.

Table 1: Mechanical properties of the superalloy SDZhS-15 in condition 1 / condition 2

Temperature, °C	YS, MPa	UTS, MPa	δ, %	Long-term strength, MPa
20	1132 / 1355	1255 / 1802	8.5 / 16	T=650°C:
650	1044 / 1310	1198 / 1558	4.4 / 8.5	>1200 (τ=100 h) – condition 1
750	1005 / 1290	1125 / 1462	2.1 / 7	>900 (τ=100 h) – condition 2
850	728 / 1065	733 / 1114	0.9 / 3	

References

[1]   R.C. Reed, The superalloys: Fundamentals and Applications. Cambridge University Press. **2006**.
[2]   M.C. Kushan, S.C. Uzgur, Y. Uzunonat, F. Diltemiz, Recent Advances in Aircraft Technology. InTech Rijeka, Croatia. **2012**, 75-96.
[3]   R.A. Hobbs, S. Tin, C.M.F. Rae, Metall. Mater. Trans. A. **2005**, 36, 2761-2773.
[4]   Sh.Kh. Mukhtarov, V.M. Imayev, A.V. Logunov P.A. et al.: submitted to Mater. Sci. & Technology. **2019**.

O–NA–06

/ v   ] P   ] } v   } (Z   ]]   ˙] v   } ˘]]   ] v P   u } Z   Z] P Z   u
/ v   } v   o   æ

Nicolas Ramenatte, Lionel Aranda, Stéphane Mathieu and Michel Vilasi

Institut Jean Lamour-UMR 7198, University of Lorraine, France, nicolas.ramenatte@univ-loraine.fr,
lionel.aranda@univ-loraine.fr, stephane.mathieu@univ-loraine.fr, michel.vilasi@univ-loraine.fr

/ v }   ] } v

The project FAIR (Additive Manufacturing for the Intensification of Reactors) intends to develop a novel class of micro-reactor/exchanger (MR-E) based on 3D printing manufacture in order to intensify the H_2 synthesis process by steam methane reforming (SMR). The device building takes advantage of the recent metallurgical progress concerning the 3D printing manufacture for creating innovative reactor-exchanger more robust and capable to withstand higher temperature and pressure during application. The success of this project will participate to the extension of the "H_2 mobility" in France.

The Ni-based superalloy was selected as substrate because it present satisfying high temperature mechanical and chemical properties when classically synthesized by melting followed by conventional heat treatments (*dissolution during 1h at 1070°C – precipitation of γ' during 8h at 720°C - precipitation of γ'' during 8h at 620°C*). The as-obtained substrate has the following composition Ni22Cr9Mo4Nb5Fe (values are wt. %) and a homogeneous γ/γ'γ''δ equiaxed microstructure [1]. In oxidizing atmosphere, typically 1000°C in air, this alloy has a satisfying behavior due the formation of a superficial protective chromia scale, but in highly carburizing atmosphere this alloy can suffer from fast degradation named Metal Dusting, so it should be protected by an aluminum reach overlay. The present study allowed characterizing the physico-chemical properties of 3D printed alloys compared to conventional melted alloys (CM). Notably, this study was particularly focused on the evolution of the microstructure of 3D samples during heat treatments and its impact on the chemical reactivity of the alloy during the aluminization and oxidation processes.

D   ] o   v D Z }

The alloys were fabricated by Polyshape [2] via the Selective Laser Melting route *(SLM).* An Inconel 625 powder obtained by gas atomization and having an average diameter of 10 μm was used. Argon was introduced as oxidation shielding gas as well as gaseous powder carrier (P=1bar). Cooling rates as high as 10^7 K/second were reached. Plates with dimensions of 10mm x 8mm x 1mm were realized.

In order to evaluate the effect of microstructure on high temperature oxidation, the as-deposited SLM samples were annealed under inert atmosphere at 1075 °C during 1, 2 and 3h.

The microstructure of the alloys was characterized by microscopy (optical and SEM, TEM) and the crystallographic structure and texture were determined by EBSD.

Oxidation behavior was evaluated under isothermal conditions using standard tests conducted at 1050 ° C for 50 h in a SETARAM TAG1750 symmetric thermobalance. The corrosion products were then analyzed by XRD and microscopy.

Z   o   v   ]   ] } v

Synthesis of 3D printed Inconel 625 via the innovative Selective Laser Melting route (SLM)

At the macroscale, the observations of the surface evidence i) a huge superficial roughness as expected for such materials, ii) the existence of fine spherical particles simply sealed on the surface. The determination of the developed area by confocal microscopy analysis leads to a 40% increase in nominal area.

At the microscale, the characterization of the microstructure shows that the as-deposited substrate was constituted of supersaturated γ grain having the nominal composition of Inconel 625 with heterogeneous grain size. The results of texture analysis by EBSD with pole figure and ODF section at $\phi_2 = 0°$ representation reveal a cube texture ({001}<100>) which means that the grains have a preferential orientation parallel with the building direction <001> (Fig.1a). The determination of internal desorientation for 0° to 15° angle shows a not equilibrated microstructure associated to the high cooling rates during manufacture. That gives rise to recrystallization during a high temperature treatment (Fig.1b). After 2 hours of treatment at 1075°C, the internal orientation significantly decreased (Fig.1c) and the microstructure is completely restructured with development of special boundaries, and the preferential orientation is lost. In parallel, the chemical composition evolution during high temperature treatment of as-deposited substrate has been studied.
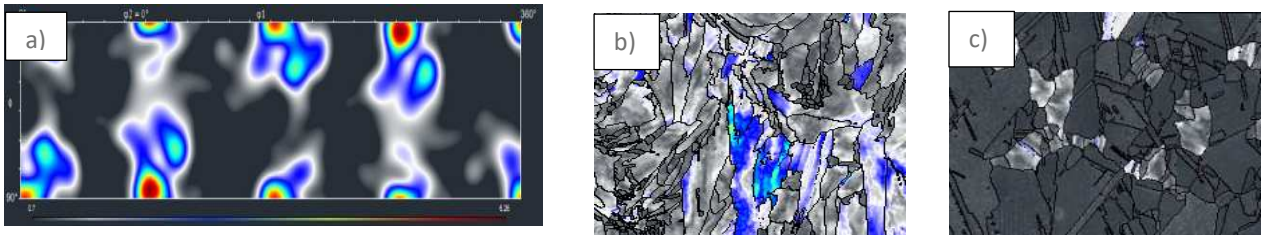
Fig. 1: a) ODF section at φ$_2$=0° that reveals a cube texture ({001}<100>) and internal disorientation of b) as-deposited material and c) after annealed during 2h at 1075 °C [3].

Oxidation behavior at 1050°C in air atmosphere

The 3D printed and CM alloys were oxidized for 50 hours to evaluate the effect of the microstructure on the oxidation rate. It appears that 3D printed alloys, annealed or not, are more sensitive to oxidation: their oxidation rate is roughly twice the oxidation rate of CMA and the Cr_2O_3 superficial layer is inhomogeneous and scarcely adherent (Fig. 2). As a result, a specific slurry process was developed for synthesizing aluminide coatings, homogeneous and adherent. In conclusion, the oxidation resistance of the composite substrate/coating material was dramatically improved.
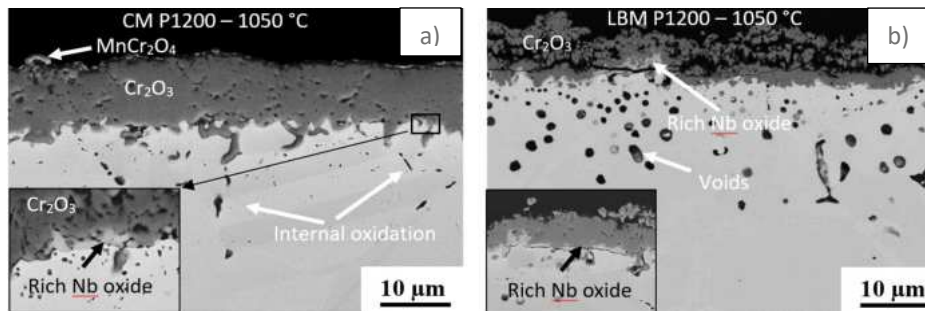
Fig. 2: Microstructure after oxidation of a) CMA and b) 3D printed alloy

References

[1] H.C. Pai, M. Sundararaman, A comparison of the precipitation kinetics of ɣ'' particles in virgin and re-solutioned alloy 625, TMS. **2005**.

[2] Polyshape http://www.poly-shape.com/.

[3] B. Beausir and J.-J. Fundenberger, Analysis Tools for Electron and X-ray diffraction, ATEX - software, www.atex-software.eu, Université de Lorraine - Metz, **2017**.

O–IA–01

Quantum-mechanical study of Fe-Al-based intermetallic compounds

Martin Friák[1], Yvonna Jirásková[1], David Holec[2], Nikola Koutná[3,4], Ivana Miháliková[1,4],
Anton Slávik[1,4], Nadezda Pizúrová[1], Ferdinand Dobeš[1], Petr Dymáček[1], Petr Šesták[1,5,6], Jan Fikar[1],
Sabina Oweisová[1,7], Monika Všianská[8,7,1], Jana Pavlů[8,7,1], Vilma Buršíková[9], Jörg Neugebauer[10] and
Mojmír Šob[7,1,8]

[1]Institute of Physics of Materials, Czech Academy of Sciences, v.v.i., Brno, Czech Republic
[2]Department of Materials Science, Montanuniversität Leoben, Leoben, Austria
[3]Institute of Materials Science and Technology, TU Wien, Vienna, Austria
[4]Department of Condensed Matter Physics, Faculty of Science, Masaryk University, Brno, Czech Rep.
[5]Central European Institute of Technology, Brno University of Technology, Brno, Czech Republic
[6]Faculty of Mechanical Engineering, Brno University of Technology, Brno, Czech Republic
[7]Department of Chemistry, Faculty of Science, Masaryk University, Brno, Czech Republic
[8]Central European Institute of Technology, CEITEC MU, Masaryk University, Brno, Czech Republic
[9]Department of Physical Electronics, Faculty of Science, Masaryk University, Brno, Czech Republic
[10]Max-Planck-Institut für Eisenforschung GmbH, Düsseldorf, Germany

Introduction

Fe-Al-based superalloys represent a promising class of materials with large potential for high-temperature applications. Their mechanical properties can be modified and tuned by adding different intermetallic compounds. To achieve an understanding of the impact of such alloying additions we have performed a systematic theoretical study of intermetallics which form when adding Ti or Co, with a particular focus on Fe_2TiAl and Fe_2CoAl. Our first principles quantum mechanical calculations were performed using the Vienna Ab initio Simulation Package (VASP) [1,2].

Results and Discussion

For Fe_2TiAl, previous theoretical studies showed a large discrepancy between *ab initio* computed magnetic moments of the stoichiometric Fe_2TiAl (about 0.9 μ_B per 4-atom formula unit, f.u., see also our own results in Fig. 1(a)) and experimental ones (0.1 μ_B/f.u.). We show [3] that deviations from the exact stoichiometry towards Fe-rich states have a huge impact on the local magnetic moments and can explain the experimental low magnetic moments (see Fig. 1(b)).
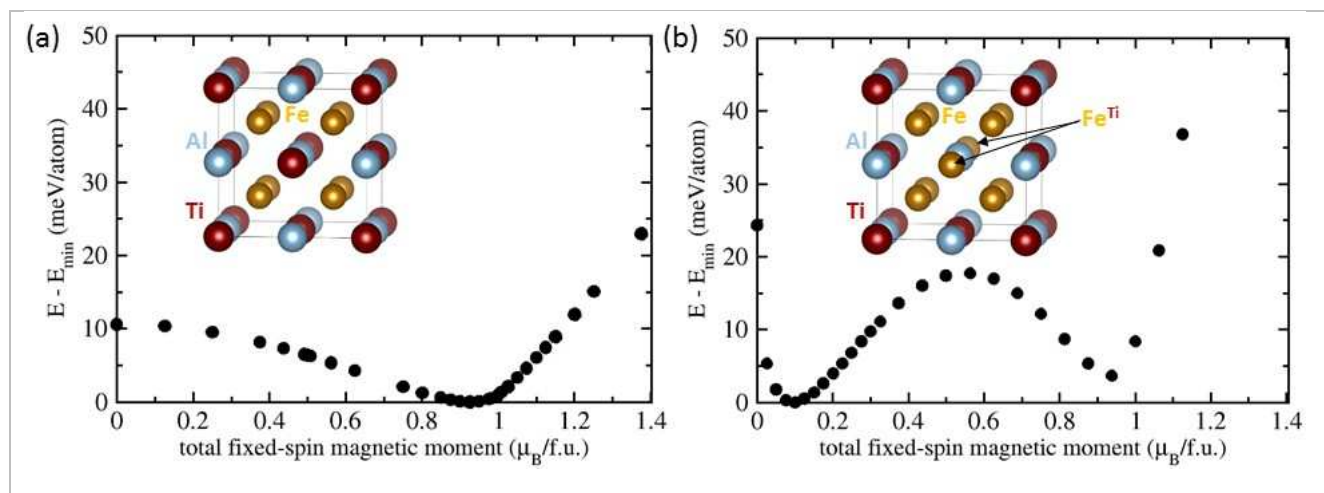
Fig. 1: Quantum-mechanically calculated changes of the energy of (a) stoichiometric Fe_2TiAl and (b) off-stoichiometric $Fe_{2.25}Ti_{0.75}Al$ as functions of the local magnetic moment. The computational supercells used for these calculations are shown in the insets. The off-stoichiometric Fe atoms on the Ti sites (Fe^{Ti}) stabilize a state with a lower magnetic moment - see Ref. [3].
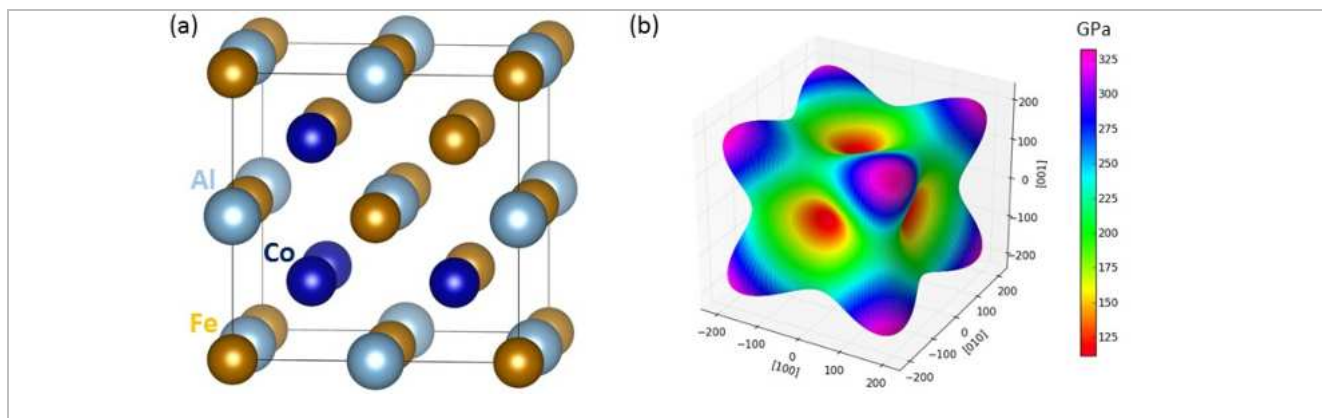
Fig. 2: Our proposed computational model of the stoichiometric Fe_2CoAl compound (a) which accurately reproduces the experimentally observed distribution of atoms in the 2nd nearest neighbor shell of Co atoms [4]. Part (b) visualizes the computed directional dependence of the Young's modulus (see Ref. [5]).

For Fe_2CoAl, previous quantum-mechanical calculations considered either full or inverse Heusler structure. However, experimental data [10] indicates that there are 3 Fe and 3 Co atoms in the 2nd nearest neighbor shell around Co atoms, implying a structure very different from the assumed one. We therefore propose a new computational model (see Fig. 2(a)) in accordance with the experimental data and determine structural, magnetic and elastic (see Fig. 2(b)) properties of this atomic configuration [5].

As a complement to our theoretical research (see also our other results in Refs. [6-8]) we have performed an experimental investigation of Fe-Al-based materials (these results are in Refs. [9-12]).

References
[1] G. Kresse and J. Hafner, Phys. Rev. B. **1993**, *47*, 558.
[2] G. Kresse and J. Furthmüller, Phys. Rev. B. **1996**, *54*, 11169.
[3] M. Friák, A. Slávik, I. Miháliková, D. Holec, M. Všianská, M. Šob, M. Palm, J. Neugebauer, Materials. **2018**, *11*, 1732.
[4] A.K. Grover, R.G. Pillay, V. Nagarajan, P.N. Tandon, J. Magn. Magn. Mater. **1980**, *15*, 699.
[5] M. Friák, S. Oweisová, J. Pavlů, D. Holec and M. Šob, Materials. **2018**, *11*, 1543.
[6] I. Miháliková, M. Friák, Y. Jirásková, D. Holec, N. Koutná, M. Šob, Nanomaterials. **2018**, *8*, 1059.
[7] M. Friák, D. Holec, M. Šob, Nanomaterials. **2018**, *8*, 1057.
[8] P. Šesták, M. Friák, D. Holec, M. Všianská and M. Šob, Nanomaterials. **2018**, *8*, 873.
[9] Y. Jirásková, N. Pizúrová, A. Titov, D. Janičkovič, M. Friák, Journal of Magnetism and Magnetic Materials. **2018**, *468*, 91.
[10] F. Dobeš, P. Dymáček, M. Friák, Kovové materiály - Metallic Materials. **2018**, *56*, 205.
[11] F. Dobeš, P. Dymáček, M. Friák, IOP Conf. Series: Materials Science and Engineering. **2019**, *461*, 012017.
[12] P. Dymáček, F. Dobeš, Y. Jirásková, N. Pizúrová, M. Friák, Theoretical and Applied Fracture Mechanics. **2019**, *99*, 18.

O–IA–02

Investigation of the machinability and casting behavior of Fe25Al1.5Ta

Heiner Michels[1], Maximilian Wagner[2], Christoph Hamm[3], Michael Appelt[4] and Matthias Bünck[5]

[1]Access e.V., Intzestr. 5, 52072 Aachen, Germany, h.michels@access-technology.de
[2]Institute of Production Management, Technology and Machine Tools (PTW), 64287 Darmstadt, Germany, M.Wagner@PTW.TU-Darmstadt.de
[3]WOLF Werkzeugtechnologie GmbH, 66892 Bruchmühlbach-Miesau, Germany, christoph.hamm@wolf-gruppe.com
[4]AWB GmbH & Co. KG, 68623 Lampertheim, Germany, michael.appelt@awb-gmbh.de
[5]Access e.V., Intzestr. 5, D-52072 Aachen, Germany, m.buenck@access-technology.de

Introduction

Due to their advantageous properties, non-ferrous high performance materials such as titanium- and nickel-base alloys are of great importance for the aerospace industry. At the same time, iron aluminide alloys feature similar mechanical and thermal properties, combined with a potential for significant economic advantage over other high performance alloys. Thus, iron aluminides present a possible alternative to high priced non-ferrous alloys and have, e.g. for the aeronautic industry, the potential to substitute established materials for components such as turbine blades.

In aerospace part production, milling represents an important finishing process. Iron aluminides are considered as difficult to cut materials, and therefore the occurring tool wear mechanisms and appearances are a primary issue in machining of such alloys. The BMWi funded ZIM project GeWeFeAl aims at identifying optimal tools and tooling parameters by a systematical analysis of the wear behavior for cast parts made of a FeAl-alloy suitable for high temperature applications. Material properties such as UTS, Young' s modulus, heat conductivity and chemical reactivity have significant impact on the tooling properties, resulting in the demand for identification of specific tools and tooling strategies for an economically sound machining of FeAl.

Materials and Methods

In the work presented, iron aluminide specimens were produced by investment casting from Fe25Al1.5Ta (in at.%). FeAlTa alloys are well researched [1-3], showing suitable properties for high temperature applications. While the high alloy price due to the amount of Tantalum currently limits wider industrial application, within GeWeFeAl the material acts as a model alloy for FeAl-alloys making use of coherent continuous precipitates, providing especially favorable high temperature properties. Samples for machining were cast on a LINN SuperCast horizontal centrifugal casting machine. For crucible and mold, a common Al_2O_3 material was used. The alloy was composed in the crucible from Fe and Al stock material and Ta by way of a master alloy (FeTa20 [wt.-%]). The melt was superheated around 60 K. Casting was done under vacuum. The cast parts were cooled under air, cooling time was 7 hours from casting down to 20 °C.

The specimens were machined using both end milling cutters and ball end milling cutters developed within the project to analyze the occurring tool wear and the influence of different tool geometries, materials and coatings. The tool wear width (VB) was measured by optical analysis and ranked for the tested tool material/coating samples.
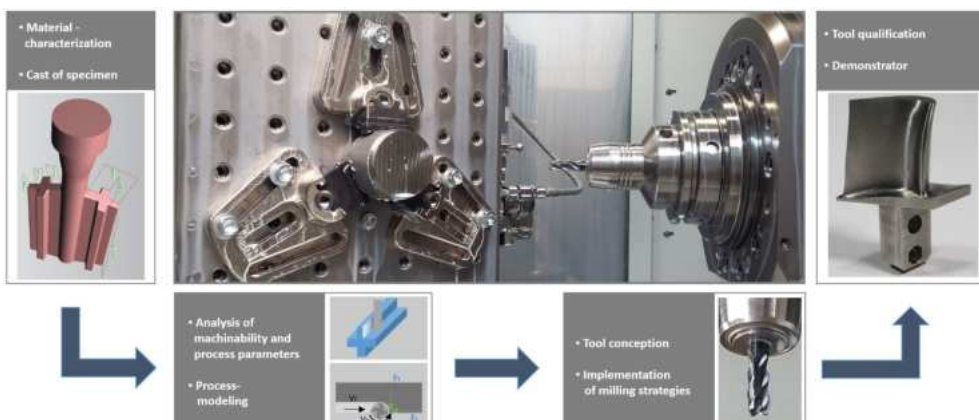
Fig. 1: GeWeFeAl Project Flow

Parallel to the sample production, the casting properties of the chosen alloy were analyzed. Form filling and solidification behavior was determined each by dedicated samples, addressing the demand of casting companies for information regarding material specific casting behavior to optimize the production process by avoiding scrap and improving yield.

Results and Discussion

For the tested range of tool geometries, materials and coatings, significant impact on the tool wear was observed. With around half of the observed maximum wear, optimal variations could be identified for all three tool parameters. The results are currently used to benchmark the milling of a demonstrator blade, comparing FeAl, TiAl, Steel and Inconel best-practice milling.
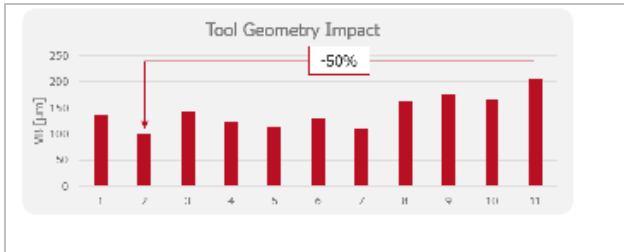
Fig. 2: Tool wear for different tool geometries	Fig. 3: Tool wear for different tool coatings
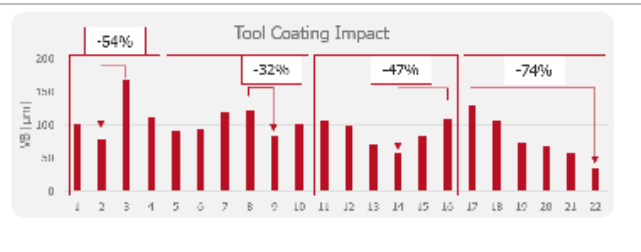
In addition, the analysis of the casting properties is ongoing. First results have proven the feasibility of the employed casting set-ups. The form filling behavior in particular appears to be much better than that of TiAl, levelling the field for the production of the demonstrator parts.

Acknowledgement

Supported by:

Federal Ministry
for Economic Affairs
and Energy

on the basis of a decision
by the German Bundestag

References

[1]   A. Hotař und M. Palm, „Oxidation resistance of Fe-25Al-2Ta (at.-%) in air, "Intermetallics, Bd. 18, pp. 1390-1395, **2010**.

[2]   P. Hanus, E. Bartsch, M. Palm, R. Krein, K. Bauer-Partenheimer and P. Janschek, "Mechanical properties of a forged FE-25Al-2Ta steam turbine blade," Intermetallics, vol. 18, pp. 1379-1384, **2010**.

[3]   M. Palm, „Fe-Al materials for structural applications ot high temperatures: Current research at MPIE," International Journal of Materials Research, Bd. 100, pp. 277-287, **2009**.

O–IA–03

Microstructure and mechanical properties of Fe-25Al-1,5Ta without and with different borides and carbides as grain refiners

Eva Kollmannsberger[1], Alexander Gußfeld[2] and Holger Saage[3]

[1]Competence Center for Lightweight Design (LLK), Faculty for Mechanical Engineering, University of Applied Sciences Landshut, Germany, Eva.Kollmannsberger@haw-landshut.de

[2]Access e.V., RWTH Aachen, Germany, a.gussfeld@access-technology.de

[3]Competence Center for Lightweight Design (LLK), Faculty for Mechanical Engineering, University of Applied Sciences Landshut, Germany, Holger.Saage@haw-landshut.de

Introduction

Cast iron aluminide alloys based on Fe_3Al are attractive for applications where excellent corrosion and oxidation resistance, as well as an appropriate balance of high specific creep resistance and low temperature ductility are desired [1]. Recent developments have concentrated on increasing the creep resistance by adding Tantalum, which leads to the formation of small precipitates based on the Laves and Heusler phases [2,3]. However, casting with low cooling rates leads to high grain sizes and, hence, reduced low temperature ductility. Therefore, grain refiners were added to reduce the grain size and improve the ductility.

Materials and Methods

The alloy Fe-25Al-1,5Ta (in atom percent) was prepared by centrifugal casting. Different boride and carbide based grain refiners of up to about 1 wt.% were added during casting. The alloys were investigated in the as-cast state and part of the samples was heat treated at 700 °C for 10 h and 100 h, respectively. The mechanical properties were determined by room temperature tensile and creep tests at 650 °C and constant strain rates. The microstructure was examined by scanning electron microscopy (SEM) before and after the tests. Furthermore, the microhardness inside single grains of the different states was examined to derive parameters for modeling the hardness contributions.

Results and Discussion

The microstructures on the examples of the alloy without grain refiner (base material) and with ZrB_2 as grain refiner are shown in Fig.1 a) and Fig. 2 a), respectively. While the grain size of the base material is above 1 mm with Laves phases on mostly straight grain boundaries, the addition of ZrB_2 stabilizes the dendritic structure with its typical wavy boundaries during cooling. This is due to the formation of a small amount of eutectic which manifests as µm sized particles at the dendrite boundaries. Because of the dendrite branching the particle arrange in almost domain like structures (Fig. 2 a)). It is known that small domain sizes can be favorable in regard to low temperature ductility of intermetallic alloys [4]. This is confirmed by tensile tests at room temperature and manifests in form of finer structures of the fracture surface compared to that of the base material (Fig. 1 b) and Fig. 2 b)). The crack path is, hence, altered by the particle reinforced branches. On the other hand the almost domain like arrangement promotes the formation of laves phases at those boundaries and the Ta content is reduced in the domain/grain interior. As a consequence, a reduced formation of Heusler/Laves phase in the grain interior leads to inferior high temperature strength. Ongoing development concentrates on identifying the right balance of room temperature ductility and high temperature strength. Within the scope of the presentation, the results of tensile and creep tests of Fe-25Al-1,5Ta with various grain refiners before and after heat treatments at 700 °C are discussed and modeled on the basis of the hardening contributions.

Fig. 1: SEM images of Fe-25A-1,5Ta without grain refiner: a) microstructure, b) fracture surface showing a mixture of intergranular and transgranular crack path with large flat fracture areas

Fig. 2: SEM Images of Fe-25A-1,5Ta with about 0,5 wt.% ZrB_2 as grain refiner: a) microstructure, b) fracture surface showing the influence of the refined dendritic branch structure
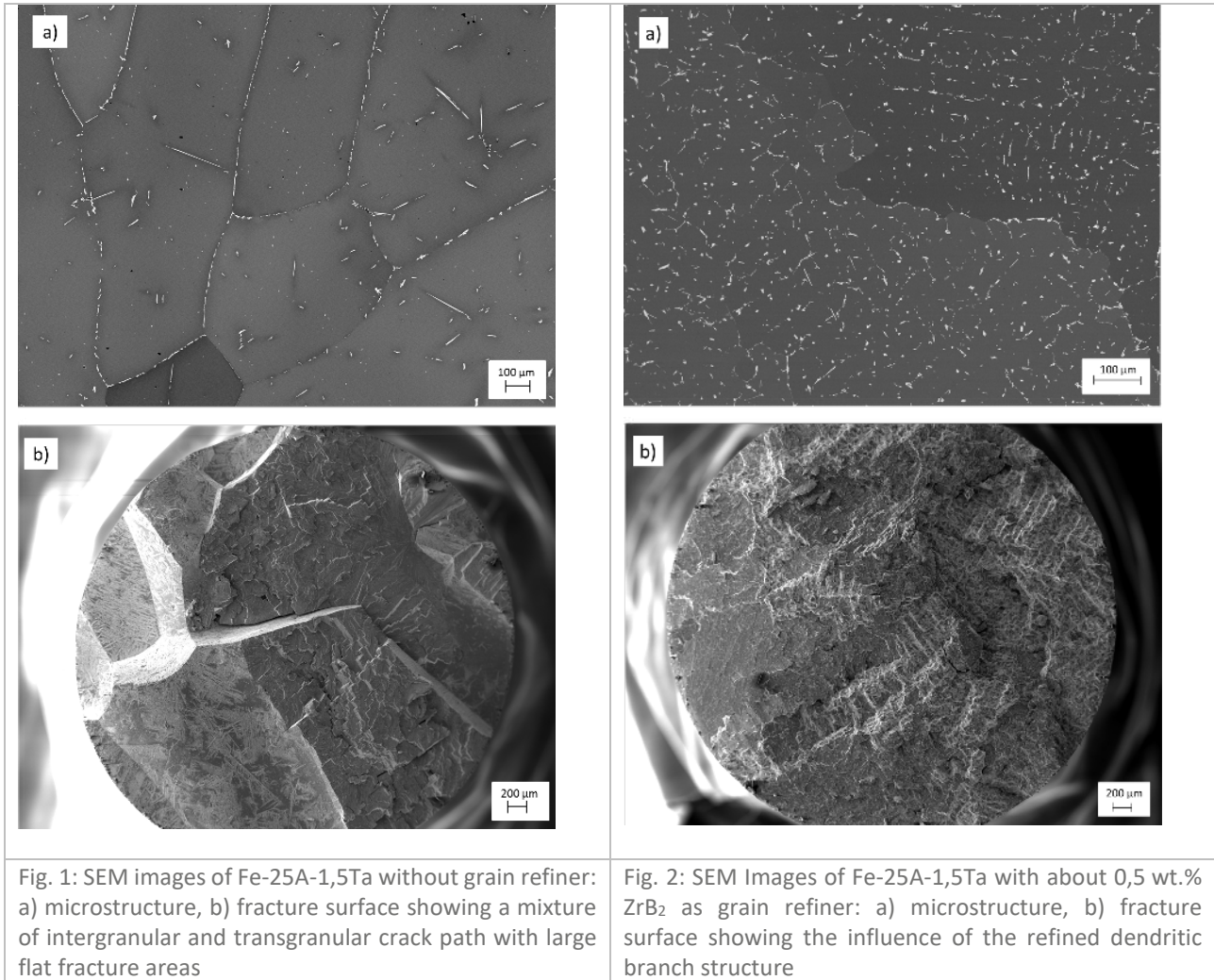
References
[1]   N.S. Stoloff, Materials Science and Engineering A. **1998**, 258, 1-14.
[2]   D.D. Risanti, G. Sauthoff: Intermetallics. **2011**, 19, 1727-1736
[3]   P. Prokopčáková, M. Švec, M.Palm: Internationial Journal of Materials Research, **2016**, 107, 396-405
[4]   Y.-W. Kim: Materials Science and Engineering. **1995**, A 192/193, 519–533.

O–IA–04

First wave combinatorial screening of generic intermetallic strengthened steels

Nele Van Steenberge[1], Laura Moli Sanchez[2] and Lode Duprez[3]

[1]OCAS N.V., Pres. J.F. Kennedylaan 3, 9060 Zelzate, Belgium, nele.vansteenberge@arcelormittal.com
[2]OCAS N.V., Pres. J.F. Kennedylaan 3, 9060 Zelzate, Belgium, laura.molisanchez@arcelormittal.com
[3]OCAS N.V., Pres. J.F. Kennedylaan 3, 9060 Zelzate, Belgium, lode.duprez@arcelormittal.com

Introduction

Maraging steels are a class of ultrahigh strength low carbon steels with a martensitic structure [1-5]. The main characteristic of them is that they are not hardened by carbon and carbide precipitation, but by the precipitation of intermetallic phases during the aging. Moreover, due to the absence or very low content of carbon, the fresh martensite, after quenching, is rather soft and easily machinable.

The typical heat treatment for these grades is a solution annealed treatment followed by water or air cooling to form martensite. During the subsequent ageing, the precipitation of intermetallics occurs giving the hardening and strengthening to the steel. During the ageing, the metastable martensite might decompose partially, forming the so-called reverted austenite.

Large number of intermetallic phases have been reported in the literature [1,2,4,5] as hardening phases for maraging steels such as: $Ni_3(Ti,Mo,Al)$, β-NiAl, Laves phases, Fe_3Si, μ-phase, θ-phase, G-phases, R-phases, etc. Each type has different kinetics of formation and different effect on properties such as strength and toughness, as illustrated in Fig 1. Moreover, often co-precipitation is observed, making this a very complex family of steels.
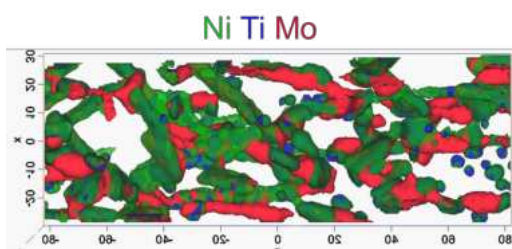
Fig. 1: Atom probe image of a 18Ni-based maraging steel, containing Ti and Mo, illustrating co-precipitation

The objective of this study is to study via a combinatorial approach, the isolated and combined effect of Ni_3Ti and β-NiAl precipitates, on strength and toughness, and their kinetics of formation, using generic ternary and quarternary alloys with different amounts of Ni, Ti and/or Al. By quantifying the isolated effect of each precipitate type, clear guidelines can be obtained on how to obtain a high strength product combined with other properties, e.g. toughness.

Materials and Methods

In the first wave of the combinatorial screening presented here consisted of processing 34 compositions, based on FeNi(Ti, Al) generic alloys, with varying combination of Ni, Ti and/or Al. Ni-contents varied from 4 to 25wt%, Ti varied from 0 to 4wt%, Al varied from 0 to 4wt%. The materials were processed via induction melting and hot rolled to 5mm, followed by air or water cooling. Heat treatment after rolling consisted of re-austenitizing at temperatures from 950 to 1200°C and aging or solely aging (direct quench from rolling).   Aging was performed in the range from 400-600°C, for times up to several days. ThermoCalc® was used to determine the required temperatures for processing.   After processing, samples were characterized by Vickers macro-hardness and Charpy V-notch impact testing. In total, close to 1000 different materials were characterized with the combinatorial approach. Microstructure was analysed via X-Ray diffraction, optical and scanning electron microscopy.

Besides the conventional ex-situ processing and characterization, "in-situ" tests with a constant heating rate of 20°C/min were applied and combined to study the kinetics of precipitation (X-Ray Diffraction, dilatometry and differential scanning calorimetry).

Results and Discussion

The first trends that can be derived from this study are the following. For ternary alloys with 4% Ni, no hardening is observed, despite the formation of large amounts of Laves phase. Increasing the amount of Ni leads to higher peak hardness and a faster hardening response. A larger Ti-content for a fixed amount of Ni, results in larger as-quenched hardness and hardening increment at peak hardness obtained, but no effect on kinetics. Comparing Ti versus Al containing ternary alloys, it is observed that Ti leads to higher strength levels at peak hardness. Moreover, this peak hardness is being reached faster. However, softening at overaging is larger/faster than for the Al-containing ternary alloys.

The combination of various in-situ techniques is a very powerful tool to quickly get information on phase transformations and precipitation kinetics upon heating and study the isolated effect of each aspect separately, e.g. on hardness. The outcome of these in-situ studies have been summarized in so-called continuous precipitation diagrams, as illustrated in Fig. 2 and 3.
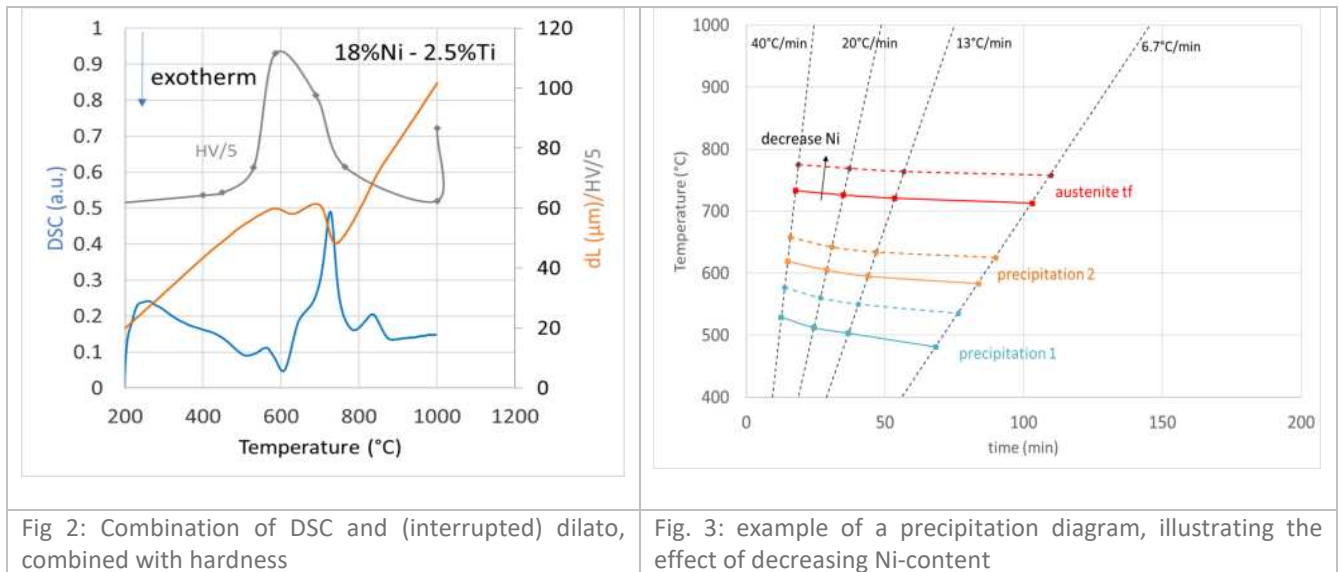
| Fig 2: Combination of DSC and (interrupted) dilato, combined with hardness | Fig. 3: example of a precipitation diagram, illustrating the effect of decreasing Ni-content |

All these data on mechanical properties will now be further integrated into an existing artificial neural network on maraging steels. Moreover, based on the results of this first wave, a selection of materials will be done for further upscaling to test more advanced properties, like H-embrittlement, and more advanced material characterization, like atom probe tomography.

References

[1] A. S. M. Handbook, Volume 4: Heat Treating., ASM International, 72-74., **1991**.
[2] Tewari R.,et. el., "Precipitation in 18 wt% Ni maraging steel of grade 350," Acta Mater. vol. 48 (5) pp. 1187-1200, **2000**.
[3] Wei Sha, Zhanli Guo, "Quantification of phase transformation kinetics in maraging steels. In: Maraging Steels (Woodhead Publishing Series in Metals and Surface Engineering), **2009**, p. 74.
[4] Stiller, K., et.al., "Precipitation in maraging and martensitic chromium steels—what can we learn using 3-DAP and EFTEM," MS&T, vol. 24, no. 6, pp. 633-640, **2008**.
[5] Raabe, D., Ponge, D., Dmitrieva, O., & Sander, B., "Nanoprecipitate-hardened 1.5 GPa steels with unexpected high ductility," *Scripta Materialia,* vol. 60, no. 12, pp. 1141-1144, **2009**.

O–IA–05

Formation of α_c intermetallic particles in Fe- and Mn-containing Al–Si casting alloys during solidification with different cooling rates

Hanka Becker, Daniel Irmer and Andreas Leineweber

Institute of Materials Science, TU Bergakademie Freiberg, Gustav-Zeuner-Straße 5, 09599 Freiberg, Germany, hanka.becker@iww.tu-freiberg, daniel.irmer@student.tu-freiberg.de, andreas.leineweber@iww.tu-freiberg.de

Introduction

Secondary, i.e. recycled, Al–Si alloys often contain the impurity elements Fe and Mn. These lead to the formation of intermetallic phases such as the α_c-*Al(Fe,Mn)Si*-phase and the β-*Al(Fe,Mn)Si*-phase. The β-phase particles have a harmful effect on the mechanical and casting properties due to their plate-shaped morphology [1]. The α_c-phase particles can have a remarkably less detrimental effect on the properties due to its wide variety of morphologies ranging from large compact or hollow polyhedral to coarse or fine dendritic and small irregular shape [2-7]. Previously, the habit of the former morphologies only has been derived from geometrical considerations and is based on {110} habit planes [3-6]. Additionally, it has recently been reported that these morphologies are correlated with certain chemical compositions [8] which, consequently, indicates a close correspondence with different stages of solidification [9].

A systematic classification and extensive characterization of such particles in relation to details of the solidification conditions and stages of solidification is still lacking. However, in terms of the required technological processing or application properties, this understanding is necessary for targeted production of unproblematic Fe-containing intermetallic particles. Therefore, the present study completes the characterization and experimentally confirms previously reported growth morphologies. It provides the links between the morphologies, chemical composition and the stages of solidification depending on the solidification condition and, thus, gives new insight on the formation of α_c-phase particles.

Materials and Methods

Model alloys Al7.1Si0.75Fe0.75Mn and Al7.1Si1.5Fe1.5Mn were solidified with cooling rates 0.05, 0.5 and 1.4 K/s within a differential thermal analysis (DTA) device and with cooling rates of 30 K/s by air-cooling and 200 K/s by water quenching. Then all samples were remelted during DTA with a heating rate of 1.67 K/s in order to obtain results about reactions during melting and correlate these to the solidification stages and, thus, to the microstructure and α_c-phase particle characteristics. The microstructures of alloys solidified with the defined cooling rates were analyzed by optical microscopy and scanning electron microscopy (SEM) including electron dispersive spectroscopy (EDS) and electron backscatter diffraction (EBSD) to access chemical composition and crystallographic orientation information of α_c-phase particles.

Results and Discussion

The α_c-phase particles with different morphologies can be systematically related to different stages of the solidification process that can be classified into a primary, co-dendritic and co-eutectic stage (Table 1). Primary α_c-phase particles evolve with increasing cooling rate in compact polyhedral to hollow polyhedral to coarse dendritic to fine flower/feathery-like dendritic morphology, all having a high x_{Mn}/x_{Fe} molar fraction ratio. The α_c-phase particles which form during the co-dendritic and co-eutectic stage of solidification show dendritic to irregular morphologies and can be distinguished by being located within the Al dendrites having an intermediate x_{Mn}/x_{Fe} ratio or within the Al-Si eutectic region and a low x_{Mn}/x_{Fe} ratio with x being the molar fraction. Based on EBSD data, identified {110} facets confirm the previously proposed morphologies and the characterization of remaining morphologies is accomplished. Thereby, the abundance of well-developed {110} facets decreases with increasing cooling rate, progress of solidification and decreasing $x_{Mn}+x_{Fe}$ content in the alloy. In combination with the temperatures from DTA of reactions involving the α_c phase, the formation of the α_c phase in the different morphologies in secondary Al-Si alloys can be related to the solidification conditions.

Table 1: Classification of the α_c-phase particles according to the stages of solidification. Some main characteristics are presented. Schematic representation of the morphologies of α_c-phase particles evolving during the different stages of solidification depending on the cooling rate. Note that the thickness of the black circles indicates increasing magnification and, therefore, the comparably decreasing size of the intermetallic α_c-phase particles. (Note, that only particles formed during solidification are considered. Post-eutectically formed particles have not been observed in the present study and are excluded from this overview.)

Primary particles	Polyhedra	Hollow polyhedra	Coarse dendrites	Fine flower/feathery-like dendritic
Typical appearance in 2D cross section				
Morphology	Compact, based on rhombic dodecahedra	Coarse branches, based on hollow rhombic dodecahedra	Branched, dendritic, min. 2nd order branches	Branched, dendritic, min. 2nd order branches
{110} faceting	Pronounced	Pronounced	Pronounced	At particle's fringe
x_{Mn}/x_{Fe} ratio	High	High	High	High

Co-dendritic particles	Irregular branched	Coarse Chinese-script/Skeleton		
Typical appearance in 2D cross section				
Morphology	Branched, at the fringe of primary particles	Branched		
{110} faceting	Rare	At particle's fringe		
x_{Mn}/x_{Fe} ratio	Intermediate	Intermediate		

Co-eutectic particles	Fine Chinese-script	Fine dispersed		
Typical appearance in 2D cross section				
Morphology	Branched	Non branched		
{110} faceting	Irregular or rare at particle's fringe	Non facetted		
x_{Mn}/x_{Fe} ratio	Low	Very low		

References

[1] T. O. Mbuya, B.O. Odera, S. P. Ng´ang´a, International Journal of Cast Metals Research. **2003**, *16*, 451–465.
[2] T. Gao, K. Hu, L. Wang, B. Zhang, X. Liu, Results in Physics. **2017**, *7*, 1051–1054.
[3] T. Gao, Y. Wu, C. Li, X. Liu, Materials Letters. **2013**, *110*, 191–194.
[4] A. Bjurenstedt, D. Casari, S. Seifeddine, R. H. Mathiesen, A. K. Dahle, Acta Materialia. **2017**, *130*, 1–9.
[5] A. Fabrizi, G. Timelli, IOP conference series: Matererials Science and Engineering. **2016**, *117*, 012017 1–6.
[6] H. Becker, A. Leineweber, Materials Characterization. **2018**, *141*, 406–411.
[7] M. Timpel, N. Wanderka, B. S. Murty, J. Banhart, Acta Materialia. **2010**, *58*, 6600–6608.
[8] H. Becker, T. Bergh, P. E. Vullum, A. Leineweber, Y. Li, Materialia. **2019**, *5*, 200198 1–13.
[9] X. Cao, J. Campbell, Metallurgical and Materials Transactions A. **2004**, *35*, 1425–1435.

O–HT–01

Intermetallic A15 precipitation hardening in chromium – alloying strategy

Mathias C. Galetz[1], Anke S. Ulrich[1], Ali Solimani[1], Petra Pfitzenmaier[2] and Uwe Glatzel[2]

[1]DECHEMA Forschungsinstitut, High Temperature Materials, Theodor-Heuss-Allee 25, 60486 Frankfurt am Main, galetz@dechema.de

[2]University Bayreuth, Metals &Alloys, Ludwig-Thoma-Str. 36 b, 95447 Bayreuth, uwe.glatzel@uni-bayreuth.de

Introduction

In recent years intermetallic reinforced refractory alloys such as the Mo-Si-B family and Nb-silicide based alloys have been widely investigated as candidate materials for application temperatures beyond the nickel-base family. All refractory alloys offer high melting points along with promising mechanical properties at high temperatures. In the last years, chromium was also reconsidered as a base metal, because its lower density compared to Ni and body centered cubic structure offering high thermal conductivity, high oxidation resistance along with high availability and thus competitive pricing. The main drawbacks that led researchers to abandon this alloy system are a ductile to brittle transition temperature (DBTT) above room temperature, poor oxidation at ultra-high temperatures (T>1000°C) due to the severe nitrogen embrittlement of non-alloyed Cr and the formation of volatile oxides. Several approaches were suggested to improve the high temperature strength such as alloying with Laves-phase or A15-phase formers, which both result in a two-phase microstructure consisting of a Cr solid solution matrix and a strengthening intermetallic phase. The majority of such studies focuses on eutectic Cr-alloys that allow no or limited deformation such as forging or microstructural optimization after casting.

In this work different alloys with either A15 forming elements (Ge, Si, Pt) or Mo that equally substitutes Cr in solid solution and A15 and their major impact on the microstructural evolution and oxidation resistance are presented.

Materials and Methods

Alloys listed in table 1 were prepared by arc melting in a compact arc melter (MAM-1, Edmund Bühler, Germany) on a water-cooled copper mold using chromium pieces (Cr > 99.95 wt.%, Plansee), silicon pieces (Si > 99.999 wt.%, GfE), germanium pieces (Ge > 99.999 wt.%, Haines & Maassen), molybdenum wire (Mo > 99.97wt.%, Plansee), and platinum pieces (Pt > 99.9 wt.%, Heraeus). The resulting droplets were cut into two test pieces, one rectangular being used (2 x ~5 x ~5mm) for oxidation at 1200°C for 100 h in a thermogravimetric analyzer, the other half of the ingot for annealing for the same time and temperature, but encapsulated in an evacuated quartz glass tube. Microstructural, chemical and phase analysis were conducted using optical and electron microscopy (SEM, Philips XL40 electron microscope), electron probe microanalyses (EPMA, JEOL JXA-8100) and X-ray diffraction (Brucker D8 advance), respectively.

Table 1: Chemical composition of the arc melted Cr-alloys measured using EPMA.

alloy	Cr/at.%	Si/at.%	Ge/at.%	Mo/at.%	Pt/at.%
$Cr_{89}Si_7Mo_2Ge_2$	88.6 ± 0.5	7.1 ± 0.4	2.0 ± 0.2	2.0 ± 0.2	-
$Cr_{89}Si_7Ge_2Pt_2$	89.0 ± 0.7	6.7 ± 0.5	2.0 ± 0.3	-	2.1 ± 0.1

Results and Discussion

In Figure 1 and 2 the $Cr_{89}Si_7Mo_2Ge_2$ and $Cr_{89}Si_7Ge_2Pt_2$ alloys are exemplarily shown after heat treatment for 100 h at 1200°C. Comparable to previously investigated binary and ternary alloys, also the quaternary alloys developed a microstructure consisting of only two phases, even though they have higher total amounts and diversity of alloying elements [1]. Both investigated alloy microstructures show a small amount of primary precipitates of up 5 μm in size, which had already been present after casting. After annealing, additional fine dispersed precipitates (secondary precipitates) appeared within the Cr matrix. All precipitates consist of A15 phase, proven by XRD, not shown in here. From the microprobe analysis on the right side of Figure 1 it becomes clear that Si, Ge and Pt are preferentially found within the A15 phase. All are strong A15 formers and able to substitute each other within this phase. Molybdenum instead is equally distributed within the Cr solid solution and the A15 phase and does not show strong partitioning, but can strengthen both phases by solid solution hardening. Alloys with molybdenum additionally show a finer distribution of the precipitates.
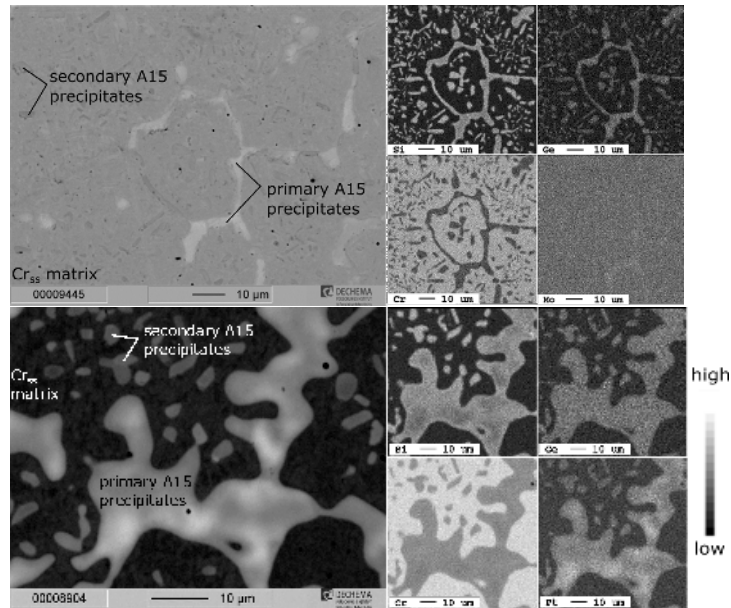
Fig. 1: Microstructure and elemental distribution of $Cr_{89}Si_7Mo_2Ge_2$ (top) and $Cr_{89}Si_7Ge_2Pt_2$ (bottom) after annealing.

Figure 2 shows a much lower mass gain behavior at 1200°C for both alloys in comparison to pure Cr and the respective binary Cr-Si alloy, indicating a protective behavior originating from the contribution of the A15 phase to the scale formation. The oxidation behavior of such alloy systems will be discussed with regard to the influence of the different alloying elements on scale formation, evaporation and nitridation resistance, and a new model to describe the oxidation resistance using a statistical growth parameter, indicating scale failure and nitridation, besides the commonly used k_p and k_v parameters.
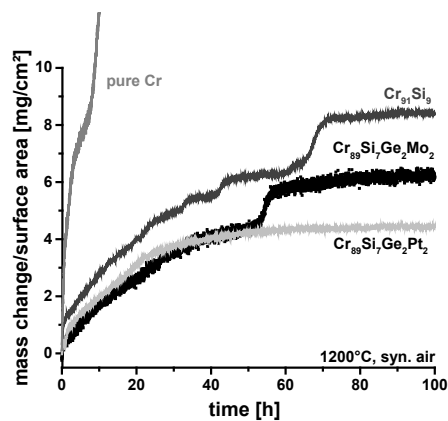
Fig. 2: Thermogravimetric analysis of the quaternary alloys at 1200°C in synthetic air. In addition, pure Cr and a binary $Cr_{91}Si_9$ alloy curve are shown.

References

[1] A. S. Ulrich, et al. "Strengthened Cr-Si-base alloys for high temperature applications." International Journal of Refractory Metals and Hard Materials. **2018**, 76, 72-81.

O–HT–02

Deformation behavior of Nb_2Co_7 as a promising candidate for a crystal-structure-dependent mille-feuille structured material

Toshiaki Horiuchi[1], Konatsu Yamada[2], Ken-ichi Ikeda[3], Seiji Miura[4] and Frank Stein[5]

[1]Laboratory of Advanced Materials for Cold Region, Hokkaido University of Science, Maeda 7-15-4-1, Teine-ku, Sapporo 006-8585, Japan, horiuchi@hus.ac.jp

[2]Division of Mechanical Engineering, Graduate School of Engineering, Hokkaido University of Science, Maeda 7-15-4-1, Teine-ku, Sapporo 006-8585, Japan, 9181103@hus.ac.jp

[3]Division of Materials Science and Engineering, Faculty of Engineering, Hokkaido University, Kita 13 Nishi 8, Kita-ku, Sapporo 060-8628, Japan, ikeda.ken-ichi@eng.hokudai.ac.jp

[4]Division of Materials Science and Engineering, Faculty of Engineering, Hokkaido University, Kita 13 Nishi 8, Kita-ku, Sapporo 060-8628, Japan, miura@eng.hokudai.ac.jp

[5]Max-Planck-Institut für Eisenforschung GmbH, Max-Planck-Straße 1, 40237 Düsseldorf, Germany, f.stein@mpie.de

Introduction

Recently, materials with "mille-feuille structure (MFS)" which is constructed by alternate stacking of microscopic hard- and soft-layer have attracted attention. The long-period stacking ordered (LPSO) phase in Mg alloys has a crystal-structure-dependent MFS, and the LPSO structured Mg alloy shows excellent mechanical properties [1]. The Co-Nb binary system contains several complex intermetallic phases such as three types of Laves phases and Nb_2Co_7 [2]. The crystal structure of Nb_2Co_7 is mS36 [3], which should be classified as a newly found crystal-structure-dependent MFS judging from its interesting mechanical features [4]. Therefore, the Nb_2Co_7 phase is considered to be a promising candidate for a new crystal-structure-dependent MFS material exhibiting the "kink strengthening phenomenon". In the present study, the deformation behavior of Nb_2Co_7 was investigated mainly focusing on the kink formation in the Nb_2Co_7 phase.

Materials and Methods

The Co-3.9 at.%Nb and Co-22.2 at.%Nb alloys were cast as ϕ20mm cylindrical ingots, and were cut into ϕ3×3mm cylindrical samples. The Co-3.9 at.%Nb alloy was heat-treated for homogenization at 1240°C for 1h to attain a single-phase fcc Co solid solution, followed by cooling to room temperature resulting in fine dispersion of metastable $L1_2$ Co_3Nb phase. Subsequently, it was subjected to an isothermal heat treatment at 900°C for up to 100h resulting in fine precipitation of equilibrium Nb_2Co_7 phase, followed by cooling to room temperature. The Co-22.2 at.%Nb alloy was heat-treated at 1000°C for 50h to attain a single-phase Nb_2Co_7, followed by cooling to room temperature. All the heat treatments were carried out in the differential thermal analyzer. Simple free bend tests, compression tests and micro-Vickers and nanoindentation hardness tests were conducted. Microstructure and crystal structure were observed and analyzed by scanning electron microscopy (SEM) and electron backscatter diffraction (EBSD) pattern analysis.

Results and Discussion

The SEM images after a free bend test for the Co-3.9 at.%Nb alloy isothermally heat-treated at 900°C for 1h are shown in Fig. 1. It is interesting that most of the Nb_2Co_7 precipitates are not broken, but they seem to deform by the formation of kinks as indicated by the arrows in Fig. 1(b), in spite of the low symmetry of its crystal structure compared with $L1_2$ structure. Figure 2 shows the results of micro-Vickers hardness tests for the Co-3.9 at.%Nb alloy before and after isothermal heat treatments at 900°C. The hardness of the sample before heat treatment is the highest, and it decreases with increasing the heat treatment time. The finely dispersed metastable $L1_2$ Co_3Nb is considered to transform to equilibrium Nb_2Co_7 during heat treatment. Therefore, the results imply that the Nb_2Co_7 phase might be relatively deformable and a promising candidate for a crystal-structure-dependent mille-feuille structured material. The authors have already revealed that the microstructure of the alloys could be changed by utilization of the metastable $L1_2$ Co_3Nb [5]. The results of nanoindentation will be discussed in detail in the presentation.
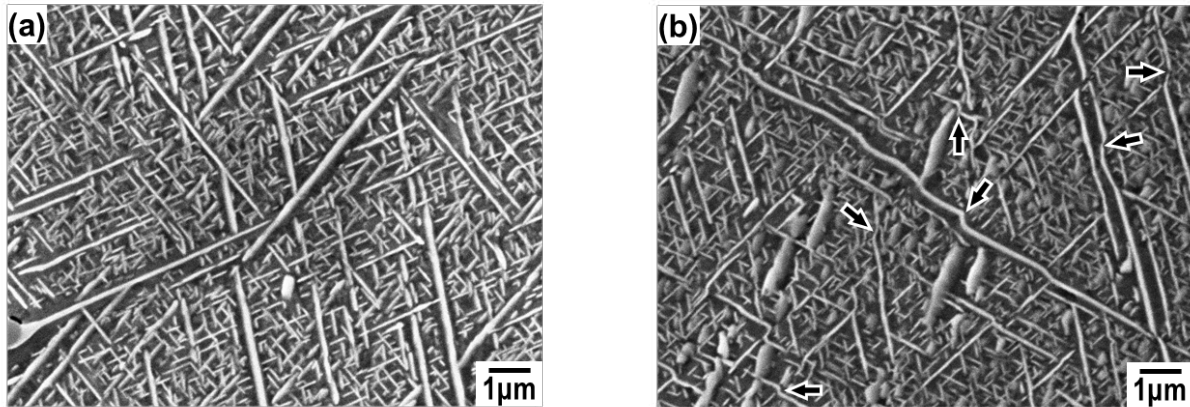
Fig. 1: The SEM images after a free bend test for the Co-3.9 at.%Nb alloy isothermally heat treated at 900°C for 1h, (a) stress free zone, (b) stressed zone. Arrows indicate kink-like appearance of Nb_2Co_7.
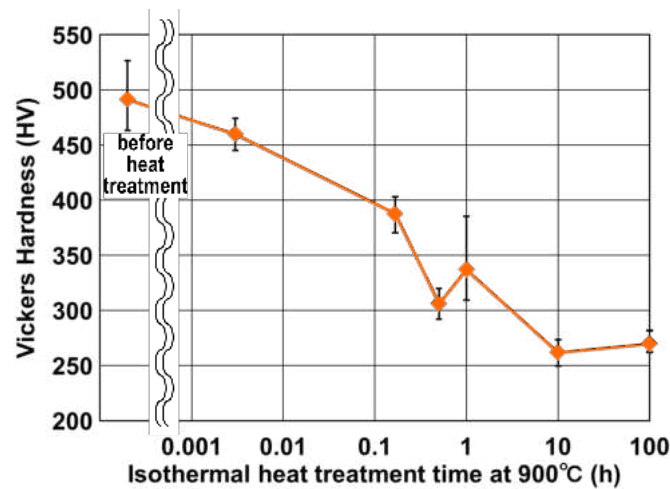
Fig. 2: Micro-Vickers hardness for the Co-3.9 at.%Nb alloy before and after isothermal heat treatments at 900°C.

References
[1]   Y. Kawamura, K. Hayashi, A. Inoue and T. Masumoto: Materials Transactions, **2001**, *42*, 1172-1176.
[2]   F. Stein, D. Jiang, M. Palm, G. Sauthoff, D. Grüner, G. Kreiner: Intermetallics, **2008**, *16*, 785-792.
[3]   A. Leineweber, G. Kreiner, D. Grüner, R. Dinnebier, F. Stein: Intermetallics, **2012**, *25*, 34-41.
[4]   L. Siggelkow, U. Burkhardt, G. Kreiner, M. Palm, F. Stein: Materials Science and Engineering A, **2008**, *497*, 174-180.
[5]   K. Yamada, T. Horiuchi, F. Stein and S. Miura: Proc. 6th International Indentation Workshop (IIW6), Sapporo, Japan, **2018**.

O–HT–03

Identification of Laves phases in a Zr or Hf containing γ-γ' Co-base Superalloy

Li Wang[1], Lin Song[1, 2], Andreas Stark[1], Michael Oehring[1], Yong Liu[3], Uwe Lorenz[1], Florian Pyczak[1, 4]

[1]Helmholtz-Zentrum Geesthacht, Centre for Materials and Coastal Research, Max-Planck-Straße 1, 21502 Geesthacht, Germany
[2]State Key Laboratory of Solidification Processing, Northwestern Polytechnical University, Xi'an, Shaanxi 710072, China
[3]State Key Laboratory of Powder Metallurgy, Central South University, Changsha 410083, China
[4]Brandenburgische Technische Universität Cottbus-Senftenberg, Konrad-Wachsmann-Allee 17, Cottbus, 03046, Germany

Introduction

There is currently an increased interest in the research and development of novel Co-base alloys which contain different intermetallic phases to harden them. The most prominent of these is the γ'-$Co_3(Al,W)$-$L1_2$ phase which can be found in the Co-Al-W system and alloys based on this system [1]. Nevertheless, the ternary Co-Al-W alloys have certain drawbacks such as γ' solvus not exceeding about 1000 °C, high mass density of the alloys due to high content of W and a low stability of the γ+γ' two phase microstructure during long-term high-temperature exposure. Thus, the possibility to improve such properties by adding alloying elements was investigated early on. While the effects of Ta, Ti, Nb, Mo, Ni and Cr were thoroughly studied and reported (e.g. [2,3]), information about the effects of other alloying elements is still scarce. Two elements of interest here are Hf and Zr with the former known to increase the γ' solvus temperature and the latter to strengthen the grain boundaries of the material [4,5]. Both elements have a rather low solubility in Co-based alloys and form additional intermetallic phases if the solubility limit is exceeded. In this contribution, the type of those phases is identified. In addition, based on the actual non-stoichiometric composition of the phases and the valence electron concentration (VEC) it is deduced why these certain types of intermetallic phases form under the given conditions.

Materials and Methods

Two alloys with nominal compositions of Co-9Al-9W-2Zr and Co-9Al-9W-2Hf (all atomic %) were produced by arc-melting and further homogenized by subsequent solution heat treatment at 1300 °C for 12 h in vacuum. On those specimens, annealing heat treatments were conducted at 900 °C in air for 200 and 5000 h. Scanning electron microscopy (SEM) with a LEO Gemini 1530 was used for microstructure characterization for which specimens were prepared by grinding and electro-polishing. High-energy X-ray diffraction (HEXRD) measurements were conducted to identify the phase constitution at the HEMS beam line run by the Helmholtz-Zentrum Geesthacht at the Deutsches Elektronen-Synchrotron (DESY) in Hamburg. The X-ray beam had an energy of 100 keV (λ = 0.1240 Å) which allowed to perform diffraction tests in transmission on specimens with a thickness of some mm. To characterize the microstructure on a smaller length scale and obtain electron diffraction data transmission electron micoroscopy (TEM) and high resolution TEM (HR-TEM) was performed with a Philips CM200 operated at 200 kV and a FEI Titan 80-300 TEM operated at 300 kV. TEM foils were prepared with standard electrolytical thinning techniques. Also, energy dispersive X-ray spectroscopy (EDS) was performed in the transmission electron microscope to measure the chemical composition of the different phases.

Results and Discussion

Besides the phases γ, γ', B2-CoAl and $D0_{19}$-Co_3W (only present in Co-9Al-9W-2Zr), which were clearly identified by HEXRD, peaks of two additional Laves type phases were also present in the HEXRD patterns (see Fig. 1a as an example for Co-9Al-9W-2Zr). In the Zr-containing alloy, this was a C15 type (*Fd-3m*) Laves phase as expected from reports in literature [6]. In the Hf containing alloy the peaks corresponded best to a C36 structure (*P6₃/mmc*), which is until now not reported in Co-Hf alloys. The fact that $D0_{19}$-Co_3W was found in Co-9Al-9W-2Zr after annealing for 5000 h at 900 °C (compare Fig. 1 b and c) but not in Co-9Al-9W-2Hf indicates that Hf can stabilize the γ+γ' microstructure against the formation of $D0_{19}$-Co_3W. In both alloys either Zr or Hf were strongly enriched in the Laves phase but both of them deviated from the stoichiometric composition with Zr and Hf contents being too low and being partly replaced by Co, Al and W. While Al is more enriched in the $ZrCo_2$ Laves phase, the enrichment of W is higher in the $HfCo_2$ Laves phase. Due to these deviations from stoichiometric composition and the differences in Al versus W enrichment when comparing $ZrCo_2$ and $HfCo_2$, the former exhibits a VEC of 7.64 and the latter of 7.79. Based on the theory of Johannes et al. [7] this explains why $ZrCo_2$ has a C15 and $HfCo_2$ a C36 type crystal structure.
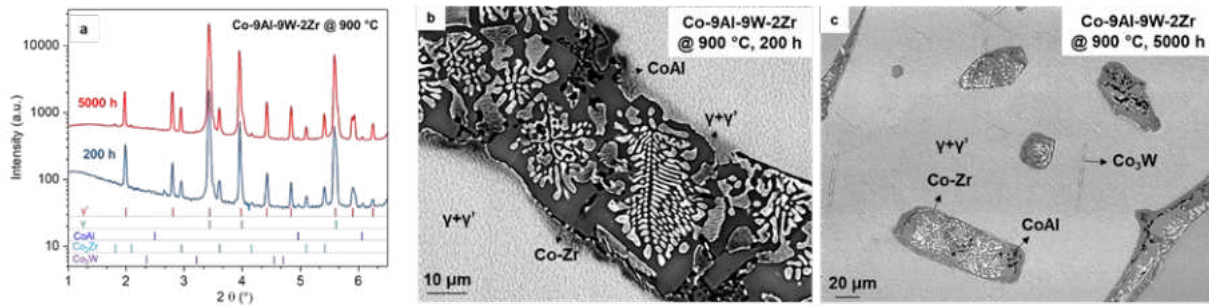
Fig. 1: HEXRD patterns and SEM micrographs of alloy Co-9Al-9W-2Zr after annealing at 900 °C for 200 and 5000 h a) HEXRD pattern. b) SEM micrograph for the specimen annealed for 200 hours. c) SEM micrograph for the specimen annealed for 5000 hours.

References
[1] J. Sato, T. Omori, K. Oikawa, I. Ohnuma, R. Kainuma, K. Ishida, Science. **2006**, 312, 90-91.
[2] A. Bauer, S. Neumeier, F. Pyczak, M. Göken, Scripta Mater. **2010**, 63, 1197-1200.
[3] Y. Li, F. Pyczak, M. Oehring, L. Wang, J. Paul, U. Lorenz, Z. Yao, J. Alloy. Compd. **2017**, 729, 266-276.
[4] T. Omori, K. Oikawa, J. Sato, I. Ohnuma, U.R. Kattner, R. Kainuma, K. Ishida, Intermetallics. **2013**, 32, 274-283.
[5] P.J. Bocchini, C.K. Sudbrack, R.D. Noebe, D.C. Dunand, D.N. Seidman, Mater. Sci. Eng. A. **2017**, 682, 260-269.
[6] K. Ishida, T. Nishizawa, J. Phase Equilib. **1991**, 12, 424-427.
[7] R.L. Johannes, R. Haydock, V. Heine, Physical Review Letters. **1976**, 36, 372-376.

O–HT–04

Phase equilibrium among γ-Ni/TCP/GCP *oP*6 phases in Ni-based alloys at elevated temperatures

Ryota Nagashima, Ryoske Yamagata, Hirotoyo Nakashima and Masao Takeyama

School of Materials and Chemical Technology, Tokyo Institute of Technology

2-12-1-S8-8, Meguro-ku, Tokyo, Japan, nagashima.r.ad@m.titech.ac.jp

Introduction

Strengthening of Ni-based superalloys is in principle using GCP (geometrically closed-packed) phase of Ni_3Al-γ' ($L1_2$). Furthermore, TCP (topologically close-packed) phases, for instance σ or Laves phases, are seen as detrimental for mechanical properties. However, a game-changing microstructural design principle without relying on γ' phase will be needed for further development of the alloys. Our group is currently constructing a novel microstructure design principle, using thermodynamically stable TCP phase for grain boundaries, together with GCP phase other than γ' phase for grain interiors, based on the grain boundary precipitation strengthening (GBPS) mechanism [1, 2]. One of the model

alloy systems for the principle is the Ni-Cr-Mo ternary system. TCP NiMo (*oP*112) and P (*oP*56) phase are thermodynamically stable over 1573 K. GCP Ni_2Cr (*oP*6) phase (T_c = 863 K) in the Ni-Cr binary system precipitates coherently from γ matrix. The phase stability is enhanced up to 1023 K by Mo in solution [3], however there are few reports that clarify the phase region of *oP*6 phase by both experiments and calculations. In this study, thus, the phase equilibria among γ, TCP, and GCP *oP*6 phases have been examined.

Materials and Methods

Two series of alloys were used as shown in Fig. 1: series I with nominal compositions of Ni-30 at. % (Cr, Mo) by replacing Cr with Mo by every 5 at. % (the alloys are referred to by their Mo content), and series II with those of (Ni, Cr)-15Mo with replacing Ni with Cr (the alloys are referred to by their Cr-Mo content). These alloys were prepared by arc melting in argon atmosphere with non-consumable tungsten electrode as a 35 g button ingot. These ingots were firstly cold rolled by 40 % in height, and homogenized at 1373 K, followed by aging at 973 - 1173 K for up to 1000 h. Microstructures were examined by scanning electron microscope (SEM) and transmission electron microscope (TEM). SEM samples were mechanically polished, followed by electro polishing in a solution of phosphoric acid with supersaturated chromic anhydride acid at 353 K. TEM discs with 0.2 mm in thickness and 3 mm in diameter were machined, and then mechanically polished, followed by twin-jet polishing in a solution of ethanol with 6 vol. % perchloric acid at 253 K. The hardness was measured by a micro-Vickers hardness machine under a load of 0.98 N.

Results and Discussion

Figure 2 shows an experimentally determined isothermal section of Ni-rich Ni-Cr-Mo ternary system at 973 K. thermodynamically stable *oP*6 single-phase region exists as an island along Ni-33at.%Cr – Ni-33 at.%Mo line. In addition, there exist two three-phase coexisting regions of γ/NiMo/*oP*6 and γ/P/*oP*6, suggesting that the novel microstructures with TCP phase at grain boundaries, together with GCP phase within grain interiors, would be controlled.
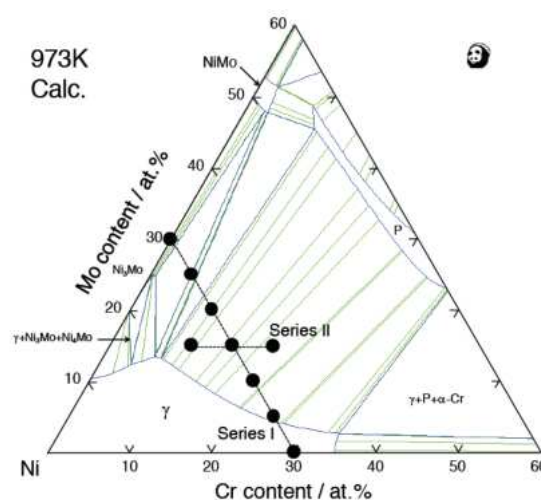
Fig. 1: Alloys studied plotted on calculated isothermal section of Ni-Cr-Mo ternary system.
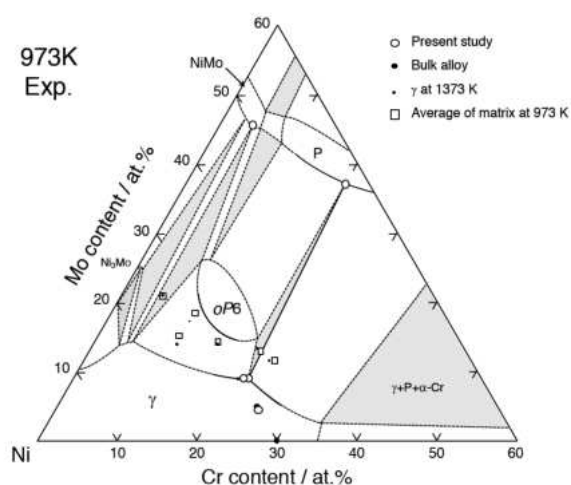
Fig. 2: An experimentally determined isothermal section of Ni-rich Ni-Cr-Mo ternary system at 973 K.
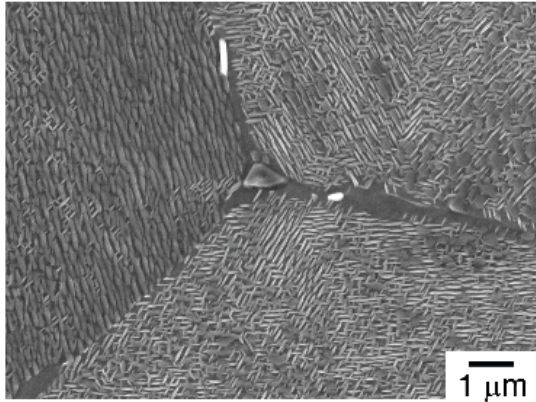
Fig. 3: SEI of Ni-15Cr-15Mo aged at 973 K for 1000 h.
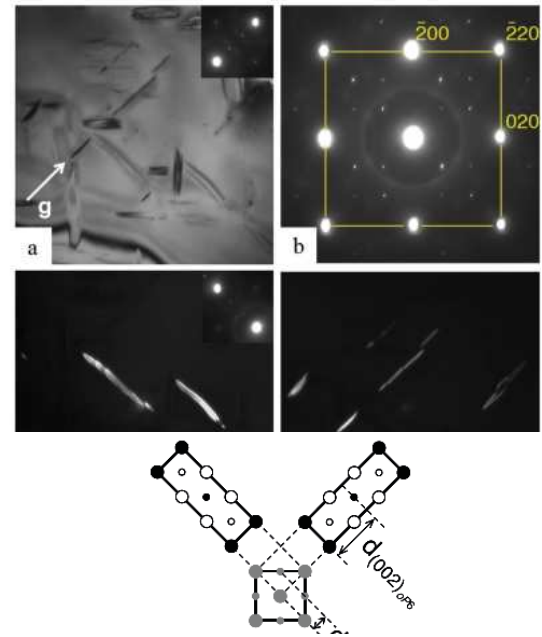
Fig. 4: TEM images of Ni-10Cr-15Mo aged at 973 K for 100 h, showing two variants of *oP*6 in A1 matrix.
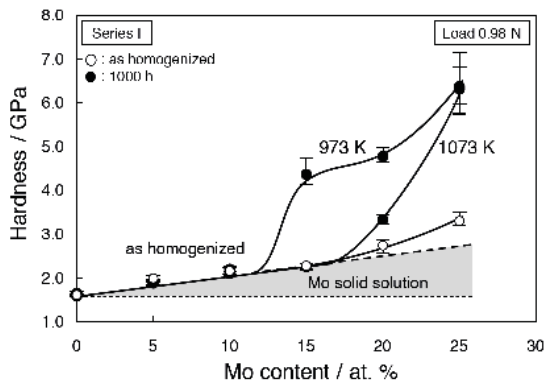
Fig. 5: Change in hardness with Mo in the alloys (series I) homogenized and aged at 973 K and 1073 K for 1000 h.
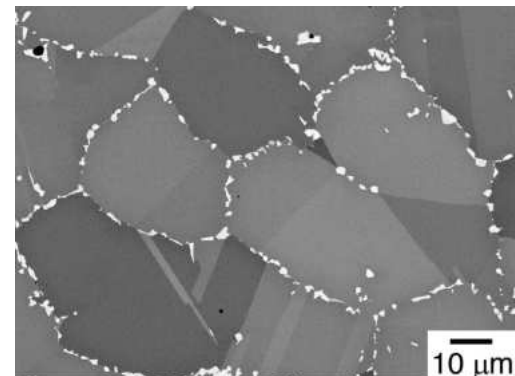
Fig. 6: BEI of Ni-15Cr-15Mo aged at 1073 K/ 1000 h.

Figure 3 shows a SEI of 15Mo, located in γ/*oP*6 two phase region, aged at 973 K/ 1000 h. Disc-like submicron-size *oP*6 phase with Widmanstätten morphology was observed within the grain interiors. TEM analysis of 10Cr, located in the same γ/*oP*6 two phase region, aged at 973 K/ 100 h, revealed that, as shown in Fig. 4, *oP*6 phase has the following crystallographical orientation relationship with the matrix: {110}$_\gamma$ // (110)$_{oP6}$, <001>$_\gamma$ // [010]$_{oP6}$. Figure 5 shows a change in hardness with Mo contents in the alloys of series I before and after aging at 973 K and 1073 K for 1000 h. The hardness of the as homogeneous alloys gradually increases because of Mo solid-solution strengthening. On the other hand, the hardness from 15Mo at 973 K and 20Mo at 1073 K tremendously increases to 4 GPa due to precipitation of *oP*6 phase. The hardness within grain remains unchanged of 2 GPa since *oP*6 single-phase region shrink with higher temperature. Thus, γ phase directly equilibrates with P phase which precipitates collaborated at grain boundary (Fig. 6).

In the presentation, the calculated phase diagram obtained by a modified existing data base will be discussed in terms of thermodynamics.

References

[1]   I. Tarigan, K. Kurata, N.Tanaka, T. Matsuo and M. Takeyama:
      Mater. Res. Soc. Symp. Proc. **2011**, *1295*, 317-322.
[2]   S. Ida, S. Kobayashi and M. Takeyama: J. Alloys Compd. **2018**, *764*, 1033.
[3]   M. Kumar and V.K. Vasudevan: Acta Mater. **1996**, *44*, 1591.

O–HT–05

Stabilizing the cubic modification of titanium trialuminide in the structure of Ti-Al₃Ti composites

Daria Lazurenko[1], Ivan Bataev[1], Andreas Stark[2], Florian Pyczak[2] and Vyacheslav Mali[3]

[1]Novosibirsk State Technical University, Karl Marks str. 20, 630073 Novosibirsk, Russia, pavlyukova_87@mail.ru, ivanbataev@ngs.ru

[2]Helmholtz Zentrum Geesthacht, Max-Planck Str., 1, 21502 Geesthacht, Germany, andreas.stark@hzg.de, florian.pyczak@hzg.de

[3]Lavrentiev Institute of Hydrodinamics, SB RAS, Lavrentiev av. 15, 630090 Novosibirsk, Russia, vmali@mail.ru

Introduction

Recently Ti-Al₃Ti composites attract significant attention due to their outstanding properties including excellent specific strength, hardness, stiffness and impact strength [1]. However relatively low fracture toughness and plasticity restrict their wide application [2]. To solve this problem, it was suggested to modify the structure of the brittle intermetallic component. Titanium trialuminide possesses the tetragonal $D0_{22}$ structure, which results from the $L1_2$ structure (which essentially is an ordered face-centered cubic lattice (fcc)) by introducing antiphase boundaries with a displacement vector of $1/2[110]$ on each (001) plane of the $L1_2$ unit cell. Due to its low symmetry, the tetragonal $D0_{22}$ structure has a limited number of independent slip systems [3], which is probably the reason for low-temperature brittleness of Al₃Ti compounds. $L1_2$ structure having 12 independent $\{111\}$ slip systems (likewise fcc structures) will be intrinsically more ductile comparing to compounds with a $D0_{22}$ one. To modify $D0_{22}$ structure of Al₃Ti to $L1_2$, one can alloy it with Fe, Cr, Cu, Mn, Co, Ni or Zn. To find out if it is possible to stabilize $L1_2$ titanium trialuminide as a component of the Ti-based composite, in situ synchrotron investigations were carried out. Based on the results obtained, the appropriate regimes of producing Ti-Al₃Ti composites with the cubic structure of intermetallic were chosen.

Materials and Methods

Cu was chosen as the alloying element for Al₃Ti. For in situ synchrotron X-ray radiation diffraction analysis, samples consisting of thoroughly mixed Al, Ti and Cu powders were prepared. The nominal composition of the mixture was Ti45-Al47-Cu8 (at. %). This ratio provided the excess of Ti in the same proportion as in the structure of multilayer Ti-Al₃Ti composites. Heating was provided by the induction furnace of a modified DIL805A/D dilatometer. The samples were heated with a rate of 10 °C/min up to the temperature of 830 °C and held at this temperature for 1 hour. The cooling rate was 50 °C/min. The experiment was carried out in high-purity argon atmosphere at a pressure of 0.8 mbar.

Diffraction patterns were obtained at Petra III synchrotron radiation source of the German Electron Synchrotron (Deutsches Elektronen-Synchrotron – DESY) in the High Energy Materials Science Beamline (P07) operated by Helmholtz-Zentrum Geesthacht. The radiation energy was 100 keV which corresponded to a wavelength of 0.124 Å. The spot size was 1×1 mm. Diffraction rings were recorded using a Perkin Elmer XRD1621 2D detector with a resolution of 2048×2048 pixels and a pixel size of 200×200 μm in transmission mode. The sample-to-detector distance was equal to 1837 mm. The Debye-Scherrer diffraction rings were continuously recorded during heating, holding, and cooling with a frequency of 0.1 Hz. The total exposition time was 4 seconds and was provided by summation of 40 frames exposed for 0.1 seconds each. Two-dimensional diffraction rings were azimuthally integrated and analyzed as typical Intensity - 2θ powder diffraction patterns.

Multilayer composites were produced by spark plasma sintering (SPS) in Lavrentiev Hydrodinamic Institute (SB RAS, Novosibirsk) using a LABOX-1575 SPS machine. Commercially pure titanium and aluminum foils were alternately stacked and interspersed by homogeneous layers of copper powder between them, and then placed in a titanium shell with an inner diameter of 26 mm. Such a set was covered with a cap with an outer diameter of 30 mm. This setup allowed performing the reactive sintering at temperatures exceeding the aluminum melting point [4]. The thickness of metallic foils was 50 μm. Sintering was performed at 830 °C under a pressure of 40 MPa for 10 minutes.

The microstructure of fabricated material was investigated by scanning electron microscopy (SEM) in the back-scattered electrons mode using a Carl Zeiss EVO 50XVP microscope equipped with an X-ACT (Oxford Instruments) energy dispersive X-ray (EDX) spectrometer. Phases formed in the MIL composite were investigated by X-ray diffraction (XRD) analysis. Diffraction patterns were recorded using an ARL X'TRA diffractometer with Cu Kα radiation. The fracture toughness was estimated based on Vickers microindentation tests using a Wolpert Group 402 MVD tester. A load on the diamond indenter varied from 0.2 to 1 kg.

Results and Conclusions

X-ray synchrotron diffraction analysis revealed that cubic modification of Al_3Ti can be stabilized by alloying with Cu. This phase forms in a ternary system through the sequences of solid-liquid and solid-solid reactions with formation of intermediate phases. The reactions in system start at approximately 575 $^\circ$C with the eutectic melting of Al and Cu. Almost simultaneously AlCu and Al_3Ti intermediate phases appear due to the liquid-solid reactions. When the liquid is almost completely consumed, the formation of cubic titanium trialuminide (Al_5CuTi_2), and AlCuTi phases starts.

The multilayer Ti-Al_3Ti composite with modified titanium trialuminide structure was successfully produced by SPS at 830 $^\circ$C. However, Al_5CuTi_2 was not the only one intermetallic phase in the resulting structure. As it was shown above, τ_2 (TiAlCu compound) always appear simultaneously with Al_5CuTi_2. It presents in the structure of the composite as an additional layer such as the final structure of the composite consisted of three layers: titanium, a thin τ_2 layer, and a thick τ_3 (Al_5CuTi_2) layer. It should be possible to minimize the thickness of TiAlCu by reducing the temperature and the holding time of sintering. Formation of the τ_2 layer in the structure of the composite is undesirable due to its high brittleness.

Indentation tests showed that the fracture toughness of the τ_3 intermetallic layer with $L1_2$ structure was significantly higher than that of the ordinary $D0_{22}$ titanium trialuminide. In the case of tetragonal titanium trialuminide, the cracks appeared around imprints with a load of 0.2 kg. Meanwhile, even applying 1 kg, cracks were not formed in the layer with the $L1_2$ cubic structure.

The approach developed in this work can be used to synthesize multilayer metal-intermetallic composites with cubic titanium trialuminide stabilized by elements other than copper (e.g., Fe, Co, Mn, Ni, Zn, etc.) as well as for fabrication of bulk cubic titanium trialuminides via solid-liquid reaction.

Acknowledgement

References

[1]   K.S. Vecchio, Synthetic multifunctional metallic-intermetallic laminate composites, JOM, **2005,** *57,* 25-31.

[2]   M. Yamaguchi, Y. Umakoshi, T. Yamane, Deformation of the Intermetallic Compound Al_3Ti and Some Alloys with An Al_3Ti Base, Mater. Res. Soc., **1986**, *81*, 275.

[3]   M.B. Winnicka, R.A. Varin, Compression ductility and fracture of boron-free and highly boron-doped Al_5CuTi_2 intermetallic compound, Scripta Metall. Mater., **1990**, *24,* 611-615.

[4]   D.V. Lazurenko, V.I. Mali, I.A. Bataev, A. Thoemmes, A.A. Bataev, A.I. Popelukh, A.G. Anisimov, N.S. Belousova, Metal-Intermetallic Laminate Ti-Al_3Ti Composites Produced by Spark Plasma Sintering of Titanium and Aluminum Foils Enclosed in Titanium Shells, Metall. Mater. Trans. A, **2015**, *46*, 4326-4334.

O–IT–08

Prospects and challenges of electron beam based additive manufacturing of intermetallics

Carolin Körner[1], Martin Franke, Thorsten Wolf, Johannes Köpf, Vera Jüchter, Alexander Klassen and Lucas Adler

[1]Chair of Materials Science and Engineering for Metals (WTM), Friedrich-Alexander-Universität Erlangen-Nürnberg (FAU), Martensstr.5 , 91058 Erlangen, Germany

In general, the processing of intermetallic phases is difficult due to their intrinsic brittleness. Additive manufacturing for the production of complex components opens up interesting perspectives for this class of materials. Selective electron beam melting is particularly promising of additive manufacturing processes. The process operates under vacuum conditions at temperatures up to above 1000°C. It therefore offers perfect protection against impurities and at the same time the possibility to minimize internal stresses.

The presentation presents the possibilities but also challenges of selective electron beam melting for the processing of intermetallic phases. Examples range from titanium aluminides for aviation to intermetallics for catalytic applications.

O–AM–01

Properties and microstructure of nano-structured NiAl-Cr(Mo) in-situ composites processed by additive manufacturing

Andreas Förner[1], Steffen Neumeier[1], Abdullah Jamjoom[2], Carolin Körner[2] and Mathias Göken[1]

[1]Friedrich-Alexander-Universität Erlangen, Germany, General Materials Properties, andreas.foerner@fau.de, steffen.neumeier@fau.de, mathias.goeken@ww.uni-erlangen.de
[2]Friedrich-Alexander-Universität Erlangen, Germany, Materials Science and Engineering for Metals, abdullah.jamjoom@fau.de, carolin.koerner@fau.de

Introduction

NiAl-Cr and NiAl-Cr(Mo) eutectic in-situ composites are promising high temperature materials due to a high melting point, excellent oxidation behaviour and their low density. To enhance the poor room temperature fracture toughness of these composites high cooling rates are beneficial to obtain fine cellular-lamellar structures [1, 2]. The aim of this research is to characterize the microstructure and mechanical properties of a NiAl-28Cr(6Mo) eutectic in-situ composite processed by electron beam melting, which provides extremely high cooling rates.

Materials and Methods

The eutectic in-situ composite NiAl-28Cr(6Mo) is processed by selective electron beam melting. SEBM provides very high solidification rates that lead to very fine cellular-lamellar microstructures on the nanometer scale. The samples are analyzed using REM and FIB as well as APT technique for microstructural characterization. Furthermore, compression tests and creep tests were performed up to 1300K. The room temperature fracture toughness was determined using microcantilevers prepared by FIB milling [3] and tested with an in-situ indenter.

Results and Discussion

The influence of process parameters during SEBM on the microstructure as well as the effect of microstructural features on the mechanical properties were investigated. Atom probe tomographies show feather-like arranged, crosslinked Cr(Mo) rods inside a NiAl-matrix, see Fig. 1. Their very fine phase distance strongly depends on the scan velocity and the power of the e-beam. The increasing amount of interfaces enhances the hardness of the in-situ composite corresponding to a Hall-Petch-like behavior. Experiments show that the exact eutectic composition is required to get good high temperature properties and room temperature fracture toughness. Cracks and fracture surfaces where analyzed and toughness increasing mechanisms like crack bridging, renucleation or deflection at NiAl - Cr(Mo) interfaces were found, see Fig.2.

In a summary, selective electron beam melting is suitable to process NiAl-Cr(Mo) in-situ composites with interesting mechanical properties, but further investigation is needed to create a competitive high temperature alloy.

Figures
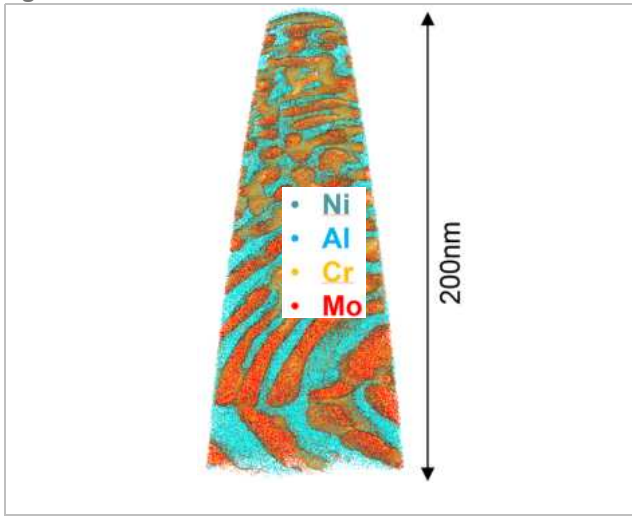
| Fig. 1: Atom Probe tomography of the nano-structured arrangement of crosslinked Cr(Mo) rods inside a NiAl-matrix | Fig. 2: SE image of a rough fracture surface of the cellular NiAl-Cr(Mo) in-situ composite |
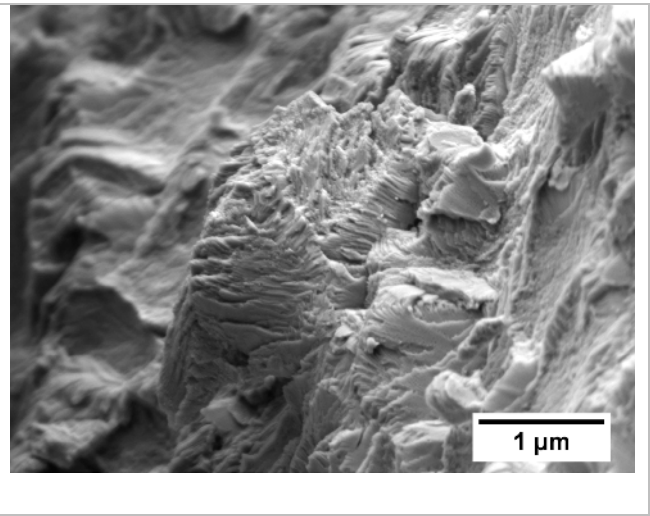
References

[1]   D. R. Johnson et al., Intermetallics. **1995**, 3, 99-113.
[2]   S. V. Raj et al., Metallurgical and Materials Transactions A. **2002**, 33, 597-612.
[3]   D. DiMaio et al., Journal of Materials Research. **2005**, 5, 299-302.

O–AM–02

Additive manufacturing of multi-phase V-Si-B alloys

Janett Schmelzer[1], Silja-Katharina Rittinghaus[2], Andreas Weisheit[2] and Manja Krüger[3]

[1]Institute of Materials and Joining Technology, Otto-von-Guericke University Magdeburg, 39106 Magdeburg, Germany, janett.schmelzer@ovgu.de

[2]Fraunhofer – Institute for Laser Technology, 52074 Aachen, Germany, siljakatharina.rittinghaus@ilt.fraunhofer.de, andreas.weisheit@ilt.fraunhofer.de

[3]Institute of Energy and Climate Research (IEK-2), Research Centre Jülich, 52425 Jülich, Germany, m.krueger@fz-juelich.de

Introduction

For improving thermodynamic efficiency of gas turbines it is necessary to develop new high-temperature materials beyond the capability of Ni-based superalloys. Next to a high melting point the reduction of the weight is also an important issue to achieve the target of increased thermodynamic efficiency. V points out as an interesting candidate, since it offers the lowest density (ρ = 6.11 g/cm^3) in comparison to other high-melting metals. Moreover, alloyed with Si and B a multi-phase microstructure, consisting of a V solid solution (V_{ss}) phase next to the intermetallic phases V_3Si and V_5SiB_2 [1,2] forms, which offers a low ductile-brittle-transition (BDTT) as well as enhanced high temperature strength and creep resistance next to an improved oxidation resistance [1].

However, due to the high melting point of the constituents ingot processing (IM) is challenging. As an alternative, multi-step powder metallurgical processes (PM) are currently used for processing bulk materials. The introduction of a one-step processing route for this type of material via additive manufacturing (AM) represents an important innovation to produce complex bulk materials with net shape geometries (e.g. turbine blades). This work shows a very first study on the printability of pre-alloyed near-eutectic V-Si-B powder materials via directed energy deposition (DED) as a method for AM. Therefore, V-Si-B powder was manufactured via gas atomization (GA) process out of solid raw materials meeting the requirements for AM regarding flowability and particle size.

Materials and Methods

Based on investigations of the ternary eutectic refractory alloy systems from Hasemann et al. [2], a near eutectic V-9Si-5B alloy composition was chosen for processing via AM. Therefore, the solid raw materials (V > 99.95 %, Si > 99.6 % and B > 99.4 % purity) were molten and superheated in a crucible (inductive heating system) and subsequently atomized (using Ar gas flow) into powder/droplets. For a quantitative determination of the elemental composition of the powder particles an ICP-OES analysis was conducted. DED samples were built out of the GA powder material. The laser beam source was a 2 kW diode laser, the beam diameter in the processing zone was 0.6 mm. The build-up was performed using induction preheating of the processing plane (700 °C) and a rising laser power (70 W - 175 W) with increasing height of the component (under Ar conditions). Investigations on the microstructure were carried out by scanning electron microscopy (SEM, ESEM XL30 FEI/Philips), energy dispersive X-ray spectroscopy (EDS) and electron backscatter diffraction (EBSD, Zeiss Merlin SEM equipped with a Nordlys EBSD camera). For this purpose, the samples were mounted and subsequently ground and polished by standardized methods [2]. To determine the microhardness of the powder particles and compacts a Vickers pyramid with a force of 1 N (HV0.1) for 5 s (Wilson VH 3300) will be carried out.

Results and Discussion

The GA V-9Si-5B powder particles, shown in Fig. 1a, appears with a regular formed shape, almost spherical, and tiny fractions of agglomerated particle compounds. A narrow sizing of the powder material (45 µm - 125 µm) provides good flow properties due to reduced interparticulate adhesive forces and less friction among the particles [3], needed for uniform build rates in the AM process.
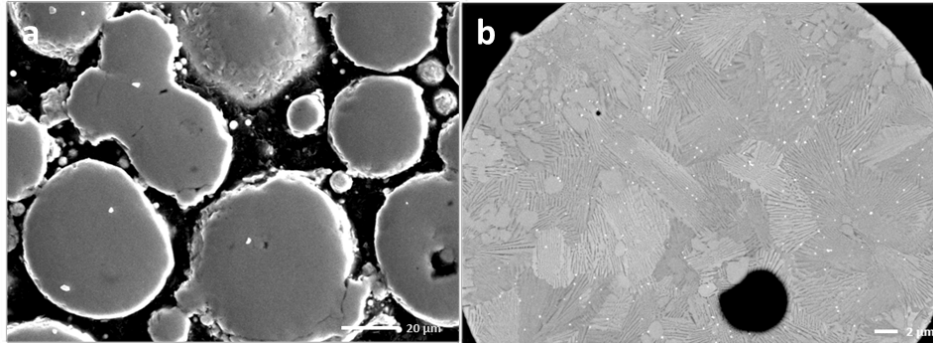
Fig. 1: a) Morphology of GA V-9Si-5B powder particles, b) Microstructure of a V-9Si-5B particle with primarily solidified V_{ss} dendrites and fine eutectic regions

The chemical composition of the powder material after GA fits the initial alloy composition V-9Si-5B (at.%), indicating a process without significant losses of the elemental raw material. Some of the GA particles show up with cavities, which can be attributed to gas inclusions from the atomization process. The microstructure of the powder particles appears with a certain fraction of primarily solidified V_{ss} dendrites (as expected according to the phase diagram [4]) surrounded by very fine eutectic regions composed of the V_{ss} phase and the intermetallic phases V_3Si and V_5SiB_2 (dark grey in Fig. 1b), indicating rapid cooling during the GA process.
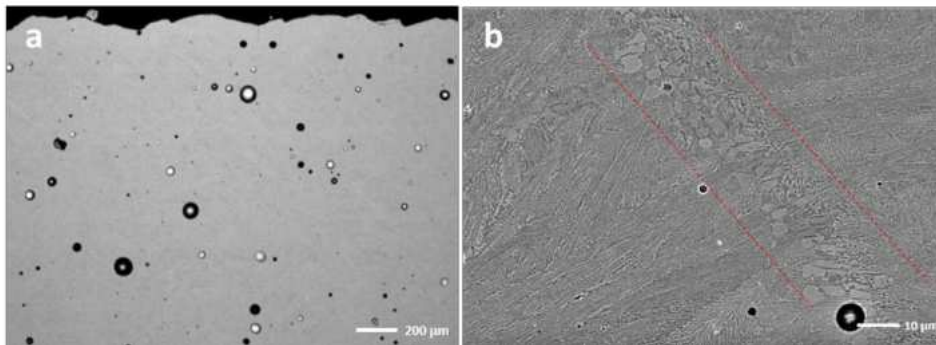
Fig. 2: a) Macrograph of DED V-9Si-5B compact, b) Microstructure showing a distinct zone from the cladding process (center) surrounded by eutectic regions of V_{ss}, V_3Si and V_5SiB_2.

Out of the powder material compact specimens with dimensions of 10 x 15 x 4 mm (height x width x depth) was successfully manufactured via DED for the first time for this class of material. In this initial state the compact and crack-free specimens indicate pore formation with an average diameter of 2 to 80 µm and a volume fraction of approximately 6 % (optical measurement, Fig. 2a). The origin of the pores might be due to the powder quality (e.g. hollow particles) or the process (e.g. Ar bubbles in the melt) which difficults the interlayer bonding or generally causes pore formation and need to be eliminated by adjusting the GA as well as the AM process. The SEM picture of the compacts (Fig. 2b) presents a microstructure showing a distinct zone of primarily solidified V_{ss} and V_3Si phases (marked within the dashed lines in Fig. 2b) resulting from the layer-wise cladding of the DED process next to eutectic structures of V_{ss}, V_3Si and V_5SiB_2. Further microstructural investigations and first mechanical tests are in progress.

References
[1] M. Krüger, Scripta Mater. **2019**, *121*, 75–78.
[2] G. Hasemann, M. Krüger, M. Palm, F. Stein, Mater Sci Forum. **2018**, *941*, 827-832.
[3] V. Seyda, Werkstoff- und Prozessverhalten von Metallpulvern in der laseradditiven Fertigung, Springer Vieweg, **2018**.
[4] C. A. Nunes, B. B. de Lima, G. C. Coelho, P. A. Suzuki, J Phase Equilib Diff. **2009**, *30*, 4, 345-350.

O–AM–03

Study on the mechanical twinning of α_2 phase in a high Nb-containing TiAl alloy after high temperature deformation

Lin Song[1,2], Fritz Appel[2], Li Wang[2], Michael Oehring[2], Uwe Lorenz[2], Florian Pyczak[2] and Tiebang Zhang[1]

[1]State Key Laboratory of Solidification Processing, Northwestern Polytechnical University, Xi'an, Shaanxi 710072, China
songlin@nwpu.edu.cn, lin.song@hzg.de, tiebangzhang@nwpu.edu.cn
[2]Institute of Materials Research, Helmholtz-Zentrum Geesthacht, Max Planck-Str. 1, Geesthacht, 21502, Germany
fritz.appel@hzg.de, michael.oehring@hzg.de, uwe.lorenz@hzg.de, florian.pyczak@hzg.de

Introduction

Twinning of the ordered $D0_{19}$-α_2 phase will require long-distance shuffling of atoms to fulfill the mirror symmetry between twin and parent lattice [1] and no evidence of twinning was reported for stoichiometric α_2 alloys so far [2]. Nevertheless, in off-stochiometric single phase α_2-based alloys, twin structures were recognized by several researchers, however, there was a remarkable disparity between the observed twinning elements [3,4]. In some cases also, the twinning elements were not determined since the twinning morphology was only observed but not analyzed. Most of the studies have pointed out that the interchange shuffling is a critical step for fully establishing twinned structures in the $D0_{19}$-α_2 phase. In general, the data indicates that the following factors support mechanical twinning in α_2 alloys: 1) off-stochiometric composition, perhaps Nb-containing; 2) high-temperature (>1000 °C) compression and 3) sample (or grain) orientation unfavorable for prismatic glide. However, in two-phase (α_2+γ) TiAl alloys, twinning of the α_2 phase was never observed. As the α_2 phase is a significant constituent of modern TiAl based alloys and thus important for maintaining strain continuity, it is important to know whether deformation twinning in this phase could be initiated also in two phase (α_2+γ) TiAl alloys under the above mentioned favorable experimental conditions which facilitates twinning in single phase α_2 alloys.

Materials and Methods

The nominal composition of the alloy is Ti–45Al–8.5Nb–0.2W–0.2B–0.02Y [at.%]. Cylinders in sizes of $\varnothing8\times12$-mm³ were cut from the ingot. High temperature compression was conducted on a Gleeble 3500 equipment at 800 °C. The heating rate was 10 °C/s and the samples were held at the testing temperature for 5 minutes to stabilize the heat transfer. A strain rate of 0.001 s^{-1} was applied, and the compression strain was set to 30%. In total, the compression test took 5 minutes. After compression, the samples were water-quenched to freeze the microstructure. Specimens for scanning electron microscopy observation were cut from the center of the compressed samples, then grinded and vibration polished. Slices for transmission electron microscopy observation were cut parallel to the loading direction. TEM foils were grinded to a thickness of 0.1 mm and further thinned to electron-transparency by twin-jet polishing.

Results and Discussion

The twinning morphology within the α_2 phase is shown in Figure 1. A number of plates are observed in Figure 1a. The α_2 phase exhibits large internal stress, as indicated by strain contrast. The selected area diffraction (SAD) pattern of this area is shown in Figure 1b. Two $[11\bar{2}0]\alpha_2$ zone axes are displayed in Figure 1b, which appear in mirror symmetry. The mirror plane, as labelled by the dashed line in the SAD pattern, is $(2\bar{2}01)\alpha_2$. After indexing the SAD pattern, an ideal twinning relationship can be determined. Twin variants can also be observed in different orientations (Figures 1c-d). The twinning elements are $K_1=(20\bar{2}1)$, $\eta_1=[\bar{1}014]$, $K_2=(20\bar{2}3)$, $\eta_2=[\bar{3}03\bar{4}]$, which are essentially the same as those observed by Lee et al. [3]. A high stress concentration appears to be necessary to initiate α_2 twinning because it is only found in certain severely deformed lamellar structures with heavy γ twinning. For the hexagonal structure, atomic shuffling is not necessarily along the shear direction, whereas the atoms have to select one of the nearest positions to complete the $D0_{19}$ structure. However, short-range diffusion should take place. Although the deformation temperature at which twinning was observed is relatively low (800 °C), during the 5 minutes' duration of the test it could well be possible for atoms to move over the necessary short distances. On the other hand, it should be noted that both the matrix and the twin do not perfectly correspond to the α_2 phase structure (only could be observed in high-resolution TEM image). A similar morphology could be generated by the formation of O phase variants, i.e., those with the "polytwin" relationship [5]. However, if such a mechanism occurs, the angle between the basal planes would be 90° or 60° rather than ⌣56° as determined in this study. Thus, O phase formation could be ruled out and the observed features really represent twins in the α_2 structure.
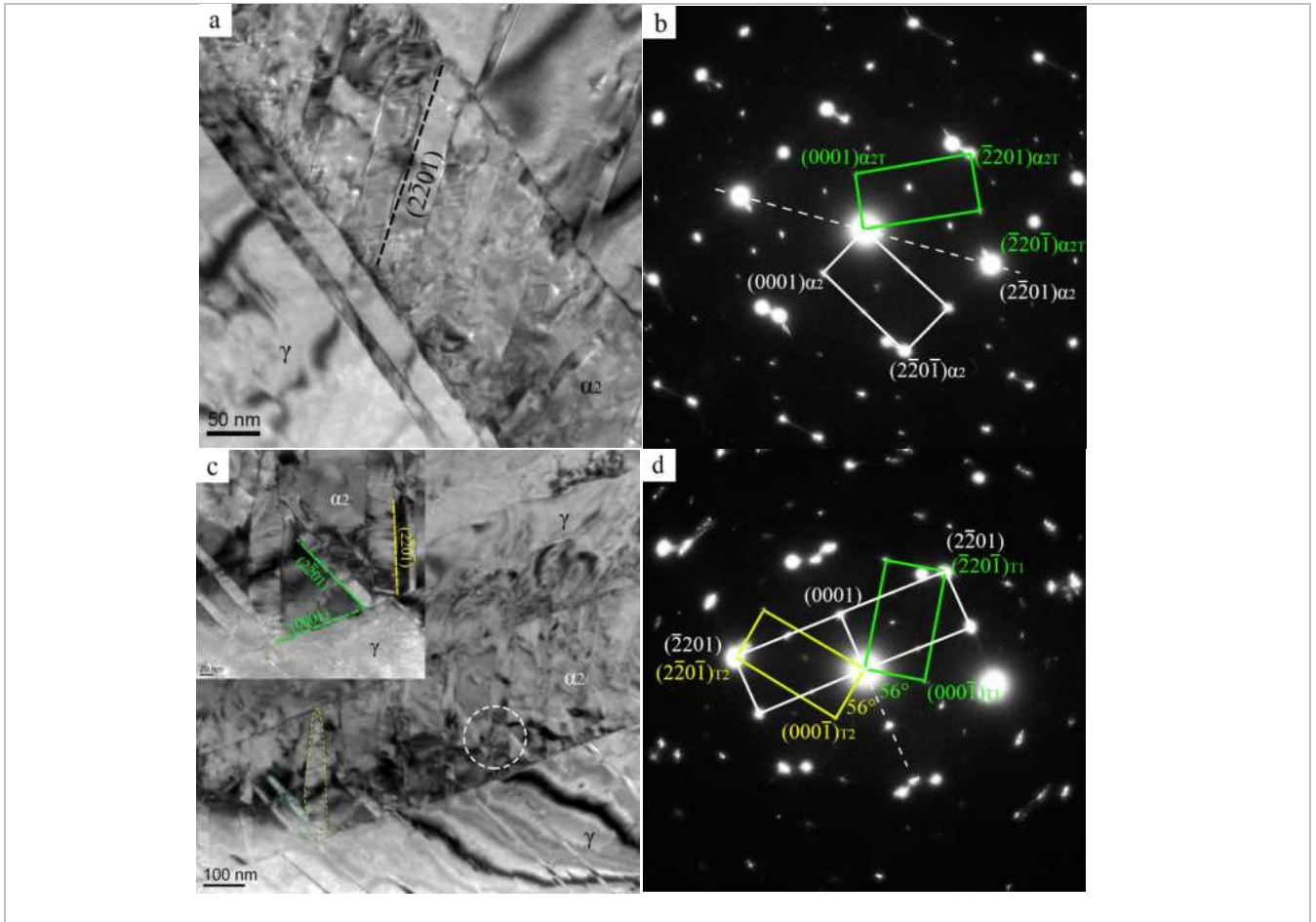
Fig. 1: (a) Multiple-twinning plates of α_2 phase with the trace of a twin interface parallel with $(2\bar{2}01)_{\alpha2}$; (b) SAD pattern of (a) in $[11\bar{2}0]_{\alpha2}$ direction, showing the mirror symmetry of twinning; (c) TEM image of two twinning variants along two $\{2\bar{2}01\}$ planes; (d) SAD pattern of the circled area in (c), showing the two branches of the twinning pattern; with a 56° angle between the basal planes of each twining grain and its matrix.

References
[1]   M.H. Yoo, C.L. Fu, J.K. Lee, J. Phys. III 1. **1991**, 1065-1084.
[2]   F. Appel, J.D.H. Paul, and M. Oehring, Gamma Titanium Aluminide Alloys: Science and Technology, Wiley, **2011**.
[3]   J.W. Lee, S. Hanada, M.H. Yoo, Scripta Metall. Mater. 33. **1995**, 509-514.
[4]   K. Kishida, Y. Takahama, H. Inui, Acta Mater. 52. **2004**, 4941-4952.
[5]   L.A. Bendersky, A. Roytburd, W.J. Boettinger. Acta Metall. Mater. 42. **1994**, 2323-2335

O–AM–04

In situ study of beta phase ordering in TiAl alloys by neutron and synchrotron diffraction

Victoria Kononikhina[1], Andreas Stark[1], Weimin Gan[2], Xiaohu Li[2], Gleb Dovzhenko[1], Michael Oehring[1], Robert Koos[3], Andreas Schreyer[4] and Florian Pyczak[1]

[1]Helmholtz-Zentrum Geesthacht, Geesthacht, Germany, Victoria.Kononikhina@hzg.de
[2]German Engineering Materials Science Centre, HZG Outstation at FRM II, Garching, Germany
[3]FRM II, Garching, Germany
[4]European Spallation Source ERIC, Lund, Sweden

Introduction

γ-TiAl alloys are currently used for production of turbine blades for two low pressure stages of advanced aero engines [1]. Having about half the density of Ni-based superalloys γ-TiAl alloys allows to reduce the engine weight and an amount of emitted CO_2. There is a strong desire to reduce production cost and improve the mechanical properties for industrial production of turbine blades. With respect to easier forging the role of the β_0-phase has been discussed in literature [2]: "With a reasonable addition of β-stabilizer, metastable β_0 (with B2 structure) phase can be maintained, which is favorable for fine-grained structure and better high-temperature deformation behaviors". Therefore, the investigation of the $\beta_0 \rightarrow \beta$ phase transformation is of high interest nowadays. In samples with different amounts of several β-stabilising elements, the kinetics of the $\beta_0 \rightarrow \beta$ transformation have been studied by in situ synchrotron and neutron diffraction experiments.

Materials and Methods

Ternary TiAl alloys, namely Ti-42Al-yX (y – 1-10 atomic % of Mo, Fe, Cr, Ta, Nb) have been produced by arc melting and then heat treated at 1100 °C for 5 or 7 days.

Neutron and synchrotron radiation have been applied for the diffraction investigation of the β phase ordering transformation. This was done in situ using a standard high temperature furnace or a dilatometer at temperatures up to 1450 °C. Neutron diffraction experiments were realized at the FRM II, MLZ (Garching near München) in a temperature range of 1100 – 1450 °C [3]. The neutron diffraction measurements needed a prolonged data collection time. Therefore, step-wise heating has been carried out. A continuous heating ramp from room temperature up to 1450 °C was used in the synchrotron radiation experiments carried out at DESY (Hamburg) as the bright high energy beam of the P07 beamline allowed for much shorter measurement times.

Spectrums were analyzed by Rietveld refinement [4] applying the batch mode of MAUD program [5].

Results and Discussion

Our alloys contain mainly α_2, β_0/β and γ phases. Smaller scattering angles when using high energy synchrotron radiation allowed to collect a higher amount of reflections of different phases simultaneously within a restricted maximum diffraction angle. Synchrotron as well as neutron diffraction results are analyzed by refinement of the phase composition and lattice constants for β_0/β, α_2/α and only a parameter for the γ phase. The synchrotron diffraction results allowed to refine the site occupancy and temperature B-factor as well as all lattice parameters of all detected phases.

There is almost no change in phase composition during heating below 1000 °C for most of the samples, however, above 1000 °C phase transformations could be observed as α_2 + γ + β_0 transformed to α + β + γ at about 1120 °C and then to α + β at about 1250 °C and finally to pure β phase at high temperatures. The γ phase content is not influenced by any of the other phase transformations and stayed constant from room temperature up to 1100 °C and slowly disappeared at higher temperatures The decrease of γ phase gives rise for a sharper increase of the β_0 and α phases content. The $\alpha_2 \rightarrow \alpha$ phase transformation takes place at about 1115 – 1140 °C almost for all ternary alloys with 2 at.%.

There is a small decrease of the β_0/β content at 1150 - 1190 °C in samples with 2 at.% of Cr and Mo. This corresponds most probably to the β_0 to β transition because of a simultaneous change in site occupancy. Figure 1 shows the phase content for Ti-42Al-2Mo based on synchrotron data. The alloy with 2 at.% of Mo exhibited the highest amount of β compared to alloys containing the same amount of other β stabilizing elements: 2Fe, 2Cr. Both neutron and synchrotron results confirmed the presence of the β_0 phase in all investigated ternary alloys except Ti-42Al-2Nb and -2Ta.

Some small amounts of additional phases were found below 1000 °C - the samples with Fe and Nb, contain τ_2 or ω_0 phases correspondingly in the temperature range of 650 – 800 °C.
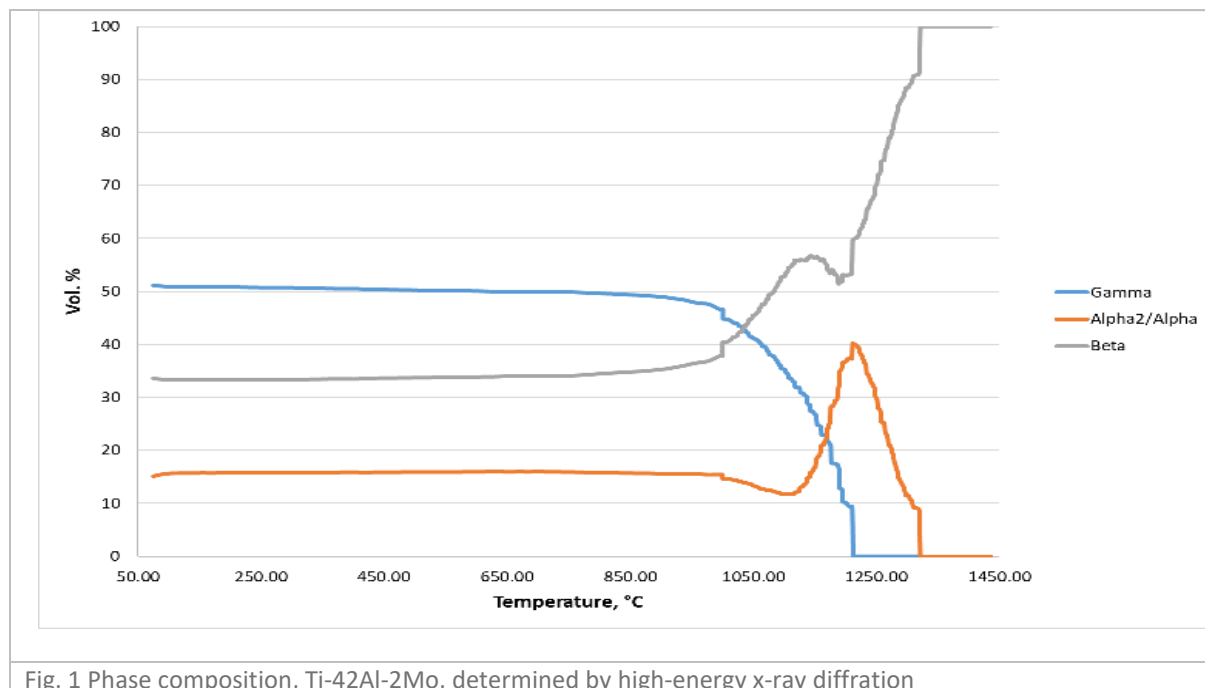
Fig. 1 Phase composition, Ti-42Al-2Mo, determined by high-energy x-ray diffration

The change of lattice constants during in-situ heating has been refined and exhibits a homogeneous increase with up to 0.02 Å difference to the room temperature values. The phase transformations $\beta_0 \rightarrow \beta$, and $\alpha_2 \rightarrow \alpha$ have been estimated via site occupancy refinement. The site occupancy coefficient refinement gave maximum values for the β phase below 70 %. This can be explained by the phase non-stoichiometry and by the different chemical composition of our alloys. However, the site occupancy coefficient for the α_2/α phase is higher than for the β phase and lies between 90 and 100 %.

The temperature of the order-disorder phase transformations was determined by both diffraction methods, synchrotron and neutron. Differences up to 20 °C were found in some alloys which can mainly be attributed to the influence of the different heating ramps.

References
[1]   B.P. Bewlay et al., Materials at High Temperatures. **2016**, *33(4-5)*, 549-559.
[2]   C.-Z.Qiu, et al., Transactions of Nonferrous Metals Society of China. **2012**, *22(11)*, 2593-2603.
[3]   V. Kononikhina, A. Stark, W. Gan, A. Schreyer, F. Pyczak, MRS Advances. **2017**, *2(26)*, 1399-1404. doi:10.1557/adv.2017.145
[4]   D. Chateigner, Combined Analysis. **2010**, Wiley, ISTE.
[5]   L. Luterotti, *MAUD*. Available from: http://maud.radiographema.eu.

O–IT–09

Properties of advanced Mo-Si-B alloys

Manja Krüger[1], Janett Schmelzer[2], Olha Kauss[2] and Georg Hasemann[3]

[1]Forschungszentrum Jülich GmbH, Institute of Energy and Climate Research (IEK-2), Leo-Brandt-Str. 1, 52425 Jülich, Germany, m.krueger@fz-juelich.de

[2]Otto-von-Guericke University Magdeburg, Institute of Materials and Joining Technology, Universitätsplatz 2, 39106 Magdeburg, Germany, janett.schmelzer@ovgu.de, olha.popovych@ovgu.de

[3]Forschungszentrum Jülich GmbH, Institute of Energy and Climate Research (IEK-2), Leo-Brandt-Str. 1, 52425 Jülich, Germany, g.hasemann@fz-juelich.de

Introduction

Current research on ultra-high temperature metallic materials focuses on multi-phase Mo-Si-B alloys, which are potential candidates for novel turbine materials or other ultra-high temperature applications. The most interesting alloy compositions in the ternary Mo-Si-B system are located within the three-phase field between the Mo solid solution (Mo_{ss}) phase and the silicides Mo_5SiB_2 (T2) and Mo_3Si (A15), known as the so-called "Berczik-triangle". Various alloy compositions were investigated in the past, and it could be shown that three-phase alloys have a good combination of high temperature strength, oxidation resistance and fracture toughness [1,2]. Furthermore, outstanding creep properties of directionally solidified near-eutectic Mo-Si-B alloys, e.g. Mo-17.5Si-8B, even above temperatures of 1100 °C, indicate the enormous potential of this type of microstructure [3]. However, ingot processing is challenging due to the high melting point of Mo-Si-B materials being typically >2000 °C (eutectic Mo_{ss}-Mo_3Si-Mo_5SiB_2 alloy: T_M ~ 2000 °C). Due to this reason, different multi-step powder metallurgical (PM) processes were often used in the past to produce dense Mo-Si-B samples under laboratory conditions [4]. However, the introduction of additive manufacturing (AM) techniques represents an important innovation that will allow the production of complex bulk materials [5].

Materials and Methods

The PM processing of different Mo-9Si-8B(-1Zr) alloys was done in a multi-step procedure: mechanical alloying (MA) followed by either cold isostatic pressing, sintering and hot isostatic pressing or field assisted sintering (FAST) as described in [6,7]. Directional solidification (DS) of near-eutectic alloys in a crucible-free furnace is described in [8]. For additive manufacturing alloys from the vicinity of the eutectic point, namely Mo-13.5Si-7.5B and Mo-16.5Si-7.5B, were chosen for the production of bulk samples by Directed Energy Deposition (DED) [5] and Laser Powder Bed Fusion (LPBF). In both processes Ar gas atomized powders were used. The bulk materials resulting from the different processes were characterized by SEM in combination with EDS, EBSD, X-ray diffraction analyses, microhardness measurements and compressive creep tests.

Results and Discussion

There is a significant correlation between the alloy composition, the process parameters and the microstructural as well as the mechanical properties. Fig. 1 shows representative micrographs of differently processed three-phase Mo_{ss}-Mo_3Si-Mo_5SiB_2 alloys. The PM alloy (left) is consolidated from mechanically alloyed powders. Typical features of such PM alloys are the fine grains (about 1-5 μm) and the homogeneous distribution of the phases. If MA leads to well-homogenized powders and the alloy contains a volume fraction of ≥ 50 % Mo_{ss}, the Mo_{ss} (light gray) forms a continuous network and the silicide phases (medium and dark gray) are insulated in the Mo_{ss} matrix. This is essential for decreasing the BDTT and improving the fracture toughness of such alloys [4,6]. The understanding for the correlation between the process parameters and the resulting properties of PM alloys is well-advanced. However, the drawback of PM processes are impurities, like oxygen.

Additively manufactured Mo-Si-B alloys are not as well-established. One of the results of an ongoing cooperative project (LextrA, funded by the BMBF) is shown in the middle of Fig. 1. As compared to the PM alloy with a similar chemical composition the microstructure evolution in the AM alloy is due to primary solidification of large Mo_{ss} islands, followed by the solidification of the eutectics. It could be shown that small, dense and crack-free samples can be manufactured from gas atomized powders by DED [5] and LPBF processes. Both variations provide a good creep behavior.

Directional solidification allows to process anisotropic microstructures as shown exemplarily in Fig. 1 (right). Eutectic Mo-Si-B alloys have a silicide matrix, their main constituent is Mo_3Si. Eutectic and near-eutectic DS alloys have an excellent creep resistance [8] and a good oxidation resistance.

FEM analyses demonstrate the great potential of multi-phase Mo-Si-B alloys as turbine blade materials in comparison to Ni-based superalloys [9]. Such calculations allow to design and tailor Mo-Si-B-X alloys for different ultra-high temperature applications considering the typical features, which result from the different processes PM, AM and DS.
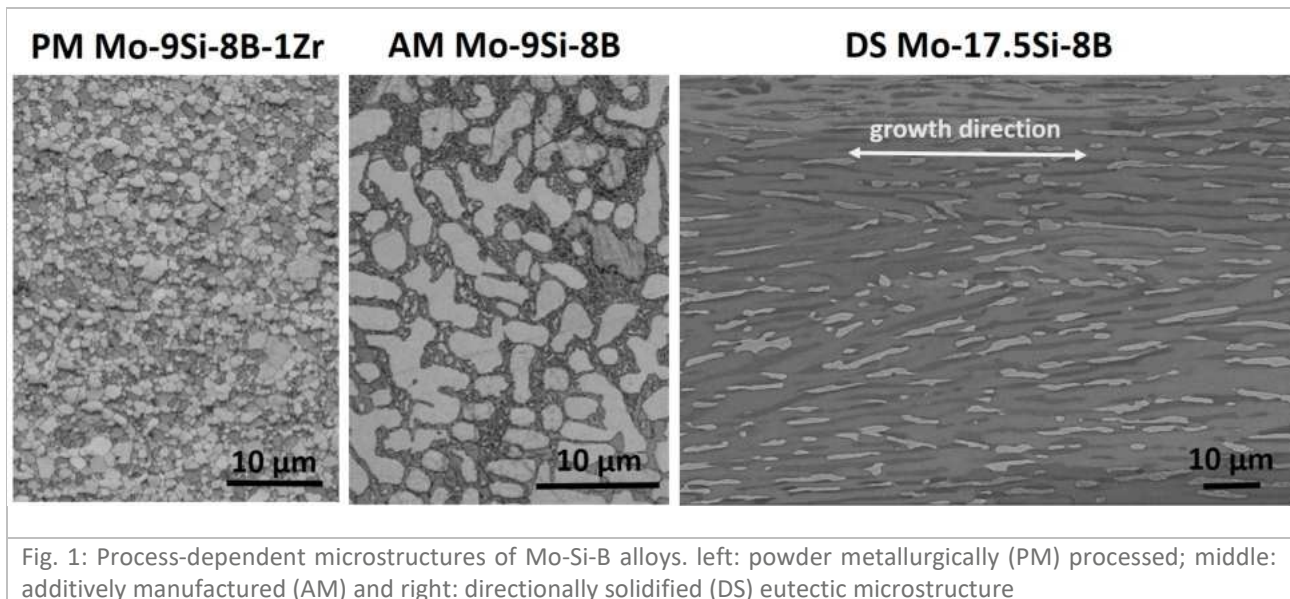
Fig. 1: Process-dependent microstructures of Mo-Si-B alloys. left: powder metallurgically (PM) processed; middle: additively manufactured (AM) and right: directionally solidified (DS) eutectic microstructure

References

[1] A.P. Alur, N. Chollacoop, K.S. Kumar, Creep effects on crack growth in a Mo-Si-B alloy, Acta Mater. **2007**. *55*. 961–974.

[2] D.M. Dimiduk, J.H. Perepezko, Mo-Si-B Alloys : Developing a Revolutionary Turbine-Engine Material, MRS Bull. **2003**. 639–645.

[3] G. Hasemann, D. Kaplunenko, I. Bogomol, M. Krüger, Near-Eutectic Ternary Mo-Si-B Alloys: Microstructures and Creep Properties, JOM. **2016**. *68*. 2847–2853.

[4] M. Krüger, P. Jain, K.S. Kumar, M. Heilmaier, Correlation between microstructure and properties of fine grained Mo-Mo3Si-Mo5iB2 alloys, Intermetallics. **2014**. *48*. 10-18.

[5] J. Schmelzer, S. Rittinghaus, A. Weisheit, M. Stobik, J. Paulus, K. Gruber, E. Wessel, C. Heinze, M. Krüger, Printability of gas atomized Mo-Si-B powders by laser metal deposition, Int. J. Refract. Metals Hard Mater. **2019**. *78*. 123–126.

[6] M. Krüger, S. Franz, H. Saage et al., Mechanically alloyed Mo-Si-B alloys with a continuous alpha-Mo matrix and improved mechanical properties, Intermetallics. **2008**. *16*. 933–941.

[7] M. Krüger, D. Schliephake, P. Jain, K.S. Kumar, G. Schumacher, M. Heilmaier, Effects of Zr additions on the microstructure and the mechanical behavior of PM Mo-Si-B alloys, JOM. **2013**. *65*. 301–306.

[8] G. Hasemann, I. Bogomol, D. Schliephake, P.I. Loboda, M. Krüger, Microstructure and creep properties of a near-eutectic directionally solidified multiphase Mo-Si-B alloy, Intermetallics. **2014**. *48*. 28–33.

[9] O. Popovych, H. Tsybenko, S. Hütter, K. Naumenko, M. Krüger, Structural analysis of gas turbine blades made of Mo-Si-B under transient thermo-mechanical loadings, Comput. Mater. Sci. **2019**. *165*. 129-136.

O–SI–05

Plastic deformability in V-rich V-Si-B alloys

Georg Hasemann[1], Christopher Müller[2], Daniel Grüner[1], Egbert Wessel[1] and Manja Krüger[1]

[1]Forschungszentrum Jülich GmbH, Institute of Energy and Climate Research, Microstructure and Properties of Materials (IEK-2), Leo-Brand-Str. 1, 52425 Jülich, Germany, g.hasemann@fz-juelich.de, d.gruener@fz-juelich.de, e.wessel@fz-juelich.de, m.krueger@fz-juelich.de

[2]Otto-von-Guericke University Magdeburg, Institute of Materials and Joining Technology, Universitätsplatz 2, 39106 Magdeburg, Germany, christopher.mueller@ovgu.de

Introduction

The refractory metal (RM) systems based on Mo and V share unique similarities in both RM-Si-B ternary systems (RM = Mo, V). Almost identical phases and phase fields can be found in which a three-phase field, consisting of a refractory metal solid solution (RM_{SS}) and the two intermetallic phases RM_3Si and RM_5SiB_2 [1,2], exists. This three-phase field is already of special scientific interest with respect to the Mo-based system and can also be found in the V-based system. Recent investigation further confirmed the existence of a ternary eutectic reaction within this three-phase field of both refractory metal systems [3–5]. A major difference between those two RM_{SS}-RM_5SiB_2-RM_3Si ternary eutectics is, however, the volume fraction of phases. While the Mo_{SS}-Mo_5SiB_2-Mo_3Si eutectic consists mainly of the of the A15-stuctured Mo_3Si phase, the major phase within its V_{SS}-V_5SiB_2-V_3Si ternary eutectic counterpart is formed by the A2-structured vanadium solid solution phase.

Compared to the Mo-Si-B system, a ternary eutectic with the V_{SS} as major phase is attractive concerning its mechanical properties. While Mo-based near eutectic Mo-Si-B alloys are very creep and oxidation resistant, their brittle-to-ductile transition temperature (BDTT) is quite high. Near-eutectic V-Si-B alloys, however, are expected to have relatively low BDTTs due to the high amount of ductile vanadium solid solution phase in the ternary eutectic microstructure.

Vanadium-based alloys are in recent focus as promising and new type of low density high temperature materials. This work describes a study of the microstructure evolution and mechanical properties by compression tests of different V-Si-B alloys as well as the V(Si) solid solution phase.

Materials and Methods

The V-Si-B alloys of the present study were taken from different primary solidification fields of V_{SS}, V_3Si, and V_5SiB_2. Furthermore, V(Si) solid solution alloys with different Si concentrations ranging from 1-7 at.% were chosen for investigation. The alloys were processed via conventionally arc-melting and samples were manufactured by electrical discharge machining.

Room temperature compression tests were performed using an electro-mechanical universal testing machine and a constant crosshead speed corresponding to an initial (engineering) strain rate of 10^{-3} s^{-1}. The room temperature yield stresses were determined by the 0.2% offset method. The obtained results were evaluated by SEM-EBSD scans and TEM.

Results and Discussion

The present study represents a first systematic study of room temperature compressive behavior of V-Si-B alloys [6]. Exemplarily, the microstructure of alloy V-10Si-10B after compression testing at room temperature is shown in Fig. 1. Beside large V_5SiB_2 primary crystals with a needle-like morphology, the alloy V-10Si-10B consists of secondary V_3Si phases and large V_{SS}-V_5SiB_2 two-phase eutectic areas. The alloy showed yielding at 1260 ±50 MPa and can be plastically deformed up to 2.5 % until brittle fracture occurs. In the deformed microstructure, cracks are clearly visible in the dark gray, primary V_5SiB_2 phases and in the gray, secondary V_3Si phases. Furthermore, crack bridging and deflection can be observed within the two-phase eutectic V_{SS}-V_5SiB_2 grains in which the V_{SS} carries the plastic deformation and is able to even stop the crack propagation at brittle-ductile interfaces.

Fig. 2 shows a small section of a deformed V_{SS}-V_5SiB_2 eutectic grain. Dislocation networks due to the plastic deformation can clearly be observed in the V_{SS} phase while the intermetallic V_5SiB_2 phase is dislocation-free. Compared to other three-phase V-Si-B alloys investigated in the present study, the volume fraction of the ductile V_{SS} phase controls the plastic deformability of these alloys. Thus, with increasing volume fraction of the V_{SS} phase the yield stress decreases while the plastic strain increases. Since alloys with three different primary phases, namely V_{SS}, V_3Si, and V_5SiB_2, are investigated, the alloy containing primary V_{SS} dendrites has the highest plastic strain compared to the other respective primary crystallization areas.

The V-Si-B alloys and the single-phase V_{SS} alloys investigated in the present work show room temperature plasticity during compression tests. This finding is really unexpected, since Mo-Si-B alloys including comparable Si and B concentrations are fairly brittle at RT and even at higher temperatures up to 800 °C. The V_{SS} phase is ductile up to its maximum Si solubility (≈ 7 at.%).
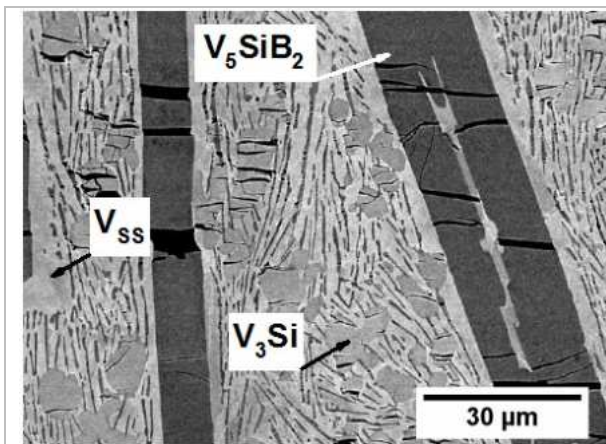
| Fig. 1: Deformed microstructure of V-10Si-10B with 2.5 % plastic strain | Fig. 2: STEM bright field image of a binary eutectic section in alloy V-10Si-10B showing the presence of dislocations only in the V_{ss} phase. |
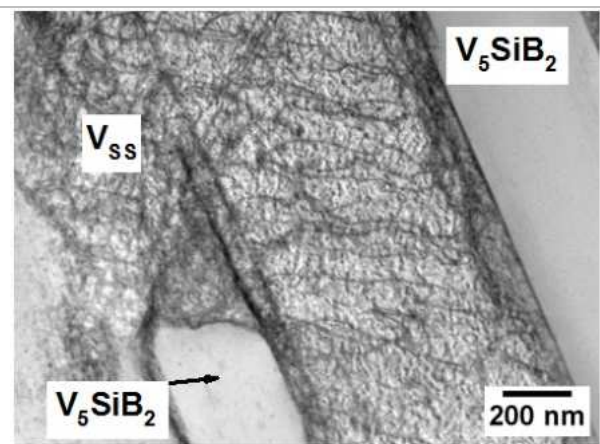
References

[1] H. Nowotny, E. Dimakopoulou, H. Kudielka, Mh. Chem. 88. **1957**. 180–192.
[2] C.A. Nunes, B.B. De Lima, G.C. Coelho, P.A. Suzuki, J. Phase Equilibria Diffus. **2009**. 345–350.
[3] S.H. Ha, K. Yoshimi, J. Nakamura, T. Kaneko, K. Maruyama, R. Tu, T. Goto, J. Alloys Compd. **2014**. *594*. 52–59.
[4] G. Hasemann, D. Kaplunenko, I. Bogomol, M. Krüger, JOM. **2016**. *68*. 2847–2853.
[5] G. Hasemann, M. Krüger, M. Palm, F. Stein, Mater. Sci. Forum **2018**. *941*. 827–832.
[6] G. Hasemann, C. Müller, D. Grüner, E. Wessel, M. Krüger, Acta Mater. **2019**. *175*. 140-147.

O–SI–06

Microstructure optimization of directionally-solidified MoSi$_2$/Mo$_5$Si$_3$ eutectic composites

Kosei Takeda[1], Yuki Kambara[2], Kyosuke Kishida[3] and Haruyuki Inui[4]

[1] Department of Materials Science & Engineering, Kyoto University, Kyoto 606-8501, Japan,
takeda.kousei.73u@st.kyoto-u.ac.jp

[2] Department of Materials Science & Engineering, Kyoto University, Kyoto 606-8501, Japan,
kambara.yuki.56e@kyoto-u.jp

[3] Department of Materials Science & Engineering, Kyoto University, Kyoto 606-8501, Japan,
kishida.kyosuke.6w@kyoto-u.ac.jp

[4] Department of Materials Science & Engineering, Kyoto University, Kyoto 606-8501, Japan,
inui.haruyuki.3z@kyoto-u.ac.jp

Introduction

MoSi$_2$/Mo$_5$Si$_3$ eutectic composites are promising materials suitable for ultra-high temperature structural applications because of its high eutectic temperature above 1900 ºC and good high-temperature mechanical properties due to their very fine microstructure of script-lamellar type developed by directional solidification (DS). However, further improvement of high temperature strength and poor fracture toughness at room temperature is required for their practical applications. Recently, we have systematically investigated the influences of ternary and quaternary additions on the microstructural characteristics and mechanical properties of MoSi$_2$/Mo$_5$Si$_3$ DS eutectic composites and have revealed that Ta addition is beneficial in improving room-temperature fracture toughness and high-temperature strength of DS MoSi$_2$/Mo$_5$Si$_3$ eutectic composite [1-4]. These previous results suggest that further improvement of room-temperature fracture toughness and high-temperature strength of the eutectic composite is highly possible if much finer and homogeneous lamellar microstructure is obtained by optimizing the growth conditions during the DS process. In this study, we have investigated the influences of growth conditions of the DS process on microstructures and mechanical properties of DS MoSi$_2$/Mo$_5$Si$_3$ eutectic composites with ternary and quaternary additions in order to establish a way to further improve their mechanical properties through microstructure optimization.

Materials and Methods

Ingots of MoSi$_2$/Mo$_5$Si$_3$ eutectic alloys with ternary and quaternary additions were prepared by arc-melting. DS ingots were grown by floating zone (FZ) method at growth rates ranging from 10 to 200 mm/h using two types of optical floating zone furnaces equipped with either (a) two halogen lamps or (b) one Xe-arc lamp as the heat source. Microstructures and chemical compositions of constituent phases of the DS ingots were investigated by scanning electron microscopy (SEM). Compression tests were carried out on an Instron-type testing machine at a strain rate of 1 × 10^{-4} s^{-1} at temperatures ranging from 1000 to 1400 °C in vacuum. The loading axis of $[1\bar{1}0]_{MoSi2}$, parallel to the growth direction of the DS ingots, was selected. Room-temperature fracture toughness were evaluated by the indentation method.

Results and Discussion

A homogeneous script-lamellar structure is observed for most DS ingots grown at relatively low growth rates, while a heterogeneous cellular-structure with the fine eutectic lamellae in the center of the cells surrounded by the coarse ones at the cell boundaries is developed at higher growth rates especially in the DS eutectic composites with ternary and quaternary additions (Fig. 1(a)). The occurrence of the homogeneous-to-cellular transition at relatively low growth rates for ternary and quaternary alloyed DS eutectic composites is found to be suppressed successfully when the DS ingot is grown using a FZ furnace equipped with a Xe-arc lamp source with a higher temperature gradient (Fig. 1(b). Average lamellar thickness of the eutectic composites with a homogeneous script-lamellar structure decreases with increasing growth rate basically following the Jackson-Hunt relationship [4]. Both high-temperature strength and room-temperature fracture toughness of Ta-alloyed eutectic composites are confirmed to be improved drastically with the decrease in the average lamellar thickness maintaining the microstructure homogeneity achieved through the optimization of the growth conditions during the DS process.

Fig. 1: Typical microstructures of $MoSi_2/Mo_5Si_3$ eutectic composites with Ta directionally solidified in FZ furnaces with (a) two halogen lamps and (b) Xe-arc lamp as the heat source. Dark and bright regions correspond to $MoSi_2$ and Mo_5Si_3, respectively.
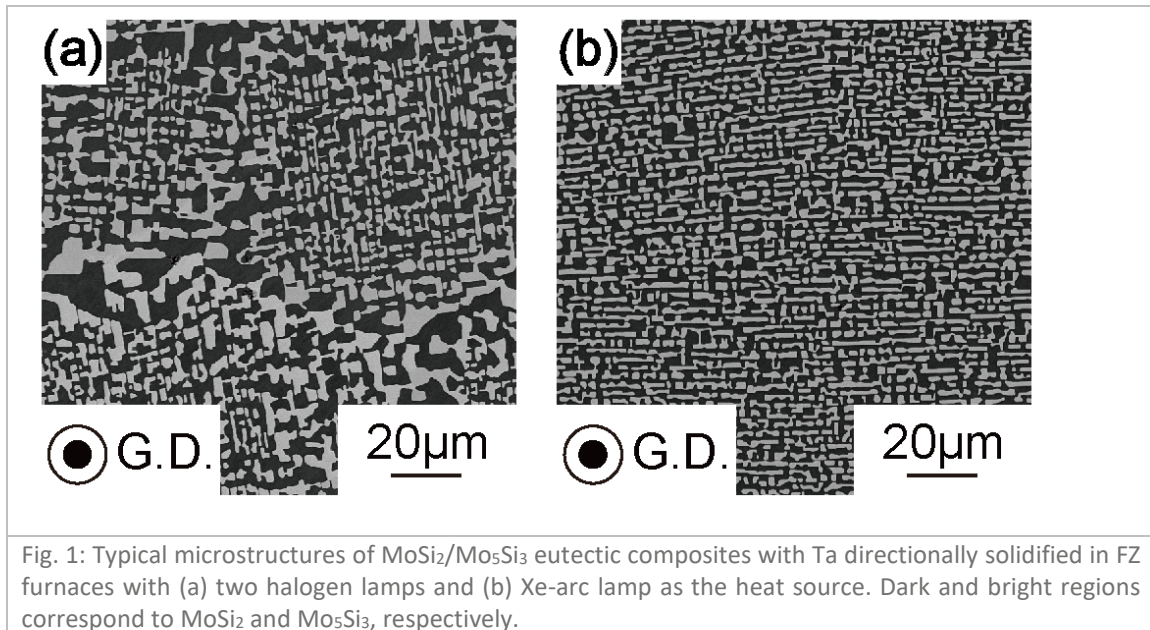
References
[1]   K. Fujiwara, H. Matsunoshita, Y. Sasai, K. Kishida, H. Inui, Intermetallics **2014**. *52*. 72-85
[2]   H. Matsunoshita, K. Fujiwara, Y. Sasai, K. Kishida, H. Inui, Intermetallics **2016**, *73*. 12-20
[3]   H. Matsunoshita, Y. Sasai, K. Fujiwara, K. Kishida, H. Inui, Sci. Technol. Adv. Mater., **2016**. *17*. 517-529
[4]   J. A. Vega, H. Matsunoshita, K. Kishida, H. Inui, Materials Charactalization **2019**. *148*. 162-170

O–SI–07

Characterisation of the oxidation and creep behaviour of novel Mo-Si-Ti alloys

Susanne Obert, Alexander Kauffmann and Martin Heilmaier

Karlsruhe Institute of Technology (KIT), Institute for Applied Materials (IAM-WK), Engelbert-Arnold-Straße 4, 76131 Karlsruhe, Germany, susanne.obert@kit.edu, alexander.kauffmann@kit.edu, martin.heilmaier@kit.edu

Introduction

In order to cope with increasing demands for materials in high temperature applications, focus is placed on the development of alternatives to Ni-based superalloys. Especially in turbine applications, Ni-based superalloys operate at their limits as the solvus temperature of γ' of about 1100 °C should not be exceeded [1]. Thereby, the turbine efficiency is limited by the maximum operating temperature in the range of 1400 °C when thermal barrier coatings or cooling techniques are applied [2]. With the aim to enhance the turbine efficiency by increasing the operating temperature, Mo-Si based alloys with melting temperatures in the order of 2000 °C are of interest. Among the different published concepts for Mo-Si based alloys, the concept of macro-alloying Mo-Si-B alloys with Ti has shown promising results regarding an adequate creep resistance combined with a suitable oxidation resistance at temperatures above 1000 °C [3, 4, 5]. The main advantages of this alloying strategy are: (i) stabilisation of Mo_5Si_3 which can substitute the less-oxidation resistant phase Mo_3Si, (ii) considerable density reduction and (iii) improvement of the creep resistance of the Mo solid solution Mo_{SS} due to solid solution strengthening by Ti. In order to further benefit from macro-alloying with Ti, ternary Mo-Si-Ti alloys have been developed. Here, one profits from eutectic (L → Mo_{SS} + Ti_5Si_3) and eutectoid reactions (Mo_3Si → Mo_{SS} + Mo_5Si_3) which result in fine lamellar microstructures [6]. These are promising regarding quick passivation of the metal substrate during oxidation even without the addition of B. An almost entirely binary eutectic alloy consisting of Mo_{SS} and Ti_5Si_3 is found to possess an outstanding oxidation resistance, even at 800 °C where pesting is typically observed in Mo-Si based alloys [6]. In contrast, an almost entire eutectoid alloy comprising Mo_{SS} and Mo_5Si_3 suffers from pesting, but shows significantly improved creep resistance compared to the eutectic alloy [6]. Both alloys possess promising low densities of only 6 to 7 g/cm^3 [6]. In order to combine both, suitable oxidation and creep resistance, novel Mo-Si-Ti alloys with tailored eutectic-eutectoid microstructures, comprising Mo_{SS}, Mo_5Si_3 and Ti_5Si_3, are developed in the present study.

Materials and Methods

Alloy development was guided by thermodynamic calculations based on the Calphad method. Therefore, the PANDAT software package (version 2018) and the commercially available database (PanMo2018a) were used. The alloys were arc-melted from high-purity elements under Ar-atmosphere in an AM/0,5 arc melter by Edmund Bühler GmbH. Samples were electrical discharged machined and differently prepared depending on their intended use: (i) oxidation and creep samples were ground down to SiC grit P2500 and (ii) metallographic samples were additionally polished to 1 μm diamond suspension and finished using colloidal suspension (OPS). Microstructural analyses were performed using a LEO EVO 50 scanning electron microscope (SEM) by Zeiss with an integrated energy dispersive x-ray (EDX) spectroscopy system. Compressive creep tests were performed under vacuum at 1200 °C at varying constant true stresses from 50 to 300 MPa on a universal testing machine by Zwick equipped with a vacuum furnace by Maytec. Cyclic and isothermal oxidation tests were carried out at 800 °C, 1100 °C and 1200 °C for up to 100 h. The cyclic oxidation tests were conducted under laboratory air in muffle furnaces provided by Gero and Nabertherm, while the isothermal tests were conducted under synthetic air using a thermogravimetric analyser STA449 by Netzsch.

Results and Discussion

Besides the eutectic Mo-20Si-52.8Ti (at%) and the eutectoid Mo-21Si-34Ti (at%) reference alloys, two novel alloy series within the chemical composition range framed by the two reference alloys were investigated. Namely, the Ti-rich alloy series A (A1: Mo-21Si-43.4Ti, A2: Mo-20.5Si-43.4Ti) and the Ti-lean alloy series B (B1: Mo-21Si-38.7Ti, B2: Mo-20.25Si-38.7Ti). The Si-content was slightly varied within these alloy series in order to adjust the amount of primary solidified Mo_{SS} which is believed to be detrimental for oxidation resistance but beneficial for creep resistance. To yield complete eutectoid decomposition of Mo_3Si, an additional heat-treatment of the B alloys at 1300 °C for 200 h is required. Microstructural analyses of the novel alloys reveal tailored, eutectic-eutectoid microstructures with adjustable volume fraction of primary solidified Mo_{SS}.

Experimental studies on the oxidation behaviour show: (i) Comparable oxidation behaviour of all alloys at 1100 °C and 1200 °C with reasonable low mass change being attributed to the formation of an outer TiO_2 oxide scale and an underlying SiO_2-TiO_2 duplex scale. (ii) Outstanding oxidation behaviour of the eutectic alloy with respect to insignificant mass change at 800 °C and formation of a mixed SiO_2-TiO_2 scale. (iii) No pesting behaviour of the A alloys at 800 °C, especially alloy A1 showed similar behaviour as the eutectic alloy. However, some inhomogeneous internal oxidation was observed, especially in alloy A2 which contains an increased volume fraction of primary solidified Mo_{SS}. Finally, (iv) pesting behaviour of the eutectoid alloy and the B alloys at 800 °C was noted. It was found that initial oxidation in the A and B alloys occurs preferentially in the eutectoid regions. Therefore, the volume fraction of eutectic might be essential to suppress pesting as in the A alloys comprising minimum 50 vol% eutectic pesting does not occur. Furthermore, it is supposed that there exists a Ti threshold content solved in Mo_{SS} for pesting to occur which increases from 24 at% (eutectoid alloy) through 28 at% (B alloys) to 31 at% (A alloys) and finally 55 at% (eutectic alloy).

On examination of the compressive creep behaviour of the A alloys, it can be noted that their minimum creep rate lies in between the creep resistant eutectoid alloy and the oxidation resistant eutectic alloy. A further slight improvement of creep resistance could be achieved by increasing the volume fraction of primary solidified Mo_{SS} (alloy A2). All alloys discussed here exhibit stress exponents between 3 and 4 which proves creep deformation to be dislocation climb controlled [6]. In conclusion, this work successfully introduces novel Mo-Si-Ti alloys with tailored, eutectic-eutectoid microstructures which enable balanced combinations of oxidation and creep resistance.

References

[1]   T. Grosdidier, A. Hazotte, A. Simon, Materials Science and Engineering. **1998**, A256, 183-196.

[2]   J. H. Perepezko, Science. **2009**, 326, 1068-1069.

[3]   D. Schliephake, M. A. Azim, K. v. Klinski-Wetzel, B. Gorr, H.-J. Christ, H. Bei, E. P. George, M. Heilmaier, Metallurgical and Materials Transactions A. **2014**, 45A, 1102-1111.

[4]   M. A. Azim, S. Burk, B. Gorr, H.-J. Christ, D. Schliephake, M. Heilmaier, R. Bornemann, P. H. Bolívar, Oxidation of Metals. **2013**, 80, 231-242.

[5]   M. A. Azim, D. Schliephake, C. Hochmuth, B. Gorr, H.-J. Christ, U. Glatzel, M. Heilmaier, Journal of The Minerals, Metals & Materials Society. **2015**, 67, 2621-2628.

[6]   D. Schliephake, A. Kauffmann, X. Cong, C. Gombola, M. A. Azim, B. Gorr, H.-J. Christ, M. Heilmaier, Intermetallics. **2019**, 104, 133-142.

P–01

New mechanism of softening in titanium aluminide – experiment and theory

<u>Nitish Bibhanshu</u> and Satyam Suwas

Department of Materials Engineering, Indian Institute of Science, Bangalore 560012, India

nitishbibhanshu@gmail.com, satyamsuwas@iisc.ac.in

Introduction

Titanium Aluminides have very high specific strength, low density and high operating temperature [1]. These properties make these alloys amenable for the replacement of Ni‑based superalloys used in gas turbines [2]. Currently, it is used in low pressure regime in as‑cast condition, but for the application in high pressure regime, it is desirable to develop wrought titanium aluminides [3]. The objective of the present investigation is to develop a theory which leads to the maximum recrystallisation during the deformation.

Materials and Methods

Titanium aluminides with nominal composition of Ti-48Al-2V-2Nb at.% were prepared from the vacuum arc melting furnace in argon atmosphere. Cylindrical samples of the dimension $\varnothing6\times9$ mm^3 were prepared and the machining was carried out in such a way that its c-axis was perpendicular to solidification direction. Hot deformation of the finished samples was performed on the Gleeble 3800, in the argon atmosphere to avoid the oxidation. The deformations were performed at the strain rate of 10 s^{-1} and for the temperatures of 1000, 1100, 1150 and 1175 ˚C (1000 and 1100 ˚C are ordered region, $\alpha_2 -$ phase and 1150 and 1175 ˚C are dis-ordered regime, α – phase). The heating rate and soaking time was 3 ˚C/s and 5 min, respectively, to equilibrate the microstructural features at the deforming temperature. To characterise the mechanism of softening, the samples were deformed to 50% (~0.7 true strain). Deformed samples were characterised by the ESEM Quanta 200 and EBSD measurements were carried out on the HELIOS.

Results and Discussion

Deformation curves and microstructural features reveal that the fraction of dynamically recrystallized grains increased with the rise in deformation temperature. With the deformation, the deviation from the orientation relationship was also identified. The result reveals that deformation in the disordered regime leads to the more deviation from the OR of TiAl and Ti$_3$Al phase. Further analysis showed that the nucleation of dynamically recrystallized grains occurs at the twin-parent grain boundary and within the laths. These recrystallized grains were forming in {111} – oriented planes when these planes tilt at a particular angle with respect to the compression direction. In addition to it, the softening behaviour and change in crystallographic orientation of the laths during hot deformation were also analysed. It was observed that these laths were twisted by 15° under the unidirectional compression. In order to comprehend the twist, tilt and dynamic recrystallization of TiAl and Ti$_3$Al laths, a new mechanism has been proposed. Mechanism explains the systematic procedure of the lath kinking, breaking, its rotation and mechanism of the dynamic recrystallisation.

References

[1] J. Guyon, A. Hazotte, F. Wagner, E. Bouzy, Recrystallization of coherent nanolamellar structures in Ti48Al2Cr2Nb intermetallic alloy, Acta Mater. 103. **2016**, 672–680.

[2] A. Lasalmonie, Intermetallics: Why is it so difficult to introduce them in gas turbine engines?, Intermetallics. 14. **2006**, 1123–1129.

[3] P.G. Handbook, D.E. Library, T.M. Companies, Gas turbine combustors. **2004**.

P–02

Analysis of local deformation behavior in TiAl based alloys under tensile loading by digital image correlation

Yotaro Okada, Ryosuke Yamagata, Hirotoyo Nakashima and Masao Takeyama

Department of Materials Science and Engineering, School of Materials and Chemical Technology, Tokyo Institute of Technology, 2-12-1, Ookayama, Meguro-ku, Tokyo, Japan, okada.y.am@m.titech.ac.jp, yamagata.r.aa@m.titech.ac.jp, nakashima.h.aa@m.titech.ac.jp, takeyama@mtl.titech.ac.jp

Introduction

γ-TiAl based alloys, mainly consisting of β-Ti, α_2-Ti$_3$Al, and γ phases, are promising material for high temperature applications up to 800°C because of their light weight and high creep strength. However, the application of this material to jet engines is limited to the last stages of low-pressure turbine blades. In order to apply this material to other parts, improvement of properties such as room temperature ductility and crack growth resistance is essential. β phase is generally considered to be a detrimental phase in TiAl based alloys because it's a hard and brittle at room temperature and soft at high temperature [1]. In our group, however, a microstructure design principle for improvement of hot workability using β phase has been developed [2], and we have demonstrated that β phase can improve creep resistance and fatigue crack growth resistance by controlling the microstructure properly [3,4]. This means β phase itself is not detrimental. In order to understand the role of each microstructure constituent in mechanical properties and obtain a new guideline for microstructure design, it is important to capture local strain behavior of each microstructure constituent at microscopic scale. In the present study, we have conducted tensile tests to TiAl alloys with microstructure constituents of α_2/γ lamellar colonies, β phase, and γ phase at room and high temperature, and local deformation behavior has been analyzed using *in-situ* and *ex-situ* SEM observation and digital image correlation (DIC) based strain measurement.

Materials and Methods

Alloys presented in this study are Ti-Al-M$_1$-M$_2$ (M: β stabilizing V or VI group element). These alloys were fabricated using cold crucible induction melting and gravity casting, and forged by one stroke at 1573 K. Then, the forged alloys were heat-treated to control microstructure based on our phase diagram studies. The microstructures consist of α_2/γ lamellar colonies, β phase, and γ phase with a wide range of volume fraction and morphology. Two typical examples are nearly lamellar (NL) and nearly β/γ globular duplex (NGDP). NL microstructure shows α_2/γ lamellar colonies with a diameter of 100 μm and small amount of β and γ grains on the lamellar colony boundaries, and NGDP microstructure shows mainly globular β and γ phases with diameters of 20 μm. The volume fraction of lamellar colony is 90% and 6% respectively. Tensile tests were performed on flat dog bone shaped specimens with a gage section of 1×3 mm^2 and a gage length of 14 mm in a FE-SEM at room temperature and 1073 K. The elongation was measured from the displacement of cross head and the distance of markers introduced with a Vickers hardness tester. In-plane strain fields after and during tensile were measured from SEM secondary electron images of sample surface using DIC technique. The spatial resolution of strain measurement is approximately 1–2 μm. Before testing, crystal orientation analysis was conducted by SEM-EBSD method.

Results and Discussion

Fig. 1 shows engineering stress vs. plastic strain curves of NL and NGDP samples at room temperature. The NL sample shows a fracture stress of 761 MPa and an elongation of 0.14%, and the NGDP sample shows a higher fracture stress and elongation of 871 MPa and 0.49%. Fig. 2 shows a backscattered electron image of NGDP sample before deformation (Fig. 2 (a)) and a strain map for the corresponding region after fracture (Fig. 2 (b)). In β/γ duplex microstructure, strain is mainly observed in γ grains and in β phase regions near β/γ phase boundaries. In γ grains, slip lines or micro twins are observed along one or more {111} plane traces, and high localized strain occurs along them. On the other hand, grain interior of β phase shows no obvious deformation feature and high strain occurs only near β/γ phase boundaries. β phase is harder than γ phase at room temperature in TiAl alloys. Thus, this localized strain near β/γ phase boundaries could be caused by dislocation pile-ups at the boundaries from deformation of γ phase. Average strain of each phase is calculated from the strain measurement and EBSD result in the area shown in Fig. 2, and γ phase shows higher strain than β and α_2 phases by a factor of 2.5–3. However, γ single phase alloy shows limited elongation of 0.06% [5]. Therefore, it is suggested that the existence of β/γ phase boundaries improves room temperature ductility of TiAl alloys by inducing deformation of β phase and multiple slip in γ grains. Deformation behavior at high temperature will also be presented.
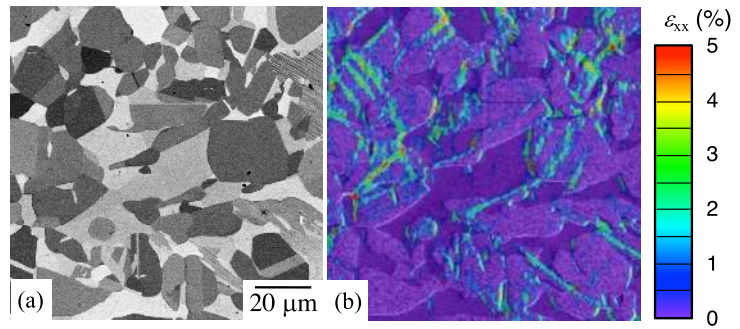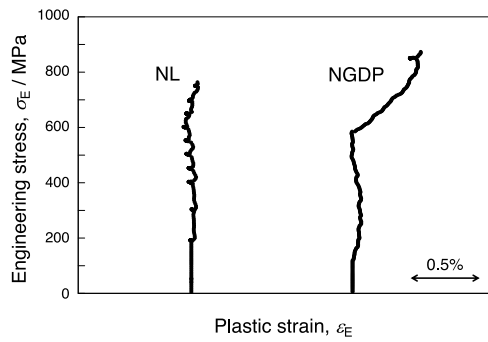
Fig. 1 Engineering stress vs. plastic strain curves of NL and NGDP samples.

Fig. 2 (a) Backscattered electron image of NGDP sample before deformation, (b) strain map for corresponding region after fracture.

References
[1]   F. S. Sun, C. X. Cao, S. E. Kim, Y. T. Lee, M. G. Yan, Metallurgical and Materials Transactions A. **2001**, *32*, 1573–1589.
[2]   M. Takeyama and S. Kobayashi, Intermetallics. **2005**, *13*, 993–999.
[3]   H. Wakabayashi, L. J. Signori, A. Shaaban, R. Yamagata, H. Nakashima, M. Takeyama, MRS Advances. **2019**.
[4]   L. J. Signori, T. Nakamura, Y. Okada, R. Yamagata, H. Nakashima, M. Takeyama, Intermetallics. **2018**, *100*, 77–87.
[5]   R. Yamagata, Y. Okada, H. Wakabayashi, H. Nakashima, M. Takeyama, MRS Advances. under reviewing.

P–03

Initial structures effect on O-phase morphology and properties of orthorhombic titanium alloys

Anatoly Volkov, Alexei Pankratov, Natalia Lagunova, Michael Leder, Elena Shushakova,
Kirill Rusakov and Maxim Kalienko

PSC VSMPO-AVISMA Corporation, Parkovaya st. 1, Verkhnaya Salda 624760, Russia, volklovav@vsmpo.ru,
pankratov_an@vsmpo.ru

Introduction

Titanium-based ortho alloys are a relatively promising direction for the development of intermetallic alloys. The temperature O phase formation about 950°C limits 600-700 °C the maximum operating temperature of this alloys, which is significantly lower than the gamma of titanium alloys (> 700 °C), but higher than solid-solution titanium alloys based on α-phase (<600 °C). Acceptable creep resistance combined with enhanced crack resistance relative to gamma titanium aluminides make the O-based alloys attractive. Unlike gamma aluminides and pseudo α-titanium alloys, β+O based titanium alloys are heat-strengthened, which gives additional advantages in adapting the properties of the alloy to the processing stage: a strength decrease at the deformation and machining stage, obtaining the target strength and complex properties in the finished geometry of the product. Despite the clear principles of structure formation [2,4,6] the questions of the strengthening O-phase morphology related with initial structure, remain open. Understandable general tendencies in relation of structural parameters and short-term properties and creep resistance in some cases change to contradict general trends.

The paper considers the influence of the type of the initial structure with a large proportion of the primary O-phase on the morphology of the selection of the strengthening O-phase, as well as the relation of the structure with mechanical properties and creep resistance.

Materials and Methods

X-ray diffraction analysis (XRD) of samples was performed on a Bruker D8 Advance diffractometer with a LynxEye detector. XRD patterns were taken in copper radiation in the following conditions: tube voltage of 40 kV, tube current of 40 mA, step size 0.02°, exposure 0.5 sec per point. The lattice parameters were refined using TOPAS 3 software by a whole pattern modeling in the angle range of 34 to 43 º 2θ. The qualitative phase analysis of the annealed samples was performed using crystallographic database PDF2007 and software package EVA13.0.0.3. The diffractometer was aligned using the corundum (NIST SRM1976b). Vickers micro hardness measurements were made using a diamond square pyramid indenter and 1000 g load by Struers Duramin 5 tester. Cold tensile testing was performed for the compliance with ASTM E8 on samples with gauge diameter 6.35 mm – two samples per each heat treatment condition. Structure was examined on sample grip sections using SEM Quanta 3D FEG with the phase contrast in back-scattered electrons. Chemical composition of phases was determind with EDS EDAX Genesis 2000 with Si-Li detector. Micro slices for SEM examination were prepared by electropolishing in electrolyte: 1 part by volume of perchloric acid ($HClO_4$), 4 parts by volume of glacial acetic acid, voltage 60-70 V.

Results and Discussion

The morphology of the release of the O phase is driven by the overcooling temperature relative to the equilibrium temperature of the release of the β-phase, as well as the number of β-phase defects at which the O-phase originates. The O-phase released in the β-grain recrystallized in β-field is on average 2 times longer with a close thickness compared to O-phase created from β-phase recrystallized in $\alpha_2 + $ β field. Homogeneous growth of the O-phase during slow cooling from these temperatures results in a similar morphology, much more coarse compared with the isothermal release. Strength and plasticity correlate well with the dispersion of the O-phase. Subsequent aging at temperatures below 750 °C changes the morphology of the O-phase in accordance with the initial morphology of the primary O-phase. In structures with a small primary O-phase homogeneous growth occurs with an increase in the volume fraction (Fig.1), and in structures with a coarse primary O-phase, a heterogeneous mechanism is released (Fig.2), and the dispersion of the O-phase increases with decrease in temperature of aging. It does not find a directly proportional response in strength and ductility, in some cases leading to softening. Resistance to creep of various structures also does not correlate with the morphology of the primary and secondary secretions of the O-phase.
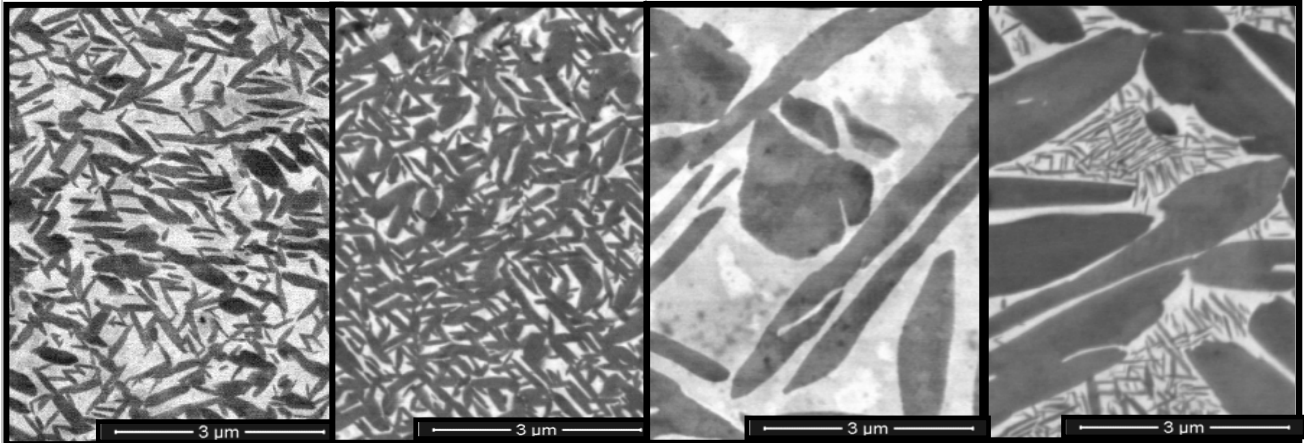
| Fig. 1: Microstructure a) initial from α_2 + β region with 50% primary O-phase, b) + 750°C, 6h aging | Fig. 2: Microstructure a) initial from β region with 50% primary O-phase, b) + 750°C, 6h aging |

References

[1] Cowen, C.J., and C.J. Boehlert, Microstructure, Creep, and Tensile Behavior of a Ti–21Al–29Nb(at.%) Orthorhombic+B2 Alloy, Intermetallics, 14 **2006**, 412–22

[2] Dey, S.R., Shibayan Roy, Satyam Suwas, J.J. Fundenberger, and R.K. Ray, Annealing Response of the Intermetallic Alloy Ti–22Al–25Nb, Intermetallics, 18 **2010**, 1122–31

[3] Shankar, Hari, N. Eswara Prasad, A.K. Singh, and T.K. Nandy, Low Temperature Flow Behavior of B2 Intermetallic Phase in Ti–Al–Nb System, Materials Science and Engineering: A, 424 **2006**,

[4] Wang, Wei, Weidong Zeng, Chen Xue, Xiaobo Liang, and Jianwei Zhang, Microstructural Evolution, Creep, and Tensile Behavior of a Ti–22Al–25Nb At% Orthorhombic Alloy, Materials Science and Engineering: A, 603 **2014**, 176–84

[5] Microstructure Control and Mechanical Properties from Isothermal Forging and Heat Treatment of Ti–22Al–25Nb at.% Orthorhombic Alloy, Intermetallics, 56 **2015**, 79–86

[6] Quantitative Analysis of the Effect of Heat Treatment on Microstructural Evolution and Microhardness of an Isothermally Forged Ti–22Al–25Nb at.% Orthorhombic Alloy, Intermetallics, 45 **2014**, 29–37

[7] Xue, Chen, Weidong Zeng, Wei Wang, Xiaobo Liang, and Jianwei Zhang, Quantitative Analysis on Microstructure Evolution and Tensile Property for the Isothermally Forged Ti2AlNb Based Alloy during Heat Treatment, Materials Science and Engineering: A, 573 **2013**, 183–89

P–04

Comparative study on the oxidation behavior of two commercial TiAl alloys at 600-900 °C in air

Lukas Mengis[1], Anke S. Ulrich[1], Alexander Donchev[1] and Mathias C. Galetz[1]

[1]DECHEMA Forschungsinstitut, Theodor-Heuss-Allee 25, 60486 Frankfurt am Main, mengis@dechema.de

Introduction

Titanium aluminides (TiAl) have been successfully implemented as high-temperature materials in today´s commercial aero-engines. However, their maximal service temperature is limited to approximately 750 °C, among others, because of their insufficient oxidation resistance [1]. Above this temperature, oxidation leads to the formation of a fast growing non-protective, mixed oxide scale that consists of mainly TiO_2 and Al_2O_3. Additionally, an undesirable oxidation-induced embrittlement of the alloys can occur, being accompanied with a degradation of the mechanical properties at room temperature [2]. As a matter of fact, the oxidation behavior of TiAl is often investigated at temperatures well above the actual service temperature of the alloys. Therefore, within this study, a comparative investigation on the oxidation behavior of two TiAl alloys has been undertaken covering a wide temperature range together with a considerable duration of exposure.

Materials and Methods

Within the scope of this study, the isothermal oxidation behavior of the two commercial TiAl alloys TNM-B1 and GE 48-2-2 (both in HIPped conditions) has been investigated at 600-900 °C for 24–1000 h in air. TGA measurements for up to 100 h in air have been additionally conducted to generate information about the fundamental oxidation kinetics of both alloys. Under the assistance of different metallographic techniques (XRD, SEM, EDS and EPMA), the basic morphology of the oxide scales as well as potential microstructural changes directly at the interface between the oxide scale and the substrate have been characterized. Moreover, four-point-bending tests and nanoindentation measurements after exposure were conducted at room-temperature in order to investigate the actual influence of oxidation on the mechanical properties.

Results and Discussion

Both alloys show a rather negligible mass gain after 100 h at 600 °C and 700 °C in air, moreover, the surfaces appear still metallic and golden in color. Interestingly, mass gain of the GE 48-2-2 alloy strongly raised at 800 °C, whereas the TNM-B1 showed only a slight increase compared to the exposure at 700 °C. Henceforth, the surfaces no longer appear metallic but are covered by a gray oxide scale. Both alloys exhibited nearly the same mass gain after exposure at 900 °C for 100 h. The thick oxide scales no longer adhered well at the surfaces but partially spalled off during cooling. Metallographic investigation of the cross sections after exposure at 600 °C and 700 °C revealed an oxide scale thickness in the nm-scale. Nevertheless, needle-like precipitates were observed within the β_0-grains, which were located directly at the surface. After 1000 h at 700 °C, these precipitates have been identified in even deeper regions of the substrate 10 µm below the thin oxide scale (Fig. 1). While only a 3 µm thick oxide scale has formed on the TNM-B1 alloy after oxidation at 800 °C, an even thicker oxide scale on the GE 48-2-2 already shows the well-known structure of oxides that can be typically observed on TiAl alloys after oxidation (Fig. 2). TiO_2 has formed as an outermost layer, followed by an Al_2O_3-rich/TiO_2 intermediate zone. Moreover, a mixed Al_2O_3/TiO_2 layer has formed below. Nitrogen ingress has lead to the formation of a continuous Ti(Al)N layer at the interface between the oxide scale and the substrate for both alloys. In case of the GE 48-2-2 alloy, Cr/Nb-rich phases were identified directly below the Ti(Al)N-layer. Henceforth, coarsen needle-like precipitates in the β_0-phase have been observed 15 µm below the oxide scale. Noticeably, EPMA analysis revealed oxygen enrichment in those near-surface β_0-grains displaying the characteristic needle-like precipitates. Moreover, under the assistance of EDS analysis, it was found, that these precipitates were α_2-Ti_3Al phase. The transformation of β_0 to α_2 led to a partitioning of the β–stabilizing elements which was characterized by a distinctive enrichment of the remaining β_0–phase in Mo and Nb.
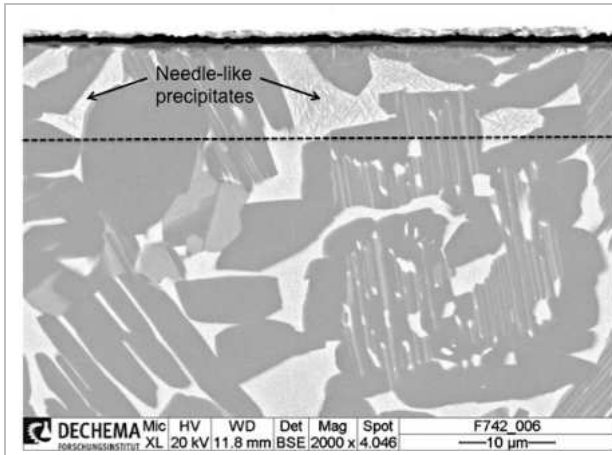
Fig. 1: BSE image of the TNM-B1 alloy after exposure at 700 °C for 1000 h in air. Needle-like precipitates are indicated by the black arrows. The affected subsurface zone is denoted by the dashed line.	Fig. 2: BSE image of a layered oxide scale that has formed on the GE 48-2-2 alloy after exposure at 800 °C for 100 h in air.
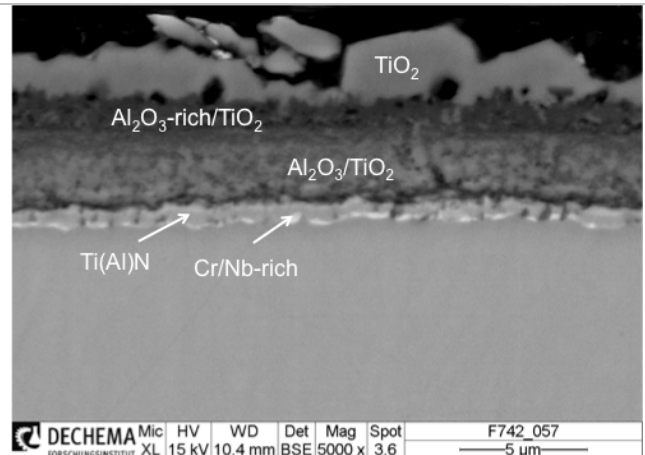
Four-point-bending tests after exposure for 100 h at 600-900 °C substantiated a noticeable degradation of the mechanical properties at room temperature for both alloys. While values for the fracture toughness and strain reached approximately the same moderately decreased level after exposure at 600, 700 and 800 °C for 100 h, a further degradation was observed after exposure at 900 °C.

References

[1]   R. Pflumm, A. Donchev, S. Mayer, H. Clemens, M. Schütze, Intermetallics, Vol. 53, **2014**, 45-55
[2]   S.K. Planck, A.H. Rosenberger, Materials Science and Engineering A325 (**2002**) 270-280

On the creep deformation and properties of the IRIS TiAl alloy at 850 °C

Alain Couret, Jean-Philippe Monchoux

CEMES, Université de Toulouse, CNRS, 29 rue Jeanne Marvig, 31055 Toulouse, France, alain.couret@cemes.fr

Introduction

The creep properties of TiAl alloys, as well as the corresponding activation parameters, have been measured in numerous TiAl alloys possessing various microstructures [1]. Due to a lack of systematic studies, the deformation mechanisms activated during creep are still poorly understood, in particular at temperatures higher than 800°C. Hence, the aim of this paper is to study the deformation mechanisms activated during the first stages of the creep of the W-containing IRIS TiAl alloy at 850°C under 150 MPa.

Materials and Methods

The material used in the present work is an IRIS-TiAl alloy (Ti-Al48-W2-B0.1, at.%) which was densified by Spark Plasma Sintering [2] at the PNF2 (Plateforme Nationale de Frittage Flash/CNRS of Toulouse, France). Its microstructure is formed by small lamellar grains (GS < 50 µm) surrounded by borders made of γ grains.

Fig. 1 shows the creep curve obtained at 850°C under 150 MPa. Under this solicitation, the minimum creep rate was 6x 10^{-8} s^{-1}, and the creep life 260 h. The durations to reach 0.2, 0.5 and 1% of plastic strain were 0.15 h, 1.86 h and 13h, respectively. To study the deformation mechanisms, TEM (Transmission Electron Microscope) investigations were performed on thin foils extracted in a sample crept at 850°C, under 150 MPa, till 1.5% of plastic strain. The TEM specimens were cut in the material with the loading axis either perpendicular, or parallel to the thin foil plane. 17 γ grains of borders and 5 lamellar zones were investigated.
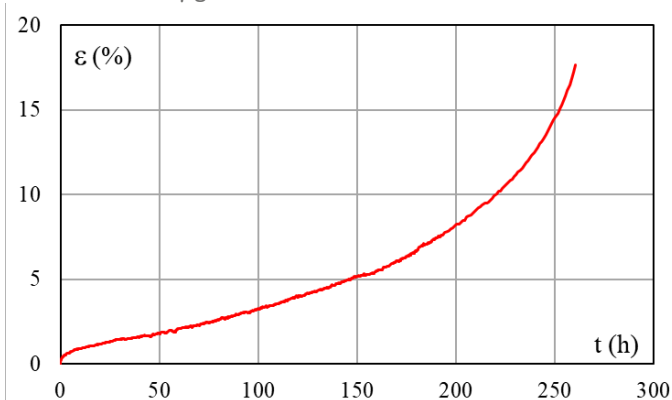
Fig. 1 : Creep curve at 850°C under 150 MPa.

Results and Discussion

Fig. 2 shows different populations of dislocations which were observed in the γ phase. They were fully characterized by TEM. The ordinary dislocations of view (a) which are elongated along their screw direction and anchored at many pinning points (arrows), were moving by glide in the (111) type planes. The main features of ordinary dislocations of view (b) is that they are lying in crystallographic planes which are perpendicular to the tensile axis of the crept sample. In this example, the dislocations are in the ($\bar{1}11$) plane but in some other cases, planes of (001) and {101} type have been found. The Burgers vector of dislocations of Fig. 2, c is [001] and the loops are in the (001) planes [3]. For these two last cases, the ordinary and [001] dislocations are moving by a climb mechanism, for which the elementary process is the nucleation and lateral propagation of a jog pair, consistently with the rectilinear aspect of the dislocations. Finally, view (d) shows a grain in which two twin systems were activated.
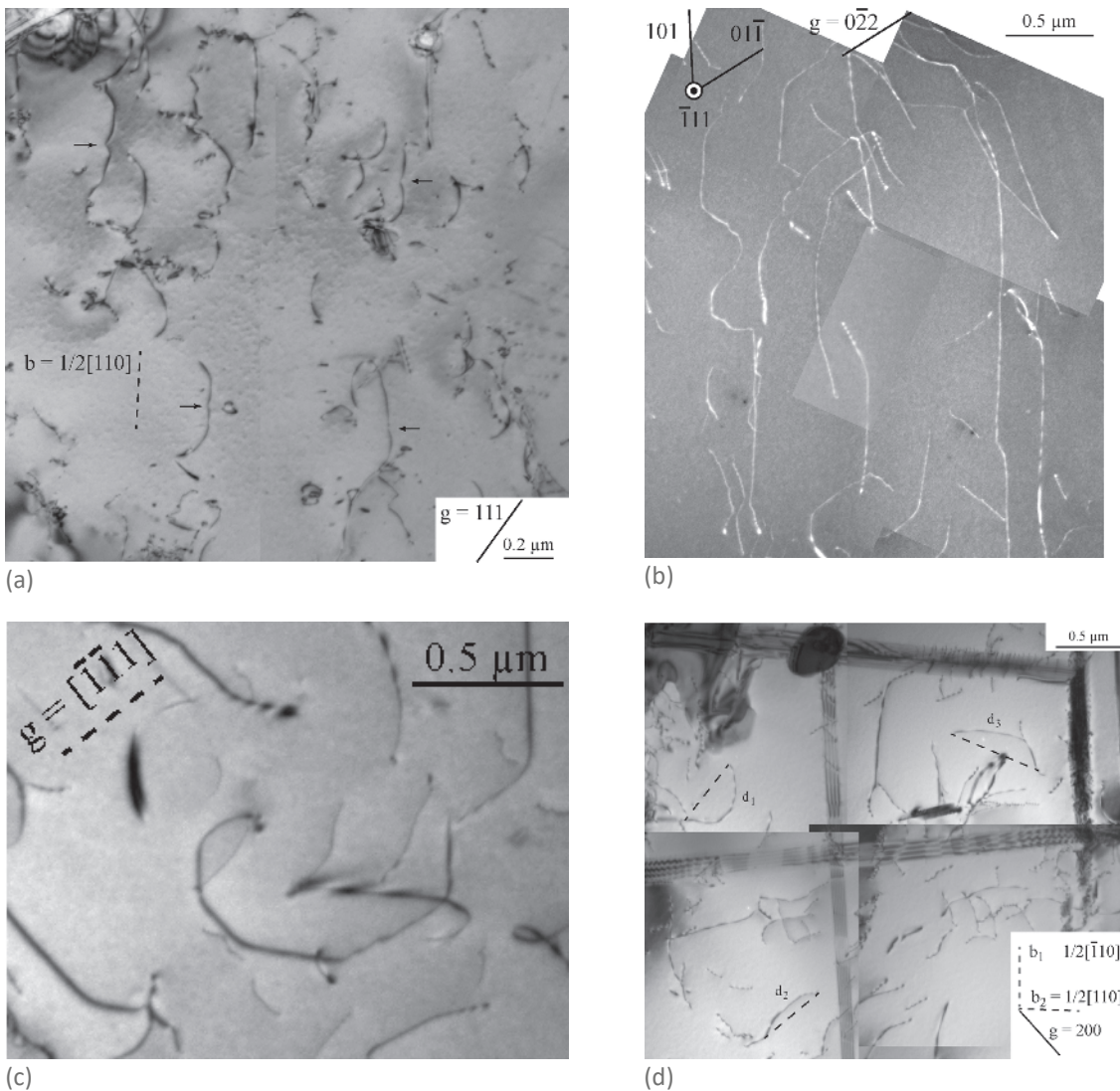
Fig. 2: deformation microstructure in the sample crept at 850°C, under 150 MPa, till 1.5% of plastic strain. (a) gliding ordinary dislocations, (b) climbing ordinary dislocations, (c) climbing [001] dislocations and (d) twins.

In the discussion section, it will be discussed why these various deformation mechanisms are activated in the same condition of stress and temperature and what is the physical processes controlling the creep deformation. It will be explained that the high value of the stress dependence for creep [1], in particular the activation volume, is reasonably explained by the glide and climb mechanisms evidenced in the present work.

Acknowledgements

References
[1] F. Appel, J. Paul, M. Oehring: Gamma Titanium Aluminides : Science and Technology, © Wiley-VCH Verla GmbH &Co. KGaA **2011**.
[2] T. Voisin, J. P. Monchoux, C. Deshayes, M. Thomas, A. Couret, Metallurgical and Materials Transactions 47A, **2016**, 12, 6097-6108.
[3] S. Naanani, J. P. Monchoux, C. Mabru, A. Couret, Scripta Mat, **2019**, 149, 53-57.

P–06

Phase equilibria investigations in the ternary Ti–Al–Nb system at elevated temperatures

Benedikt Distl[1], Martin Palm[1], Frank Stein[1], Markus W. Rackel[2], Katja Hauschildt[2]
and Florian Pyczak[2]

[1]Max-Planck-Institut für Eisenforschung GmbH, Max-Planck-Straße 1, 40237 Düsseldorf, Germany, distl@mpie.de
[2]Helmholtz-Zentrum-Geesthacht, Institut für Werkstoffforschung, Max-Planck-Straße 1, 21520 Geesthacht, Germany

Introduction

Alloys based on γ-TiAl are of great interest for high temperature applications, such as turbine blades, due to their high specific strength at elevated temperatures [1], which makes these materials a desirable substitute for currently used materials. With the addition of refractory elements like Nb, Mo and W, the high temperature properties can be further improved due to their stabilizing effect on the disordered β-phase. The cubic crystal structure of the β-phase improves the hot workability of such alloys due to the availability of more independent slip planes. On the other hand, during cooling the ordered β_0-phase is formed which inhibits an improvement of the ductility at room temperature [2]. An optimization of the alloy composition of higher-component TiAl-based alloys to achieve the best possible properties can be done either by extensive and costly trial-and-error experiments or by thermodynamic modelling in a computational CALPHAD (**CAL**culation of **PHA**se **D**iagram) approach provided that a reliable set of experimental data is available. However, such data are partly missing or the existing literature is inconsistent especially in the high-temperature range above 1000°C as is exemplified in Fig. 1 for the Ti-Al-Nb system at 1100°C [3-6].
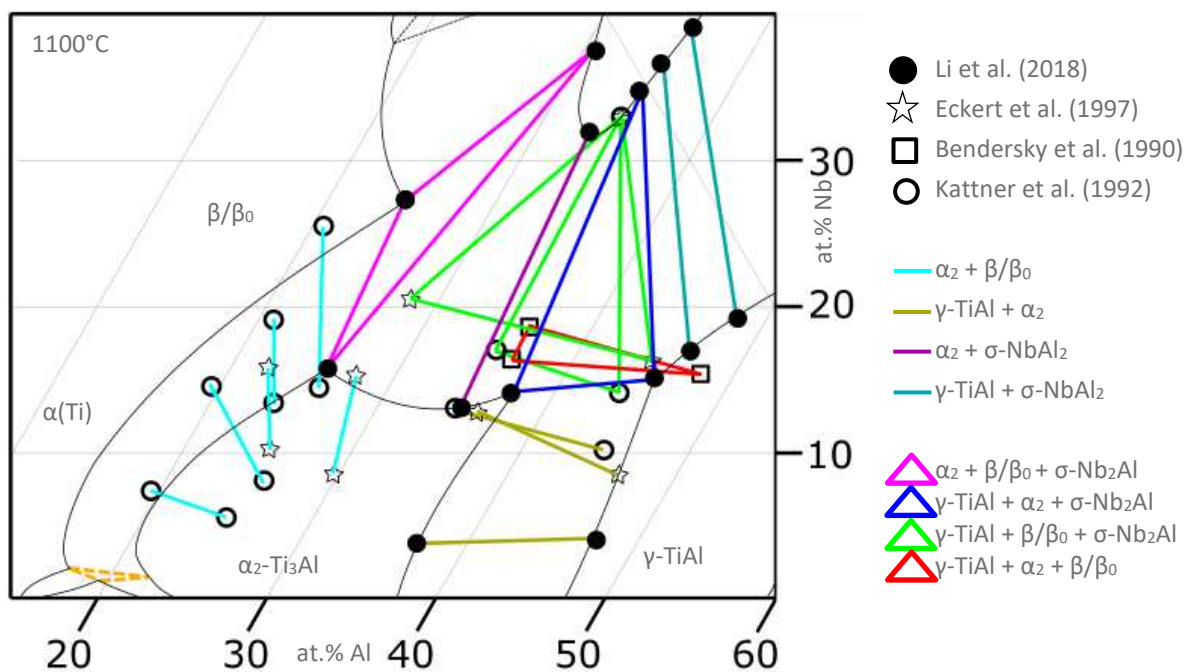
Fig. 1: Experimentally determined partial isothermal section at 1100°C from Li et al. [3] superimposed with experimental results from Eckert et al. [4], Bendersky et al. [5] and Kattner et al. [6] regarding phase equilibria between the phases α_2-Ti$_3$Al, γ-TiAl, β/β_0 and σ-NbAl$_2$

One reason for these inconsistencies could be the problem to completely quench the high-temperature phase equilibria, for example, due to the occurrence of the massive transformation of α(Ti) to γ-TiAl upon cooling. In order to tackle these problems, the European project ADVANCE was launched as a collaboration between the Max-Planck-Institut für Eisenforschung, the Helmholtz-Zentrum-Geesthacht, the Montanuniversität Leoben (Austria), and Thermo-Calc Software AB (Sweden). The project aims to optimize and improve the existing CALPHAD database for next generation Ti–Al–X alloys with sophisticated studies of phase equilibria at elevated temperatures. Alloys from eight ternary systems Ti–Al–X (X = Nb, Mo, W, Zr, Si, O, B, C) and two quaternary systems Ti–Al–Nb–Y (Y = Mo, W) will be heat-treated and investigated in detail. The first experimental results of the studies in the ternary Ti–Al–Nb system are presented here.

Materials, Methods and First Results

A series of ternary Ti–Al–Nb alloys were produced out of high-purity elements Ti (99,995 %), Al (99,999 %) and Nb (99,9%) using vacuum arc melting in high-purity Ar-atmosphere. Subsequently, the alloys were encapsulated in quartz capsules for heat treatments up to 1100°C. For higher temperatures, a special double crucible technique described by Kainuma et al. [7] was applied. Since the exact alloy composition and the impurity levels especially of oxygen and nitrogen play an important role in the determination of phase equilibria, they were cross-checked before and after the heat treatment using several methods (inductively coupled plasma atomic emission spectroscopy (ICP-AES), melt combustion and wet chemical analysis). The microstructure was examined using light optical microscopy (LOM) and scanning electron microscopy (SEM). Utilizing powder X-ray diffraction (P-XRD), electron backscatter diffraction (EBSD), and electron probe microanalysis (EPMA), the types and compositions of all phases were determined. Phase transition temperatures were measured by differential thermal analysis (DTA) and differential scanning calorimetry (DSC). For certain samples, these results were cross-checked using in situ synchrotron high-energy XRD (HEXRD).

In Fig. 2, a lamellar microstructure from an alloy with the nominal composition Ti-45Al-5Nb (in at.%) after DTA measurement (heating- and cooling rate: 20 K/min) up to 1450°C is shown. Inside the grey γ-TiAl matrix, there are brighter α_2-Ti_3Al lamella that form upon cooling resulting in the expected two-phase microstructure. In addition, the relatively slow cooling rate creates coarser lamella compared to water-quenched samples [2]. Further work includes heat treatments and evaluation of measured data to construct isothermal sections at different temperatures to resolve the inconsistences in literature.

Fig. 2: SEM-BSE picture of a lamellar two phase microstructure consisting of α_2-Ti_3Al (white) + γ-TiAl (grey) after DTA measurement up to 1450°C

References

[1] H. Clemens and S. Mayer, Advanced Engineering Materials, **2013**, *15*, No.4, 191-215.
[2] F. Kong, N. Cui, Y. Chen, X. Wang, Metallurgical and Materials Transactions A, **2018**, *49*, 5574-5584.
[3] L. Li, L. Liu, L. Zhang, L. Zeng, Y. Zhao, W. Bai, Y. Jiang, Journal of Phase Equilibria and Diffusion, **2018,** *39*, 549-561.
[4] M. Eckert, K. Hilpert, H. Nickel, Bericht des FZ Jülich *No. 3399*, **1997**, 1-200.
[5] L.A. Bendersky, W.J. Boettinger, B.P. Burton, F.S. Biancaniello, C.B. Shoemaker, Acta Metallurgica et Materialia, **1990**, *38*, 931-943.
[6] U.R. Kattner and W.J. Boettinger, Materials Science and Engineering, **1992**, *A152*, 9-17.
[7] R. Kainuma, M. Palm, G. Inden: Intermetallics. **1994**, *2*, 321-332.

P–07

Phase composition and microstructure of TiAlZr alloys

Fabian Kathöfer[1] and Florian Pyczak[1,2]

[1]BTU Cottbus-Senftenberg, Konrad-Wachsman-Allee 17, 03046 Cottbus, Germany, fabian.kathoefer@b-tu.de
[2]Helmholtz-Zentrum Geesthacht, Max-Planck-Str. 1, 21502 Geesthacht, Germany, florian.pyczak@hzg.de

Introduction

Titanium aluminide alloys (TiAl), especially alloys based on the intermetallic γ-phase, have attracted much attention as a substitute for Ni-based alloys as highly promising high temperature structural materials. This is due to their low density, high specific strength and specific elastic moduli as well as good corrosion resistance [1,2]. However, the processing of these alloys is still challenging and expensive, since for example the necessary temperatures for hot forming between 1100 °C and 1250 °C bring currently available die materials to their limits. Fortunately, by an appropriate tuning of the alloy composition it is possible to form phases and microstructures at the forming temperature which provide good deformation capabilities. The addition of alloying elements can not only lead to a shift of the transition temperatures of the phases but can also improve mechanical properties. For instance the addition of Zirconium (Zr), a β-stabilizing element, lowers the phase transformation temperatures of the 'softer' disordered α and β phases and has other additional beneficial effects e.g. solution strengthening on TiAl alloys [3]. While TiAl systems with addition of elements like Niobium and Molybdenum are well investigated so far, only a few studies on the effects of Zr additions in TiAl systems exist.

Materials and Methods

Based on the work of Kainuma et al. [4] and own thermodynamic calculations using ThermoCalc software with the database 'TCTI1' [5] 9 different alloy compositions Ti – (39;41;43)Al – (3.5;5.5;7.5)Zr (all in at.%) were produced. As starting material buttons with a mass of ca. 100 g were prepared by arc melting and remelted at least 12 times to homogenize the samples. The microstructures were observed using scanning electron microscopy (SEM) with a TESCAN Mira II XMH microscope and thermodynamic reactions during heating were investigated by differential scanning calorimetry (DSC) using a NETZSCH DSC 404 F3 Pegasus. The DSC tests were performed in the temperature range of 700 °C – 1450 °C with a heating rate of 10 K/min in pure Argon (99.9999 %).

Samples of all alloys were annealed in a Nabertherm high temperature furnace in air. The temperature was controlled by a type S thermocouple positioned near the specimens. The specimens were held at 1300 °C for 0.5 h and slowly furnace cooled. The DSC measurements help to identify phase transitions, which will be seen as endothermic reactions in the heating cycle. To better associate peaks shown in the DSC curves seen in Fig. 2 with certain reactions, specific heat treatments of were performed at 880 °C, 920 °C, 1100 °C and 1200 °C for 4 h in air. These samples were water quenched afterwards to retain the high temperature microstructure. HEXRD was performed to verify the types of the occurring phases when comparing with the SEM investigations and thermodynamic calculations.

Results and Discussion

As an example of the present work, Fig. 1-3 show the calculated phase contents over temperature, the corresponding DSC curve of the same alloy and the microstructure evolution of the sample Ti-39Al-5.5Zr. This and all other samples show an endothermic reaction peak in the temperature range of 1115 °C - 1170 °C, which can be identified as the disordering reaction of $\alpha_2 \rightarrow \alpha$. Only some of the samples also show an endothermic reaction peak at around 910 °C. Based on the thermodynamic calculations, this might be the solvus temperature of the Al_3Zr_2-phase. Furthermore, the thermodynamic calculations predict the Al_3Zr_2 - phase to dissolve for the lower Zr-content samples (3.5 at.% Zr) at even lower temperatures. This cannot be seen in the current DSC measurements.

To clearly identify the occurring phases and transitions, first in-situ XRD measurements are done. Also the microstructure investigation of the samples heat-treated at 880 °C indicate Zr - enrichments at some grain boundaries as well as inside former α - grains seen in Fig 3.a) and 3.b) as brighter areas. We expect this to be the Al_3Zr_2 - phase predicted in the thermodynamic calculations. The amount of these Zr-enrichments seems to decrease with increasing heating temperature until they cannot be observed anymore after a heat-treatment at 1100 °C (see Fig 3.c). The effect of this Zr - enrichments on the phase formations and deformation behavior is still part of the current investigations.
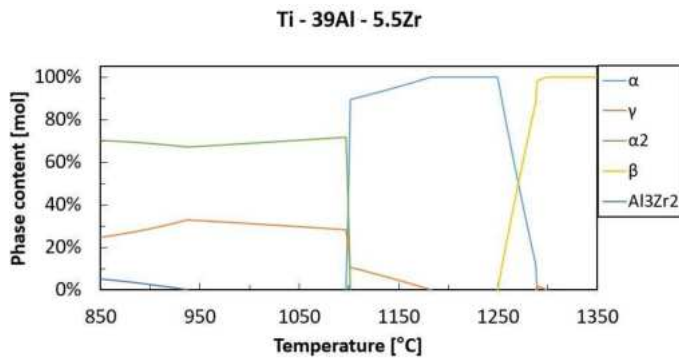
Fig. 1: Calculated phase contents in dependence of the temperature
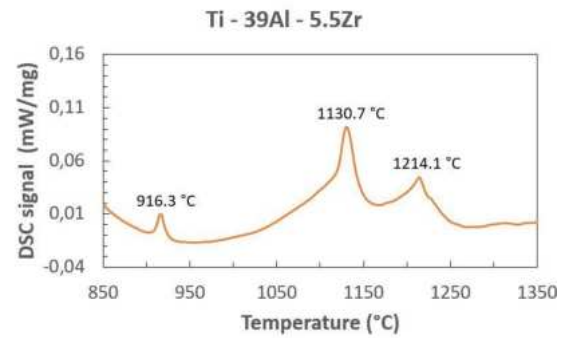
Fig. 2: DSC curve of Ti-39Al-5.5Zr sample
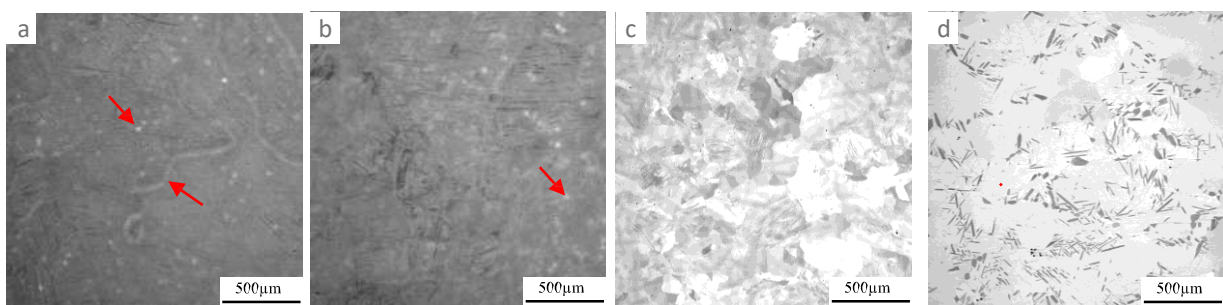
Fig. 3: SEM pictures of the different microstructures of Ti-39Al-5.5Zr after heat treatments of 4h in air with fast cooling afterwards (water quenched). a) at 870 °C; b) at 920 °C; c) at 1100 °C; d) at 1200 °C. The red arrows indicate Zr-enrichments.

References

[1]   F. Appel, J. Paul, M. Oehring (Eds.), Gamma Titamium Aluminde Alloys - science and technology, Wiley-VCH, Weinheim, **2011**.

[2]   F. Appel, H. Clemens, F.D. Fischer, Modeling concepts for intermetallic titanium aluminides, Progress in Materials Science. **2016**, *81*, 55–124.

[3]   X.J. Jiang, Y.K. Zhou, Z.H. Feng, C.Q. Xia, C.L. Tan, S.X. Liang, X.Y. Zhang et al., Influence of Zr content on β-phase stability in α-type Ti–Al alloys, Materials Science and Engineering. **2015**, *A639*, 407–411.

[4]   R. Kainuma, Y. Fujita, H. Mitsui, I. Ohnuma, K. Ishida, Phase equilibria among α (hcp), β (bcc) and γ (L10) phases in Ti–Al base ternary alloys, Intermetallics. **2000**, *8*, 855–867.

[5]   ThermoCalc Software, ThermoCalc Software TCTI1.

P–08

Experimental evaluation of the isothermal section of the Ti–Al–Zr ternary system at 1273 K

Zhara Kahrobaee, Frank Stein and Martin Palm

Max-Planck-Institut für Eisenforschung GmbH (MPIE), 40237 Düsseldorf, Germany, z.kahrobaee@mpie.de

Introduction

Ti-Al alloys comprise a new class of intermetallic materials, targeted for more energy-efficient automotive and aircraft engines [1]. Their properties at high temperatures, specifically creep and oxidation resistance, can be substantially improved by alloying [2]. Development of new alloys today not any longer solely relies on experimental trials. CALPHAD (CALculation of PHAse Diagram) modelling [3], by which phase diagrams and phase transitions can be calculated and from which, e.g., phase fractions in dependence on temperature can be derived, has become an important tool for developing new alloys. The modelling gives essential information about the expected microstructures from which potential properties of novel alloys can be concluded. CALPHAD calculations crucially depend on the underlying database. Within a large-scale collaborative project, the partners Helmholtz-Zentrum Geesthacht, Germany, Montanuniversität Leoben, Austria, Thermo-Calc Software AB, Sweden, and MPIE will essentially improve thermodynamic data for a number of Ti–Al–X(–Y) systems for a next generation of advanced CALPHAD databases for TiAl alloys [4].

Ti-Al-Zr at 1273 K

Phase equilibria in Ti–Al(–X…) systems are highly sensitive to the amount of impurities [5]. Small amounts of oxygen can already lead to significant changes in phase equilibria [6]. As Ti and Zr are extremely prone to oxygen uptake, this could be one reason for existing discrepancies in phase equilibria in the Ti–Al–Zr system, e.g. at 1273 K.

The Ti–Al–Zr system has been critically evaluated by Tretyachenko [7], including three partial isothermal sections. The one at 1273 K merely shows phase equilibria among the phases γTiAl and α_2Ti$_3$Al and those between αTi, βTi and α_2Ti$_3$Al as dashed lines. The most comprehensive study of phase equilibria at 1273 K was performed by Yang et al. [8]. However, phase equilibria determined in the ternary system do not match well with those established for the Ti–Al subsystem [6]. Figure 1 shows the Ti–Al rich part of the isothermal section as determined in [8] and experimental results from other investigations [9-12]. In addition, the phase boundaries from the latest assessment of the Ti–Al system are given [6]. Figure 1 shows that substantial differences between these investigations exist. E.g., values for the solid solubility of Zr in γTiAl at 1273 K vary between about 8 at.% [8], 10 at.% [9] or even at least 15 at.% [11].

Materials and Methods

In order to settle these uncertainties, six alloys have been prepared by crucible free levitation melting from high-purity elements. Slices of the manufactured alloys were cut on a diamond wire saw, encapsulated in quartz tubes back-filled with Ar and annealed at 1273 K for 100 h. Ti filings were used as getter to minimize the uptake of impurities. Compositions of the alloys and their impurity contents in the as-cast condition and after heat treatment were established by wet chemical analysis. Phases were identified by X-ray diffraction (XRD) and compositions of the coexisting phases were established by electron probe microanalysis (EPMA).
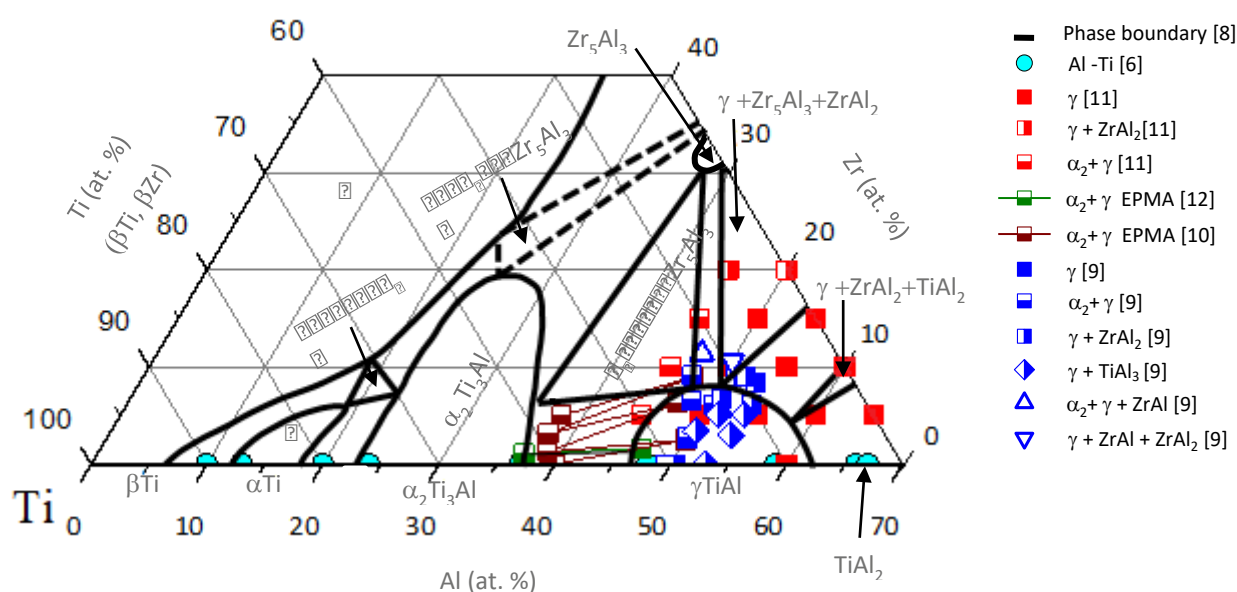
Fig. 1: Partial isothermal section of the Al-Ti-Zr ternary system at 1273 K. Phase boundaries are from Ref. [8] with additional data from Refs. [6, 9-12].

Acknowledgements

References

[1]   H.Clemens, S. Mayer: Adv. Eng. Mat. **2013**, 15, 191-215.

[2]   R.K. Gupta, B. Pant, P.P. Sinha: Trans. Indian Inst. Met. **2014**, 67, 143-165.

[3]   H.L. Lukas, S.G. Fries, B. Sundman: "Computational Thermodynamics: The Calphad Method". **2007**. Cambridge University Press.

[4]   Next Generation TiAl Alloys Advanced by New European Consortium https://news.thermocalc.com/next-generation-tial-alloys-advanced-by-new-european-consortium/ (assessed 28 March 2019).

[5]   F. Froes: "Titanium: physical metallurgy, processing, and applications". **2015**. ASM International.

[6]   J.C. Schuster, M. Palm: J. Phase Equil. Diffus. **2006**, 27, 255-277.

[7]   L. Tretyachenko: in: G. Effenberg, S. Ilyenko (Eds) „Light Metal Systems. Part 4. **2006**, Springer, Berlin, 54-67.

[8[F. Yang, F.H. Xiao, S.G. Liu, S.S. Dong, L.H. Huang, Q. Chen, G.M. Cai, H.S. Liu, Z.P. Jin: J. Alloys Compd. **2014**, 585, 325-330.

[9]   K. Kasahra, K. Hashimoto, H. Doi, T. Tsujimoto: J. Japan Inst. Met. **1987**, 51, 278-284.

[10] K. Hashimoto, H. Doi, K. Kasahara, T. Tsujimoto, T. Suzuki: J. Japan Inst. Met. **1988**, 52, 816-825.

[11] D. Tanda, T. Tanabe, R. Tamura, S. Takeuchi: Mat. Sci. Eng. **2004**, A387, 991-995.

[12] R. Kainuma, Y. Fujita, H. Mitsui, I. Ohnuma, K. Ishida: Intermetallics. **2000**, 8, 855-867.

P–09
Phase equilibrium and mechanical properties of bcc-V/MAX two-phase alloys

Hiroto Kudo[1], Seiji Miura[2], Ken-ichi Ikeda[3] and Nobuaki Sekido[4]
[1]Graduate Student, Department of Materials Science and Engineering, Hokkaido University, kita13 Nishi8, Kita-ku, Sapporo 060-8628, Japan, h_k_0404@eis.hokudai.ac.jp
[2] Division of Materials Science and Engineering, Faculty of Engineering, Hokkaido University, Kita 13 Nishi 8, Kita-ku, Sapporo 060-8628, Japan, miura@eng.hokudai.ac.jp
[3] Division of Materials Science and Engineering, Faculty of Engineering, Hokkaido University, Kita 13 Nishi 8, Kita-ku, Sapporo 060-8628, Japan, ikeda.ken-ichi@eng.hokudai.ac.jp
[4] Graduate School of Engineering, Tohoku University, Sendai 980- 8579, Japan, sekido@material.tohoku.ac.jp

Introduction
Recently Max phases have attracted attentions because of its high strength, high melting point and low density [1]. However, Max phases composed of transition elements together with C and Si or Al show a delamination along basal slip plane during plastic deformation. The present authors conducted a broad search of ternary phase diagrams composed of C and Al with transition element, and found V solid solution phase equilibrates with V_2AlC Max phase. We conducted experimental study on the phase equilibrium at 1200 °C, solidification path and compression tests for mechanical property measurements.

Materials and Methods
According to the phase diagram [2], we prepared alloy ingots with a nominal composition of V63.6at.%-Al27.2at.%-C9.1at.%. An Ar-arc melting machine was used to melt the sample several times, and a part of ingot sealed in a silica tube was subjected to a heat-treatment at 1473 K for 1 week. Microstructure observation using FE-SEM and WDS analysis for determining the composition of each phases are conducted, and the EBSD analysis was also conducted to understand the crystallographic orientation relationship between bcc-V and MAX phase. Parallelepiped samples with a dimension of 3 x 3 x 6 mm^3 ware prepared and were subjected to the compression test at room temperature and 673 K.

Results and Discussion
It was confirmed that the alloys with and without the heat-treatment show two-phase microstructure, however, plate-like V_2AlC-MAX phase spheroidized during the heat-treatment. It was also confirmed that the bcc-V and MAC phase has a certain crystallographic orientation relationship. Some of large size MAX phase plates are also found in the specimen, and cracks tend to propagate on or neat the large MAX phase during the compression tests. On the other hand, it was confirmed that the bcc-V and MAX phase show a bending during compression tests, it strongly suggests the simultaneous plastic deformation of these two phases (Fig.2).

Acknowledgement
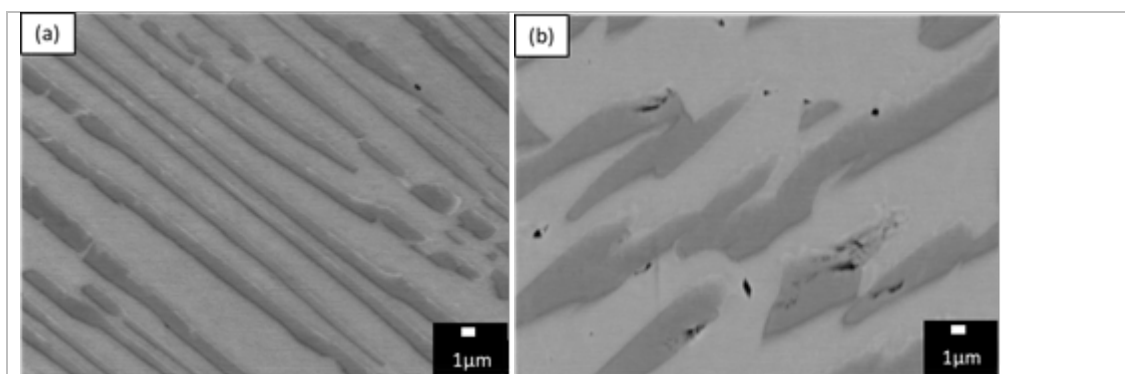
Fig. 1: SEM image of (a)as-cast and (b)heat treated V63.6at.%-Al27.2at.%-C9.1at.% alloy

Fig. 2: (a) phase map (green:V$_2$AlC, red:bcc); (b) inverse pole figure map of as-cast V63.6at.%-Al27.2at.%-C9.1at.% alloy by SEM- EBSD, after compression at 673K
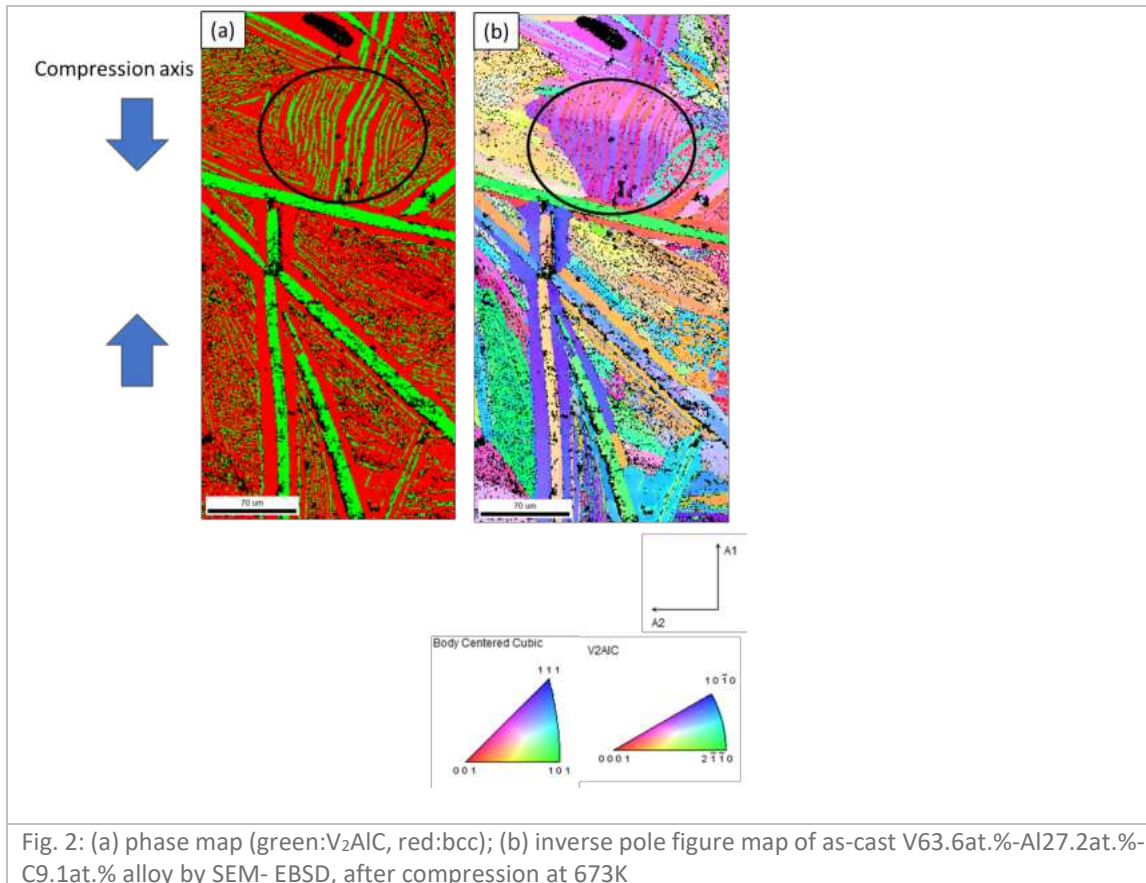
Reference

[1]   M. W. Barsoum and T. El-Raghy: Am. Sci. **2001**, *89*, 334-343.

[2]   B. Hallstedt, CALPHAD: Computer Coupling of Phase Diagrams and Thermochemistry. **2013**, *41*, 156-159.

P–10

Structural related intermetallic phases in the Nb-Cu-Sn system

Jonas Lachmann, Nicolas Huber and Andreas Leineweber

Institute of Materials Science, TU Bergakademie Freiberg, Gustav-Zeuner-Straße 5, 09599 Freiberg, Germany,

Jonas.Lachmann@iww.tu-freiberg.de, Nicolas.Huber@student.tu-freiberg.de,

Andreas.Leineweber@iww.tu-freiberg.de

Introduction

Production of Nb_3Sn superconductor in multifilamentary wires for use in high-field magnets, involves elaborate heat treatment steps starting from composite billets containing mainly Cu, Nb and Sn as elements in form of precursor materials. During such processing different intermetallic phases from the Nb-Cu-Sn system develop as intermediates, which will affect the microstructure and thus the superconducting properties of the finally generated Nb_3Sn filaments developed in the wires. In the last years, in contradiction to the long-term belief, also a ternary phase with the composition $Nb_{0.75}Cu_{0.25}Sn_2$ was found and called "nausite" [1,2]. However, this phase is not included in the currently available Nb-Cu-Sn phase diagrams. Structural investigations [2] revealed the hexagonal $NiMg_2$ type structure (space group $P6_222$) which is closely related to the orthorhombic $CuMg_2$ type structure of the binary $NbSn_2$ phase.

The present contribution deals with investigations of heat treated $Nb-Cu_6Sn_5$ diffusion couples starting from Nb substrate and deposited Cu-Sn layers serving as models for early stages of intermetallic formation during heat treatment of Nb-Cu-Sn wires. The investigations revealed problems in the distinction of the $NbSn_2$ and nausite phases due to their chemical and structural similarities. It was demonstrated by energy dispersive X-ray spectroscopy (EDX) that both phases exhibit a ternary homogeneity range. Careful analysis of Kikuchi patterns recorded in the course of electron backscatter diffraction (EBSD) was necessary to distinguish the two phases.

Materials and Methods

Ternary diffusion couples were produced from Nb plates by depositing Cu + Sn double layers by electroplating or physical vapor deposition. After deposition each sample was sealed in fused silica under Ar atmosphere and then heat treated at 220°C for 48 h to form Cu_6Sn_5 layer on top of the Nb substrate. Afterwards samples were heat treated at 300 / 400 / 500°C for different periods of time and subsequently quenched in ice water. For investigation, samples were cut and embedded as a cross-section, ground, polished (down to 0.04 µm) and covered by vaporized C for ensuring electric conductivity for the studies at the scanning electron microscope (SEM).

The SEM used was a *JEOL JSM-7800F*. An accelerating voltage of 20 kV was applied, and imaging was done using the backscattered electrons. Moreover, EDX and EBSD were employed for getting information about elemental distribution and orientation of the phases. The OIM Analysis-Software (EDAX) was used for acquisition and indexing of the Kikuchi patterns. Besides, for getting a more detailed insight in the Kikuchi patterns of both phases, the pattern simulation software ESPRIT DynamicS (Bruker) was utilized.

Results and Discussion

The heat treatments of the diffusion couples described above led to the formation of different sequences of phases depending on the temperature-dependent interdiffusion kinetics and availability of the different elements. Due to the treatments $NbSn_2$ and/or nausite were formed in contact to the Nb substrate.

The ternary phase nausite derives from the binary $NbSn_2$ phase by partial substitution of Nb by Cu. EDX measurements indicate the formation of nausite with Cu contents reaching from 6 to 13 at.%. Problems in distinction of $NbSn_2$ and nausite based on EDX in particular occurs in case of very thin layers (Fig.1). Hence, in addition EBSD was employed for phase differentiation. However, because of the structural similarities of both phases, namely strands of quadratic Sn antiprisms and parallel linear chains of Nb respectively Cu in stacking planes along the c-direction, both phases exhibit similar Kikuchi patterns. Nevertheless, slight differences between the patterns can be employed if the image quality is sufficient. Kikuchi patterns with a [001] pole from $NbSn_2$ and nausite, shown in Fig. 2, reveal, on the one hand, strong bands which are in common to both structures, and, on the other hand, weaker bands which can be used to differentiate between them.
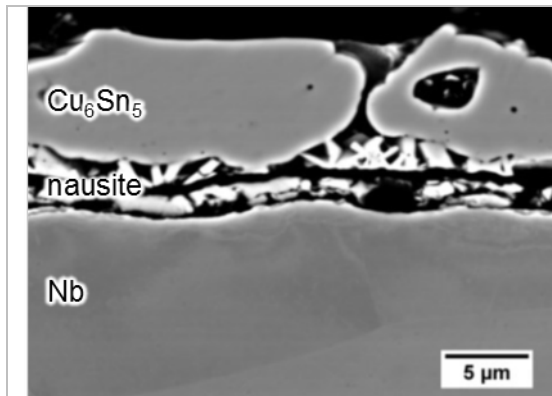
Fig. 1: Backscattered electron contrast image of cross-section of Nb-Cu$_6$Sn$_5$ diffusion couple after heat treatment at 300°C.	Fig. 2: Kikuchi pattern of NbSn$_2$ (left) and nausite (right) in the region of a [001] pole. Through a sufficient image quality slight differences in visible bands can be found. Their position and direction is indicated with white arrows.
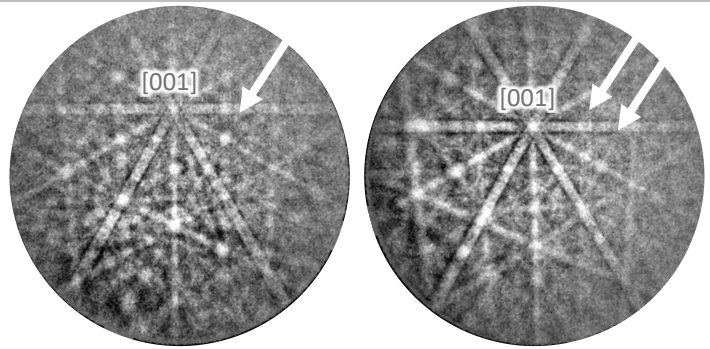
References

[1]   M.T. Naus, P.J. Lee, D.C. Larbalestier, IEEE Transactions on Applied Superconductivity, **2001**, *11*, 3569-3572.

[2]   S. Martin, A. Walnsch, G. Nolze, A. Leineweber, F. Léaux, C. Scheuerlein, Intermetallics, **2017**, *11*, 16-21.

P–11

Alloying Impact on phase stability in ZrAl$_3$

David Holec[1], Dominik Nöger[1], Florian Schmid[2] and Stefan Pogatscher[2]

[1]Department of Materials Science, Montanuniversität Leoben, Franz-Josef-Strasse 18, 8700 Leoben, Austria, david.holec@unileoben.ac.at

[2]Christian Doppler Laboratory for Advanced Aluminium Alloys, Chair of Nonferrous Metallurgy, Montanuniversität Leoben, Franz-Josef-Strasse 18, 8700 Leoben, Austria

Introduction

During homogenization, Al$_3$Zr-particles precipitate out of super-saturated Zr-alloyed aluminum alloys. These particles serve for grain size stabilization via Zener drag and depending on their size and distribution can also contribute positively to an increased strength. These beneficial effects have long been used in the high strength Al-Zn-Mg alloys, but are not widely used in other classes of alloys. Al$_3$Zr exhibits three different crystal structures, L1$_2$, D0$_{22}$ and D0$_{23}$. Only the L1$_2$ structure shows a favorable coherent grain boundary with the aluminum matrix. However, high temperatures and a certain alloy composition, in particular a high Si content, promote the detrimental transformation from L1$_2$ → D0$_{22}$/D0$_{23}$. In particular, for novel alloy design (e.g. Al-Mg-Si-Zr alloys), doping with other elements may help to stabilize the preferred L1$_2$ structure.

Materials and Methods

We have employed first principles methods based on Density Functional Theory as implemented in Vienna Ab initio Simulation Package, together with the generalized gradient approximation of the electron-electron exchange and correlation interaction.

The considered structures (Fig. 1) are the most stable D0$_{23}$ phase together with two metastable L1$_2$ and D0$_{22}$ phases. The differences between these configurations can be described by differently stacked (001) planes containing Zr atoms: ...AAAAAA... for the L1$_2$, ...ABABA... for the D0$_{22}$ and ...AABBA... for the D0$_{23}$ structure.

A large set of 16 doping elements was probed for their impact on relative phase stability. For this purpose, supercells with 64 atoms were constructed, each containing 1 ternary alloying element, corresponding to approx 1.5 at%.

Fig. 1: ZrAl$_3$ phases studied in this work: (a) L1$_2$, (b) D0$_{22}$ and (c) D0$_{23}$ structures.

Fig. 2: Formation energies as functions of the alloying element in the amount of 1.5 at.%. The dashed lines show reference values for unalloyed state.
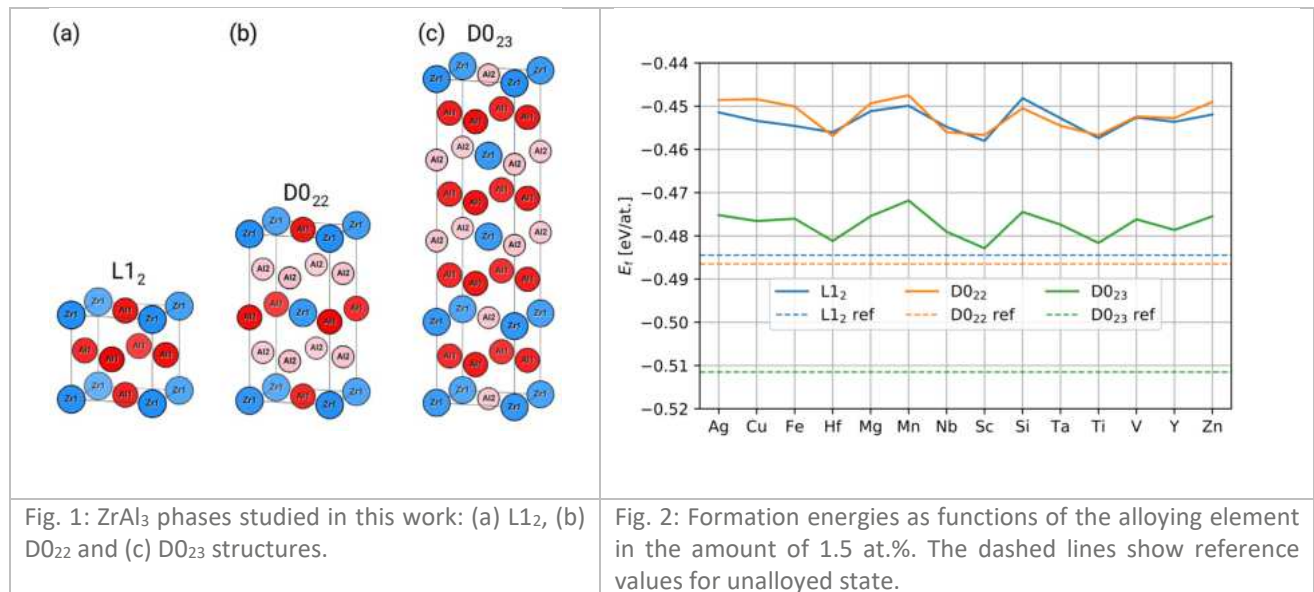
Results and Discussion

As a first step, we have evaluated site preference for the alloying elements. Majority of the elements exhibit weak site preference meaning that an element would occupy the Al sublattice for Al-lean compositions while it would sit on the Zr sublattice for Zr-lean compositions. Out of this rule stand Ag, Cu, Fe, Mn, and Zn with a strong Al sublattice preference and Er and Y with a strong Zr sublattice preference. Strong preference means that a particular element prefers to sit e.g. on Zr-sublattice even for Zr-rich compositions thus generating an additional anti-site defect.

Subsequently, we evaluated formation energies (Fig. 2). Clearly, none of the here considered elements chemically stabilizes any of the phases with respect to the unalloyed state. However, it is interesting to realize that some elements, e.g. Cu or Ag, stabilize the $L1_2$ phase on the expense of the $D0_{23}$, which is now the least stable one. Such result leads to a concept of alloying-stabilization of the desired $L1_2$ phase and hence avoiding completely the $D0_{23}$ phase.

To further support this concept, we have also studied energy barriers for stacking generating stacking faults in the L12 structure, e.g. from ...AAAAA… to ...AABBB… Such information is interpreted as a kinetic stabilization and complements the alloy design based solely on the energy of formation.

In our contribution we will present the above described analysis in detail together with the suggested novel alloys. Time permitting we will also report on our preliminary experimental results.

P–12

Early stage phenomena of kink formation in the Mg-Zn-Y LPSO phase investigated by micropillar compression

Kouhei Ohkage, Kyosuke Kishida and Haruyuki Inui

Department of Materials Science and Engineering, Kyoto University, Kyoto 606-8501, Japan,
ookage.kouhei.85u@st.kyoto-u.ac.jp, kishida.kyosuke.6w@kyoto-u.ac.jp, inui.haruyuki.3z@kyoto-u.ac.jp

Introduction

Mg-TM(transition metal)-RE(rare earth) ternary alloys containing a precipitation phase with a long-period stacking-ordered (LPSO) structure has attracted attention as a new lightweight structural material because they exhibit high strength and good ductility simultaneously. Such attractive mechanical characteristics are considered to be related to the heavily kinked structure of the Mg-LPSO phase introduced during hot extrusion. Previous studies on the compression deformation of directionally solidified ingots of various Mg-LPSO phases suggested that the formation of the kinked structure can be interpreted with the dislocation-based kink band formation mechanisms such as the Hess and Barrett model [1-3]. However, the controlling factors that trigger the formation of the kinked structure has not been fully clarified yet. Recently, we have investigated deformation microstructures developed in the Mg-Al-Gd ternary alloys containing platelet precipitates of the Mg-Al-Gd LPSO phase and revealed the possible occurrence of deformation twinning in the LPSO phase [4]. More recently, we have systematically conducted micropillar compression experiments of single crystalline Mg-Zn-Y LPSO phase as a function of the loading axis orientation and specimen size and confirmed the activation of non-basal slips in addition to basal slip and the formation of kinked structure depending on the loading axis orientation, specimen size and strain rate [5]. In this study, we have investigated the initial stage of kink formation by micropillar compression of 14*H*-type Mg-Zn-Y LPSO phase single crystals with the loading axis orientation parallel to the basal plane.

Materials and Methods

DS ingots with a nominal composition of Mg-7at%Zn-8at%Y were used for the present study. Single crystalline micropillars of the 14*H*-type LPSO phase were fabricated by focused ion beam (FIB) technique. Loading axis was selected to be parallel to the a-axis of the LPSO phase, which is parallel to that of the parental HCP Mg. In-situ micro-compression tests were conducted in scanning electron microscope equipped with a field emission gun (FE-SEM) under the loading rate control mode (corresponding nominal strain rate: 10^{-4}-10^{-5}/s). Microstructures of micropillars before and after the compression test were investigated by FE-SEM and transmission electron microscopy (TEM).

Results and Discussion

Heavily kinked structure was confirmed to be developed very rapidly accompanied by a large strain burst of more than about 30% plastic strain observed in the stress-strain curve, when the loading axis is parallel to the basal planes (Figs 1 and 2). Careful inspection of the stress-strain curve revealed the occurrence of a very slight deviation from the elastic region in prior to the large strain-burst. In addition, frame-by-frame analysis of SEM movie obtained during the in-situ experiments indicated that the slight deviation in the stress-strain curve was accompanied by a localized shape change, which may not be interpreted as either elastic buckling or bulging. These results suggest that the occurrence of some kind of plastic deformation, possibly deformation twinning or non-basal slip, triggers the rapid development of heavily kinked structure in the single crystalline micropillars of the Mg-LPSO phase compressed along the basal plane.
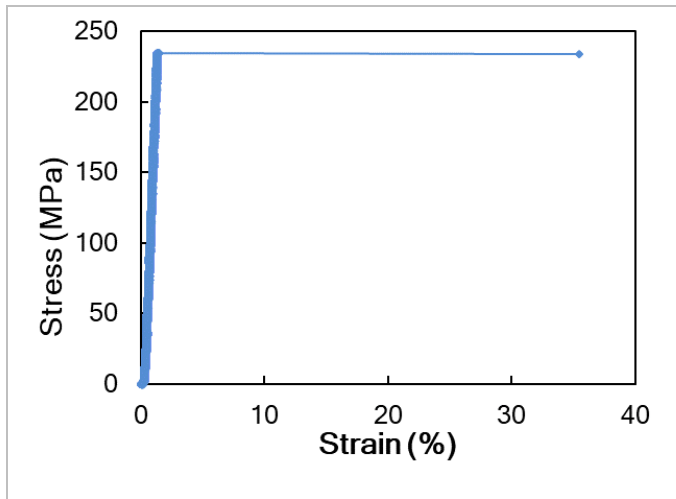
| Fig. 1: A typical stress-strain curve for the a-axis compression of a single crystalline micropillar of the Mg-LPSO phase. | Fig. 2: An SEM image of the micropillar specimen after the compression test shown in Fig. 1. |
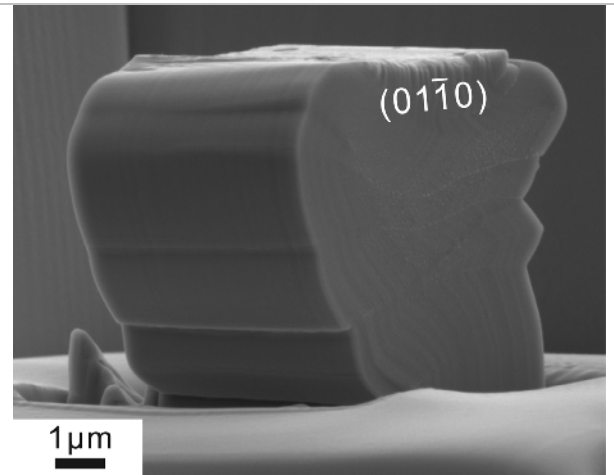
References
[1] K. Hagihara, N. Yokotani, Y. Umakoshi, Intermetallics**. 2010**, *18*, 267-276.
[2] K. Hagihara, Y. Sugino, Y. Fukusumi, Y. Umakoshi, T. Nakano, Mater. Trans. **2011**, *52*, 1096-1103.
[3] J.B. Hess, C.S. Barrett, Trans. Am. Inst. Min. Metall. Eng. **1949**, *185*, 599-606.
[4] K. Kishida, A. Inoue, H. Yokobayashi, H. Inui, Scripta Mater. **2014**, *89*, 25-28.
[5] A. Inoue, K. Kishida, H. Inui, K. Hagihara, MRS Symp. Proc. **2013**, *1516*, 151-156.

P–13

Simulation of cyclic functional and mechanical behavior of porous NiTi samples obtained by selective laser melting

Elizaveta Iaparova[1], Aleksandr Volkov[2], Margarita Evard[3] and Fedor Belyaev[4]

[1]Universitetskiy prospekt, 28, 198504 St. Petersburg, Russian Federation, elizaveta_iaparova@outlook.com
[2]Universitetskiy prospekt, 28, 198504 St. Petersburg, Russian Federation, volkov@math.spbu.ru
[3]Universitetskiy prospekt, 28, 198504 St. Petersburg, Russian Federation, m.evard@spbu.ru
[4]Universitetskiy prospekt, 28, 198504 St. Petersburg, Russian Federation, belyaev_fs@mail.ru

Introduction

Porous shape memory alloys (SMA) especially NiTi are perspective smart materials for implants and damping devices. Their properties significantly depend on the peculiarities of the porous structure. For about twenty years, porous NiTi has been produced by the methods of powder metallurgy. Now it has become possible to prepare porous NiTi samples by methods of additive manufacturing, which are ecologically preferable because of the absence of waste products. The structure of such samples is accurately determined. Most of the works devoted to modeling of porous SMA describe its mechanical behavior in isothermal conditions and consider a sample as a composite with an inclusion, where the dense part of the structure is characterized by a proper constitutive model. Just a few works describe the shape memory effect in porous SMA samples.

Materials and Methods

In this work, mechanical and functional properties of porous NiTi produced by selective laser melting are calculated. The samples have a regular cubic structure consisting of a set of interporous ligaments. Such SMA carcass with properties described by the microstructural model [1] is considered to determine the behavior of the representative volume of the sample. It allows modeling superelasticity and shape memory effect as well as the evolution of inelastic strain during cyclic loads.

Results and Discussion

Calculation of the strain under cyclic thermomechanical loading at martensitic state, each cycle including loading, unloading, heating and cooling is performed. Stress-strain curves and dependences of recoverable and irrecoverable strain on the cycle number are obtained. Modelling of deformation diagram at the first cycle of for the sample with porosity 45% is presented in Fig. 1. In another series of calculations a simulation of shape memory effect under different stresses and cycling at austenitic state is realized. Calculations are performed for the samples with porosity 32%, 45%, and 58% to compare with experimental data [2]. Fig. 2 shows the simulation results of irrecoverable deformation during cycling at body temperature. It is seen that the results of modelling are in a good correspondence with the experimental curve. Therefore, it is concluded that the model is suitable for modelling the behavior of porous SMA obtained by methods of additive manufacturing.

| Fig. 1: Stress-strain curve of first cycle for 45% porous NiTi sample. | Fig. 2: Irrecoverable strain during cycling for 32% porous NiTi sample. |
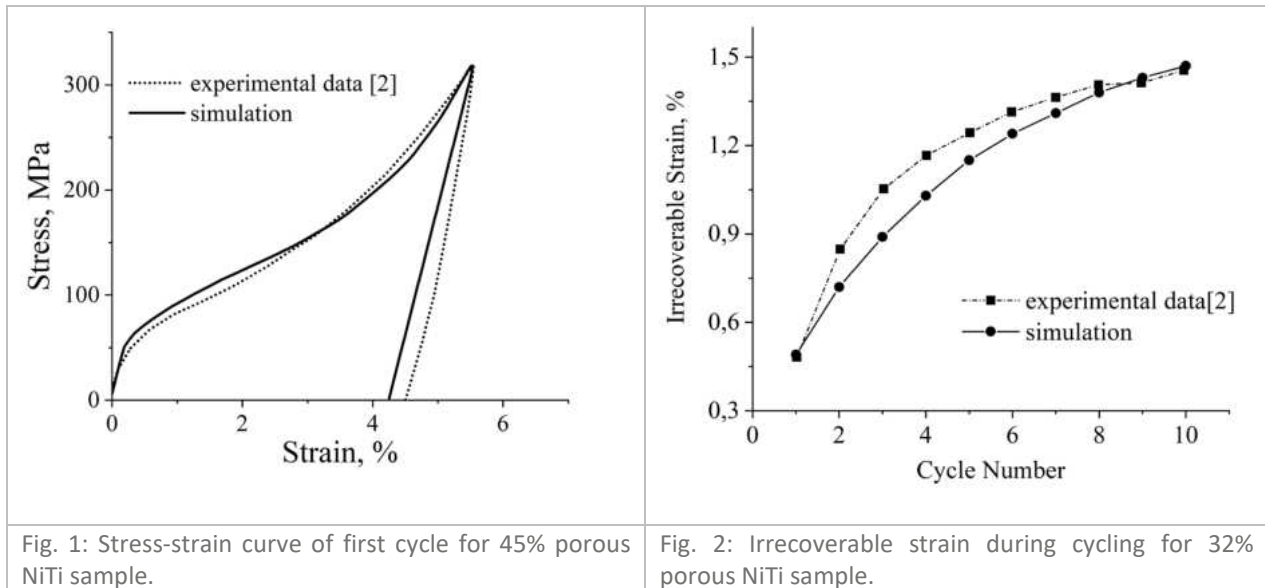
References

[1]   F.S. Belyaev, M.E. Evard, A.E. Volkov, AIP Conference Proceedings. **2018**, *1959*, 070003.
[2]   S. Saedi, A.S. Turabi, M.T. Andani, C. Haberland, M. Elahinia, H. Karaca, Smart Materials and Structures. **2016**, *25 (3)*, 035005.

P–14

Internal friction measurements on a Ni-Ti-Hf high temperature shape memory alloy

Mikel Pérez-Cerrato[1], José M. San Juan[1] and María L. Nó[2]

[1]Department of Physics of Condensed Matter, Faculty of Science and Technology, University of the Basque Country (UPV/EHU), Apdo 644, 48080 Bilbao, Spain, mikel.perez@ehu.es, jose.sanjuan@ehu.es

[2]Department of Applied Physics II, Faculty of Science and Technology, University of the Basque Country (UPV/EHU), Apdo 644, 48080 Bilbao, Spain, maria.no@ehu.es

Introduction

The applications of Shape Memory Alloys (SMAs) are usually limited by the range of their transformation temperature, for instance Ni-Ti cannot surpass the 100ºC and Cu-Al-Ni SMAs are limited to 200ºC temperature mark. However, the unique properties of the shape memory effect can be very useful at high temperatures, providing more reliable actuators and with a fewer number of components. For these reasons, there is an increasing interest on developing and testing SMAs with transformation temperatures over 100ºC. This kind of materials are commonly referred as High Temperature Shape Memory Alloys (HTSMAs).

The temperature of the martensitic transformation is a parameter that depends on the alloy composition as well as on microstructural properties. A way of developing HTSMAs that has been studied is the fabrication of ternary Ni-Ti-X alloys (with X = Pd, Pt, Zr, Hf). The elements Pd and Pt are used as substitutes of Ni, while Zr and Hf will act as substitutes of Ti. In the case of our material of interest, Ni-Ti-Hf, the transformation temperature can rise up to 290ºC [1].

In this work we present the characterization of a Ni-Ti-Hf HTSMA by mechanical spectroscopy. Valuable information on the thermo-mechanical properties of the material can be obtained from this kind of measurements, such as the internal friction spectra, the transformation temperatures, and we demonstrate with the present results that even the Clausius-Clapeyron coefficient.

Materials and Methods

The material used within this work was a $Ni_{49.5}Ti_{35.5}Hf_{15}$ (at.%) alloy produced by induction melting inside a graphite crucible. The ingot was hot worked to form sheets of 0.9 mm width. Samples for mechanical spectroscopy measurements were water-cut into rectangular cross section rods (0.9 × 5 × 50 mm^3). The mechanical spectroscopy experiments were performed in a sub-resonant torsion pendulum designed to work in a range of temperatures between 90 K and 1150 K, and frequencies between 10^{-4} Hz and 10 Hz, as described in reference [2]. Internal friction is measured as the tangent of the phase difference between stress and strain. Microstructural analysis of the material was made in a scanning electron microscope (SEM) operated at 15 kV. Samples were mechanically polished with diamond particles down to 0.25 μm.

Results and Discussion

Figure 1 depicts the general appearance of the sample at low magnification. Apart from the Ni-(Ti,Hf) polycrystalline matrix, a measurable amount of precipitates in the form of dark and bright spots distributed all over the matrix are clearly observed. Through EDS and EBSD analysis the nature of these precipitates were determined. The bright grains are HfC, probably formed during the casting process inside the graphite crucible, while the dark stains are titanium rich precipitates with a $(Ti,Hf)_2Ni$ composition. In spite of the general appearance of the material's surface, the sample shows very clean transformation cycles and an excellent thermo-elastic behaviour, as will be shown in the following results.

The internal friction measurements act as an anelastic probe for the phase transformation, and from these experiments, it is possible to obtain the volume fraction of transformed martensite n(T), as well as the start and finish temperatures of the direct and reverse transformation (M_s, M_f, A_s and A_f) as it is depicted in Figure 2. In addition, the internal friction spectra can be analysed, through the model for martenitic transformation [3], in order to obtain the Clausius-Clapeyron coefficient.
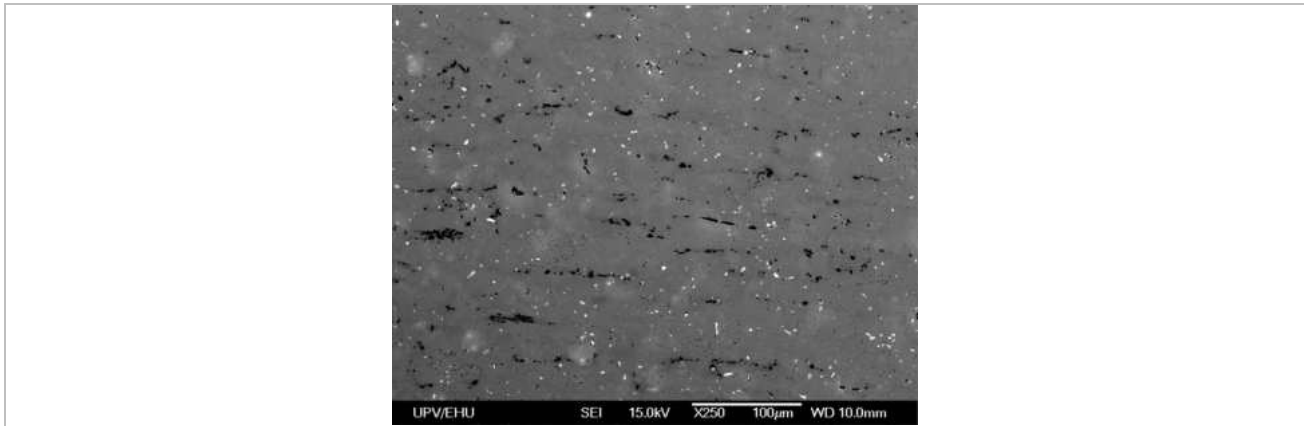
Fig. 1: SEM image of the sample. The matrix contains a visible amount of dark and bright precipitates. The surface composition was checked via EDX measurements. Dark spots correspond to (Ti,Hf)2Ni precipitates, while brighter ones are HfC particles.
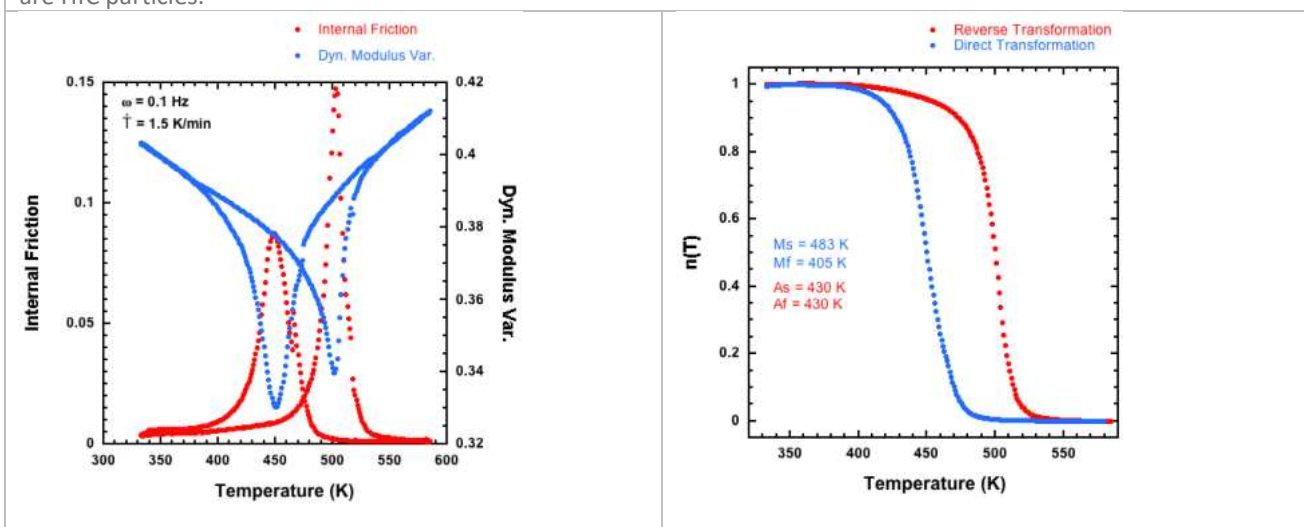
Fig. 2a: Internal friction spectra and dynamic modulus variation data, showing the martensitic transformation. Measurements were done with a heating/cooling rate of 1.5 K/min and a frequency of 0.1 Hz. These parameters have an impact on the intensity of the peaks (but not on the transformation temperatures), which are analyzed through the theoretical model [3].

Fig. 2b: From the data in 2a, we can obtain the transformed volume fraction of martensite n(T). This function allows us to determine the transformation temperatures (usually taken at 2% and 98% fraction).

References
[1]   J. Frenzel, A. Wieczorek, I. Ophale, B. Maass, R. Drautz, G. Eggeler; Acta Mater. **2015**, 90, 213-231.
[2]   I. Gutierrez-Urrutia, M.L. Nó, E. Carreño-Morelli, B. Guisolan, R. Schaller, J. San Juan; Mater. Sci. Eng. A **2004**, 370, 435-439.
[3]   G. Gremaud, J.E. Bidaux, W. Benoit; Helv. Phys. Acta **1987**, 60, 947-958.

P–15

Strain variation during isothermal martensitic transformation in Ti$_{49}$Ni$_{51}$ shape memory alloy

Aleksei Ivanov[1], Natalia Resnina[1], Sergey Belyaev[1] and Vladimir Andreev[2,3]

[1]Saint-Petersburg State University, Universitetskaya nab. 7-9, 199034 Saint-Petersburg, Russian Federation

st033007@student.spbu.ru

[2]MATEK-SMA Ltd., Karier 2a – 137, 117449 Moscow, Russian Federation

[3]Baikov Institute of Metallurgy and Materials Science, RAS, Leninskii Pr. 49, 119991 Moscow, Russian Federation

Introduction

Last time it was found that the martensitic transformations might occur in NiTi-based alloys during the isothermal holding at temperatures above [1-8] or below [1-5] the M$_s$ temperature (start temperature of the forward martensitic transformation on cooling). It is known that on cooling the shape memory alloys under a constant load, the oriented martensite appears that lead to the strain variation [9]. On subsequent heating the oriented martensite transformed to austenite and the strain completely or partially recovered. If the martensite may appear in quenched Ni-rich NiTi alloy under isothermal condition in a stress-free state, hence it may be assumed that during isothermal holding under a constant stress, the oriented martensite should appear and it must be accompanied by the strain variation as it was observed on cooling under a stress. However, the strain variation during isothermal martensitic transformation in NiTi alloy has never been studied. Therefore, the aim of the present work was to study the strain variation during the B2 → B19' martensitic transformation under isothermal holding of the Ni$_{51}$Ti$_{49}$ alloy under a stress of 50 MPa.

Materials and Methods

The wire samples of the Ni$_{51}$Ti$_{49}$ alloy (produced by MATEK-SMA Ltd.) with a diameter of 1.5 mm and a length of 100 mm were quenched from 850 ^{o}C for 10 min into water to prevent the formation of precipitates and subjected to 100 thermal cycles through a temperature range of the martensitic transformation (from -196 ^{o}C to 100 ^{o}C) to stabilize the phase transition temperatures. The samples were put to special grips of the Shimadzu AG-50kN testing machine, loaded by 50 MPa at room temperature at which the alloy was in the austenite phase and subjected to following procedure: cooling under a stress to T* temperature, holding at a constant temperature T* for 60 min and heating to 25 ^{o}C. Additionally, the samples were cooled and heated under a stress of 50 MPa in a temperature range of 25 ^{o}C to T* to study the strain variation in the thermal cycles without holding. The T* temperature was chosen above or below the M$_s^{\sigma}$ temperature (start temperature of the forward martensitic transformation that occurred on cooling under a stress of 50 MPa).

Results and Discussion

Fig. 1 shows the strain variation during the first (blue line) and the second (red line) steps of the procedure that described above when the holding temperature of T* was -35 ^{o}C. It is seen that the strain increases not only on cooling but also during holding of the sample at a constant temperature and completely recovers on heating. It is seen that strain recovery in the cycle where the holding took place after cooling (ε_1^{SME}, blue line) was larger than in the cycle without holding (ε_2^{SME}, red line), hence the strain that appeared on holding was initiated by the reversible deformation mechanisms.
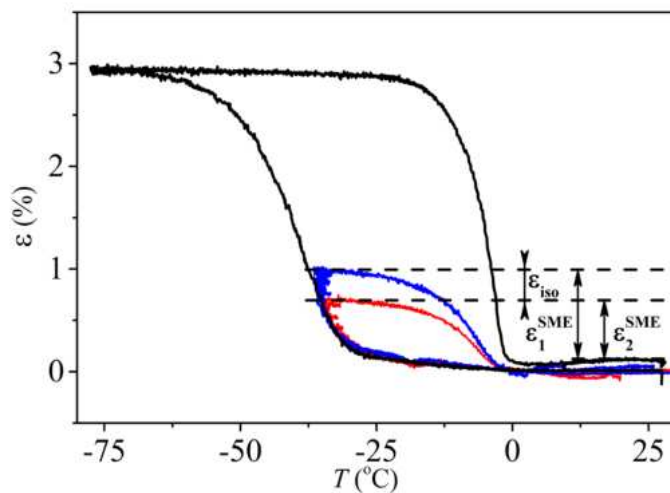
Fig. 1: Strain variation on the temperature that was obtained on cooling of the $Ni_{51}Ti_{49}$ alloy in full temperature range of the martensitic transformation (black line), in incomplete thermal cycle from 25 °C to -35 °C (red line) and in incomplete thermal cycle with the intermediate holding at -35 °C (blue line).

The isothermal strain variation was studied during holding at different temperatures and it was found that the maximum isothermal strain of 0.4 % was observed on holding at a temperature of T*=-37 °C that was equal to M_s^σ-6 °C. The shift in the holding temperature above or below to the T = M_s^σ -6 °C decreased the isothermal strain. The holding of the sample at temperatures which are larger than M_s^σ and lower than M_f^σ is not accompanied by the strain variation. Thus, the results of the study show that the strain variation takes place on holding of the quenched $Ni_{51}Ti_{49}$ alloy at temperatures that are lower than M_s^σ temperature. All strain that appears on holding under a stress of 50 MPa is completely reversible on heating hence, this strain is induced by the reversible deformation mechanisms. As the strain variation occurs on holding under a stress in the vicinity of M_s^σ temperature then the martensite reorientation can not be responsible for the strain variation, hence this strain is induced due to the isothermal formation of the oriented martensite during the transformation from austenite to martensite at constant temperature under stress. On subsequent heating the oriented martensite transforms to austenite and all strain recovers.

References
[1]   S. Xue, W. Wang, D. Wu, Q. Zhai, H. Zheng, Materials Letters. **2012**, *72*, 119-121.
[2]   T. Fukuda, S. Yoshida, T. Kakeshita, Scripta Materialia. **2013**, *68*, 984-987.
[3]   T. Fukuda, M. Todai, T. Kakeshita, Scripta Materialia. **2013**, *69*, 239-241.
[4]   Y. Ji, D. Wang, X. Ding, K. Otsuka, X. Ren, Physical Review Letters. **2015**, *114*, 055701.
[5]   N. Resnina, S. Belyaev, E. Demidova, A. Ivanov, V. Andreev, Materials. Letters. **2018**, *228*, 348-350.
[6]   S. Kustov, I. Golovin, M. L. Corró, E. Cesari, Journal of Applied Physics. **2010**, *107*, 053525.
[7]   S. Kustov, D. Salas, E. Cesari, R. Santamarta, J. Van Humbeeck, Acta Materialia. **2012**, *60*, 2578-2592.
[8]   N. Resnina, S. Belyaev, A. Shelyakov, Scripta Materialia. **2016**, *112*, 106-108.
[9]   K. Otsuka, X. Ren, Progress in Materials Science. **2005**, *50*, 511-678.

P–16

Strain variation induced by the martensitic transformation during isothermal holding of Ti$_{40.7}$Hf$_{9.5}$Ni$_{44.8}$Cu$_5$ shape memory alloy

Elena Demidova[1], Sergey Belyaev[1], Natalia Resnina[1] and Alexander Shelyakov[2]

[1]Saint-Petersburg State University, 7/9 Universitetskaya nab., 199034 Saint-Petersburg, Russia, lena-demi@yandex.ru, spbelyaev@mail.ru, resnat@mail.ru

[2]National Research Nuclear University MEPhI (Moscow Engineering Physics Institute), 31 Kashirskoe shosse, 115409 Moscow, Russia, alex-shel@mail.ru

Introduction

Shape memory alloys demonstrate unique properties such as unelastic strain recovery on heating (shape memory effect) or on unloading (pseudoelasticity). These effects are due to thermoelastic martensitic transformations which take place on cooling and heating of the shape memory alloy. It is known that these transitions are athermal so, the phase variation is possible only on temperature or stress variation [1]. However, last years it has been found that in some NiTi-based shape memory alloys the thermoelastic martensitic transformation austenite → martensite could realize during holding at a constant temperature [2-5]. This effect may be used to obtain the strain variation under isothermal holding under stress because, it is known that the formation of the oriented martensite crystals during austenite → martensite transformation under a stress is accompanied by the strain accumulation [1]. So, one may suppose, that if the oriented martensite crystals appear during isothermal holding under a constant stress then an increase in strain should be observed. However, this effect has not been studied so, it was the aim of the present work

Materials and Methods

In [6] it was shown that in the Ti$_{40.7}$Hf$_{9.5}$Ni$_{44.8}$Cu$_5$ alloy the B2 → B19' martensitic transformation occurred during isothermal holding that is why this alloy was used in the present study. To determine the strain variation under isothermal conditions, the experiments were carried out in following procedure. The sample was cooled and heated in a full martensitic transformation temperature range under a constant tensile stress σ and the temperatures of the strain variation were determined (M^σ_s, M^σ_f - start and finish temperatures of strain variation on cooling, A^σ_s, A^σ_f – start and finish temperatures of strain variation on heating). Then, the sample was cooled under a stress of σ down to the holding temperature T*, held for 60 min, and heated up to a temperature that was greater than A^σ_f. On the next step, sample was cooled under a stress σ down to the same holding temperature T* and immediately heated up to a temperature that was greater than A^σ_f. The isothermally accumulated strain was determined as difference between the maximum strain attained on the second and on the third steps. The constant stress was varied from 100 MPa to 350 MPa and the holding temperature was chosen as M^σ_f< T* <A^σ_s.

Results and Discussion

The results of this study firstly showed that an additional strain appeared during isothermal holding (Fig. 1).This strain completely recovered on further heating hence it was associated with the isothermal martensitic transition. Dependencies of isothermal strain ε$_{iso}$ on holding duration were obtained for different temperatures and it was found that strain rose up to the saturation with time. The saturation value depended on holding temperature and the maximum of isothermally accumulated reversible strain was observed within the temperature range of the forward transition despite the value of a constant stress that was applied to the sample during holding. No strain variation was observed on holding at a constant temperature, which was much larger than M^σ_s or less than M^σ_f. It was found, that the influence of the stress value on the maximum value of isothermal strain was non-monotonic and the maximum of isothermal strain equal to 2.9 % was attained when the constant stress was 235 MPa.
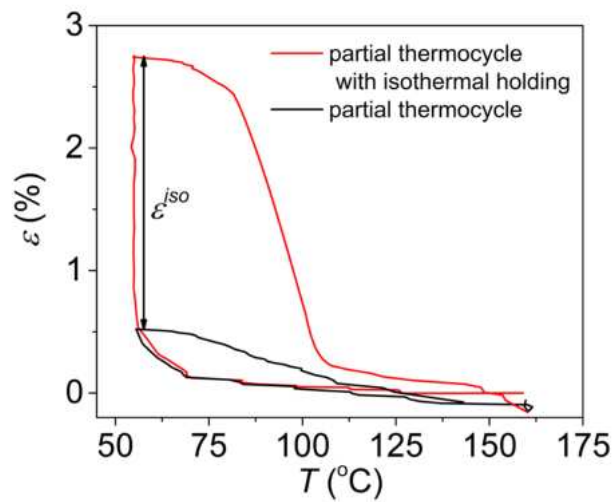
Fig. 1: Strain variation obtained on cooling and heating the $Ti_{40.7}Hf_{9.5}Ni_{44.8}Cu_5$ alloy under a stress of 235 MPa in the range of 160 °C - 55 °C with or without isothermal holding

References
[1]   Otsuka K., Ren X., Progress in Materials Science. **2005**, *50*, 511-678.
[2]   Kustov S., Salas D., Cesari E., Santamarta R., Van Humbeeck J. Acta Materialia. **2012**, *60*, 2578-2592
[3]   Fukuda T., Yoshida S., Kakeshita T. Scripta Materialia. **2013**, *68*, 984-987.
[4]   Ji Y., Wang D., Ding X., Otsuka K., Ren X. Physical Review Letters. **2015**, *114*, 055701-1 - 055701-5.
[5]   Resnina N. Belyaev S., Demidova E., Ivanov A., Andreev V. Materials Letters. **2018**, *228*, 348-350
[6]   Resnina N., Belyaev S., Shelyakov A. Scripta Materialia. **2016**, *112*, 106-108.

P–17

Isothermal nature of magnetic-field-induced martensitic transformation in NiCoMnIn metamagnetic shape memory alloy

Yoshiki Yano[1], Kodai Niitsu[2], Ryosuke Kainuma[3] and Haruyuki Inui[4]

[1]Department of Materials Science & Engineering, Kyoto University, Kyoto 606-8501, Japan
yano.yoshiki.37z@st.kyoto-u.ac.jp

[2]Department of Materials Science & Engineering, Kyoto University, Kyoto 606-8501, Japan
niitsu.koudai.8z@kyoto-u.ac.jp

[3]Department of Materials Science, Graduate School of Engineering, Tohoku University, Sendai 980-8579, Japan
kainuma@material.tohoku.ac.jp

[4]Department of Materials Science & Engineering, Kyoto University, Kyoto 606-8501, Japan
inui.haruyuki.3z@kyoto-u.ac.jp

Introduction

Dynamics of thermal-elastic martensitic transformation (MTs) is described by the nucleation and growth processes. While the former is involved with only the forward MT, the latter is both the forward and reverse MTs. Isothermal forward MT behavior with a C-shaped curve in the TTT (Time-Temperature-Transformation) diagram has been discussed in terms of the thermal activation process of nucleation by Kakeshita et al.[1], but not studied well for the reverse MT. Recently, the existence of a thermal activation process related to habit plane motion has been reported by Niitsu et al.[2]. Considering that the dominance of nucleation and growth differs with respect to the direction of MTs, isothermal dynamics of the reverse MT is expected not to be the same as that of the forward one. In the present study, we investigated the isothermal and athermal behaviors of magnetic-field-induced MT in NiCoMnIn metamagnetic shape memory alloy to get a comprehensive interpretation that can describe the dynamics of both forward and reverse isothermal MTs simultaneously.

Materials and Methods

Ingot of $Ni_{45}Co_5Mn_{36.7}In_{13.3}$ alloy was prepared by induction melting under an argon atmosphere. The fabricated ingot was annealed at 1173K for 90 hours for homogenization. In addition to this, for ordering stabilization, the second annealing at 623K for 6 hours was conducted with subsequent quenching into ice water. Magnetization measurements were carried out using MPMS. To figure the *T-H* phase diagram on this material, magnetization was measured along *M-H* scanning routes at settled temperatures ranging from 80 to 180K. Isothermal evolution of reverse/forward MTs was monitored with the magnetization at various fixed temperatures and magnetic fields.

Results and Discussion

The critical values of forward MT starting magnetic field H_{Ms}, reverse MT finishing magnetic field H_{Af} and equilibrium magnetic field H_0 were determined from the magnetization curves as shown in Fig.1. Isothermal holdings of both forward and reverse MTs shows logarithmic evolutions of transforming fraction, though the forward and reverse MTs show intermittent and continual changes respectively according to whether the nucleation event exists or not. Accordingly, its temperature and time dependences were not analogous with respect to transforming directions; while isothermal forward MT showed iso-fraction C-shaped curves in the TTT diagram as reported elsewhere, isothermal reverse MT showed only lower half of C-shaped curve that terminates at the reverse MT finishing temperature (Fig.2). The increasing hysteresis upon cooling in this alloy is due to the development of thermal activation nature of MT[3,4]. By decomposing the hysteresis into thermal activation and non-thermal activation components, the origin of different isothermal MT behaviors between forward/reverse MTs was discussed. We propose a new interpretation that can describe the dynamics of forward/reverse isothermal MTs simultaneously by taking into account the thermal activation and athermal processes of nucleation and growth.
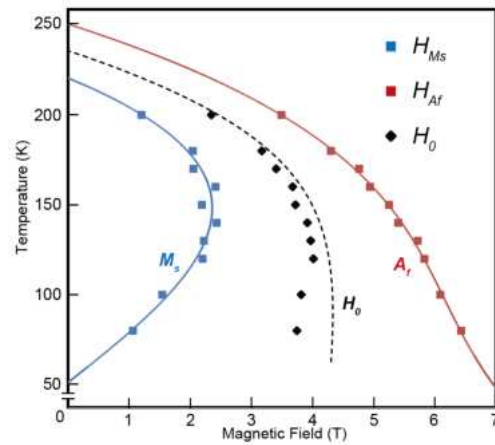
Fig. 1: Magnetic-field vs. temperature phase diagram with the critical magnetic-fields of H_{Ms}, H_{Af}, and H_0.
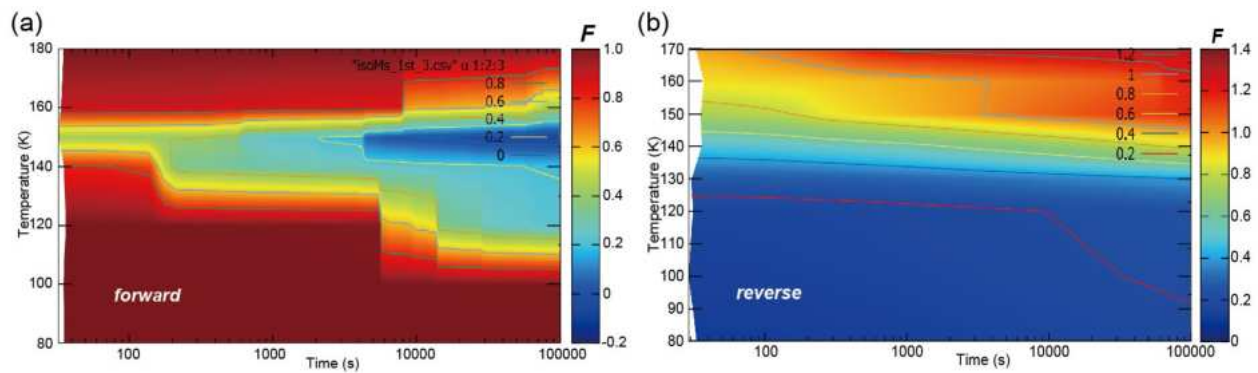
Fig. 2: TTT diagrams of the forward MT (a) and the reverse MT (b). Isothermal forward and reverse MT showed C-shaped curve and lower half of C-shaped curve respectively.

References
[1]   T. Kakeshita, K. Kuroiwa, K. Shimizu, T. Ikeda, A. Yamagishi and M. Date, Mater. Trans. JIM, **1993**, 34, 423-318.
[2]   K. Niitsu, T. Omori and R. Kainuma, Appl. Phys. Lett. **2013**, 103, 242406.
[3]   S. Kustov, I. Golovin, M.L. Corro and E. Cesari, J. Appl. Phys., **2010**, 107, 053525.
[4]   T. Fukuda, T. Kakeshita and Y. Lee, Acta. Mater., **2014**, 81, 121-127.

P–18

Formation of intermetallics during solid-liquid inter-diffusion bonding of Pd/Ni assembly using In interlayer

Tung-Han Chuang[1], Yan-Cheng Lin[2], Pei-Ing Lee[1] and Po-Ching Wu[1]

[1]Institute of Materials Science and Engineering, National Taiwan University, No. 1, Roosevelt Rd., Sec. 4, Taipei 106, Taiwan, tunghan@ntu.edu.tw, leepeiing@gmail.com, brian19960510@gmail.com

[2] Wire Technology Co., LTD, No. 27, Aly. 56, Ln. 320, Sec.1, Shatian Rd., Dadu Dist, Taichung 432, Taiwan, yancheng@wiretech.com.tw

Introduction

For the manufacturing of IC and LED devices using the metal organic chemical-vapor deposition (MOCVD) process, hydrogen with a 9N high purity is required. Palladium is often used as the material for hydrogen purification (Ref. 1). For this purpose, multiple Pd fine tubes are assembled with a stainless steel head to form a Pd cell. A traditional brazing or laser welding can cause the deformation of these fine Pd tubes with a diameter of about 2 mm and a thickness of about 60 μm. In contrast, a soldered Pd cell cannot endure the operation temperatures over 350 ºC for a hydrogen purifier. In a previous paper, solid-liquid interdiffusion bonding (SLID) method using Sn interlayer has been applied for the bonding of Pd sheet with Ni plate to simulate the Pd/Ni assembly of a hydrogen purifier at temperatures between 275 ºC and 350 ºC (Ref. 1, 2). In this study, the bonding temperature was reduced to 200 ºC through the employment of an In thin film.

Materials and Methods

In this study an In thin film was employed for the SLID bonding of a palladium sheet (0.1 mm thickness) with a Ni plate (1 mm thickness). Similar to the bonding cases in Ref. 1, the Pd sheet was ground with 4,000 Grit SiC paper, electroplated with a 3 μm In thin film interlayer, and then assembled with a Ni plate in case I. In case II, the Pd sheet was coated with 4 μm In and then electroplated with an additional 3 μm Ag layer and then bonded with a 4 μm In-coated Ni plate. In case III, the Pd sheets were pre-coated with a 6 μm Ni layer, which was further heated at 450 ºC for 30 min in case IV. The pre-treated Pd sheets in Cases III and IV were electroplated with a double layer of 4 μm In/3 μm Ag and then assembled respectively with a In-coated Ni plate similar to that in Case II. The SLID process was conducted in a vacuum furnace of 5.3×10^{-4} Pa, and the assembly was heated at 200 ºC for 30 min under a pressure of 3 MPa.

Results and Discussion

For the SLID bonding in case I, Fig.1a shows that the Pd sheet and Ni plate reacted with the In interlayer to form $PdIn_3$ and Ni_3In intermetallic compounds, respectively. However, long cracks appeared between the Ni_3Sn_4 and PdSn intermetallic layers, and the bonding strength was very low. The appearance of cracks at the interface between $PdIn_3$ and Ni_3In Ni_3Sn_4/PdSn interface and the Pd/Ni assembly failed in this case. Through the inserting of an Ag thin film between the In-coated Pd sheet and Ni plate in case II, an Ag_3In layer formed between the Ni_3Sn_4 and PdSn intermetallic layers, and the crack in Fig.1a was eliminated as revealed in Fig.1b.

In case III, the Pd sheet was electroplated with 6 μm Ni film, 4 μm In, and 3 μm Ag. The coated Pd sheet was then SLID bonded with a 4 μm In-coated Ni plate. Figure 1c shows sound interfaces without any voids or cracks in the Pd/Ni joints and a $Ni/Ni_3In/Ag_3In/Ni$ intermetallics multilayers appeared at the interface. However, the electroplated Ni film can be delamated from the Pd surface during the electroplating processes of In and Ag layers on the Ni-coated Pd sheet. Therefore, the Ni-coated Pd sheet was pre-heated at 450 ºC for 30 min, resulting the solid solution of Ni in Pd (Ref.3), and then electroplated with In and Ag layers before being SLID bonded with the In-coated Ni plate (Case IV in Fig.1d). In this case, a similar $Ni/Ni_3In/Ag_3In/Ni$ intermetallics structure as that in case III formed between the Ni-coated Pd sheet and Ni plate.
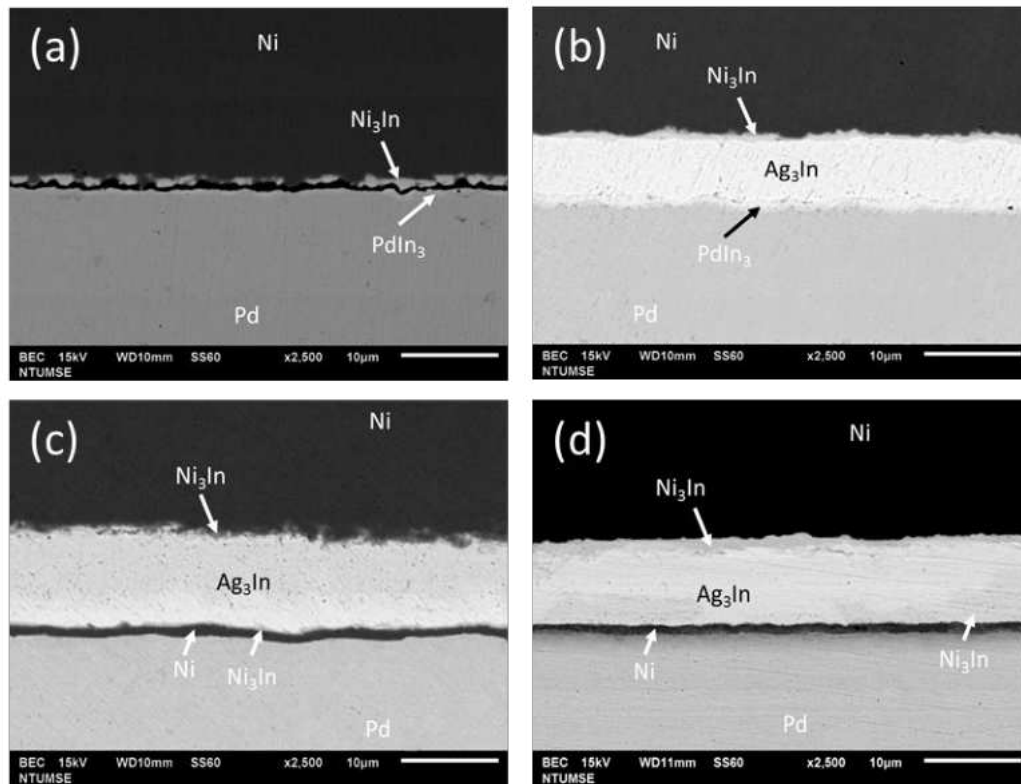
Fig. 1. Intermetallics formed at the interfaces of Pd/Ni couples SLID bonded at 200 ºC for 30 min using an In interlayer: (a) Case I, (b) Case II, (c) Case III, (d) Case IV.

References
[1]   C. H. Chuang and Y.C. Lin, Welding Journal, **2016**, 95, 442s-449s.
[2]   S. Bader, W. Gust, and H. Hieber, Acta Metall. Mater., **1995**, 43, 329-337.
[3]   A. Nash, and P. Nash, Bull. Alloy Phase Diagrams., **1984**, 5, 446-450.

P–19

Effect of bcc and sigma phase particles on grain growth and strengthening in a CoCrFeNiMn high entropy alloy

Margarita Klimova, Dmitry Shaysultanov, Sergey V. Zherebtsov and Nikita D. Stepanov

Belgorod National Research University, Belgorod 308015, Russia, Klimova@bsu.edu.ru, Shaysultanov@bsu.edu.ru, Zherebtsov@bsu.edu.ru, Stepanov@bsu.edu.ru

Introduction

The so-called high-entropy alloys have recently emerged as a new class of advanced metallic materials with complex, multicomponent chemical composition [1]. Although it was initially believed that the solution structures will be beneficial for obtaining balance between high strength and ductility, later it was revealed that presence of ordered phases is needed to provide sufficient strength without sacrifice in ductility [2]. In the present work we demonstrate how precipitation of the second phases, namely bcc and sigma phases, affects mictostructure and mechanical properties development in the the equiatomic CoCrFeNiMn alloy, which is widely considered as "model" single solid solution phase high entropy alloy [3].

Materials and Methods

The equiatomic CoCrFeNiMn alloy (Co20.6Cr19.9Fe19.5Ni20.9Mn19.1 in at.%) was produced by vacuum arc melting and homogenized at 1000°C for 24 hours. The homogenized alloy was cold-rolled to 80% reduction and then annealed at 500°C, 600°C, 700°C, 800°C or 900°C for 1 hour, and for 1, 2, 5 10 or 50 hours at 600°C; the annealing was followed by air cooling.

Results and Discussion

The CoCrFeNiMn alloy in the cold-rolled condition has a single fcc phase heavily-deformed lamellar microstructure composed of twin boundaries and shear bands mostly aligned with the rolling direction.

Isochronal annealing at 500-900°C for 1 hour resulted in recrystallization of the fcc matrix (600-900°C) and precipitation of the Cr-rich bcc (500-700°C) and sigma (600-800°C) particles. Annealing at 500°C did not result in significant changes of microstructure in comparison to that of deformed condition; yet some bcc phase particles appeared in the fcc matrix. At a higher temperature (600°C) the majority of the fcc matrix was found to be recrystallized with a size of the recrystallized grains of 1.3 μm. Further increase in annealing temperature resulted in complete recrystallization and led to a gradual increase in the fcc grain size from 2.0 μm after annealing at 700°C to 17.1 μm – at 900°C. The size of the bcc/sigma particles increased with the annealing temperature whereas the fraction of the second phase particles exhibited a non-monotonic dependence.

Isothermal annealing at 600°C resulted in the growth of the recrystallized fcc grains and coarsening of both the sigma and bcc particles. The average grain size increased from 1.3 μm to 3.8 μm with an increase in the annealing time from 1 to 50 hours. A number of near-equilibrium triple junctions of grain boundaries and annealing twins suggesting normal grain growth as the main mechanism of microstructure evolution were observed. The sigma particles located at grain boundaries increased from 260 to 820 nm with an increase in the annealing time from 1 to 50 hours; the bcc particles under the same conditions increased from 70 to 120 nm only.

Grain growth and particle coarsening can be expressed by power law functions of annealing time with the exponents of about 3.6, 4, and 7 for grains, sigma and bcc, respectively. Coarsening of the sigma particles seems to be controlled mainly by grain boundary diffusion. Meanwhile the bcc particles exhibited much slower coarsening kinetics, that can be associated with the phase dissolution during annealing due to the non-equilibrium nature. The fcc grains coarsening kinetics only slightly faster than that of the grain boundary sigma particles thereby suggesting the main contribution of grain boundary diffusion to fcc grains growth.
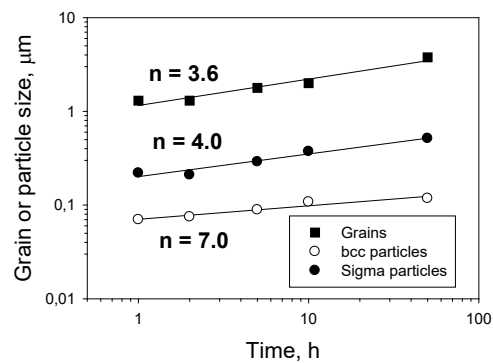
Fig. 1: Size of the fcc grains and bcc or sigma particles as a function of annealing time at 600°C

Furthermore, it was found that the fcc grain growth was limited by the particles as per the Zener drag mechanism. An increase in the annealing time at 600°C from 1 to 50 hours was also accompanied by a pronounced increase in the fraction of the sigma phase and a decrease in the fraction of the bcc phase.

Strength of the alloy increased after annealing for 1 hour at 500°C and 600°C in comparison with the cold rolled condition, while annealing at higher temperatures resulted in pronounced softening together with increased ductility. The quantitative analysis had revealed that strengthening after annealing at low temperatures was associated with the bcc/sigma particles precipitation.

Increase of the annealing time at 600°C from 1 to 50 hours resulted in softening and increase of ductility. However, even after 50 hours annealing the alloy maintained relatively high strength (yield strength of 685 MPa) which can be ascribed to the grain boundary (Hall-Petch) strengthening due to fine fcc grains preserved by pinning effect of the sigma particles.

References

[1]   J.-W. Yeh, S.-K. Chen, S.-J. Lin, J.-Y. Gan, T.-S. Chin, T.-T. Shun, C.-H. Tsau, S.-Y. Chang, Advanced Engineering Materials. **2004, *6***, 299-303.
[2]   D.B. Miracle, O.N. Senkov, Acta Materialia. **2017,** *122*, 448–511.
[3]   B. Cantor, I.T.H. Chang, P. Knight, A.J.B. Vincent, Materials Science and Engineering A. **2004**, *375*, 213–218.

P–20

Plastic deformation behavior of single crystalline Cr-Co-Ni equiatomic medium entropy alloy

Kazuki Ehara[1], Kodai Niitsu[2], Kyosuke Kishida[2] and Haruyuki Inui[2]

[1] Department of Materials Science and Engineering, Kyoto University, Kyoto 606-8501, Japan,
ehara.kazuki.75r@st.kyoto-u.ac.jp

[2] Department of Materials Science and Engineering, Kyoto University, Kyoto 606-8501, Center for Elements Strategy Initiative for Structural Materials (ESISM), Kyoto University, Kyoto, Japan, niitsu.koudai.8z@kyoto-u.ac.jp, kishida.kyosuke.6w@kyoto-u.ac.jp, inui.haruyuki.3z@kyoto-u.ac.jp

Introduction

Medium/high entropy alloys are a class of multi-component solid solution alloys with (nearly) equiatomic compositions, which are considered to be stabilized because of the large contribution of configurational entropy to their Gibbs energy [1]. Some of these alloys exhibit exceptional mechanical properties such that the strength and tensile elongation increase simultaneously with decreasing temperature [2] and it endows the outstanding combinations of high strength and high tensile elongation especially at low temperature [3]. Among various medium/high entropy solid solution alloys discovered so far, the Cr-Co-Ni equiatomic solid solution alloy with the face-centered cubic (FCC) structure has been reported to exhibit both the highest strength and the highest elongation in a polycrystalline form [4]. However, the detailed mechanisms endowing these excellent mechanical properties remain unclear in many aspects mainly because of the lack of fundamental studies using single crystals. In the present study, we investigated the plastic deformation behavior of single crystals of the Cr-Co-Ni equiatomic alloy through uniaxial compressive and tensile tests to clarify the origin of excellent mechanical properties.

Materials and Methods

Single crystals of the Cr-Co-Ni equiatomic solid solution alloy were prepared by directional solidification using an optical floating zone furnace in an argon atmosphere. The specimens for compressive and tensile tests oriented along [-123] crystallographic directions were cut by wire electric discharge machining. Compressive tests were performed at temperatures in the range of 13 - 1073 K and at strain rates in the range of 1×10^{-5} - 5×10^{-3} s^{-1}. Tensile tests were conducted at room temperature and liquid nitrogen temperature and at a strain rate of 1×10^{-4} s^{-1}. The specimens after mechanical tests were observed using optical microscope (OM), scanning electron microscope (SEM), transmission electron microscope (TEM) and scanning transmission electron microscope (STEM).

Results and Discussion

The strong temperature dependence of the critical resolved shear stress (CRSS) of the [-123]-oriented single crystals are observed; the value at liquid nitrogen temperature is almost twice larger than that at room temperature (Fig. 1). The activation volume of the alloy is found to be quite low when it is compared to that for binary FCC alloys. The stress-strain curves obtained from tensile tests exhibit a widely extended easy glide region (stage I) and high work hardening rate at a linear hardening region (stage II). This is considered to be attributed to a relatively low stacking fault energy for this alloy. Deformation twinning and hexagonal close-packed (HCP) transformation on conjugate plane were observed in the thin-foiled specimens after fracture at both room and liquid nitrogen temperatures. They contribute to high work hardening rate and allow plastic instability to be postponed; as a result, the good strength-ductility combination is achieved.
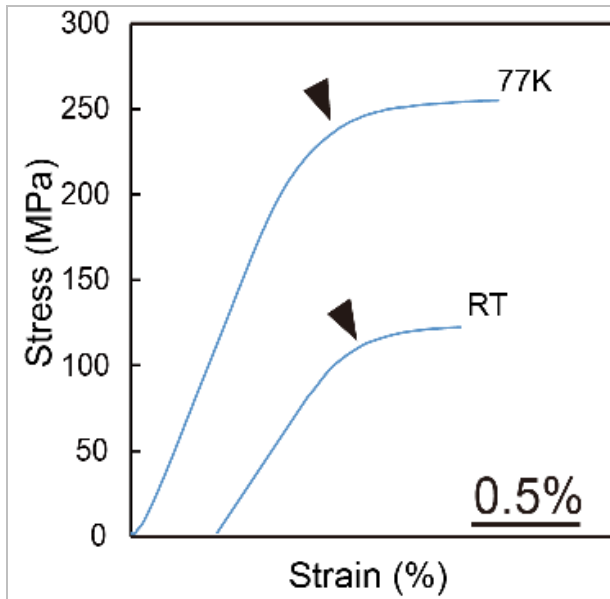
Fig. 1: Compressive stress-strain curve at RT and 77 K.

References
[1] J.W. Yeh, Minerals, Metals and Materials Society, **2013**, *65*
[2] A. Gail, E.P. George, Intermetallics, **2013**, *39*, 74-78
[3] G. Laplanche et al, Acta Materialia, **2016**, *118*, 152-163
[4] Z. Wu et al, Acta Materialia, **2014**, *81*, 428-441

P–21

Thermodynamic stability of a nanocrystalline highly concentrated solid solution alloy

Matheus A. Tunes[1], Graeme Greaves[2], Thomas M. Kremmer[1], Cláudio G. Schön[3], Stefan Pogatscher[1], Philip D. Rack[3], Stephen E. Donnelly[2] and Yanwen Zhang[3]

[1]Chair of Non-Ferrous Metallurgy, Montanuniversität Leoben, Austria, matheus.tunes@unileoben.ac.at
[2]Ion Beam Centre, University of Huddersfield, United Kingdom
[3]Department of Metallurgical and Materials Engineering, University of São Paulo, Brazil

Introduction

Concentrated solid solution alloys (CSA) has attracted much attention in metallurgy and materials science due to their superior set of properties when compared with conventional dilute solid solution alloys [1-2]. In contrast to the latter, CSAs are a class of multicomponent alloys with five or more elements in solid solution but mixed at (or closer to) equiatomic proportions [1-2]. The minimisation of the Gibbs free energy due to the equiatomic mixing is believed as part of the reasons to stabilise CSAs in a single-phase random solid solution, thus possibly avoiding the formation of complex intermetallic or secondary phases, although the exact physical mechanisms behind the high phase stability of CSAs are currently under intense investigation [3]. A prominent field of research on CSAs is their microstructural response to energetic particle irradiation exposure. Recent reports indicated that by tuning the elemental composition, CSAs can be designed to control the mobility of crystalline defects and their migration pathways, thus leading to superior radiation resistance [4]. Due to such recent experimental observations, these complex alloys are now under consideration as candidate materials to the next fleet of nuclear reactors and intense research has been prioritised into elucidate how displacive irradiation changes the microstructure and properties of CSAs when compared with conventional solid solution alloys. In addition, the possibility of engineering CSAs in nanostructured manner could potentially further increase the radiation tolerance as nanocrystallites are known to be active sinks for point defects [5]. By nanoengineering an ultrafine-grained CSA via magnetron sputter-deposition methods, this work investigates whether such nanocrystalline CSA is structurally stable under thermal annealing (equilibrium conditions) and ion irradiation (non-equilibrium conditions). The development of nanocrystalline metallic alloys using the concepts from CSAs could shed light to the development of new materials with enhanced radiation tolerance and stability [5,6]. Nevertheless, the experiments herein reported are also used to reflect on the core-effects of CSA alloys as well as their constitute hypothesis such as high-entropy effect and sluggish diffusion.

Materials and Methods

CoCuCrNiFe thin solid films with thicknesses of 70 nm were sputter-deposited onto NaCl substrates from pure elemental metal targets of their constitutive elements. A detailed report on the deposition methods of such nanocrystalline CSA thin films can be found elsewhere [5,6]. After deposition, TEM lamellae for ion irradiation and thermal annealing were prepared directly into Mo mesh grids.

Electron microscopy methods were used in this work to investigate the thermodynamic stability of a new sputter-deposited ultrafine-grained CSA – the CoCuCrNiFe. Firstly, the generation of point defects in excess concentration levels as a result of the atomic collisions was used to analyse microstructural response of the CSA specimens varying temperature and dose. For this, several heavy ion irradiations *in situ* within a Hitachi H-9500 Transmission Electron Microscope (TEM) were carried out at the temperatures of 293, 573 and 773 K up to a dose of 7.6×10^{15} ions·cm^{-2} (11 displacements-per-atom or dpa) in the MIAMI-2 Facility. Post-irradiation Scanning Transmission Electron Microscopy (STEM) characterisation was performed in a new FEI Talos F200X equipped with high resolution Super-X Energy Dispersive X-ray Spectroscopy (EDX) system at Montanuniversität Leoben. Following the *in situ* heavy ion irradiation results, complementary experiments of thermal annealing *in situ* in a TEM were also carried out.

Results and Discussion

Initial TEM screening of the pristine specimens revealed that the microstructure of the CoCuCrNiFe CSA as deposited is composed of nanocrystallites with sizes around of 7—10 nm as shown in the bright-field TEM micrograph in Fig. 1(a). In addition, as shown in Fig. 1(a), the CSA microstructure is composed of voided grain boundaries in agreement with Movchan-Demichishin-Thornton (MDT) zone models for thin solid films deposited at low homologous temperatures. TEM results show that the heavy irradiation induces noticeable grain growth as the temperature increases from 293 to 773 K, Fig. 1(a-d), however, the irradiated samples at 773 K have shown evidence of radiation-induced segregation as assessed by the STEM-EDX analysis in Fig.1(e-g). These results also indicate that the maximisation of the entropy by mixing the elements close to the equiatomic composition is not sufficient to prevent grain growth with concurrent phase transformations at intermediary temperatures (773 K). It will be shown that the nanocrystalline alloy was observed to be stable under either thermal annealing and irradiation only in the narrow temperature range from 293 to 523 K.
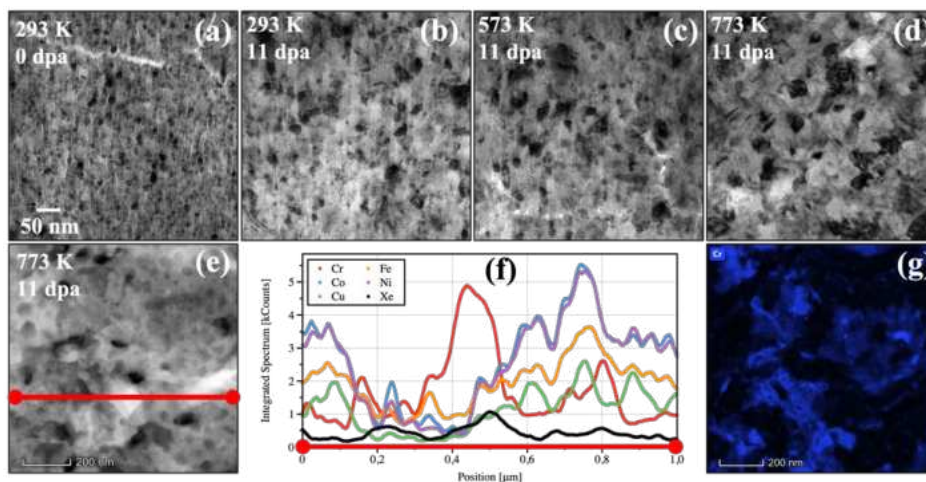
Figure 1: The microstructural evolution of CoCuCrNiFe ultrafine-grained CSA under 134 keV Xe$^+$ irradiation: underfocused (1000 nm defocused) micrographs showing the (a) pristine samples at 293 K and the irradiated samples at (b) 293 K, (c) 573 K and (d) 773 K after 11 dpa. Micrograph (e) show High-Angle Annular Dark Field of the 773 K irradiated sample in which the line-scan in (f) shows segregation of Cr further confirmed with (g) Cr EDX mapping. Note: the scale in (a) applies to images (b-d).

References

[1]   M.-H. Tsai, J.-W. Yeh, High-Entropy Alloys: A Critical Review, Mater. Res. Lett., **2014**, *2*. 107–123.

[2]   D.B. Miracle, O.N. Senkov, A critical review of high entropy alloys and related concepts, Acta Mater, **2017**, *122*. 448–511.

[3]   C.G. Schön *et al.*, Acta Mater., **2018**, *148*. 263–279.

[4]   Y. Zhang *et al.,* Influence of chemical disorder on energy dissipation and defect evolution in concentrated solid solution alloys, Nat. Commun., **2015**, *6*, 8736.

[5]   Y. Zhang *et al.*, Thermal stability and irradiation response of nanocrystalline CoCrCuFeNi high-entropy alloy, Nanotechnology, **2019**, *30*, 294004.

[6]   Z. An *et al*., Solid-solution CrCoCuFeNi high-entropy alloy thin films synthesized by sputter deposition, Mater. Res. Lett., **2015**, *3*, 203–209.

P–22

On grain refinement of Fe-25Al-1.5Ta (at. %) alloy

Emir Subašić, Alexander Gußfeld and Heiner Michels

Access e.V., Intzestr. 5, 52072 Aachen, Germany, e.subasic@access-technology.de,
a.gussfeld@access-technology.de, h.michels@access-technology.de

Introduction

Low raw material cost of FeAl intermetallics in combination with their excellent corrosion resistance, increased flow stress [1] and creep strength [2] at elevated temperatures, compared to P92 as a standard material used for steam turbine parts, favor them for energy sector applications. High temperature gas turbine blades under dynamic load as well as large cast parts under static load – like housings – belong to their possible applications. One of the main reasons why this class of materials is not more widely employed for actual production of such parts is its brittleness at room temperature, caused partly by columnar grains [3] developed in its microstructure. At the same time, the castability, feeding and cracking behavior of FeAl intermetallics after grain refinement treatment have not been comprehensively researched yet. Grain size reduction could be a resolution for both challenges: ductility at room temperature could be increased [4] and castability improved. While grain refinement is a standard treatment for most commercial ferrous or aluminum alloys, a suitable grain refinement treatment of FeAl intermetallics is still missing.

This paper offers results obtained during a study on grain refinement of Fe-25Al-1.5Ta (at. %) treated by different refinement agents and additions.

Materials and Methods

The study presented was carried out with FeAl-based alloy Fe-25Al-1.5Ta (at. %), because of its superior high temperature creep and corrosion resistance. The impact of two well-known grain refiners, TiC and TiB2, was investigated. Projected chemical composition of the melt was 72.27 % Fe, 24.68 % Al, 1.47 % Ta, 0.31 % Si, 0.64 % Ti and 0.64 % C (at. %) for trials with TiC and 71.78 % Fe, 24.51 % Al, 1.46 % Ta, 0.31 % Si, 0.64 % Ti and 1.29 % B (at. %) for trials with TiB2. Casting trials were conducted with a Linn High Therm Supercast centrifugal casting machine. The alloy charge was placed in a ceramic crucible together with the grain refiner. Melting was carried out under vacuum and the melt was poured in a non-preheated permanent copper mold. The melt had a pouring temperature of 1540 °C. Evaluation of results was done by light optical microscopy and by scanning electron microscope (SEM). Grain count was obtained by mean linear intercept method at different positions.

Results and Discussion

The results obtained by light optical microscopy are given in Fig 1 and Fig 2. Measured mean grain counts have shown that grain refinement by use of TiC (Fig. 1) resulted in 7.7 times finer microstructure compared to reference case where no grain refiner was used. On the other hand, grain refinement with TiB_2 (Fig. 2) resulted in 3.7 times finer microstructure than in reference case.

According to the measurements, one can conclude that addition of either TiC or TiB_2 results in grain refinement of the final microstructure for Fe-25Al-1.5Ta (at. %). Comparison of obtained grain counts suggests a twofold stronger impact on grain size reduction exhibited by TiC than by TiB_2, thus giving a clear advance for use of this additive for grain refinement of Fe-25Al-1.5Ta (at. %).

Outlook

Ongoing research attempts to give more information on impact of diverse grain refiners on ductility of Fe-25Al-1.5Ta (at. %). By subsequent heat treatment the phase stability of carbides and borides, depending on the grain refiner added, is going to be tested. Casting trials with sand molds and ceramic shells will be carried out as well; a comparison of thus obtained results with current trials will give an answer on the question, which combination of grain refiners and mold materials could be selected in order to gain the best properties of a casting made of FeAl-based alloy. Numerical simulation of the casting process provides local cooling rates, which is a solid basis for establishing a correlation between cooling rate and grain size. In cooperation with project partners from the Centre of Excellence for Lightweight Design at Landshut University of Applied Sciences and Chair of Corrosion and Corrosion Protection at RTWH Aachen University, a comprehensive data set including thermomechanical properties and corrosion resistance of FeAl-based alloys will be completed.

Fig. 1: FeAl-based alloy Fe-25Al-1.5Ta (at. %), grain refined with TiC: Upper image is obtained by automated large-scale image acquisition under 50x magnification and processed by MosaiX method; The green framed rectangular area is zoomed and displayed at lower image

Fig. 2: FeAl-based alloy Fe-25Al-1.5Ta (at.%), grain refined with TiB2: Upper image is obtained by automated large-scale image acquisition under 50x magnification and processed by MosaiX method; The yellow framed rectangular area is zoomed and displayed at lower image
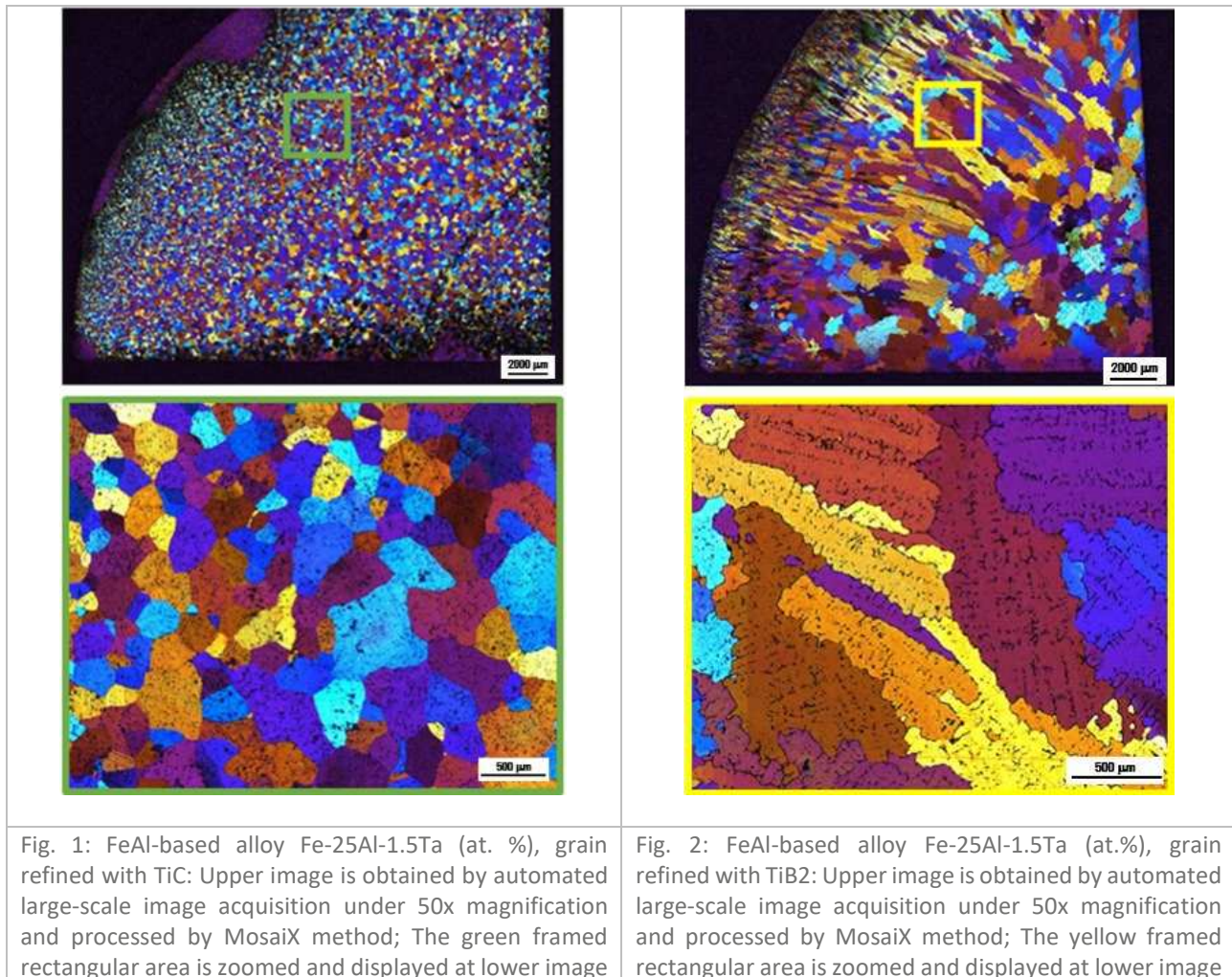
References
[1] D.G. Morris, M.A. Muñoz-Morris, I. Gutierrez-Urrutia, L.M. Requejo, Precipitation in ductile Fe–18Al–5Cr alloys with additions of Mo, W and C and effects on high-temperature strength, Intermetallics, 17, **2009**, 404-413.
[2] X. Li, P. Prokopčáková, M. Palm, Microstructure and mechanical properties of Fe–Al–Ti–B alloys with additions of Mo and W, Materials Science and Engineering: A, 611, **2014**, 234-241.
[3] P. Janschek, K. BauerPartenheimer, R. Krein, P. Hanus, M. Palm, Forging of Steam Turbine Blades with an Fe3Al-based Alloy, Mater. Res. Soc. Symp. Proc. 1128, **2009**, 47.
[4] D.G. Morris, M.A. Morris-Muñoz, The influence of microstructure on the ductility of iron aluminides, Intermetallics, 7, **1999**, 1121-1129.

P–23

Casting of iron aluminides – an investigation on an industrial scale

Bruna N. Ramirez and Cláudio G. Schön

Department of Metallurgical and Materials Engineering, Escola Politécnica da Universidade de São Paulo, Av. Professor Mello Moraes, 2463 Butantã, São Paulo - SP, 05508-030, Brasil, brunaniccoli@usp.br

Introduction

Iron aluminides are long being considered as potential candidates for substitution of stainless steels in structural applications at moderate to high temperatures, since these alloys show a significantly reduced density compared to steels combined with excellent corrosion and sulfidation resistance [1, 2, 3]. Iron aluminides are, however, brittle materials at room temperature, which is seen by industry as a hindrance to their use. For this reason, research on iron aluminides are directed to adding alloy elements such as Cr, Ti, Zr, C to improve the mechanical properties [4][5][6]. However, brittle metals, such as gray cast iron or non-modified Al – Si alloys are widely employed in engineering for the production of components through a casting route, including in situations in which structural integrity is critical.

Another difficulty reported for industrial-scale casting of iron aluminides is the reduction of melting capacity of steel-based with Al addition due foundry defect occurrence resulting from excessive contraction and slag formation [7][8]. For this reason, previous studies about iron aluminide casting process claim that these alloys require special cast methods, such as Exo-Melt process [7], which may render the cost of manufacturing castings of these materials unfeasible. The present work aimed at analyzing the viability of a casting process on an industrial scale of model iron aluminides. Issues like the possibility of achieving grain refinement through the addition of TiB_2 innoculant, the interaction between melt and refractory lining, and an assessment of linear contractions and of fluidity are investigated using large scale melts, typical of the ones used in a foundry.

Materials and Methods

Fe28Al, Fe28Al6Cr and Fe28Al6Cr1Ti (at.%) alloys were prepared and tested in a foundry laboratory, which reproduces a typical foundry shop. Each alloy was cast with and without the addition of 0.05% and 0.10% wt. innoculant (Al- 5Ti-1B, wt.%, master alloy, in the form of bars). The alloys were prepared in a low frequency induction furnace (120 kW, Inductotherm), with a maximum capacity of 100 kg (of ferrous alloys). The crucible lining was made of a refractory cement composed 50 of 86% wt. Al_2O_3 and 14% wt. MgO. Each alloy was prepared as single batch using the raw materials listed in Table 1, the amounts of which were calculated for a total load of 60 kg of material and a loss of 17.5% Al and 32.2% Cr was also assumed.

The A36 steel was initially loaded and heated in the furnace with Cr and Ti (in case they were used), but some aluminum had to be added to use the heat of reaction for complete melting of the load. No inert gas protection system was employed, therefore slag formation was minimized by the addition of perlite ore ($\approx$ 74 wt.% SiO_2 and 14 wt.% Al_2O_3).

Melt	A36 Steel	AA5052	Cr	FeTi
Fe28Al	51.0	10.8	0.0	0.0
Fe28Al6Cr	47.0	11.2	5.2	0.0
Fe28Al6Cr1Ti	45.2	9.2	6.6	2.5

Table 1: Charge composition (in kg) used for the three melts.

All casting experiments were partitioned so that a portion of the liquid metal was poured into a heated foundry ladle with maximum capacity of 30 kg, where the innoculant was added (if this was the case) in the prescribed quantity. Then the metal contained in the pan was poured into a fluidity spiral mold and into inverted Y-shaped sand molds, using coarse sand with thermoactive resin. The chemical composition of the samples was analyzed using X-ray spectroscopy (XFR) for Si, Mn, Al, Cr and Ti and the LECO combustion method for C and S. The metal samples were analyzed by optical microscopy (LOM), scanning electron microscopy (SEM), energy-dispersive X-ray spectroscopy (EDS) and Vickers microhardness (load = 3 N).

Results and Discussion

Figure 1 shows the macrostructure of the Y-shaped ingots of Fe28Al alloy with different quantities of innoculant (0.00%, 0.05% and 0.10% wt). The microstructures show a heterogeneous grain size distribution, caused by different cooling rates in different parts of the mold. The addition of 0.05% Al-5Ti-1B in the Fe28Al alloy has produced a reduction of grain size by about 33% compared with the grain size in the alloy without innoculant. The same is observed for the case of 0.1% inoculant, leading to a reduction estimated 60% in the grain size. Figure 2 shows the microstructures of the

samples of the three melts and in the three levels of inoculation investigated in the present work. All images correspond to a single-phase matrix containing small precipitates, which were investigated by EDS. Most of these particles are consistent with the composition of the κ-carbide (Fe_3AlC_x), but particles with composition consistent with TiC, as well a Cr-containing carbide were also identified. The images also show the dramatic effect of composition and inoculation level on the grain size of the alloys. The results of the fluidity spiral show that the more complex the alloy is, the less fluid becomes the melt, however, this result could be a consequence of changes in pouring temperature, which could not be avoided during the proceeding. The melts interacted heavily with the refractory lining, reducing the capacity of the furnace during operation. This shows that atmosphere control is necessary for these alloys for normal operation.

Fig. 1: Macrographs of the Fe28Al melt investigated in the present work.

Fig. 2: Casting microstructures of the samples corresponding to melt Fe28Al: (a) - no inoculant, (b) - 0.05% Al5Ti1B and (c) - 0.10% Al5Ti1B; to melt Fe28Al6Cr: (d) - no inoculant, (e) - 0.05% Al5Ti1B and (f) - 0.10% Al5Ti1B; and to melt Fe28Al6Cr1Ti: (g) - no inoculant, (h) - 0.05% Al5Ti1B and (i) - 0.10% Al5Ti1B.

References

[1]   Deevi, S.C., Sikka, V.K.. Nickel and iron aluminides: an overview on properties, processing and application. Intermetallics. **1996**, 4:357–375.

[2]   Morris, D.G., Dadras, M.M., Morris, M.A.. The influence of Cr addition on the ordered microstructure and deformation and fracture behaviour of a Fe-28%Al intermetallic. Acta Metall Mater. **1993**, 41:97 – 111.

[3]   Morris, D.G., Muñoz-Morris, M.A.. Development of creep-resistant iron aluminides. Mater Sci Eng A. **2007**, 462:45 – 52.

[4]   Mckamey, C. G.; Horton, J. A.; Liu, C. T. Effect of Chromium on Room Temperature Ductility and Fracture Mode in FeAl. Scripta Metallurgica. **1998**, 22: 1679-1681

[5]   Palm, M.. Concepts derived from phase diagram studies for the strengthening of Fe–Al-based alloys. Intermetallics. **2005**, 13: 1286-1295.

[6]   Vodičková, V.; Hanus, P.; Vlasák, T.; Švec, M.; High temperature properties of non-critical Fe-Al alloys doped by non critical or "slightly–critical" elements. IOP Conf. Ser.: Mater. Sci. Eng., 329, 01, **2007**.

[7]   Sikka, V. K.; Wilkening, D.; Liebetrau, J.; Mackey, B.. Melting and casting of FeAl-based cast alloy. Materials Science and Engineering: A. **1998**, 258: 229-235

[8]   Kratochvı, P. The history of the search and use of heat resistant Pyroferal© alloys based on FeAl. Intermetallics. **2008**, 16: 587- 591

P–24

Pro-FeAl – process development for economic, efficient turbine components made out of FeAl

Michael Ghosh, Heiner Michels and Matthias Bünck

Access e.V., Intzestr. 5, 52072 Aachen, Germany, m.ghosh@access-technology.de,
h.michels@access-technology.de, m.buenck@access-technology.de

Introduction

Several alloys with major content of iron and aluminium combine advantageous material properties such as lightweight, wear- and corrosion-resistance, recyclability, low cost raw materials (Fe and Al), and good processability [1, 2]. However, up to now the limited strength at elevated temperature (> 600°C) and a low ductility at room temperature hamper their ability to challenge steel or even nickel-based alloys and prevent a wider industrial application range. Furthermore, only limited experience regarding the cause-and-effect relationship between process conditions and device properties has been acquired in the past.

To address these disadvantages the German government funded 3-year-project 'Pro-FeAl' [1] started in January 2019. Pro-FeAl brings together 4 industrial (Siemens AG, Rolls Royce Deutschland, Leistritz Turbinentechnik, Otto Junker) and 3 scientific partners (MPI für Eisenforschung, Karlsruher Institut für Technologie, Access e.V.). The project's main goals are to evaluate the competitiveness of FeAl alloys with respect to their applicability for parts in conventional power plants (e. g. turbine blades, casings) and to deliver essential contributions for establishing appropriate production routes for in-spec FeAl components.

Material Properties and Process Routes

By producing FeAl samples, representing components of power generation machines, essentially 5 process routes are evaluated and compared in 'Pro-FeAl' (Fig.1): Casting Technology (CT), Forging Technology (FT), Additive Manufacturing (AM) and the combined process routes CT+FT and AM+CT.
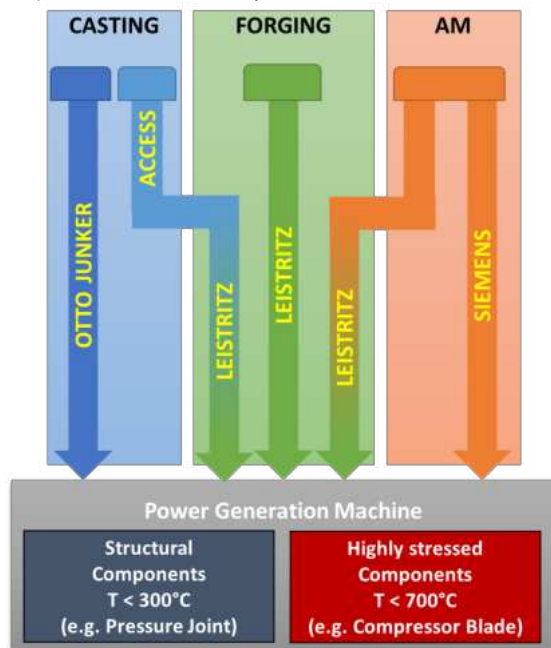
Fig. 1: Process routes for manufacturing FeAl alloys intend to be used for components of power generation machines.

The test matrix is split in a low (< 300°C) and a high temperature (< 700°C) application range. Additionally, heat and other treatments are included in the investigations. For low temperature applications, high corrosion-resistance, sufficiently high ductility and a low density are of most importance while at higher temperatures creep, fatigue, wear- and oxidation-resistance are in focus. In detail the following questions shall be answered by 'Pro-FeAl':

- Which FeAl-alloys are suitable for which process route?
- How do the main material properties (strength, fatigue, ductility,…) depend on the process route and the component design?
- How can the FeAl-alloys be improved further for industrial processing?

'Pro-FeAl' Project Plan: Materials and Methods

At the beginning of the project target-specifications for each process route and each sample part are defined by Siemens and Rolls Royce (1. Definition Phase). According to these specifications appropriate selections of FeAl alloys were made taking advantage of MPIE´s experience in FeAl-alloy development.

Further on, assisted by the use of simulation tools, the process details and the design aspects of the samples will be defined for each route. In the second part of the project (2. Manufacturing Phase) processing of the different samples takes place, accompanied by their characterization and evaluation (3. Evaluation/Characterization Phase). The latter comprises the analysis of the alloy compositions, their microstructures and numerous static and dynamic mechanical properties at different temperatures.

All measurements and findings from these experiments will be collected and utilized for each production route to carry out optimized sample production (4. Optimization Phase) including characterization and evaluation of the samples. Finally, the results of the different process routes will be compared with each other and against the target-specifications and summarized in a 'catalogue of knowledge' (5. Benchmark Phase).

Access's contributions in 'Pro-FeAl'

Within the Pro-FeAl project Access and Leistritz bundle their experience in the combined process route of casting and forging sample parts for high temperature applications (representing a turbine blade) (Fig. 1). The dependence of the sample properties from its design and from the details of the process conditions will be evaluated for different FeAl-compositions. The expected advantage of the combined route compared to the monolithic forging technology is reduced material usage and a possible omitting of the first forging step at Leistritz by employing a pre-contoured cast part from Access. In the definition and manufacturing phases, Access designs, optimizes (supported by simulation) and builds a casting system for pouring FeAl alloys, whose exact composition will be selected beforehand by MPIE. This includes the application of reusable copper dies for gravity casting, taking advantage of the material's high thermal conductivity. In the evaluation/characterization phase Access executes metallographic investigations by microscopy, SEM and computer tomography on the cast samples to characterize properties like alloy composition, grain size distribution, cracks, pores and cavities. This will be used to improve the casting process in the optimization phase. Eventually the optimized results of the combined casting and forging route will be incorporated in the final comparison of the 5 process routes and aligned with the target-specifications.

Acknowledgement

Supported by:

Federal Ministry
for Economic Affairs
and Energy

on the basis of a decision
by the German Bundestag

References

[1] M. Palm, „Concepts derived from phase diagram studies for the strengthening of Fe-Al-based alloys", Intermetallics, Bd. 13, pp. 1286-1295, **2005**.

[2] D. Hardwick und G. Wallwork, „Iron-aluminium alloys: a review of their feasibility as high temperature materials", Review on High-Temperature Materials 4, pp. 47-74, **1978**.

[3] Pro-FeAl: Prozessentwicklung für wirtschaftliche, effiziente Turbinenkomponenten aus Eisenaluminiden (BMWI-Kennzeichen 020E-41V7889)

P–25

Development of Fe-Al-Nb(–B) alloys for high-temperature applications

Angelika Gedsun and Martin Palm

Max-Plack-Institut für Eisenforschung GmbH, 40237 Düsseldorf, Germany, a.gedsun@mpie.de

Introduction

For high-temperature structural applications, e.g. compressor blades for steam turbines, novel heat and corrosion resistant alloys with improved strength are required. Fe–Al based alloys show outstanding corrosion and wear resistance additionally to their low density and good mechanical properties [1]. They are therefore considered as a cost-effective alternative to replace stainless steels or even Ni-based superalloys in specific applications.

In the Fe–Al–Ta system, precipitation of the stable hexagonal C14 Laves phase is preceded by the formation of the coherent, metastable $L2_1$ Heusler phase, which improves strength and creep resistance up to 750°C, but coarsens at higher temperatures [2].

Through thermomechanical processing, heat treatment or doping, the formation of the stable Laves phase can be widely influenced [3].Thereby microstructures with fine, evenly distributed Laves phase precipitates inside the Fe–Al matrix and at grain boundaries can be attained.

To further reduce the costs, Ta can be replaced by Nb. Also in the Fe–Al–Nb system, precipitation of the stable Laves phase is preceded by the precipitation of the metastable, coherent $L2_1$ Heusler phase [4]. Since the mechanism is the same as in the Fe–Al–Ta system, tuning of the microstructure and therefore of the properties may be achieved in a similar way [5].

However, in order to control the microstructure, a deeper understanding of the precipitation and hardening mechanisms is required. For further development of Fe–Al–Nb(–B) alloys, the microstructural evolution of heat-treated alloys of different compositions is studied followed by mechanical testing.

Materials and Methods

Fe–Al-Nb(–B) alloys with five different composition, containing 25–34 at.% Al, 2–3 at.% Nb and 0.01 at.% B were produced by induction melting in argon atmosphere. The actual compositions were established by wet chemical analysis.

The alloys were annealed at 700°C for 1, 10, 100 and 1000 h and cooled in air. The microstructure of the alloys in the as-cast condition and after heat treatment is analyzed by light optical microscopy (LOM) and scanning electron microscopy (SEM).The chemical compositions of the phases are established by EPMA (electron probe microanalysis) with wavelength-dispersive spectrometry (WDS). For determining the crystallographic structures of the phases, X-ray diffraction (XRD) is performed on powdered samples.

Mechanical tests include hardness measurements, tensile and compressive tests, 4-point bending tests, Charpy impact and creep tests. The experiments are performed on alloys in the as-cast condition and after annealing at 700°C for 1000h.

Results

Figure 1a, b shows micrographs of Fe–32Al–3Nb(–0.01B) in the as-cast condition. Coarse grains of Fe–Al with a grain size of 50–100 µm form the matrix. Along the grain boundaries, an eutectic consisting of Fe–Al + C14 Laves phase is visible. Only few precipitates have formed inside the grains. The alloy doped with boron shows a considerable larger fraction of the eutectic. No eutectic is found in Fe–25Al–2Nb, which was annealed at 700°C for 1h (Fig. 1 c, d). The grain boundaries are nearly fully covered by Laves phase. Within the Fe–Al matrix, besides some coarser precipitates, numerous fine, oriented precipitates are visible (Fig. 1d). Similar oriented precipitates have been observed in Fe–Al–Ta and Fe–Al–Nb alloys and identified as coherent $L2_1$ Heusler phase [3, 4].
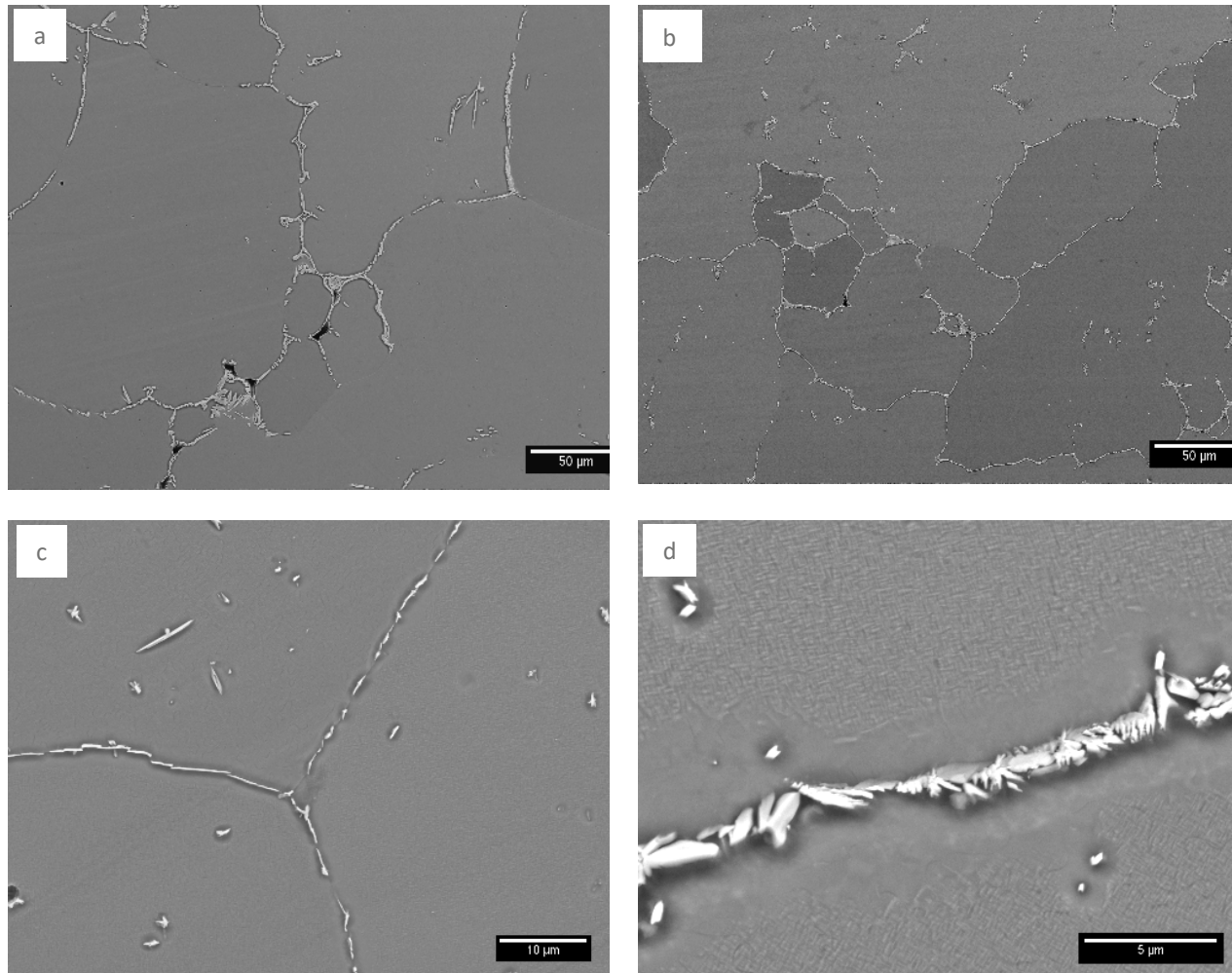
Fig.1: Backscattered electron images of the alloys a) Fe–32Al–3Nb as cast, b) Fe–32Al–3Nb–0,01B as cast, c and d) Fe–25Al–2Nb annealed at 700°C for 1h.

References

[1] C.G. McKamey, *Iron aluminides*, in: N.S. Stoloff, V.K. Sikka (Eds.), Physical metallurgy and processing of intermetallic compounds. Chapman & Hall, New York, **1996**, 351-391.

[2] D.D. Risanti, Sauthoff, Microstructures and mechanical properties of Fe–Al–Ta alloys with strengthening Laves phase. Intermetallics. **2011**, 19, 1727-1736.

[3] P. Prokopčáková, M. Švec, M. Palm, *Microstructural evolution and creep of Fe–Al–Ta alloys.* Int. J. Mater. Res. **2016**, *107*, 396-405.

[4] D.G. Morris, L.M. Requejo, M.A. Munoz-Morris, *A study of precipitation in DO_3 ordered Fe-Al-Nb alloy.* Intermetallics. **2005**, *13*, 862-871.

[5] S.A. Azmi et al., Microstructure and mechanical properties of Fe–Al–Nb–B alloys. MRS Advances. **2017**, 2, 1353-1359.

P–26

Precipitation behavior of Nb_2Co_7 from Nb-supersaturated Co-solid solution in Co-rich Co-Nb binary alloys

Konatsu Yamada[1], Toshiaki Horiuchi[2], Seiji Miura[3] and Frank Stein[4]

[1]Division of Mechanical Engineering, Graduate School of Engineering, Hokkaido University of Science, Maeda 7-15-4-1, Teine-ku, Sapporo 006-8585, Japan, 9181103@hus.ac.jp

[2]Laboratory of Advanced Materials for Cold Region, Hokkaido University of Science, Maeda 7-15-4-1, Teine-ku, Sapporo 006-8585, Japan, horiuchi@hus.ac.jp

[3]Division of Materials Science and Engineering, Faculty of Engineering, Hokkaido University, Kita 13 Nishi 8, Kita-ku, Sapporo 060-8628, Japan, miura@eng.hokudai.ac.jp

[4] Max-Planck-Institut für Eisenforschung GmbH, Max-Planck-Straße 1, 40237 Düsseldorf, Germany, f.stein@mpie.de

Introduction

The Co-Nb binary system contains several intermetallic phases with complex crystal structure such as three types of Laves phases and Nb_2Co_7 [1]. The $L1_2$ Co_3Nb phase exists as a metastable phase in this system and that is considered to play the role of effective nucleation sites for precipitation of Nb_2Co_7 [2,3]. The authors have previously reported that the precipitation behavior of Nb_2Co_7 from the Nb-supersaturated Co solid solution might be discontinuous precipitation [2]. However, precipitation behavior of Nb_2Co_7 still remains poorly understood. The objective of the present study is to elucidate the precipitation behavior of Nb_2Co_7 from Nb-supersaturated Co solid solution experimentally.

Materials and Methods

The Co-3.9 at%Nb alloy was vacuum induction melted and was cast as ϕ20mm cylindrical ingot, and was cut into cylinders of ϕ3×3mm. The samples were heat-treated for homogenization in the differential thermal analyzer (DTA) at 1240˚C for 1h in order to attain single-phase fcc-Co solid solution. Some samples were cooled from 1240˚C to 900˚C and were kept for up to 100h for isothermal heat treatments, followed by cooling to room temperature at a cooling rate of 30˚C/min. Others were directly cooled from 1240˚C to room temperature at a cooling rate of 30˚C/min in order to form $L1_2$ Co_3Nb, and were subsequently heated again to 700˚C or 900˚C at a heating rate of 20˚C/min and were subjected to an isothermal heat treatment for up to 100h, followed by cooling to room temperature at a cooling rate of 30˚C/min. Microstructural observation, crystal structure analysis and composition analysis were performed by scanning electron microscopy (SEM), electron backscatter diffraction (EBSD) and electron probe micro analyzer (EPMA).

Results and Discussion

The resultant SEM microstructure and EBSD analysis for the sample after isothermal heat treatment at 700˚C for 100h are shown in Fig. 1. Relatively large precipitates were observed along grain boundaries, and finer plate-like precipitates were also observed inside few grains. It should be noted that a precipitation free zone (PFZ) was observed in the vicinity of most of the precipitates along grain boundaries. This sample contained metastable $L1_2$ Co_3Nb before heat treatment, however, all the precipitates in Fig.1 are considered to be equilibrium Nb_2Co_7 from their plate-like morphologies. The crystal structure of the matrix phase was fcc inside grains without any precipitates, and hcp along grain boundaries and in the vicinity of precipitates. The authors have revealed that the matrix with fcc structure becomes stable with increasing the Nb content in it while the hcp structure can only exist with very low Nb contents [2,3]. Therefore, the Nb content in the matrix phase along grain boundaries and in the vicinity of precipitates is expected to be lower than that in the rest of this phase. The results of composition analysis by EPMA for the same sample are shown in Fig. 2. The Nb depression zone was clearly observed along grain boundaries and in the vicinity of precipitates, which implies continuous precipitation of Nb_2Co_7 in this sample. Precipitation behavior from the matrix phase without containing intermediate $L1_2$ Co_3Nb will be discussed in detail in the presentation.
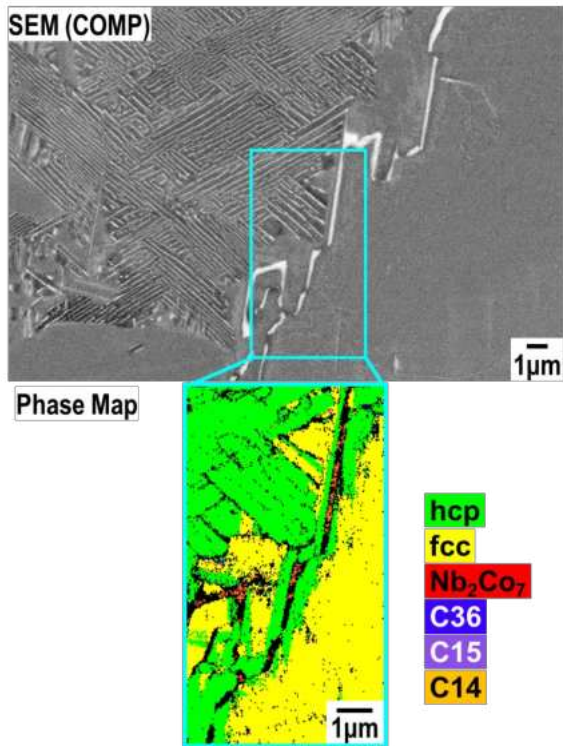
Fig. 1: The resultant SEM microstructure and EBSD analysis for the sample after isothermal heat treatment at 700˚C for 100h.
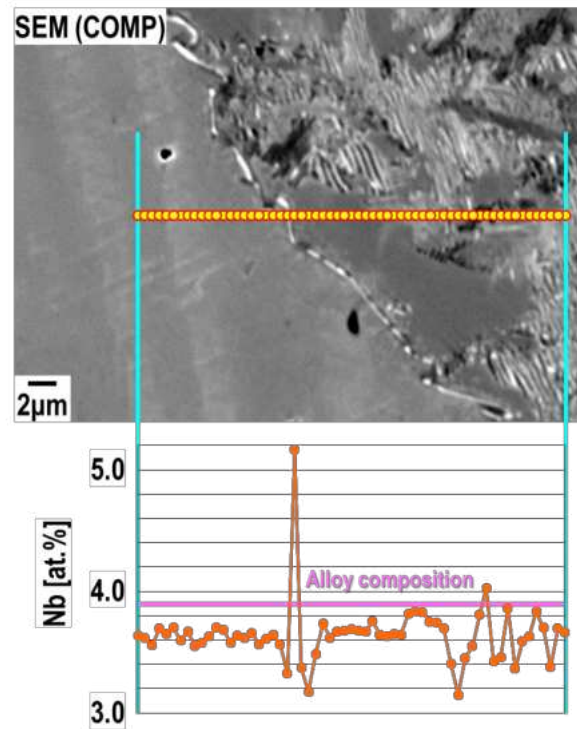
Fig. 2: The results of composition analysis by EPMA for the sample after isothermal heat treatment at 700˚C for 100h.

References

[1] F. Stein, D. Jiang, M. Palm, G. Sauthoff, D. Grüner and G. Kreiner: Intermetallics, **2008**, *16*, 785-792.

[2] T. Horiuchi, F. Stein, K. Abe and K. Yamada: Proc. Intermetallics 2017, Bad Staffelstein, Germany, **2017**, 142-143.

[3] K. Yamada, T. Horiuchi, F. Stein and S. Miura: Proc. 6th International Indentation Workshop (IIW6), Sapporo, Japan, **2018**.

P–27

Structural and phase transformations occurring during fabrication of Ni-Al-Cr-based alloy reinforced by AlN and Cr$_2$N

A. I. Logacheva, <u>M. S. Gusakov</u>, I. A. Logachev and Zh. A. Sentyurina

JSC «Kompozit», Pionerskaya St. 4, 141076 Korolev, Russian Federation, info@kompozit-mv.ru

Introduction

The problem of high-temperature strength for intermetallic alloys operating above a brittle to ductile transition temperature may be successfully solved by fabricating a composite structure with an intermetallic matrix reinforced by ceramic particles, for example nitrides.

We discuss structural and phase transformations, which are occurring during fabrication of Ni-Al-Cr-based alloy with nitrides particles by Plasma Rotating Electrode Process (PREP) and Hot Isostatic Pressing (HIP). In conclusion, high-temperature mechanical properties and functional characteristics of the of Ni-Al-Cr-based alloy reinforced by AlN and Cr$_2$N are presented.

Materials and Methods

The initial ingots for the PREP process were manufactured by the VIM + VAR method. Atomization (PREP) was carried out at the upgraded equipment - PREP-9I (JSC «Electromechanica», JSC Kompozite, Russia). The HIP process was carried out in an ABRA equipment (Sweden). For high-heat treatment and nitriding XVAC series (Xerion advanced heating GmbH) furnace was used.

The granulometric composition of the powder was investigated by laser diffraction (Analysette 22, Fritsch GmbH). The phase composition was determined by X-ray diffraction analysis on a DRON-3 setup (Russia) using Co-Kα radiation at 2θ = 10-140°. The microstructure of the experimental samples was studied with optical microscopy (OM) using an Axiovert 200 MAT/M inverted metallographic microscope and with scanning electron microscopy (SEM) on a Hitachi S-3400N microscope equipped with an energy dispersive X-ray spectrometer NORAN. Mechanical tests of experimental samples were carried out using the universal testing machine Gleeble 3800.

Results and Discussion

We used powders with particle size distribution of 40-80 µm, obtained by the PREP method at an electrode rotation speed of 24,000 rpm. A spherical shape, a low level of gas porosity and the absence of satellites (Figure 1) characterize powder particles. This powder was subjected to nitriding at a temperature of 950 °C, at this temperature chromium nitrides are formed and no sintering of powder particles takes place, which is important for the HIP operation.

The parameters of the HIP were chosen based on the fact that it is necessary to prevent grain growth and at the same time to create conditions for the formation of more stable aluminum-based nitrides. The two-stage HIP mode is most suitable for this purpose, where in the first stage, at a temperature of 1250 ° C and a pressure of 160 MPa, the mechanism of plastic deformation is realized. In the second stage, at a temperature of 900 ° C and a pressure of less than 100 MPa, a diffusion mechanism is implemented.

The described approach allows obtaining a compact state with a density of 99.9% and a grain size of about 40 µm. The compact has a uniform microstructure with β-NiAl-based matrix. Ceramic phases concentrate on the prior particle boundaries (Figure 2).
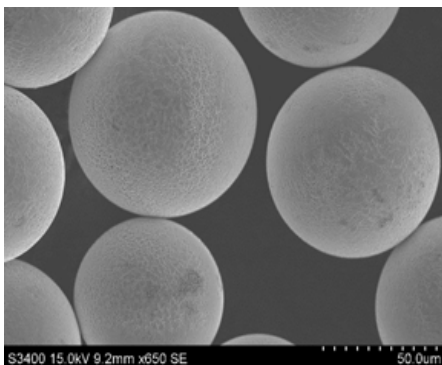
Fig. 1: Powder surface microstructure
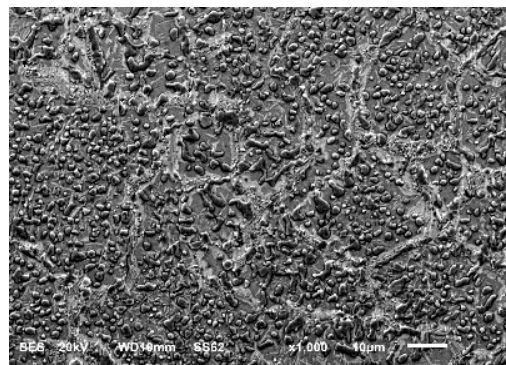
Fig. 2: Microstructure of the Ni-Al-Cr-based alloy reinforced by AlN and Cr$_2$N

The phase transformations occurring during atomization, nitriding and HIP is presented in table 1. It can be seen that at the compaction stage a significant redistribution of the β-NiAl and γ´-Ni₃Al phases, as well as nitride-based phases, has occurred.

Table 1: Phase transformations occurring during fabrication of Ni-Al-Cr-based alloy reinforced by AlN and Cr_2N particles

Symbol	Structure	% wt		
		Powder	Powder after nitriding	After HIP
β-NiAl	B2	69.5	61.5	52.0
γ´/ γ -Ni3Al	Ll2/ Al	13.0	22.5	21.5
α-Cr	A2	17.5	7.2	6.5
CrN	B1	-	5.8	-
Cr₂N	L3	-	3.0	8.0
AlN	-	-	-	12.0

The results of compressive tests at a strain rate of $10^{-2}s^{-1}$ are presented in Figures 3 and 4. The true yield strength at 800 °C is 737 MPa, and at 1000 ° is 475 MPa.
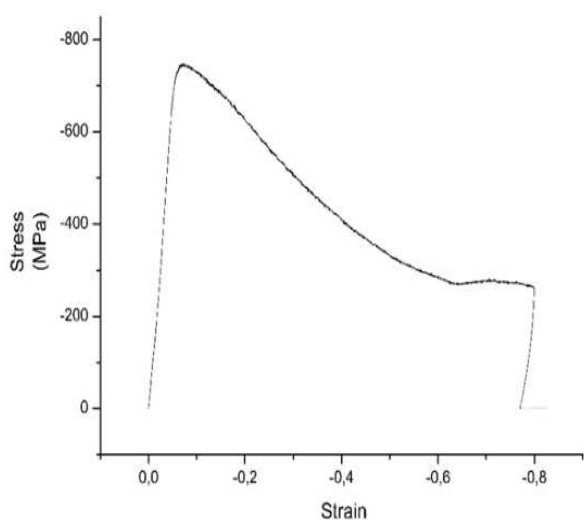
Fig. 3: The results of compressive tests at 800 °C
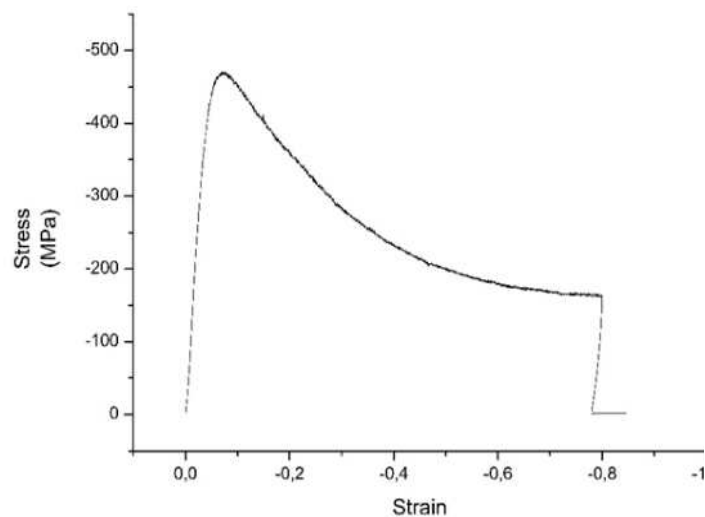
Fig. 4: The results of compressive tests at 1000 °C

P–28

Alloying effects in vanadium solid solutions

Christopher Müller[1], Georg Hasemann[2] and Manja Krüger[2]

[1]Otto-von-Guericke University Magdeburg, Institute of Materials and Joining Technology, Universitätsplatz 2, 39106 Magdeburg, Germany, christopher.mueller@ovgu.de

[2] Forschungszentrum Jülich GmbH, Institute of Energy and Climate Research, Microstructure and Properties of Materials (IEK-2), Leo-Brand-Str. 1, 52425 Jülich, Germany, g.hasemann@fz-juelich.de, m.krueger@fz-juelich.de

Introduction

Vanadium alloys provide great potential as a new type of lightweight material for high temperature applications, e.g. as turbines for energy conversion, due to its low density in combination with a high melting point. In particular, V-Si-B alloys show outstanding mechanical properties at high temperatures, which are comparable with the well-known nickel base superalloy CMSX-4 [1]. Recent studies have also shown that multi-phase V-Si-B alloys, unlike the similarly composed Mo-based ones, reveal plasticity at room temperature. This seems to be due to the vanadium solid solution phase (V_{SS}), which also has the largest volume fraction in the ternary eutectic V_{SS}-V_5SiB_2-V_3Si [2,3]. In this way, it can be concluded that the plasticity of such alloys can be controlled with the phase fraction of V_{SS}. In order to develop and optimize V-base alloys, the V_{SS} phase and its properties must also be investigated in relation to the chemical composition.

However, the effects of several alloying elements on the mechanical properties of vanadium solid solutions at room temperature are examined insufficiently yet. Therefore, the alloying effects of various elements (V-X systems) on the microstructure and mechanical properties of vanadium-based alloys have been investigated in the present study.

Materials and Methods

In the present study, binary V - X (X= Si, Cr, Zr, B) alloys with nominal compositions up to 7 at.% X were manufactured by means of an arc-melting process. As a result, single-phase vanadium solid solutions (V_{SS}) and two-phase alloys (V_{SS} + intermetallic phases) were produced. The chemical alloy compositions were verified by using ICP-OES (inductively coupled plasma optical emission spectroscopy). SEM (Scanning Electron Microscopy) and XRD (X-ray Diffraction) methods were used to examine the microstructure, to identify phases and to measure element concentrations in the respective phases.

Microhardness measurements and room temperature compression tests were carried out in order to determine the mechanical properties in dependence of the alloying components. The compression tests were performed at a constant crosshead speed according to an initial (engineering) strain rate of 10^{-3} s^{-1} and the yield stresses were determined by the 0.2 % offset method. All investigations were performed in the as-cast state.

Results and Discussion

The present study addresses the alloying effects and microstructure - property relationship in different vanadium solid solutions. Therefore, inter alia V-Si alloys with Si concentrations of 1, 3, 5 and 7 at% Si were prepared. Exemplarily, the respective as-cast microstructure of the alloys V-5Si and V-7Si are shown in Fig. 1 and Fig. 2. While the alloys up to 5 at.% Si are single phase V_{SS} alloys, V-7Si shows a two-phase microstructure with small V_{SS}-V_3Si eutectic regions between the primary V_{SS} dendrites.

The results of the compression tests at room temperature suggest that Si is a very effective solid solution strengthener. V-5Si has a compressive yield stress of 613 ± 16 MPa and the V-7Si alloy shows yielding at 762 ± 32 MPa. All V-Si alloys show room temperature plasticity well over 20 %. These results with respect to the plastic deformation of V-Si alloys at room temperature are promising compared to those of the Mo-Si system. With increasing Si content (even minor concentrations of 0.3 at.%), the ductility of Mo-Si alloys drops steeply at room temperature [4].
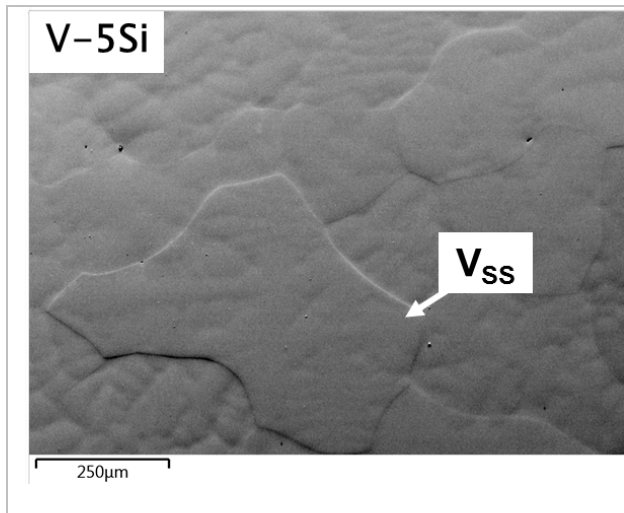
Fig. 1: Microstructure of alloy V-5Si (Forward Scattered Electron Image)	Fig. 2: Microstructure of alloy V-7Si (Forward Scattered Electron Image)
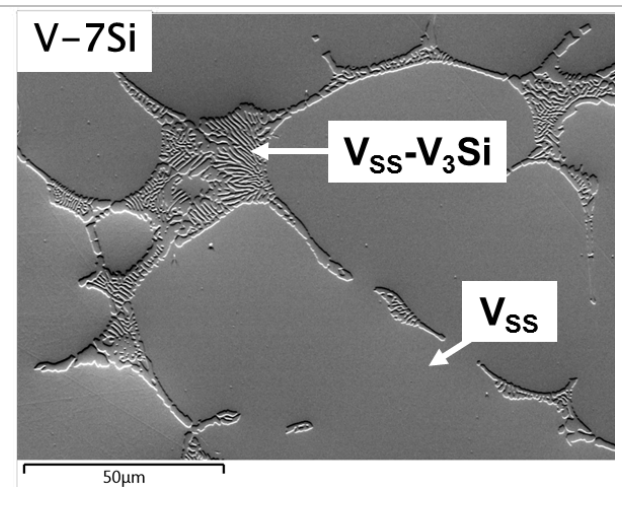
References

[1]   M. Krüger, Scripta Materialia, **2016** (121) 75 - 78.
[2]   G. Hasemann, C. Müller, D. Grüner, E. Wessel, M. Krüger, submitted to Acta Materialia, **2019**.
[3]   G. Hasemann, M. Krüger, M. Palm, F. Stein, Materials Science Forum, **2018.** *941*. 827 - 832.
[4]   D. Sturm, M. Heilmaier, J.H. Schneibel, P. Jéhanno, B. Skrotzki, H. Saage, Materials Science and Engineering A, **2007**. *463*. 107 - 114.

P–29

Plastic deformation behavior of single crystals of Fe-Cr sigma phase at room temperature

Masaomi Okutani, Nobuyuki Kadota, Kyosuke Kishida and Haruyuki Inui

Department of Materials Science and Engineering, Kyoto University, Kyoto 606-8501, Japan,

okutani.masaomi.24r@st.kyoto-u.ac.jp, kadota.nobuyuki.64n@kyoto-u.jp, kishida.kyosuke.6w@kyoto-u.ac.jp,

inui.haruyuki.3z@kyoto-u.ac.jp

Introduction

The intermetallic sigma phase with a complex crystal structure of the $D8_b$-type ($tP30$, space group: $P4_2/mnm$, c/a ~0.52, Fig. 1) [1] has received growing attentions because some recent studies have revealed that creep strength, ductility, yield strength and tensile strength of stainless steels can be improved if the distribution and morphology of the sigma phase are properly controlled [2]. However, there is still a lack of fundamental understanding on inherent mechanical properties of the sigma phase itself, which are essential in elucidating their actual roles in these alloys. This is due mainly to the fact that no systematic studies on deformation behavior using single crystals have been made so far because of the difficulty in obtaining large single crystals sufficient for performing standard bulk mechanical tests. Recently, micropillar compression tests of single crystals have been proved to be useful for studying fundamental deformation behavior of hard and brittle materials such as high temperature intermetallics, semiconductors and ceramics [3-5]. In the present study, we have investigated room temperature deformation behavior of single crystals of the Fe-Cr sigma phase as a function of loading axis orientation and specimen size by micropillar compression methodology in order to clarify the deformation mechanisms of the Fe-Cr sigma phase.

Materials and Methods

Ingots with a nominal composition of Fe-50at％Cr were prepared by arc-melting. The ingots were cut into small blocks, which were then cold rolled and heat-treated to obtain polycrystalline specimens of Fe-Cr sigma phase. Single-crystalline micropillars with 11 different loading axis orientations and a square cross section were fabricated using the focused-ion beam (FIB) technique. Compression tests were performed on a nanoindenter equipped with a flat punch diamond tip. All micropillars were tested under a constant displacement rate mode (initial strain rate: $1\times10^{-4}s^{-1}$) at room temperature in the air. Deformation microstructures of the deformed micropillars were investigated by scanning electron microscopy (SEM), transmission electron microscopy (TEM), and scanning transmission electron microscopy (STEM). Specimens for TEM/STEM observations were prepared by the FIB-SEM lift-out technique.

Results and Discussion

Plastic flow was observed for all tested micropillars mostly exhibiting a smooth transition from elastic to plastic deformation similar to those observed for ductile materials (Fig.2). Four different slip systems including {110}<001> slip system, which is one of the operative slip systems in β-uranium with the same crystal structure as the sigma phase, were identified to be operative depending on the loading axis orientations. The values of critical resolved shear stress (CRSS) for the four identified slip systems are extremely high about 1.2 ~ 2.5 GPa. However, relatively good plastic deformability more than 5 % compressive strain was observed for most loading axis orientations tested, which clearly indicates that the Fe-Cr sigma phase is not inherently brittle at least under uniaxial compressive loading.
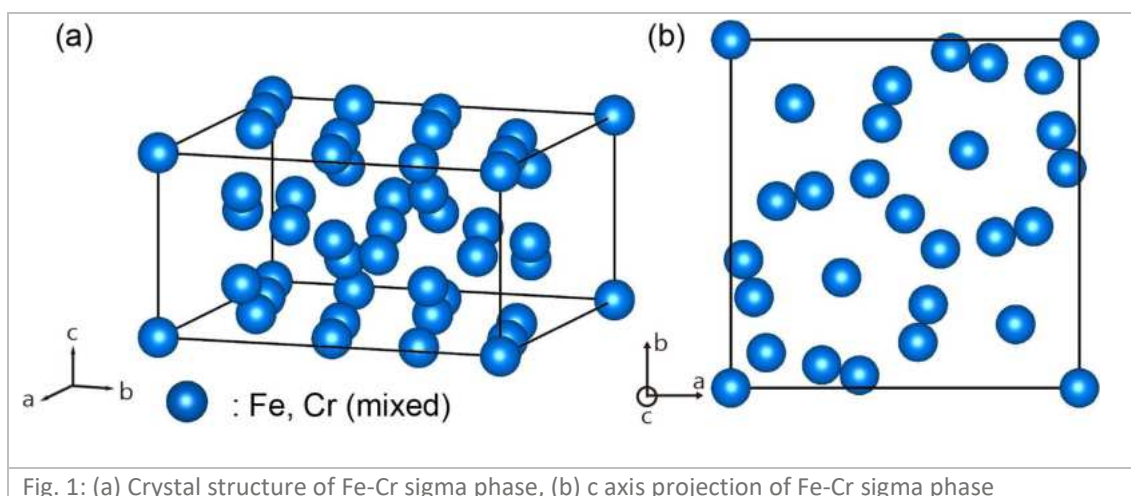
Fig. 1: (a) Crystal structure of Fe-Cr sigma phase, (b) c axis projection of Fe-Cr sigma phase

Fig. 2: Selected engineering stress-strain curves for [$\bar{8}92$]-oriented and variable sized micropillars of single crystal in Fe-Cr sigma phase at room temperature.
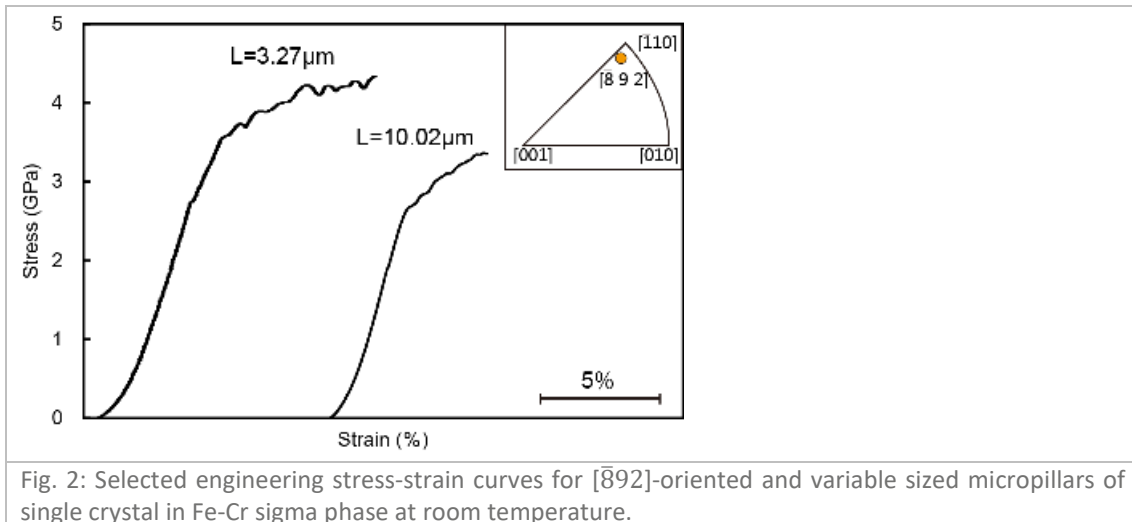
References

[1] H. L. Yakel, Acta Cryst., **1983**, *39*, 20-28

[2] K. H. Lo, C. H. Shek, J. K. L. Lai, **2009**, *65*, 39-104

[3] N. L. Okamoto, D. Kashioka, M. Inomoto, H. Inui, H. Takebayashi, S. Yamaguchi, Scripta Materialia, **2013**, *69*, 307-310

[4] K. Kishida, T. Maruyama, H. Matsunoshita, T. Fukuyama, H. Inui, Acta Materialia, **2018**, *159*, 416-428

[5] M. Higashi, S. Momono, K. Kishida, N. L. Okamoto, H. Inui, Acta Materialia, **2018**, *161*, 161-170

P–30

The reaction of refractory carbides (borides) with iridium

Victor V. Lozanov and Natalya I. Baklanova

Institute of Solid State Chemistry and Mechanochemistry SB RAS, 18 Kutateladze str., 630128 Novosibirsk, Russia,
lozanov.25@gmail.com, baklanova@solid.nsc.ru

Introduction

Iridium and iridium-based intermetallics, especially $HfIr_3$ and $TaIr_3$ ($L1_2$-type structure) have high melting points, high hardness, and good oxidation resistance. Therefore, they can be considered as promising candidates for high-temperature applications [1-3]. The common approach for obtaining the intermetallics is arc-melting [1]. To obtain the homogeneous products, a long-term annealing at high temperatures is usually used. Therefore, this is a very energy-consuming method. Another way to obtain iridium-based intermetallics is the solid-state reaction of refractory carbides, HfC or TaC, with iridium [2, 3]. It was stated that only one intermetallic phase, namely, MIr_3 (M=Hf or Ta) is formed as a product of the interaction [2, 3]. No other intermetallics were detected.

Diborides HfB_2 or TaB_2 could be also used as reagents for obtaining the iridium-based intermetallics by analogy with corresponding carbides. Unfortunately, no data about reaction of iridium with hafnium or tantalum diborides were found. It is known that boron has more affinity to iridium than carbon is. According to the phase equilibrium of the iridium-boron system, there are several iridium borides [4]. It is also known that there are at least three ternary compounds in the Hf-Ir-B system, including the perovskite-type $HfIr_3$-based solid solution with composition up to $HfIr_3B_{0.45}$, hexagonal boron-rich $HfIr_3B_4$ phase, and tetragonal $Hf_3Ir_5B_2$ phase [5]. The crystal structures of the $HfIr_3B_2$ and $HfIr_5B_4$ phases have not been completely characterized [5]. All above-mentioned ternary phases were synthesized by arc-melting from elements with subsequent annealing. Contrary, only one ternary hexagonal $Ta_7Ir_6B_8$ phase was detected in the Ta – Ir – B system [6]. This phase was also prepared by arc-melting approach.

Thus, the aim of this work was triple one, firstly, to study the intermetallic products formed during solid state reaction of refractory carbides with iridium; secondly, to study the reactions between HfB_2 and TaB_2 with iridium; finally, to compare the peculiarities of reactions of iridium with carbides and borides.

Materials and Methods

As initial substances, iridium (purity 99.96%), hafnium carbide (purity not less 99%), tantalum carbide (purity not less 99%), hafnium diboride (purity not less 99%) and tantalum diboride (purity not less 99%) powders were used. The iridium and carbide (or boride) powders were mixed in the 1:1 and 3:1 molar ratio and then heat treated in the 1000 – 1600°C temperature range as described in [7, 8]. Products were analyzed by X-ray powder diffraction (CuKα radiation, 2Θ range 10 – 130°) using D8 Advance diffractometer (Bruker, Germany). Qualitative and quantitative phase analysis was performed with DIFFRAC[plus] software. Lattice parameters were refined with the Topas 4.2 (Bruker, Germany). The morphology of obtained products were investigated by high-resolution scanning electron microscopy (SEM, MIRA 3 LMU, TESCAN, Czech Republic) equipped with energy dispersive spectroscopy (EDS) instrument INCA Energy 450 (Oxford Instruments Nanoanalysis). The variation coefficient is reached ~1% for the EDS analysis of the main elements (content more than 10% (wt.)).

Results and Discussion

The first appearance of product of the solid state reaction of hafnium carbide with iridium is registered by the XRD analysis at temperatures as low as 1000 – 1100°C [7]. The lattice parameter of intermetallic product was determined to be larger than that reported earlier for the stoichiometric $HfIr_3$ (3.961Å vs. 3.935Å). It suggests that the $HfIr_3$-based solid solution with Hf-rich composition is formed. The positions and shapes of the intermetallic solid solution peaks are changed with increasing of the treatment temperature. The observable data are in good agreement with the assumption of formation series of the $HfIr_3$-based solid solutions. It is noteworthy that the estimated compositions are varied from $HfIr_{2.43}$ up to $HfIr_{3.36}$. The EDS analysis of intermetallic grains confirmed that their elemental compositions fall into the homogeneity range estimated by the quantitative XRD analysis.

Tantalum carbide starts to react with iridium at 1100°C [8]. The lattice parameter of the intermetallic product $TaIr_3$ was determined to be equal to 3.886Å that corresponds to the stoichiometric one. With increasing of the temperature, the displacement of the peak positions was observed that can be related to the formation of the $TaIr_3$-based solid solutions. The homogeneity range was estimated to be very narrow (2% (mol.)).

Raman spectroscopy of products obtained in the course of the reactions of iridium with HfC (or TaC) detected the free carbon phase. Moreover, the thin carbon sheets can be observed on the surfaces of the intermetallic grains. Based on the obtained results, it was supposed that the carbon does not solute into intermetallic phase. No ternary phases were detected in the Hf (Ta) – C – Ir systems.
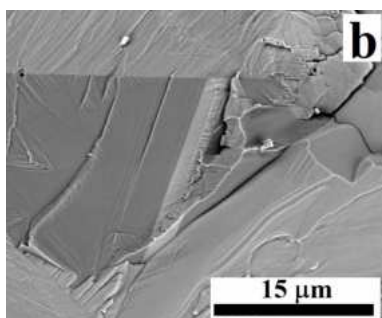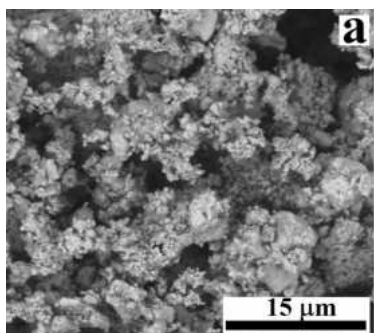
Figure 1. The typical morphology of reaction mixtures after heat treatment at 1600°C: a – carbide with iridium, b – boride with iridium.

The products of the reaction of iridium with hafnium or tantalum diborides were determined at 1000°C by the XRD analysis. The $IrB_{0.9}$ phase was detected. With increase of temperature up to 1200°C, the $IrB_{1.1}$ and the intermetallic $HfIr_3B_{0.45}$ (or $TaIr_3$) phases were also observed in the XRD patterns. No other binary or ternary intermetallic products were detected. One can note that the reactions between iridium and borides are solid-state ones in the 1000 – 1200°C temperature range. With increase of the temperature (1300°C and higher), the mechanism of reaction was changed. This is because the liquid Ir-B eutectics are formed [4]. New ternary Hf – Ir – B and Ta – Ir – B intermetallic phases were detected in products.

Based on the obtained results, one can conclude that the mechanism of the reaction of iridium with carbides and borides is greatly different. The difference is connected with possibility of boron to form the ternary Ir – M(Hf, Ta) – B intermetallic phases. Contrary, carbon does not form the ternary Ir – M(Hf, Ta) – C intermetallic phases.

References

[1]   Y. Yamabe-Mitarai, H. Murakami, Intermetallics. **2014**, *48*, 86-92

[2]   H. Holleck: Binäre und ternäre Carbid- und Nitridsysteme der Übergangsmetalle. Gebrüder Borntraeger Berlin, Stuttgart, **1984.**

[3]   J.R. Strife, J.G. Smeggil, W.L. Worrell, Journal of the American Ceramic Society. **1990**, *73*, 838-845.

[4]   I. Zeiringer, X. Cheng, X.-Q. Chen, E. Bauer, G. Giester, P.F. Rogl, Science China Materials. **2015**, *58*, 649-668.

[5]   P. Rogl, H. Nowotny, Journal of the Less-Common Metals. **1979**, *67*, 41-50.

[6]   Q. Zeng, M. Kohout, R. Gumeniuk, N. Abramchuk, H. Borrmann, Y. Prots, U. Burkhardt, W. Schnelle, L. Akselrud, H. Gu, A. Leithe-Jasper, Y. Grin, Inorganic Chemistry. **2012**, *51*, 7472-7483.

[7]   V.V. Lozanov, N.I. Baklanova, N.V. Bulina, A.T.Titov, ACS Applied Materials & Interfaces. **2018**, *10*, 13062-13072.

[8]   N.I. Baklanova, V.V. Lozanov, A.T. Titov, Corrosion Science. **2018**, *143*, 337-346.

P–31

In-situ observation of phase and microstructure evolution during directional solidification of novel intermetallic structural materials

<u>Camelia Gombola</u>[1], Ioannis Sprenger[1], Alexander Kauffmann[1], Volodymyr Bolbut[2], Georg Hasemann[2], Michael Oehring[3], Malte Blankenburg[3], Norbert Schell[3], Peter Staron[3], Florian Pyczak[3], Manja Krüger[2], Martin Heilmaier[1]

[1]Karlsruhe Institute of Technology (KIT), Institute for Applied Materials (IAM-WK), Engelbert-Arnold-Str. 4, 76131 Karlsruhe, Germany, florian.gang@kit.edu
[2]Otto von Guericke University, Institute for Materials & Joining Technology, Universitaetsplatz 2, 39106 Magdeburg, Germany, georg.hasemann@ovgu.de
[3]Helmholtz-Zentrum Geesthacht, Centre for Materials and Coastal Research, Institute of Materials Research, Max-Planck-Str. 1, 21502 Geesthacht, Germany, florian.pyczak@hzg.de

Introduction

For new high temperature materials beyond Nickel-based superalloys [1], loading under creep conditions is a critical property for material choice and design of the microstructure. Thus, directional solidification is a promising process, due to the formation of single-crystalline components or components at least exhibiting an elongated microstructure parallel to the growth and/or loading direction. For example, incorporating an aligned second phase (e.g. Cr or Mo) into NiAl [2] increases the creep properties along the growth direction or may act as a crack arrester, increasing the damage tolerance of the component.

Especially for single-crystal Ni-based superalloys, directional solidification has been applied on an industrial scale for a considerable amount of time, advancing this method beyond the current applications is still challenging. Novel materials or changes in the component geometry require significant changes in the process parameters. A knowledge-based advancement of the process is difficult, as to some extent the possibility to characterize the production process as well as the materials behavior "in-situ" is limited. Investigations are almost exclusively limited to a post-process characterization of developed microstructure. Extending the possibilities for in-situ characterization to materials systems for structural applications, considerably exceeding melting points of 1000 °C, is the overall goal of the BMBF-funded joint project "FlexiDS" between the Otto-von-Guericke University Magdeburg (OVGU) and the Karlsruhe Institute of Technology (KIT), in cooperation with the Helmholtz-Zentrum Geesthacht (HZG).

Materials and Methods

The aims of this joint project are to gain unprecedented in-situ insights into the solidification of the aligned microstructure and to clarify the influence of varying solidification parameters (e.g. solidification velocity) on the microstructure evolution in intermetallic compounds of the systems Fe-Al, Ti-Al, NiAl-(Cr,Mo) and Mo-Si-B. Moreover, solid-state reactions occurring slightly below the solidus temperature (e.g. eutectoid decomposition of the ε-phase in Fe-Al) should be observed in-situ.

For this purpose, a state-of-the-art industrial relevant floating zone furnace was set up at the High Energy Materials Science beamline (HEMS), operated by Helmholtz-Zentrum Geesthacht, at the PETRA III storage ring at the Deutsches Elektronen-Synchrotron (DESY, Hamburg, Germany), Figure 1. The high photon energy of 100 keV was used for x-ray diffraction in transmission mode. Due to the short wavelength a deep penetration of the samples is given and the high photon flux allows a very short total counting time for measurements - now it is possible to perform in-situ observation of directional solidification in short timescale. The zone melting device is using inductive heating employing a HF coil to induce a locally confined melting zone in rod-shaped samples. Melting temperatures up to 2200 °C can be reached. The melting temperature and temperature gradient are checked by pyrometric measurements. The directional solidification process is performed under protective atmosphere (e.g. Ar) to avoid oxidation of the sample material. Moreover, the whole process is monitored employing high-resolution ZSB cameras.
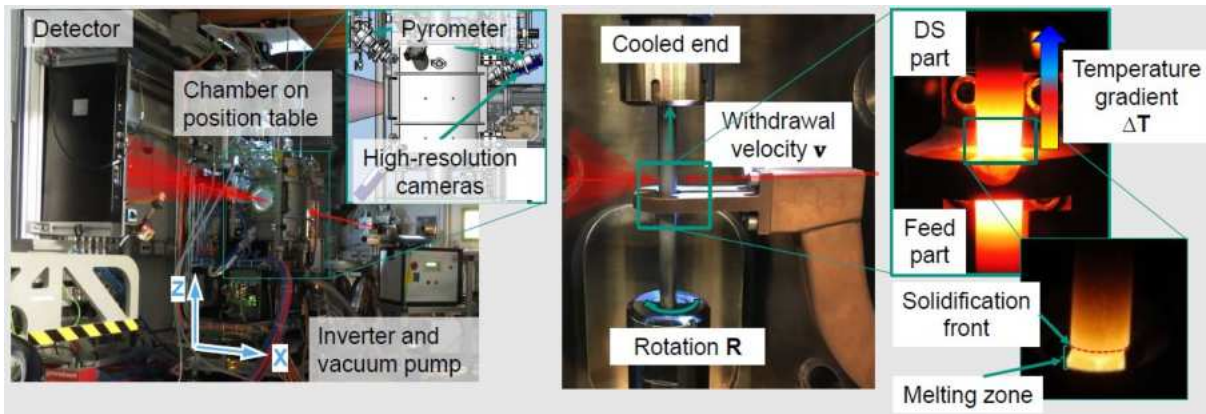
Fig. 1: Illustration of the experimental setup at the Petra III Beamline (HEMS, P07) at DESY Hamburg

Results and Discussion

Depending on the materials system, different questions will be addressed. For example, for Al-rich Fe-Al alloys, consisting of 55 – 65 at.% Al, the phase relations between the high temperature ε phase (Fe5Al8) and the by eutectoid decomposition evolving phases FeAl and FeAl2, which are stable at ambient temperature, will be reviewed. As the ε phase solidifies directly from the melt, has a narrow compositional range and cannot be stabilized to ambient temperatures, results can only be obtained employing in-situ experiments at elevated temperatures. For the ternary eutectic composition in the Mo-Si-B system, the growth characteristics (coupled or non-coupled) as well as the texture evolution during directional solidification can be clarified, Figure 2. For TiAl alloys the growth mode and growth direction of the solidifying phases will be studied in dependence of the solidification conditions.
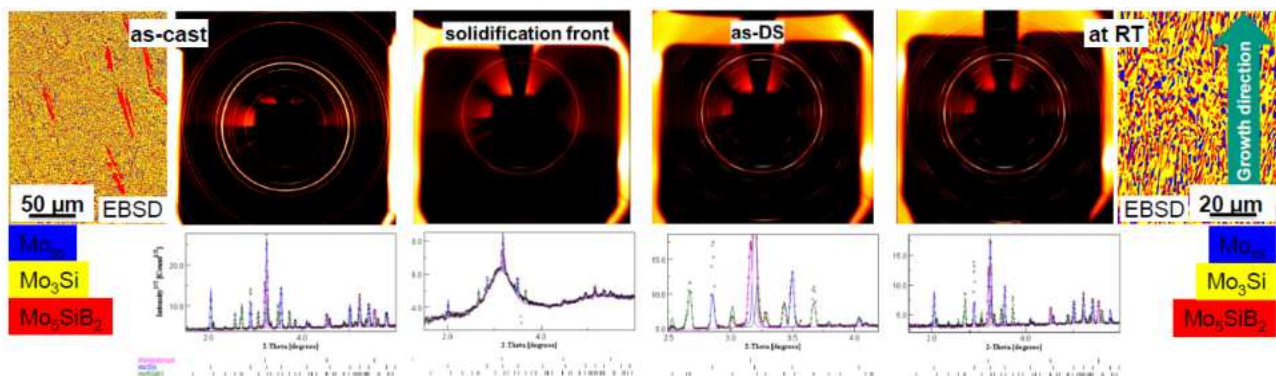
Fig. 2: The diffraction pattern clearly indicate a coupled ternary eutectic growth of MoSS, Mo5SiB2 and Mo3Si phases in the Mo-Si-B system and an elongated grain orientation parallel to the solidification direction

References

[1]   R. C. Reed: The Superalloys: fundamentals and applications, Cambridge University Press, Cambridge, UK, **2006**.
[2]   T. Haenschke, A. Gali, M. Heilmaier et al.; J. Physics: Conference Series 240, **2010**, doi:10.1088/1742-6596/240/1/012063.

NOTES

www.conventus.de

Success through
versatile
solutions

As a full-service PCO, we provide you with intelligent and innovative solutions in an advisory and implementing manner.

conventus
CONGRESSMANAGEMENT

NETZSCH

Proven Excellence.

PREPARE
+ MEASURE
+ CHARACTERIZE

RESULTS
+ NETZSCH

EXCEPTIONAL
RESULTS

REFRACTORY TESTING

HYPHENATED TECHNIQUES

SEEBECK COEFFICIENT &
ELECTRICAL CONDUCTIVITY

THERMAL DIFFUSIVITY &
CONDUCTIVITY

DYNAMIC MECHANICAL
THERMAL ANALYSIS

DIFFERENTIAL SCANNING
CALORIMETRY

SIMULTANEOUS THERMO-
GRAVIMETRY-DIFFERENTIAL
SCANNING CALORIMETRY

THERMOGRAVIMETRIC
ANALYSIS

DILATOMETRY

DIELECTRIC ANALYSIS

THERMOMECHANICAL
ANALYSIS

MULTIPLE MODE
CALORIMETRY

ACCELERATING RATE
CALORIMETRY

NETZSCH Analyzing & Testing
www.netzsch.com/ta